Dynamics of water and aqueous solutions in geometrical confinement

Dynamik von Wasser und wässrigen Mischungen in eingeschränkten Geometrien

Zur Erlangung des Grades eines Doktors der Naturwissenschaften (Dr. rer. nat.) genehmigte Dissertation von Matthias Sattig, M.Sc. aus Dieburg
Tag der Einreichung: 13. Juni 2016, Tag der Prüfung: 06. Juli 2016

Juli 2016
Darmstadt — D 17

1. Gutachten: Prof. Dr. Michael Vogel
2. Gutachten: Prof. Dr. Franz Fujara

TECHNISCHE UNIVERSITÄT DARMSTADT

Fachbereich Physik
Institut für Festkörperphysik

Dynamics of water and aqueous solutions in geometrical confinement
Dynamik von Wasser und wässrigen Mischungen in eingeschränkten Geometrien

Genehmigte Dissertation von Matthias Sattig, M.Sc. aus Dieburg

1. Gutachten: Prof. Dr. Michael Vogel
2. Gutachten: Prof. Dr. Franz Fujara

Tag der Einreichung: 13. Juni 2016
Tag der Prüfung: 06. Juli 2016

Darmstadt — D 17

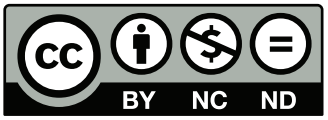

Erklärung zur Dissertation

Hiermit versichere ich, die vorliegende Dissertation ohne Hilfe Dritter nur mit den angegebenen Quellen und Hilfsmitteln angefertigt zu haben. Alle Stellen, die aus Quellen entnommen wurden, sind als solche kenntlich gemacht. Diese Arbeit hat in gleicher oder ähnlicher Form noch keiner Prüfungsbehörde vorgelegen.

Darmstadt, den 13. Juni 2016

_____

(Matthias Sattig)

Abstract

Water is one of the most vital substances for life, science, and technology. In many situations, water is confined to very narrow geometries, for example, in living cells it is severely confined in between biomolecules. The peculiarities of such systems are not yet understood and have drawn a lot of attention in current research. Additionally, the anomalous behavior of water in the bulk, e.g. the density anomaly, is not yet explained. The most common theories aiming to rationalize the behavior of water base on the assumption of a liquid-liquid phase transition at very low temperatures. Direct observation of water at these temperatures is impossible due to crystallization. In water confined in narrow geometries or in aqueous mixtures freezing is suppressed and observation of liquid water at very low temperatures is possible, what can provide valuable information about the nature of water and the interactions in biologically relevant systems.

The aim of this thesis is to characterize the dynamical behavior of water and aqueous mixtures in the regularly structured mesoporous silica MCM-41 over a large temperature range. For this purpose, ^{2}H NMR methods are used, which can provide information about time scales and geometry of the motional mechanism. These capabilities render ^{2}H NMR a valuable method to investigate supercooled liquids in confinement.

The research in this work shows that current theories on water in confinement are incomplete. A dynamic crossover is found near the suggested liquid-liquid phase transition temperature. It is accompanied by the emergence of a second dynamically distinguishable water species, suggesting that the observed transition is not caused by a liquid-liquid phase transition but rather by a solidification of the pore internal water. The residual liquid resides at the pore walls and shows the characteristic behavior of a β-process. This process is found in many systems where water is close to an interface and shows several universal features. One is an additional mild crossover at ca. 185 K that may be related to a glass transition. A new method is introduced to measure the temperature dependence of the corresponding α-process and a novel model of water in confinement is proposed in order to explain the present findings.

In comparison to water, the glass former glycerol does not show such drastic confinement effects in MCM-41. On reduction of the confinement size, the glycerol molecules merely show a slight acceleration of dynamics. The weak influence of the confinement on glycerol shows that a generalization of the proposed interpretation model for water is not applicable to other simple liquids.

Bulk and confined aqueous mixtures have been investigated in this work in a broad temperature range and their dynamics were characterized. The added alcohols in the mixtures are structurally similar and vary mainly in their hydrogen bonding capabilities. It was found that the phase behavior of the mixtures strongly depends on the interactions between the constituents. In the MCM-41 confinement, phase separation happens in mixtures where water clusters are prefered to spatially extended H-bond network of both water and alcohol molecules. The results indicate that water clusters in the pore center rather than at the interface. Depending on the pore size and the size of the solvent, the water cluster may reach a critical size for crystallization. Crystallization was not found in previous studies of similar mixtures in smaller confinements, demonstrating the importance of the pore size and the specific interactions for investigations of dynamics of water and aqueous mixtures.

Zusammenfassung

Wasser ist essentiell für das Leben sowie in Forschung und Technologie. In vielen Fällen liegt Wasser in stark eingeschränkten Geometrien vor. Ein Beispiel sind lebende Zellen, in welchen Wasser von großen Mengen an Biomolekülen umgeben ist. Die Eigenschaften solcher Systeme sind bisher unverstanden. In den gängigsten Theorien zum Verhalten von Wasser wird ein Flüssig-Flüssig Phasenübergang bei sehr tiefen Temperaturen postuliert. Da Wasser bei diesen Temperaturen kristallisiert, ist eine direkte Beobachtung dieses Effekts aber nicht möglich. In eingeschränkten Geometrien und in wässrigen Mischungen mit anderen kleinen Molekülen ist das Gefrieren unterdrückt, sodass flüssiges Wasser bei sehr tiefen Temperaturen untersucht werden kann. Die Forschung an Wasser und Wassermischungen kann daher wertvolle Informationen über die Natur von Wasser und biologisch relevanten Mischungen liefern.

Das Ziel dieser Arbeit ist die Charakterisierung des dynamischen Verhaltens von Wasser und wässrigen Mischungen in mesoporösem MCM-41 über einen weiten Temperaturbereich. Zu diesem Zweck werden ^{2}H-NMR-Methoden verwendet. Diese können Informationen über die Zeitskalen und die Geometrie der Bewegungsprozesse in Wasser liefern. Aufgrund dieser Möglichkeiten ist ^{2}H-NMR eine geeignete Methode zur Untersuchung von unterkühltem Wasser.

Die durchgeführten Messungen zeigen, dass die aktuellen Theorien zu Wasser in beschränkten Geometrien erweitert werden müssen. Eine Veränderung des Temperaturverhaltens wird in der Nähe des vorausgesagten Flüssig-Flüssig Phasenübergangs gefunden. Sie wird begleitet von der Entstehung einer zweiten, dynamisch unterschiedlichen Wasserspezies. Dies deutet darauf hin, dass das Temperaturverhalten nicht durch den Phasenübergang dominiert wird, sondern durch Verfestigung des Wassers im Porenzentrum. Die restliche Flüssigkeit befindet sich an den Porenwänden. Sie zeigt die Eigenschaften eines β-Prozesses. Dieser Prozess wird in vielen Systemen gefunden, in welchen sich Wasser nahe an Grenzflächen befindet und zeigt mehrere universelle Eigenschaften. Eine dieser Eigenschaften ist eine schwache Änderung des Temperaturverhaltens bei 185 K, welche möglicherweise mit einem Glasübergang in Verbindung gebracht werden kann. In der vorliegenden Arbeit wird eine neue Methode vorgeschlagen, um den zugehörigen α-Prozess zu detektieren und zusätzlich wird ein erweitertes Erklärungsmodell vorgestellt, um Wasser in beschränkten Geometrien zu beschreiben.

Der Glasbildner Glyzerin zeigt keine starken Effekte durch das MCM-41. Bei verringerter Porengröße zeigen die Glyzerinmoleküle nur eine leichte Beschle-

unigung ihrer Dynamik. Der geringe Einfluss auf Glyzerin zeigt, dass eine Übertragbarkeit des vorgeschlagenen Interpretationsmodells für Wasser auf andere einfache Flüssigkeiten nicht möglich ist.
Die Dynamik wässrige Mischungen mit und ohne Confinement wurden ebenfalls in einem weiten Temperaturbereich charakterisiert. Die zugefügten Alkohole sind strukturell sehr ähnlich und unterscheiden sich hauptsächlich durch ihre Möglichkeiten Wasserstoffbrücken zu bilden. Eine starke Abhängigkeit des Phasenverhaltens der Mischungen von den spezifischen Wechselwirkungen wurde gefunden. Phasenseparation geschieht bevorzugt in jenen Mischungen, in welchen Cluster von Wasser statt eines ausgedehnten Wasserstoffbrückennetzwerkes gebildet werden. Die Messungen deuten an, dass sich das Wasser bevorzugt in der Porenmitte statt an der Grenzfläche befindet. Je nach Größe der Poren und des Kosolvents können die Wassercluster eine Größe erreichen, bei welcher sie kristallisieren. In früheren Untersuchungen an ähnlichen Mischungen in kleinerem Confinement als in dieser Arbeit wurde keine Kristallisation gefunden. Dies unterstreicht die Bedeutung der Porengröße und der individuellen Wechselwirkungen in Untersuchungen der Dynamik von Wasser und wässrigen Lösungen.

Contents

1 Introduction

Water is one of the most important substances on earth. It allows life as we know it to exist. It plays major roles in climate and geology, it is essential in nature, in many fields of science like biology and medicine, and in many technological applications. Water covers a huge part of the earth's surface and is a main component of the human body. Despite its major relevance for basically all aspects of our lives, our knowledge about water is still not yet complete. Water exhibits a number of anomalous properties, for example, a density maximum at 4 °C. These anomalies still lack a proper explanation.

In the past, many studies were performed to investigate the behavior of water. One main focus was to clarify its importance in biological processes. In biological systems, water is mostly found in close vicinity to other molecules. An example for this is the interior of living cells, where plenty of proteins, lipids, polysaccharides, as well as DNA, RNA and several small organic and anorganic molecules are solved in an aqueous solution called cytoplasm. The concentrations of additional molecules are high and water is confined on a sub-nanometer scale [1]. Thus, not only the behavior of pure bulk water is of enormous interest, but also its dynamical behavior in spatial confinement. To fully understand the mechanisms underlying life, as for example why proteins only work in presence of a solvent [2], it is necessary to investigate the mutual interactions of water and other molecules involved.

It was proposed that the main reason for the anomalous behavior of water is its ability to form hydrogen bonds (H-bonds). H-bonds are rather weak compared to, e.g., covalent bonds. Nevertheless, H-bonds plays a crucial role in the behavior of water. Several hypotheses have been postulated to explain water behavior [3–5]. The most popular ones suggest a liquid-liquid phase transition between two water phases in the deeply supercooled regime [6, 7]. At ca. 225 K and at elevated pressure water was proposed to change from a high density liquid to a low density liquid in a first order phase transition, due to the tetrahedral ordering of the water H-bonds. So far, the phase transition has not been directly observed in experiments, because the access to the temperature region of interest is hampered by crystallization that occurs inevitably in the so called *no-man's land* between ca. 150 K and 230 K [8]. In addition to the manifold of experimental studies, several simulations have been performed to clarify the existence of this low temperature phase transition.

Two possibilities to circumvent crystallization is to confine water to nanoscopic volumes or to mix it with additional solvents. With crystallization suppressed it is possible to investigate liquid water at temperatures low enough to observe the possible implications of the hypothesis introduced above. In this way, the search for physical explanations of the water anomalies is linked to the field of water in confinement. Competing results have been found in various studies. Many researchers provided evidence in favor of the proposed liquid-liquid phase transition, others argued against this interpretation.

The objective of this work is to add to the understanding of water in narrow geometries. For this purpose water confined in the common confinement material, mesoporous silica MCM-41 is investigated. Previous studies on this system have been performed before, but they do not agree in their interpretation: While some researchers found a drastic change in the dynamics at the proposed phase transition and interpreted it as evidence for the latter [9], others found no indications for this kind of behavior in the same systems [10]. Here, ^{2}H NMR is utilized in order to determine the dynamical behavior of D_2O in MCM-41. The research survey includes a variation of the confinement size, in order to identify a model describing the dynamics.

^{2}H NMR is a valuable tool to thoroughly characterize the dynamics of a deuterated molecular species in a wide range of correlation times. Combining several different techniques rotational dynamics can be observed over twelve orders of magnitude in time. In addition, insights into the mechanism of reorientation can be obtained that are not accessible to other methods or only in a narrow dynamic range. Hence, ^{2}H NMR is able to provide valuable information and can help to gain a deeper insight into the properties of a sample.

The application of MCM-41 gives rise to the question of how far the enclosed liquid is influenced by its interaction with the confinement. To help answering this question, a MCM-41 material with functionalized inner surface is investigated as well. In addition, water in mixtures with alcohols is investigated. Those mixtures can be used for multiple purposes. A study of the concentration dependence can help to further improve the understanding of water behavior and its interaction with other molecules. This knowledge can be transferred to biologically and technically relevant systems by successively increasing the complexity of the added solute up to the point of proteins. By variation of solute and concentration and by altering the inner surface of the confinement it is also possible to single out finite-size effects and guest-host interactions. This is one of the aims of the research unit FOR1583 in the framework of which this thesis was done.

The structure of this thesis

The thesis begins by introducing the current state of research on supercooled liquids, with a focus on supercooled water in chapter 2. This includes an overview over features of supercooled water and water mixtures in confinement. In the subsequent chapter 3 deuteron NMR is introduced. It is the main method employed to characterize dynamics in this work. The basics of NMR are explained and supplemented by a theoretical background for the performed experiments. In chapter 4 the experimental setup is detailed. Additionally, the characterized samples and preparation methods are presented. The results of the NMR experiments performed on D_2O confined to MCM-41 will be discussed in chapter 5. There, the dynamics will be characterized over a large temperature range, in different types of confinement. The results will be compared with two competing model explanations. Chapter 6 will characterize glycerol in similar MCM-41 confinements, in order to compare results for a good glass former to the results obtained for water. In chapter 7, a determination of the magnetic field dependence of characteristic NMR parameters are presented. Chapter 8 will then present the results obtained from several water-alcohol mixtures confined to MCM-41. Those will be compared with the findings of the group of J. Swenson, our collaboration partner in this project. In the final chapter 9 the key findings of the this thesis will be summarized.

2 Supercooled liquids, water, and aqueous mixtures

This work deals with water and water mixtures in a broad temperature range. In this chapter, the exceptional behavior of water is discussed and the most common thermodynamical concepts are presented, which try to explain those properties. All models indicate that the mechanisms underlying the anomalous behavior manifest themselves in observable features of the dynamical properties of water. They are assumed to be most pronounced in the deeply supercooled regime where water usually only exists in one of its crystalline forms. The characterization of those dynamical properties is the main goal of this thesis.
Therefore, the properties of supercooled liquids, in particular, the dynamics close to the glass transition, are discussed in section 2.1. Subsequently follows the discussion of the anomalous behavior of water in section 2.2. There, the most widely accepted theories explaining its behavior are introduced. Common concepts to circumvent crystallization and investigate water in the supercooled regime are presented in section 2.3. Those include mixing water with anti-freezing agents, for example salts or short alcohols, or with larger biomolecules, e.g. proteins [7, 11]. The interactions between water and the solute suppress freezing. An alternative route to avoid crystallization is to confine water within severe spatial limitations. The interactions with the interface as well as the finite size of the systems can prevent the phase transition. The final section in this chapter, section 3.9, shortly introduces common experimental methods used in the research on confined water.

2.1 What is a supercooled liquid, what is a glass?

When a liquid is cooled, it will eventually reach its melting temperature T_m, where it freezes. Crystallization can occur in a homogeneous or heterogeneous way. In the first case, crystal nuclei larger than a critical size are formed spontaneously and induce freezing of the whole sample. In the second case, impurities in the system act as seeds for crystallization. Some liquids, especially when they are very pure, can be cooled below this temperature and become *supercooled*. The phenomenology of supercooled liquids is presented in this section. The discussion in this thesis is far from being complete. For good reviews on the topic, the reader is referred to the articles of Cavagna [12], Ediger and Harrowell [13], Debenedetti and Stillinger [14] and Angell [15].

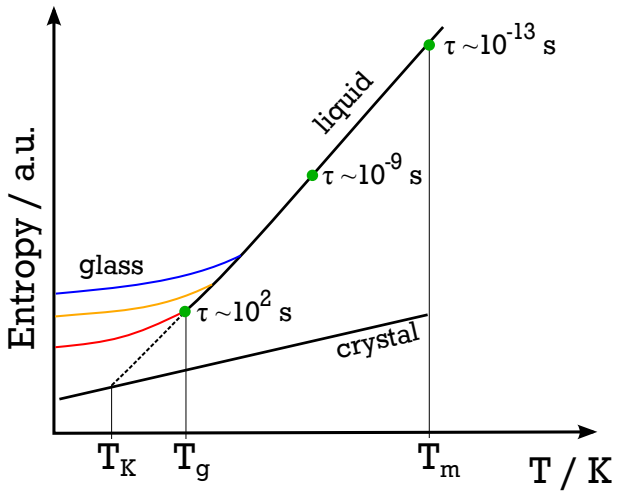

Figure 2.1.: Sketch of the liquid and crystal entropy over temperature. Green dots mark common values of the correlation time at certain temperatures, colored lines represent the behavior below T_g for different cooling rates. The blue line corresponds to the highest, the red line to the lowest cooling rate. Reproduced after [12].

2.1.1 Supercooling a liquid

When crystallization at T_m can be circumvented, the liquid becomes supercooled. This can be achieved in several ways: Heterogeneous freezing can be avoided by using pure liquids with as few impurities as possible. Homogeneous crystallization can be suppressed in two ways. First, the number of spontaneously forming crystal nuclei can be reduced by using smaller samples. The chance of spontaneous freezing is proportional to the volume [12]. For example, water was supercooled to temperatures of 229 K in ultra pure micrometer sized water droplets [16]. A second way is to apply high cooling rates. Then the crystallization is quenched since the liquid is not given enough time for growth of a nuclei [12]. This was used to prepare amorphous glasses of water: By applying cooling rates larger than 10^7 Ks^{-1} so called *hyperquenched glassy water* (HGW) can be created, while *amorphous solid water* (ASW) results from vapor deposition on cooled substrates, see in section 2.2 for details.

In the supercooled state, the crystal is energetically favorable over the liquid and hence, the supercooled liquid is metastable. The situation is sketched in figure 2.1 for the entropy S. Similar relations hold for the specific volume. Upon cooling, the entropy of the liquid S_{liq} decreases monotonically with a slope given by the specific heat c_p:

$$\left(\frac{dS}{dT}\right)_p = \frac{c_p}{T} \tag{2.1}$$

The entropy of the liquid and associated specific heat are larger than those of the crystal state. At the Kauzmann temperature T_K, the entropy of both, crystal and liquid, would intercept. This is called the Kauzmann paradox or *entropy crisis*, since such an intersection of an amorphous and a crystalline state is not physical [12, 17]. However, before this point is reached, the dynamical glass transition is encountered at the temperature $T_g > T_K$. At T_g the entropy levels and the heat capacity becomes comparable to that of the crystal [14]. The change in heat capacity prevents the intersection of the entropy of liquid and crystal and thus, the Kauzmann paradox. Below T_g, the system is trapped in one of the available amorphous states and cannot leave it on the experimentally available time scale. The system cannot sample through all energetically available states, its ergodicity is broken [12]. On infinite time scales ergodicity would be restored below T_g. Hence, the glass transition is a dynamical phenomenon rather than a thermodynamical event. The exact temperature at which the glass transition occurs depends on the cooling rate. Slower cooling causes a lower transition temperature T_g, while at higher cooling rates the glass is formed at higher temperatures. Usually, the glass transition temperature T_g is defined as the temperature where the shear viscosity η reaches $\eta(T_g) = 10^{12}$ poise or equivalently where the structural relaxation time τ reaches $\tau = 10^2$ s. These definitions of T_g agree well with the values for T_g obtained from *differential scanning calorimetry* (DSC). In DSC, the glass transition is observed as step in the measured heat flow. The onset of the step is conveniently used to define T_g. The glass transition does not affect the structure of the supercooled liquid: Scattering experiments observed no structural changes when cooling below T_g [12, 18]. Therefore, most studies concerning the glass transition focus on the dynamical properties such as diffusion coefficients or the structural relaxation times.

2.1.2 Dynamics on cooling towards the glass transition

The properties of materials can be characterized by *correlation functions* (CF). While the structure, is often described using pair-CFs, dynamics can be addressed by auto-CFs $F(t_1,t_2)$. They correlate properties of a single particle at a time t_1 and at a time t_2. Motion leads to a decay of such auto-CF. In the most simple cases this can be expressed by an exponential decay with a characteristic time τ:

$$F(t') = \exp\left[-\left(\frac{t'}{\tau}\right)\right], \tag{2.2}$$

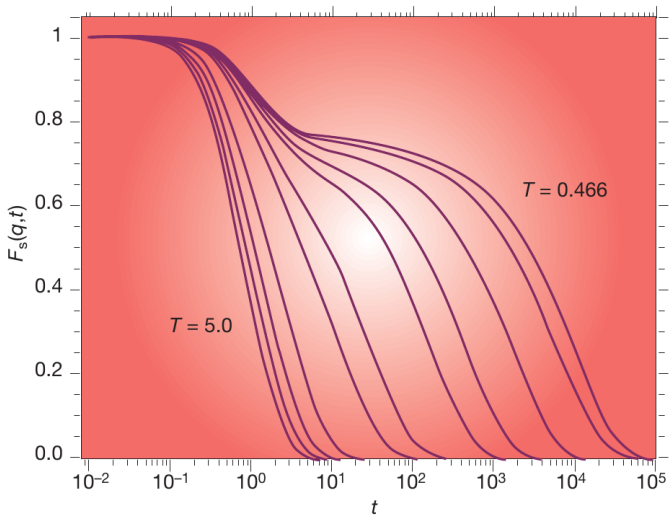

Figure 2.2.: Two-step decay of CF encountered in supercooled liquids: at highest temperatures an one-step decay is visible, at lower temperatures, a two-step decay is found. The faster one corresponds to vibrational motions, the slower one to the structural relaxation. Figure adapted from [14].

where $t' = t_2 - t_1$ is defined by assuming thermal equilibrium. A process behaving this way is called Debye process and can be found in simple liquids. At ambient temperatures above the melting point T_m, a liquid usually exhibits correlation times on the order of $\tau \sim 10^{-13}$ s. On cooling towards the glass transition, the motion slows down drastically by up to 15 orders of magnitude, to reach 100 s at he glass transition T_g.

When the liquid is cooled below its melting temperature T_m and approaches the glass transition temperature T_g, the CF start to show a pronounced two step decay [19, 20], as sketched in figure 2.2. The decay at short times correspond to the vibrational motions of the molecules. Vibrations will not be addressed in this work. The second decay results from to the structural relaxation process, or α-process, of the liquid. The structural relaxation process describes the motions of particles that leave the local cage formed by their neighbors and pass into a new environment. In the isotropic case usually found in bulk liquids, the α-process destroys all correlation.

Besides the α-process, a secondary relaxation is often found in glass forming materials, designated as β-process[1]. The corresponding time scale is shorter than that of the α-relaxation and larger than that of the vibrations. The β-process is often considered as strongly localized motion. Glass forming liquids were classified as *type A* glass formers or *type B* glass formers. In type B glass formers a β-process is found well separated from the structural relaxation. In type A glass formers no separate β-process is observable, but a so called *excess wing* is

[1] It is not to be mixed up with the vibrational processes.

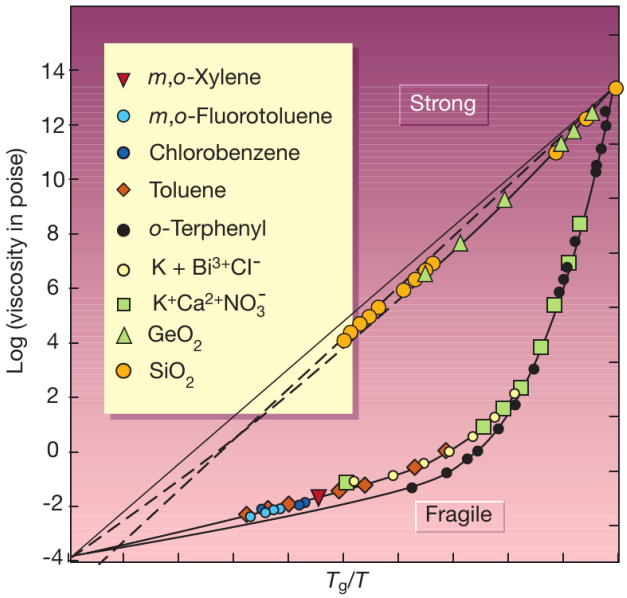

Figure 2.3.: Examples of strong and fragile glass formers. Figure adapted from [14].

found close to the α-process. The excess wing exhibits properties similar to a β-process. Therefore, it is still a matter of debate, whether the excess wing and the β-process are similar processes independent from the α-process or whether the excess wing or the β-process are features connected to the structural relaxation.

The temperature dependence of the characteristic time of the α-process τ exhibits two distinct kinds behavior: It can follow a *strong* or a *fragile* temperature dependence. Strong glass formers show an Arrhenius (ARR) type behavior

$$\tau(T) = \tau_0 \exp\left(\frac{E_a}{k_B T}\right), \tag{2.3}$$

while fragile liquids show a temperature dependence described by the *Vogel-Fulcher-Tammann* (VFT) equation

$$\tau(T) = \tau_0 \exp\left(\frac{D}{k_B(T - T_{VFT})}\right). \tag{2.4}$$

Examples for strong and fragile glass formers are shown in the Angell plot, figure 2.3. There, an ARR behavior appears as a straight line with a slope given by the activation energy E_a. The VFT law appears curved and it diverges at the VFT temperature T_{VFT}. To characterize the liquid behavior, the *fragility m* was defined as the slope at the glass transition point

$$m = \left(\frac{\partial \log_{10} \eta}{\partial (T_g/T)} \right)_{T=T_g} = \kappa \left(\frac{T_{VFT}}{B+\kappa} + 1 \right), \qquad \kappa = \log_{10} \left(\frac{\tau(T_g)}{\tau_0} \right) \tag{2.5}$$

A perfectly strong glass exhibits $m = \kappa$, while m is higher in the case of a fragile glass former. A well known example of a strong glass former is silica (SiO_2), which is among the strongest known materials [7]. In contrast, mildly supercooled water is among the most fragile liquids [21]. A strong behavior is often found in liquids that show a network structure, caused by directed interactions [14]. Fragile glass formers usually show non-directional interactions and do not form networks very well [12]. The Adam-Gibbs theory strives to rationalize the origins of the temperature behavior of a liquid.

The Adam-Gibbs theory

The theory of Adam, Gibbs and Di Marzio, conveniently called Adam-Gibbs (AG) theory, is a purely thermodynamic reasoning to resolve the apparent paradoxes formulated by Kauzmann and Flory [22, 23] and to describe the dynamics of a supercooled liquid. The theory is based on the calculations of Gibbs and Di Marzio [24, 25], in which they have shown that a system with vanishing configurational entropy must undergo a second order phase transition at the temperature T_k. In addition, the AG theory introduces the concept of *cooperatively rearranging regions* (CRR) [26]. Those are the smallest clusters of particles, that can move independently of their environment. The particles in a CRR must move together and, thus, only a limited set of states Ω is available to a CRR. AG assumed the set Ω to be constant, independent of temperature and size of the CRR. In contrast, the CRRs themselves grow with lowering temperature. The configurational entropy S_c of a cluster with n particles can be written as

$$S_c(n) = \frac{\log \Omega}{n}. \tag{2.6}$$

By increasing the size n of a cluster, the correlation length of cooperative motion $\xi^d \sim n$ grows. Jenckel [27] proposed an exponential growth of the relaxation time with the correlation length $\tau \sim \exp(\xi^\psi)$. Under the assumption $\psi = d$, the AG gives the temperature dependence of the correlation time implicitly by the temperature dependence of the entropy:

$$\tau \propto \exp \left(\frac{A}{TS_c(T)} \right) \tag{2.7}$$

When the configurational entropy S_c is expressed by the excess entropy of the liquid with respect to the crystal, $S_c = S_{liq} - S_{cr}$, it can be written as

$$S_c(T) = \Delta c_p \frac{T - T_k}{T_k}. \tag{2.8}$$

This results in the well known VFT expression of the correlation time:

$$\tau(T) = \tau_0 \exp\left(\frac{AT_k}{\Delta c_p T(T - T_k)}\right) \approx \tau_0 \exp\left(\frac{B}{T - T_k}\right) \tag{2.9}$$

With those considerations Adam, Gibbs, and Di Marzio were able to resolve the entropy crisis and at the same time establish the connections between configurational entropy, a correlation length ξ and the correlation time τ close to the glass transition. More complex theories have been developed to describe the dynamics at temperatures much higher than T_g and to refine the AG approach. Those theoretical frameworks are out of scope of this work. For an introduction to the *mode coupling theory* and the *random first order transition theory* the interested reader is referred to references [12, 28].

2.1.3 Dynamic heterogeneities and non-exponential correlation functions

The α-relaxation of supercooled liquids typically exhibit a pronounced non-exponential decay. Then the CF is often described by a *Kohlrausch-William-Watts* (KWW) function [18, 29, 30]:

$$F(t) = \exp\left[-\left(\frac{t}{\tau}\right)^{\beta}\right] \tag{2.10}$$

In addition to the characteristic time τ, a stretching parameter β is introduced. The stretching can be explained by two effects. First, there is the *homogeneous* case, in which the molecular motion is strongly correlated. For example, correlated forward-backward motion intrinsically stretches the CF of every single molecule, resulting in a stretched overall CF. By contrast, in the *heterogeneous* case, a distribution of correlation time $G\big[\log(\tau)\big]$ exists, e.g. due to different local environments within the sample. The values of τ and can vary over several orders of magnitude [31, 32]. The overall CF is the sum of the individual CF of all molecules and hence, stretches in accordance to the distribution $G\big[\log(\tau)\big]$ [14, 33]. Advanced studies using hole-burning techniques in *dielectric spectroscopy* (DS) [17] or multi-time correlation functions in NMR [34], have shown that both origins of non-exponentiality can be found in a supercooled liquid at the same time.

Stretched exponential CF are often approximated by a KWW function. This provides a measure of the time scale of the motion that can be compared to other experiments. Nevertheless, the KWW formula describes the correlation decays only in some situations appropriately. The shape of the decay curve depends on the specifics of the motional mechanisms within the sample. Therefore, other functional forms are also used to fit the data. In ^{2}H NMR, direct access to the shape of the correlation function is possible for slow dynamics using the *stimulated echo* (STE) experiment, see section 3.4. In the case of faster dynamics, input from frequency domain methods like DS is used to supplement ^{2}H NMR. In the frequency domain, the susceptibility $\chi(\omega)$ is measured, see section 3.9 for details. Several functional forms are conveniently used to approximate the susceptibilities or the *spectral densities* (SD) J(ω):

$$\mathrm{J}(\omega) = \frac{\chi''(\omega)}{\omega} \propto \int_{-\infty}^{\infty} \mathrm{F(t)} e^{\iota\omega \mathrm{t}} \mathrm{dt}. \tag{2.11}$$

When the distribution G$\left[\log(\tau)\right]$ is symmetrically broadened the *Cole-Cole* (CC) form [35]

$$\mathrm{J_{CC}}(\omega) = \frac{\sin\left(\frac{\pi}{2}\right)(\omega\tau)^{\alpha}}{\omega\left[1+(\omega\tau)^{2\alpha}+2\cos\left(\frac{\pi}{2}\right)(\omega\tau)^{\alpha}\right]} \tag{2.12}$$

can often be applied. In the case of an asymmetrically stretched high-frequency flank, the *Cole-Davidson* (CD) form [35]

$$\mathrm{J_{CD}}(\omega) = \frac{\sin\left[\gamma \arctan(\omega\tau)\right]}{\omega\left[1+(\omega\tau)^2\right]^{\frac{\gamma}{2}}} \tag{2.13}$$

is a good description. Both are special cases of the *Havriliak-Negami* (HN) function [35]

$$\mathrm{J_{HN}}(\omega) = \frac{\sin\left\{\gamma \arctan\left[\frac{(\omega\tau)^{\alpha}\sin\frac{\pi\alpha}{2}}{1+(\omega\tau)^{\alpha}\cos\frac{\pi\alpha}{2}}\right]\right\}}{\omega\left[1+2(\omega\tau)^{\alpha}\cos\frac{\pi\alpha}{2}+(\omega\tau)^{2\alpha}\right]^{\frac{\gamma}{2}}}. \tag{2.14}$$

The CC spectral density can be derived from eq. (2.14) by setting $\gamma = 1$, while the CD spectral density is obtained by setting $\alpha = 1$. These three SD have been used purely empirically for some time. Later it was shown that the CC form is the frequency domain representation of the Mittag-Leffler function [36]. The CD spectral density is not equivalent but closely related to a KWW function [37].

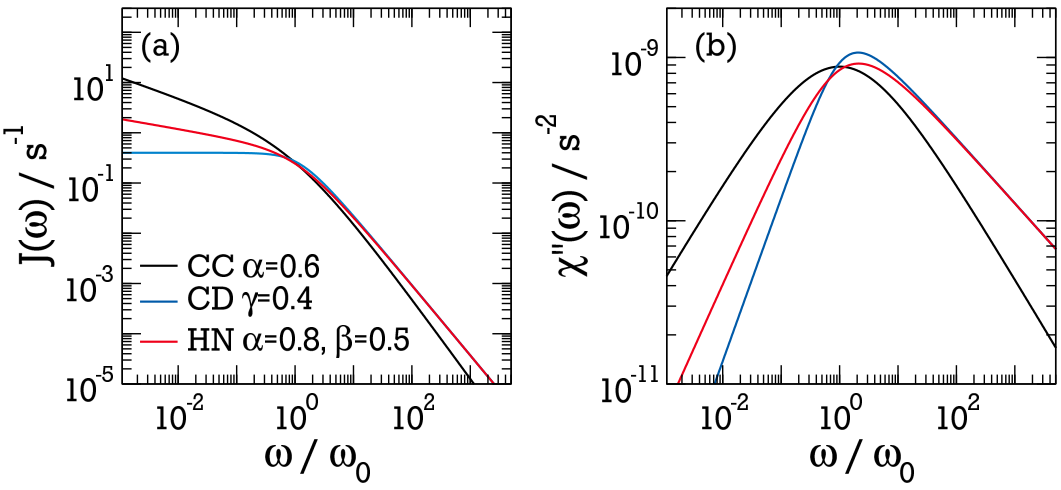

Figure 2.4.: Plots of the CC, CD, and HN spectral density (a) and the imaginary part $\chi''(\omega)$ of the respective susceptibilities (b).

Owing to the large success in describing DS data with the CC, CD, or HN SD, they were adopted in the evaluation of ^{2}H NMR data [38].

In the susceptibility representation, the main difference between the CC and CD forms is their shape: on a logarithmic frequency axis the CC exhibits a symmetric shape of the loss peak with a slope of $\omega^{\pm\alpha}$ on both flanks. The CD in contrast is asymmetric exhibiting a slope of ω^1 on the low frequency flank and $\omega^{-\gamma}$ on the high frequency side of the peak. Exemplary plots of CC, CD, and HN functions are depicted in figure 2.4. Panel (a) shows the SD defined in equations (2.12) - (2.14), in (b) the imaginary part of the susceptibility $\chi(\omega)$ is shown. In supercooled liquids the structural relaxation is often properly described by a CD [31], while secondary relaxations are often well approximated by a CC. The shape of the SD can be determined by NMR using field cycling methods, see in section 3.6.

Correlation time averages

When a distribution of correlation times $G\big[\log(\tau)\big]$ exists, it is not straightforward to give a single correlation time to characterize the timescale of the distribution. Often different experimental methods report differently averaged correlation times. The characteristic time of dynamics is often defined by the inverse of the maximum $\tau = \omega_{\max}^{-1}$ of the dielectric loss $\chi''(\omega)$ or by the mean correlation time $\langle\tau\rangle$. Both methods result in rather different values for different distribution functions, e.g. due to fractal behavior in the HN form [35]. The mean logarithmic correlation time can be defined by [39]:

$$\langle \ln\tau \rangle = \int_{-\infty}^{\infty} \mathrm{d}(\ln\tau)\mathrm{G}(\ln\tau)\ln\tau. \tag{2.15}$$

This quantity can be calculated for all common forms of distributions and allows for better comparison of experimental data. By employing the properties of the logarithmic moments of the distribution functions mean logarithmic time constants can be expressed as [39]

$$\ln\tau_{\mathrm{m}} \equiv \langle \ln\tau \rangle = \begin{cases} \ln\tau & \text{Cole-Cole, Logarithmic Gauss} \\ \ln\tau + \Psi(\gamma) + \mathrm{Eu} & \text{Cole-Davidson} \\ \ln\tau + \left(1 - \frac{1}{\beta}\right)\mathrm{Eu} & \text{Kohlrausch-Williams-Watts} \end{cases} \tag{2.16}$$

In this equation Eu is the Euler constant (Eu ≈ 0.5772) and Ψ is the derivative of the gamma function Γ. The parameters β, γ and τ are the stretching parameters and the time constant of the respective distribution, c.f. eqs. (2.10, 2.12 - 2.14). In this work, the correlation time τ_{m} will be used to characterize the time scale of a dynamical process independent of the specific distribution function used for data analysis.

2.2 The anomalous properties of water

Water is a simple molecule. It consists of two hydrogen atoms covalently bound to an oxygen. The HOH opening angle is 104.5°, close to the tetrahedral angle [40]. Nevertheless, water is rather special and exhibits many anomalies: It is the only naturally occurring inorganic liquid and exhibits unusually high melting and boiling temperatures compared to other non-metallic compounds [41]. A simple p-T phase diagram is sketched in figure 2.5. The exact number of anomalies of water depends on the source and varies somewhere between thirty up to a hundred [42]. The best known anomaly is the density maximum at 277.15 K. It is responsible for floating of ice and survival of fishes in shallow ponds in winter. Less known are other properties that nevertheless play important roles in thermodynamic calculations, e.g. the minima of the isothermal compressibility κ_{T} at 319.15 K and of the isobaric heat capacity $\mathrm{c_p}$ at 308.15 K [3]. The response functions κ_{T} and $\mathrm{c_p}$ are connected to volume and entropy fluctuations which usually decrease upon cooling. In water this is not the case and it is found that volume and entropy are anti-correlated, such that an increase in volume is connected to decreasing entropy [6]. In the crystalline state, it can exist in sixteen different forms of ice [42, 43].
Water molecules interact hydrogen bonds (H-bond). This type of bonding is strongly directed [44]. A water molecule has the ability to form up to four

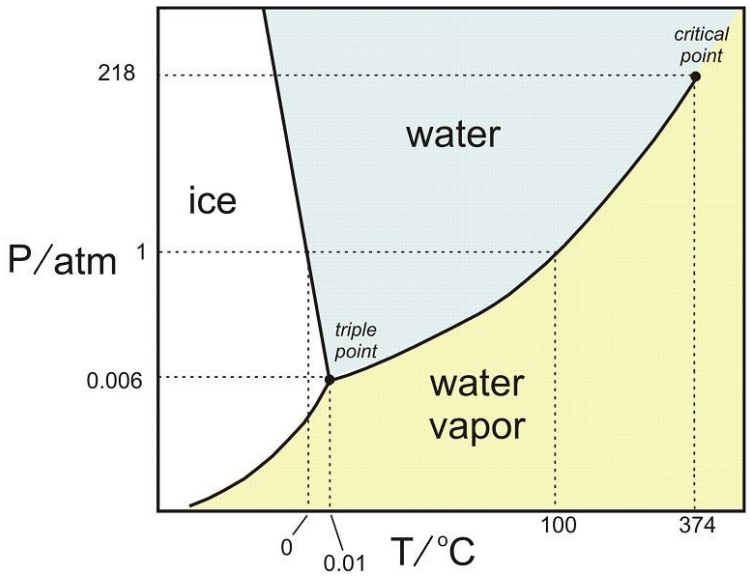

Figure 2.5.: p-T diagram of water. Figure adapted from [47].

H-bonds to other water molecules. Thereby, a tetrahedral network of bonds is established. The lifetime of a bond is limited, thus the network is transient and exhibits no long range structure [41]. The network was identified as the origin of the anomalous properties of water [40, 45]. The structuring introduced by the directional character of the H-bonds also influences the density: The network requires larger intermolecular distances than in an unstructured state [45]. Upon cooling the motion in the sample slows down and the network becomes more stable, since the average life time of a bond increases. The thermodynamic anomalies of water become more and more pronounced at lower temperatures [41].

Extrapolation of some of the properties of bulk water suggest the existence of a singularity at 225 K [3, 46]. Indications for a divergence were found for example in static quantities such as the isothermal compressibility, and in dynamic properties such as the shear viscosity [46]. The apparent thermodynamic singularity is located deeply in the supercooled region of water. Thus, investigations of water properties at low temperatures below the melting point are necessary in order to understand the properties of water. Several theories have been proposed to explain the features of water and other anomalous liquids by means of thermodynamic reasoning involving the supercooled state. Three models were widely discussed in literature [7]:

- The *stability limit conjecture* (SLC) was proposed by Speedy in 1982 [3, 48]. It assumes the apparent divergence observed at about 225 K to be caused by the crossing of a spinodal line. This is the line $T_s(p)$ in the p-T phase diagram of water marking the limit of water stability, i.e. the limit

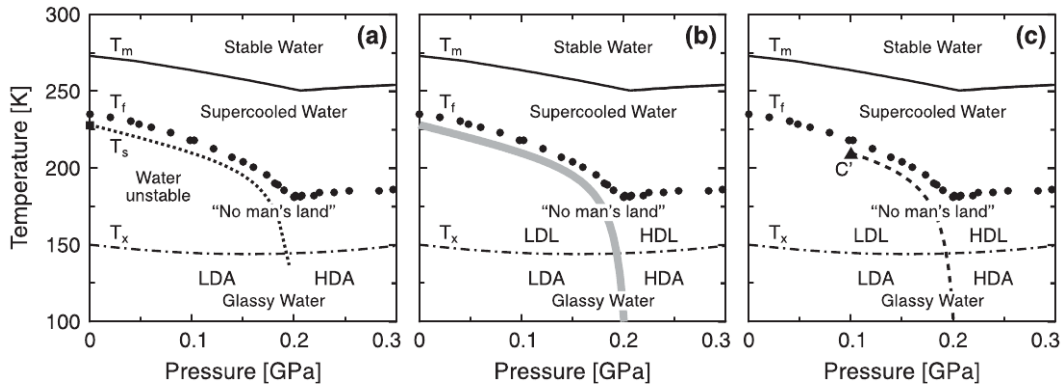

Figure 2.6.: Sketches of (a) the stability limit conjecture marked by the dotted line T_s, (b) the singularity free interpretation, and (c) the liquid-liquid critical point hypothesis. The grey line in (b) is the the locus of extreme values of the response functions and C′ in (c) is the second critical point. In all panels, T_m is the melting temperature, T_H the homogeneous nucleation temperatures, the nucleation temperature upon heating amorphous ice. The figure is adapted and modified from [6].

where water becomes mechanically unstable, see figure 2.5. The locus of the spinodal is given by [3]:

$$\lim_{p \to p_s} \left(\frac{\partial p}{\partial T} \right)_V = 0^- \tag{2.17}$$

It was theorized, that the spinodal line in the low temperature region is the same one that in the superheated region of water. The spinodal in both temperature regions are connected in the negative pressure region. The SLC predicts that the low temperature LDA form of water is different from supercooled water above T_s and that no singularity occurs at ca. 225 K, see the sketch figure 2.6 (a).

- The *singularity free interpretation* (SFI) was first given by Sastry et al. [5]. They showed in general that a liquid exhibiting a density minimum, a negative sloped *temperature of maximum density*, and a non-retracing liquid-gas spinodal may show the anomalous features observed in water. No singularity is necessary to explain the anomalies and a locus of maximal thermodynamics response caused by relaxation phenomena exists [6]. The situation is sketched in figure 2.6 (b). The mere presence of the observed features does not support the existence of a critical point or the connection of spinodal lines. Still, the other scenarios are not ruled out by this interpretation [5]. The SFI predicts that water above and below T_m to be thermodynamically continuous.

- The *second critical point hypothesis* or liquid-liquid critical point (LLCP) hypothesis was proposed by Poole et al. [4]. In their study, they used MD simulation of the ST2 water potential in the deeply supercooled regime. The simulations showed indications of a first-order phase transition that terminates in a second critical point C′. The phase transition separates two liquid phases of water, the *low density liquid* (LDL) and the *high density liquid* (HDL). They are the liquid forms of the respective amorphous glasses LDA and HDA. The critical point is situated in the no-man's land, as sketched in figure 2.6 (c).

  A very similar theory was proposed by Angell [7] in terms of a order-disorder transition. Similar to the LLCP it predicts a first order phase transition between the two liquids, but no critical point, at least not at positive pressures. It is therefore, usually called the *critical-point free scenario*.

The LLCP theory and the SFI both predict that on cooling water first becomes supercooled in a higher density phase. At the phase transition it transforms from HDL to LDL water and undergoes a glass transition to LDA at even lower temperatures. At ambient pressures below the pressure of the critical point C′ no phase transition occurs, but the *Widom-line* is crossed, marking the location of maximal fluctuations in the one-phase region. *Neutron scattering* (NS) and X-ray investigations on the structure of liquid water support this idea: they have shown a gradual adjustment of the water structure towards that of LDA on cooling [16,49]. In contrast, the occurrence of different forms of amorphous ice as HGW and ASW which are both considered of LDA type, and several other LDA and HDA types are taken as evidence against the thermodynamic continuity [50].
A variety of simulation studies were conducted to settle the topic of the existence of the proposed first order phase transition in water. The results are contradicting: Evidences assisting the existence of the transition and the LLCP have been found [4, 51–55], but as many studies have rejected those ideas [56–59].
Experimental studies on supercooled water suffer from the existence of the no-man's land. Nevertheless, different investigations where performed to learn about the low temperature regime. Small and very pure water samples were used to avoid heterogeneous nucleation at T_m and supercool water as low as possible [6, 12]. In current experiments using this approach, no thermodynamical divergence was observed but an increased tetrahedral ordering down to 229 K [16]. Nevertheless, the structural properties in the supercooled liquid are expected to be rather similar to the normal liquid [12]. Therefore, dynamical properties of the liquid are more promising to help clarify the question of the existence of the singularity. A pronounced transition was proposed for the temperature dependence of the motional correlation times. Due to the larger

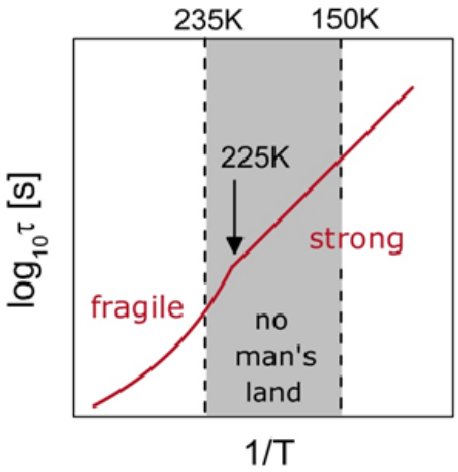

Figure 2.7.: Sketch of the proposed fragile-to-strong transition (FST) in water at ambient pressure [60]. The figure is courtesy of Prof. Dr. M. Vogel.

disorder, the HDL is expected to exhibit a larger structural entropy and according to the AG theory, this results in a fragile behavior, see section 2.1.2. In contrast, a locally ordered H-bond network in LDL, exhibits a nearly constant entropy, causing the correlation times to show a strong behavior. On crossing the phase boundary, a *fragile-to-strong transition* (FST) was postulated by Ito et al. [60], see figure 2.7. The FST is expected to be observable also at ambient pressures, well below the critical pressure [61]. The diverging fluctuations of a phase transition continue well beyond the critical point in form of finite fluctuations, the Widom-line. In fact, in the mildly supercooled regime, water is one of the most fragile liquids, see e.g. [21]. Experiments on HGW [62] and ASW [63], showed a strong temperature dependence above the proposed glass transition of $T_g = 136\,K$ [64][2]. This was taken as an evidence for the existence of the FST at roughly 225 K [60]. Still, a direct observation of the transition is prevented by the crystallization of water. Therefore, several experimental routes were developed, which allow for observation of water at temperatures well in the no-man's land. They will be discussed next.

2.3 Entering the no-man's land: confinement and solution

In order to investigate the dynamics of liquid water in the no-man's land spatially restricted geometries have been proven a useful tool. Supercooled liquids have been investigated in geometrical confinement for some years now [65,66]. The studies usually aim for the investigation of the properties of the enclosed materials, for usage in technological applications, e.g. in lithography [67] and

[2] Note, that this T_g is not generally agreed on and still a matter of research.

drug transport [68] and the understanding of the confining effects themselves [69]. Of special interest are the interactions between host material and the guest liquids, as well as the influence of the size and the dimensionality of the confinement, e.g. on the length scale of cooperative [66]. The main effects of confinement on the enclosed liquids are discussed in the following. This starts with general confinement effects in section 2.3.1, followed by a discussion of the effects on water in confinement 2.3.2. The concluding part of the chapter gives an introduction into the topic of soft confinement, especially water mixture, see section 2.3.3.

2.3.1 Effects of restricted geometry

There are a manifold of effects of confinement on the guest molecules. A benchmark for the effects is the change of the melting temperature ΔT_m or of the glass transition temperature ΔT_g [66]. Very often the shift of the glass transition temperature $\Delta T_g = T_{g,bulk} - T_{g,conf}$ is taken as a reference. Several key factors have been identified as sketched in figure 2.8.
Reducing the size of the confinement usually causes an acceleration of dynamics, and thereby, a negative shift $\Delta T_g < 0$ [70,71]. The effect is often attributed to the limited length scale of cooperative motion ξ [66]. This implies a strong dependence on the size of the confinement, which is made use of in NMR cryoporometry. There, the depression of the melting point is used to calculate the pore size of a sample using the Gibbs-Thomson equation [72, 73]. The latter equation implies an inverse dependence of the melting point depression and the confinement size. In case of cylindrical pores it can be expressed by [74]:

$$\Delta T_m(d) = \frac{2C_{GT}}{d} \tag{2.18}$$

Here d is the pore diameter and C_{GT} is a material specific constant depending on the surface free energy.

Density effects can alter the dynamics in the confinement, see figure 2.8 (b). In experiments using liquids in confinements, no bulk reservoir is available to compensate different thermal expansion of the liquid and the matrix, see figure 2.8 (b). Usually the motion of molecules is accelerated as the density is reduced [75]. From studies of partially filled pores, it was argued that this effect plays only a minor role even in hard confinement where the host material may not adapt to the reduced density, see [66] for details.
The guest-host interactions act between confinement and the enclosed liquid and are strongly depending on the used materials. Studies found a positive shift $\Delta T_g > 0$ when the confinement attracts the guest material, and negative

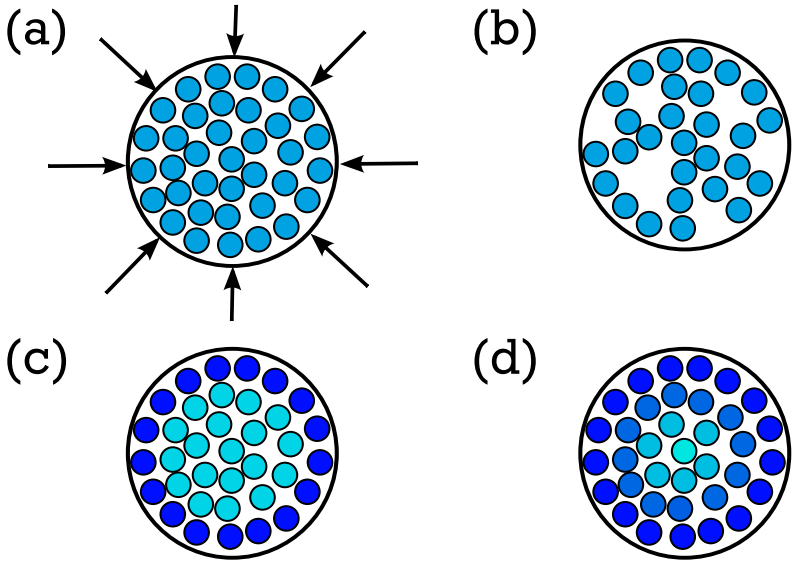

Figure 2.8.: Schematic effects of confinement on the enclosed liquids: (a) finite-size effect due to restricted spatial dimensions, (b) density effects, and surface interaction leading to a (c) two layer model, and (d) gradual decrease of the distortion.

ΔT_g when there is a repulsive force [76]. The influence of the surface on the guest was modeled in different ways. Some researchers proposed a core-shell model, where the surface of the confinement acts mainly on a small layer in vicinity of the interface. The inner core is only weakly or not at all affected by host material [77–79], see figure 2.8 (c). The model was successfully adapted to describe the dynamics of glycerol confined to sol-gel glasses by introducing exchange between the surface layer and the bulk layer [80]. More recent experiments [81, 82] and simulation studies [83, 84], indicate that the influence of the interface decays gradually into the confinement, exhibiting length scales up to the nanometer range, see figure 2.8 (d).

DS studies have found that the loss peaks of the confined liquid are significantly broadened compared to that of the bulk liquids [80, 85, 86]. The dynamics are more heterogeneous in the confinement. Similar broadening was found for example in NMR studies [87, 88]. It is likely caused by the strongly influenced molecules close to the interface [89]. The dynamics of those molecules differ from the bulk behavior, e.g. MD simulations [84] and DS studies [10] found a symmetric broadening of the loss peak rather than an asymmetric broadening usually found in bulk liquids [31]. Additionally, dynamics are slowed down close to immobile surfaces [84]. Besides the slow down of dynamics close to the confining material many studies have found the surface layer to be non-freezing at all temperatures, even though the bulk liquid in the center may crystallize in

sufficiently large confinements [72, 74, 75].

Depending on the surface interaction finite-size effects can be altered to result in a positive shift of ΔT_g. If there are strong attractive forces the slowdown of the molecules at the interface can decelerate molecules away from the matrix due to the cooperativity of the molecules. The overall effect can be a frustration of the overall dynamics [90]. Such a slowdown was for example found in MD simulations of water confined to neutral pores [91]. There, water molecules were fixed in position to effectively provide a rigid confinement for the residual water molecules. In this situation the guest-host interactions are the same as between the guest molecules themselves. The liquid molecules exhibit decelerated dynamics even in a distance of about 1 nm to the pore walls.
Finally, in case of mixtures in spatial confinement, the strong guest-host interactions can also result in phase separation of the constituents [92, 93]. Contrary, the confinement was found to suppress phase separation in certain cases [94].

In summary, many aspects have to be taken into account when the dynamics of a liquid in spatially restricted geometry is investigated. The special case of water has therefore triggered studies of many of its properties in different confining materials. An overview over this topic is given next.

2.3.2 Water in confinement

The proposal of a second critical point in water at ca. 225 K and the difficulty of studying it in bulk water [16, 95] triggered a series of investigations of supercooled water in confinement. Different routes of confining water have been followed. One of them is mixing water with small molecules in binary mixtures, seer in chapter 8 for details. In this section, the focus is on water enclosed in rigid confinement. Where it is illustrative, studies of water in the vicinity of soft but comparatively immobile molecules, e.g. polymers and proteins are included.
In the first studies, the focus was set on the investigation of water embedded in three different systems. First to mention are mesoporous vycor glasses [96] which suffer from the problem of too large pores. With diameters larger than 5 nm [97] and a rather broad distribution of diameters it was not possible to suppress crystallization in the temperature region of interest.
A second class of confinement materials was found in the material group of zeolites, see [98]. They usually exhibit free cage sizes of only up to 1.2 nm [99] with some exceptions where the pores show much larger diameter of about 4.4 nm [100]. Again, the pore sizes are not in the interesting size range from ca. 2 nm to 3 nm, where bulk behavior is assumed to be present but freezing is suppressed [74]. Additionally, most zeolites exhibit charged ions in contact

with the inner surface of the cavity. This has a rather strong influence on the contained water rendering it impossible to investigate the bulk properties.
The same problem occurs with the third material, Na vermiculite clay. Here, the water is intercalated between clay layers with a rather small distance of ca. 1.2 nm or less [85]. Despite those difficulties it is worth looking at the clay systems later in short, due to its two dimensional structure.[3]

Uncharged, uniformly sized: the model MCM-41

Due to the disadvantages of the other confinement materials, the ordered silica matrix MCM-41 [102, 103] became the focus of interest in the studies of confined water. It features small pore size distributions and pore diameters that can be tuned within the whole range of interest from 1.4 nm to 5 nm [104]. Additionally, it provides long term stability against water [105].
Using MCM-41 as a confinement, various studies were performed and yielded contradicting results. *Quasi elastic neutron scattering* (QENS) studies [9, 106, 107], and NMR studies [97, 108, 109] found a pronounced FST in the correlation times and the diffusion coefficients of water in MCM-41 pores of 1.4 nm and 1.8 nm. Some of the QENS data [9] are shown in figure 2.9. The transition was found at a temperature $T_L \approx (225 \pm 3)$ K at atmospheric pressures. This is in very good agreement with the predictions from the LLCP hypothesis [60], compare chapter 2.2. The measured pressure dependence of T_L is in agreement with the predicted location of the second critical point [9].
The FST was observed in a variety of other systems, including hydration water of proteins [107, 110] and DNA [111], in water confined to zeolites [100] and cement paste [112], in water in aerogels [113] and in salt mixtures [114]. In those studies, different techniques were used including Optical Kerr Effect, ^{1}H NMR *pulsed field gradient* (PFG) experiments and ^{1}H NMR *field cycling* (FC) experiments. A majority of those studies were performed by the group of S.H. Chen using the QENS technique. Other researchers gave concerns regarding the validity of the data evaluation especially in the NS experiments: It has been shown that an improved fitting routine eliminates the FST [115]. The NMR measurements were criticized as well [116]: No sign of the FST was found using ^{2}H NMR to investigate the hydration water of proteins. In [117] it was shown that cross relaxation plays an important role in NMR diffusometry and renders the determination of diffusion coefficients at or below T_L impossible. Despite the criticism, the discovery of a pronounced transition in the correlation times of water were used as support for the LLCP hypothesis. It was argued that the observed behavior of confined water reflects the behavior of

[3] Investigations using clay confinement are disadvantageous due to another reason: sample preparation in some cases took up to a year [101] and thus, requires patient experimentalists.

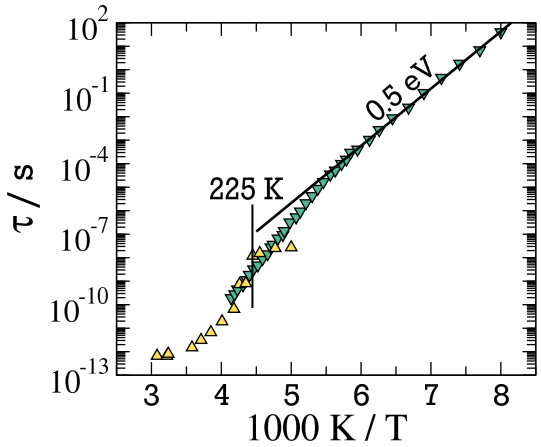

Figure 2.9.: Correlation times of water measured in MCM-41 by QENS (d=1.8 nm) [9] and DS (d=2.1 nm) [10], the black line is an Arrhenius fit to the data for T<180 K resulting in E_a = 0.5 eV.

the structural relaxation of bulk water. The measured time constants τ below the transition extrapolate to a glass transition temperature T_g that is inconsistent with any proposed value of T_g for water [85, 118, 119], suggesting that, below the crossover, the QENS data do not describe the structural relaxation. Nevertheless, it was concluded that the observed crossover is due to the structural α-process, and therefore, the kink in the correlation time is the expected FST which fulfills the predictions of the LLPT scenario, see figure 2.10 (a).

In view of the criticisms expressed above, a large group of researchers refuse to acknowledge the FST on basis of their experiments. Besides the NMR measurements mentioned above [116, 117], strong rejection of the idea relies on dielectric measurements on confined water. Such investigation on MCM-41 of pores with 2.1 nm [10, 120] showed no sign of a FST in the temperature region at the proposed T_L. Those measurements nicely continued the high temperature QENS data above ca. 230 K, c.f. figure 2.9. The dielectric correlation times show a mild crossover at about 180 K. The process observed at temperatures below that crossover shows characteristic signs of a β-relaxation [121–123].

The question whether this behavior is specific to the studied system or reflects the general characteristics of water, was pursued by the investigation of water in softer types of confinement, see section 2.3.3 and chapter 8 for more details. Although it was shown that water dynamics in solution with small molecules show some peculiarities [124], those studies revealed the universality of the low temperature water relaxation in the vicinity of surfaces. The universality was found in studies on molecular sieves [85, 125], large polymers [126], sugars [127] and biological systems as proteins [116] and DNA [126]. The

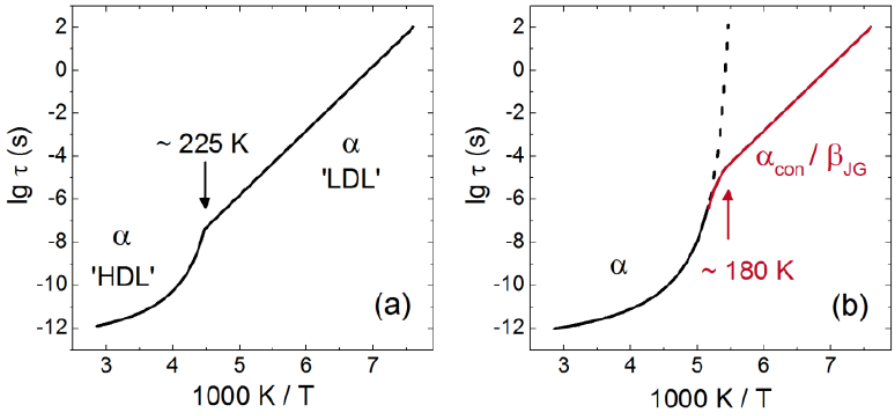

Figure 2.10.: Sketch of the two models, which aim to describe dynamics of confined water. (a) FST in the α-relaxation, due to transition from high-density (HDL) to low-density (LDL) liquid. (b) Transition from α-relaxation to α_{con}-relaxation due to limited growth of correlation. Figure adapted from [123].

observation in all those systems lead to an alternative model trying to explain water dynamics in confinement.

In this model, no significant change in the temperature dependence of confined water in the vicinity of 225 K happens, but the observed correlation times follow an ARR temperature dependence down to ca 180 K. There, a mild crossover to an Arrhenius behavior with a lower activation energy $E_a = 0.5$ eV is observed, see in figure 2.10 (b). It was proposed that the system's α-process continues even below T_L=225 K with a continuous growth of the cooperative length ξ. When ξ reaches the length scale of the confinement the α-relaxation becomes unobservable and a new process dominates the observed behavior. In literature, it is argued whether this process is the α-process of the confined system α_{con} [11, 123, 128] or whether it is a β-process of Johari-Goldstein (JG) type [11, 123, 129]. Since the length scale in various systems may be different, this low temperature relaxation does not exhibit identical dynamics in all systems. Still, it shows four distinct and universal features in all systems [123]:

1. The peak in the dielectric loss ϵ'' exhibits a symmetric broadening, which can be described by a Cole-Cole function, see eq. (2.12).

2. The activation energy of the low temperature process below the crossover at ca. (185 ± 20) K is $E_a = (0.50 \pm 0.03)$ eV [11].

3. The time scale of the process varies in all systems. It becomes faster when more *unfrozen* water is present [130]. The MCM-41 system with 2.1 nm shows the fastest dynamics.

4. The process shows all characteristics of a β-process below the crossover [121, 126, 131]. Some researchers argue that it may be a Johari-Goldstein like β-process of water [132].

Besides the universality of the observed process close to surfaces, it is still a matter of debate whether it reflects the behavior of the structural relaxation of bulk water or whether it is governed by confinement effects. In the latter case, it is not settled yet, if the relaxation is the structural relaxation of the confined liquid or rather a secondary process, possibly a JG-β-process.

2.3.3 Binary mixtures with water

Many studies investigated the behavior of bulk aqueous mixtures, see e.g. [11, 69, 101, 119, 130, 133, 134], and research is still going on [135, 136]. Most works on the topic focus on water-alcohol mixtures for several reasons.
First, the H-bonding properties of alcohols can be employed to probe the H-bonding properties of water and how water reacts to a distortion of the network structure it forms in the bulk state [135, 136]. By a proper choice of the solute and by variation of the concentrations the interaction within the mixture can be systematically tuned [101, 119]. Therefore, water mixtures are often investigated with the aim to extrapolate the concentration dependence to the behavior of bulk water. For this purpose also water mixtures with salts found application [7]. The most important results from those studies are a wide universality of the low temperature water relaxation in a broad range of systems [11, 123], which was already introduced in the last section.
A second reason to study mixtures of water with alcohols is motivated by the biological point of view. Large efforts are taken to understand the mutual interaction of water with proteins and related biological functional molecules. Several theories exist that try to explain the very complex behavior in those systems, including the slaving-concept of Frauenfelder [137] and models formulated by Doster [138], Chen [107], and Ngai [139], see e.g. [140] for an overview. Alcohol molecules in mixtures with water can help to approach this topic, by studying the dynamics of short molecules first and then increase complexity by successively increasing the molecular weight.
A third point that is to be considered, is the phase behavior of aqueous mixtures. In all studies, phase separation can pose a serious problem when interpreting the data [135, 141]. In technological applications such effects, can endanger the outcome of the process. Therefore, it is important to characterize the temperature and concentration dependent phase behavior of mixtures, especially those involving water due to their outstanding importance.
Besides careful studies of mixtures in their bulk state, the points mentioned here, can be investigated by confining the mixtures in narrow spatial geometries.

Confined binary mixtures

By confining water mixtures to narrow geometries, the properties of the system can be tuned to an even larger extent. The finite-size effects suppress crystallization, allowing for further increase of the water concentration in the mixtures without freezing. This was used in a study of glycerol and water confined to MCM-41 [142]. There, it was proposed that the glass transition of water is situated at temperatures above the glass transition of glycerol, possibly at 225 K.
In addition, finite-size effects suppress the formation of an extended H-bond network. Depending on the dimensionality of the confinement, this can affect one, two or three dimensions. Thereby, the formation of H-bond networks and their ability to adapt to reduced dimensions can be investigated. In the confinement provided in Na-vermiculite clay [86] it was found that the network of bonds can adapt to very severe restrictions. The basic properties of the liquid are conserved even though the residual volume was basically two dimensional. The interactions with the surface may trigger phase segregation or suppress it, an important aspect in technological applications. In hydrophilic confinement micro-phase segregation was observed. The water was proposed to cluster at the pore surface [86, 129, 142, 143]. This separation is likely promoted by the high hydroaffinity of the confinement. It is therefore an interesting topic of research, to investigate the influence of different hydroaffinities. This can be achieved in different confinements or by modifying the confinement's surface.
Studying mixtures of water with simple molecules can provide a basic knowledge of those systems. In subsequent research this knowledge can be used for understanding the properties of more complex systems, eventually it can help to clarify the properties of technological and biological relevant systems as for example proteins.

A model system: propylene glycols

A widely used model system to investigate the influence of confinement on binary mixtures are propylene glycol-water mixtures and related mixtures [11, 119, 124, 130, 134, 144–152]. Often 1,2-propylene glycol (PG), propylene glycol monomethyl ether (PGME) and glycerol (GLY) [119]. All three monomers consist of a backbone of three carbon atoms and exhibit a varying number of hydroxyl groups (OH) from a single one in PGME up to three in GLY. In addition to PGME, the dimer DiPGME was utilized in the present study. The molecules are sketched in figure 2.11.
PG, PGME and DiPGME have been used in this work to study the properties of confined mixtures, while glycerol was utilized as a model glass former. All different molecules are well characterized in their pure state, as well as in

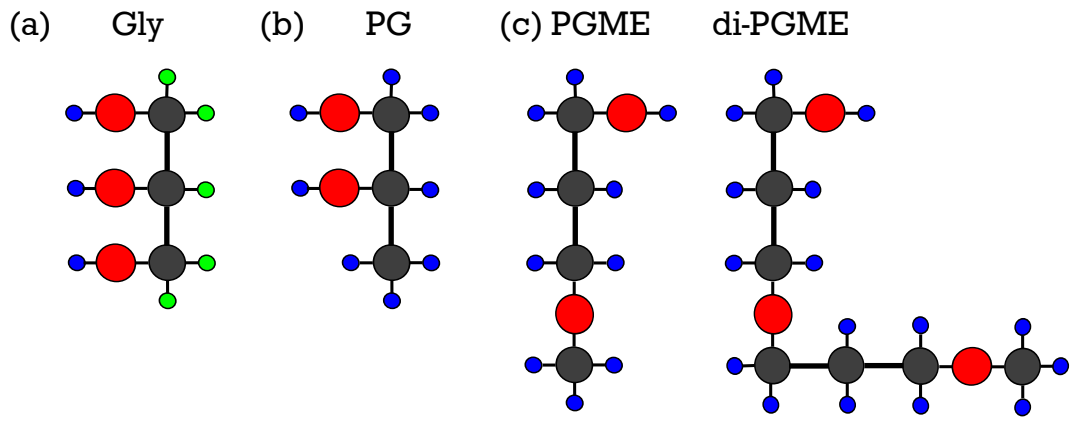

Figure 2.11.: Sketch of the different propylene glycols used in this work: (a) GLY, (b) PG, and (c) PGME and its dimer DiPGME. Carbon atoms are black, oxygen atoms are red and hydrogen atoms are blue. Green: deuterons in the case of deuterated glycerol-d_5.

mixtures with water, see chapter 8 for details on the findings. Despite their structural similarities the alcohols exhibit a rather different dynamical behavior [69, 119], rendering them ideal candidates to investigate the influence of confinement on the guest liquid.

3 Nuclear magnetic resonance

Nuclear magnetic resonance (NMR) is a versatile tool to study many microscopic properties of a material including its structure and dynamics. In this chapter, the basic concepts of NMR will be discussed. The description will focus on the method of ^{2}H NMR which is the main technique utilized in this thesis. The following discussion is based on several common text books [153–156] as well as two PhD theses [157, 158] and the review article [38] as main references. They will not be referenced explicitly. The last section in this chapter, 3.9, gives an overview over several other methods, commonly used to study supercooled liquids. Literature data obtained by those methods will be used as references in this work.

3.1 Introduction to NMR

In NMR the interactions of nuclei exhibiting a non-vanishing nuclear spin $\hat{I}$ with external magnetic and sample internal electromagnetic fields are used to probe a large number of material properties. When a spin $\hat{I}$ is placed in a strong external magnetic field $\mathbf{B}_0 = \mathrm{B}\hat{\boldsymbol{e}}_z$, it will be subject to the Zeeman effect. The degeneracy of the energy levels is lifted into different energy levels[1]

$$E = -\gamma m_I \mathrm{B}. \tag{3.1}$$

Here, $m_\mathrm{I} = I, I-1, ..., -I$ are the possible z-components of the spin angular momentum $\hat{I}_\mathrm{z}\mathbf{B}_0 = m_I \boldsymbol{B}_0$. The proportionality constant γ is called gyromagnetic ratio. The differences in energy of the levels result in different occupation numbers. They are characterized by the Boltzmann distribution. Therefore, a surplus of spins is orientated along the magnetic field $\mathbf{B}_0$ creating a macroscopic magnetization of the sample $\boldsymbol{M} \propto \boldsymbol{B}_0$. The spins precess around the magnetic field axis with the Larmor frequency ω_0:

$$\boldsymbol{\omega}_0 = -\gamma \mathbf{B}_0. \tag{3.2}$$

Recent NMR techniques make use of pulsed experiments. In addition to the static magnetic field $\mathbf{B}_0$, a second magnetic field $\mathbf{B}_1$ is applied perpendicular to $\mathbf{B}_0$. $\mathbf{B}_1$ oscillates with the Larmor frequency. It is created by a coil wound

[1] In this and the following sections $\hbar = 1$ will be used for simplicity

directly around the sample. It is usually applied for short times generates so called *radio frequency* (rf) pulse. The rf pulses cause transitions between the different energy levels of a spin. The macroscopic effect of a rf pulse is a precession of the magnetization around the $\mathbf{B}_1$ axis perpendicular to the $\mathbf{B}_0$ axis. When the magnetization is tilted away from the equilibrium orientation, i.e. the z-axis, it starts precessing around the z-axis with the Larmor frequency. The precessing magnetization induces a voltage in the B_1 coil which is detected in the experiment.
The precession frequency of a spin is altered by additional internal magnetic fields $\mathbf{B}_{\text{int}}$ generated by interactions within the sample. In eq. (3.2), the field $\mathbf{B}_{\text{loc}} = \mathbf{B}_0 + \mathbf{B}_{\text{int}}$ on the site of the spin must be taken into account. The strength of the interactions is measured in the shift of precession frequency. It is usually given in units of frequency (Hz). Some of the most important interactions in NMR spectroscopy are briefly introduced here:

1. The *scalar coupling* or *J-coupling* is an indirect interaction which is mediated through chemical bonds connecting two spins. The spin of a nucleus couples to local electrons via the hyperfine interaction. Thus, two nuclear spins can influence each other by manipulating the electronic states in the covalent bonds connecting them, see figure 3.1 (a). J-coupling is the weaker the more bonds the nuclei are apart. Its typical strength is in the order of a few hertz.

2. The *chemical shift* is due to the electronic environment of the nucleus. The external magnetic field induces angular motion of the electrons. This diamagnetic effect partially shields the external field on site of the nucleus, see figure 3.1 (b). The distribution of electrons varies according to the chemical structure of the sample, enabling identification of certain chemical groups. The strength of the chemical shift is usually in the range of a few hundred hertz, proportional to the external field.

3. The *dipole–dipole* interaction is due to the dipolar field of a spin at the position of a second spin. The strength of the field depends on the distance of both spins and on their relative orientation, see figure 3.1 (c). The dipolar coupling interaction can be utilized in many experiments, e.g. for measuring distances, structure and molecular dynamics. Its coupling strength usually is about 10 kHz – 100 kHz.

4. The *quadrupolar interaction* (QP) originates from the interplay of a nuclear quadrupolar moment Q with an *electrical field gradient* (EFG). The EFG arises from the non-isotropic distribution of the electrons e.g. due to a bond, while the quadrupolar moment arises from a non-spherical distribution of electric charges in the nucleus, see figure 3.1 (d). Q vanishes for spin $I = 1/2$ particles. If the QP interaction is present, its coupling

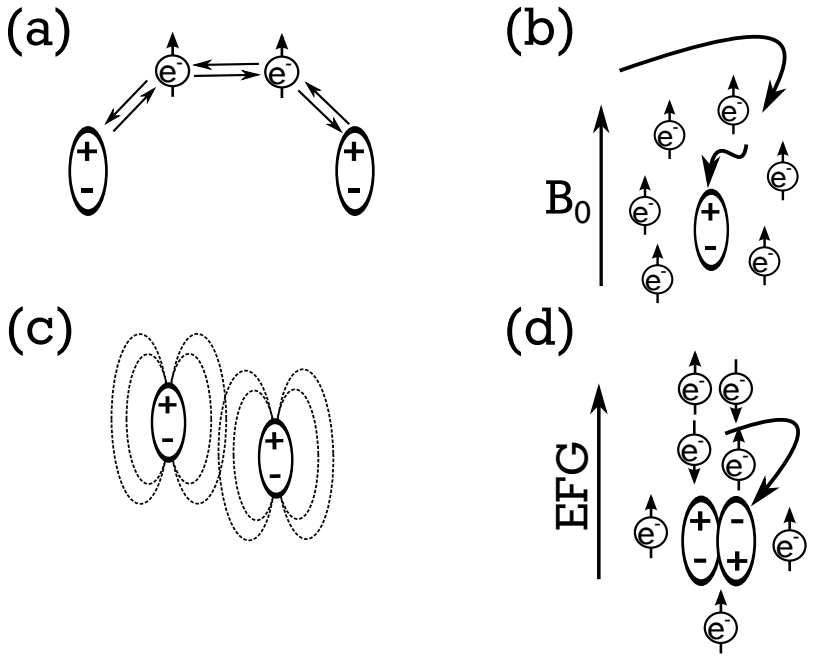

Figure 3.1.: Sketch of the behavior of different NMR interactions: (a) J-coupling, (b) chemical shift interaction, (c) dipole-dipole interaction , and (d) quadrupolar interaction.

strength is usually large compared to other interactions. It is often in the range from 1 kHz – 1 MHz. The QP interaction is discussed in more detail in section 3.2.5.

The spectrum of frequency shifts $\omega_0 - \omega_{\text{int}}$ due to the internal field can be measured by Fourier transformation NMR. A rf pulse is used to rotate the magnetization into the x-y plane, where the spins precess with the local Larmor frequency. The magnetization therefore contains contributions of all spin signals that can be extracted by Fourier transformation of the time measured time signal. This detected signal is subject to relaxation effects causing the signal to decay over time. This signal is conveniently called *free induction decay* (FID).

Two relaxation effects are important for the magnetization to return to equilibrium. Those are the spin-spin relaxation (SSR) and the spin-lattice relaxation (SLR). SSR is caused by local differences in the precession frequency, which causes a decay of phase coherence of the individual spins. The macroscopic magnetization in the x-y plane is lost due to this effect. The SLR causes the return of the magnetization to the quantization axis parallel to $\mathbf{B}_0$ after a disturbance e.g., by a rf pulse. Thereby, energy needs to be transferred to the lattice. Both relaxation mechanisms can be connected to local fluctuations, which are caused by molecular motion within the sample. Thus, both relaxation

mechanisms can be used to determine dynamical properties of the sample. The relaxation effects are discussed in more details in section 3.3.
In this work the main experimental method is ^{2}H NMR. The deuteron possesses a nuclear spin of I = 1, and thus, the QP is the dominating interaction. The rest of this chapter will treat the quantum mechanical description of NMR. The focus is set on ^{2}H NMR.

3.2 Quantum mechanical description of NMR

3.2.1 The density matrix formalism

In NMR macroscopic samples with a large number of particles are investigated. Modeling such a sample with the Schrödinger equation including all interactions is a too complex task even with modern computation power. The problem is usually approached in a quantum statistical way. The system is split into a state mixture consisting of the spin subsystem on the one hand and all other degrees of freedom on the other hand. These are summarized as *the lattice*. The Hamiltonian $\mathscr{H}$ contains all interactions among the spins and those connecting the spin system to the lattice and thereby determines the state of the system. In this situation, the density matrix formalism is a powerful way of handling the spin evolution. The density matrix $\hat{\rho}$ is given by

$$\hat{\rho} = \sum w_\mathrm{n} |\psi_\mathrm{n}\rangle\langle\psi_\mathrm{n}|. \tag{3.3}$$

Here w_n is the probability for the system to be in state n. The expectation value of an observable can be defined by

$$\langle \hat{\mathrm{A}} \rangle = \mathrm{Tr}\left[\hat{\rho}\hat{\mathrm{A}}\right]. \tag{3.4}$$

Here, Tr[...] denotes the trace. The time evolution of the density matrix determines the time evolution of the NMR observable, by the von-Neumann equation:

$$\frac{\mathrm{d}\hat{\rho}}{\mathrm{dt}} = -\imath\left[\mathscr{H}, \hat{\rho}\right] \tag{3.5}$$

Here, $\imath$ denotes the complex number $\imath = \sqrt{-1}$. Note that $\hbar = 1$ is used for simplicity. If the Hamiltonian $\mathscr{H}$ is independent of time eq. (3.5) can be solved by utilizing the unitary time propagator:

$$\hat{\mathrm{U}}(t) = e^{-\imath\mathscr{H}t}. \tag{3.6}$$

Then, the formal solution to the von-Neumann equation reads

$$\hat{\rho}(t) = \hat{\mathrm{U}}(t)\hat{\rho}(0)\hat{\mathrm{U}}^{\dagger}(\mathrm{t}) \tag{3.7}$$

In thermal equilibrium, the density of states is given by the Boltzmann distribution and can be written as

$$\hat{\rho} = \frac{1}{Z}\exp\left(-\frac{\mathscr{H}}{k_B T}\right), \qquad \text{withZ} \qquad = \mathrm{Tr}\left[\exp\left(-\frac{\mathscr{H}}{k_B T}\right)\right], \tag{3.8}$$

where $\mathrm{k_B}$ is Boltzmann's constant.
When merely rotational dynamics are of interest, as e.g. in ^{2}H NMR, the time evolution of the density matrix $\hat{\rho}$ is usually calculated using the method of *irreducible spherical tensor operators* (IST), see in for an introduction [153, 155]. They are defined using a separation of spatial contributions (R) and spin contributions (T) to the Hamiltonian [155]:

$$\mathscr{H}_{\mathrm{x}} = \mathrm{a_x}\sum_{l=0,2}\sum_{m=-l}^{l}(-1)\hat{\mathrm{R}}_{\mathrm{l},-\mathrm{m}}\hat{\mathrm{T}}_{\mathrm{l,m}}. \tag{3.9}$$

This general form of the Hamiltonian is a second-rank tensor (l = 2). All NMR Hamiltonians can be expressed in this form by adjusting the constant $\mathrm{a_x}$. The $\hat{\mathrm{T}}_{\mathrm{l,m}}$ operators are defined using the angular momentum operators $\hat{I}_\alpha$. Their evolution under the influence of the interactions in NMR is well known, see e.g. in [153]. The time dependence of the density matrix can therefore be handled in a simple manner without solving the von-Neumann equation explicitly.

3.2.2 The Zeeman Hamiltonian

In NMR, the external magnetic field is usually strong compared to all additional fields. Thus, the Zeeman effect, compare eq. (3.1), is the dominant effect and is treated first. Assuming the magnetic field to be aligned with the z-axis the Zeeman Hamiltonian can be written as

$$\mathscr{H}_{\mathrm{Z}} = -\gamma\hat{\mathbf{I}}\mathbf{B_0} = -\gamma\hat{I}_{\mathrm{z}}B_0. \tag{3.10}$$

The Zeeman energy splitting is some orders of magnitude lower than the thermal energy at room temperature, even in very strong fields[2]. Therefore, the Zeeman Hamiltonian can be expanded into a Taylor series:

[2] e.g. for a deuteron at 7 T and 300 K it is $\mathrm{k_B T} \approx 10^{-2}\,\mathrm{eV} \gg 10^{-5}\,\mathrm{eV} \approx -\gamma B_0 \Delta \mathrm{m_I}$

$$\hat{\rho} \propto \mathbb{1} + \frac{\gamma B_0}{k_B T}\hat{I} + ... \tag{3.11}$$

The equilibrium magnetization can then be calculated using eq. (3.4), resulting in

$$M_0 \propto \frac{\gamma^2 I(I+1)}{k_B T} B_0. \tag{3.12}$$

This is the Curie magnetization, which is inversely proportional to the temperature of the sample.
The effect of the Zeeman interaction on a spin $I = 1$ with initial state $\hat{I} = \hat{I}_\alpha$, where $\alpha = x, y$, can be computed by inserting eq. (3.11) into eq. (3.7). Using the Pauli spin matrices (see for example in [153]) the time evolution of $\hat{\rho}$ can be calculated to be

$$\hat{\rho}(t) = \hat{I}_x \cos(\omega_0 t + \phi) + \hat{I}_y \sin(\omega_0 t + \phi). \tag{3.13}$$

This is a precession around the magnetic field axis $\mathbf{B}_0$ with the Larmor frequency ω_0, where the phase ϕ depends on the initial state. Before effects of the other interactions important to ^{2}H NMR are discussed, the transformation to a rotating frame of reference is introduced.

3.2.3 The rotating frame

As discussed above, the Zeeman interaction leads to a precession of the spins around the axis of the magnetic field with the Larmor frequency, see eq. (3.13). This effect does not contain information about the sample and can be eliminated by considering a new reference frame that rotates with a frequency ω_{rot}. The magnetization that precesses with ω_0 in the laboratory frame rotates with the altered precession frequency $\omega_0 - \omega_{rot}$ in the rotating frame. In the resonant case,

$$\omega_0 = \omega_{rot}, \tag{3.14}$$

the spin is static in the rotating frame. In the calculations of the spin state the Larmor frequency in eq. (3.2) must be substituted by $\omega_0 - \omega_{rot}$:

$$\hat{\rho}^{rot}(t) = e^{-\imath(\omega_0-\omega_{rot})\hat{I}_z t}\hat{\rho}(0)e^{-\imath(\omega_0-\omega_{rot})\hat{I}_z t} = \hat{\rho}(0). \tag{3.15}$$

Thus, the Zeeman interaction can be excluded from the calculations by transformation into the rotating frame. The following discussions will be performed

in the rotating frame, dropping the superscripts. One must keep in mind that all Hamiltonians must be transformed into the rotating frame by

$$\mathscr{H}^{\mathrm{rot}} = \hat{U}^{\dagger}\mathscr{H}^{\mathrm{lab}}\hat{U} \tag{3.16}$$

where $\hat{U}$ was defined in eq. (3.6). The transformation simplifies the subsequent discussion of the important interactions in NMR.

3.2.4 Radio frequency pulses

In ^{2}H NMR experiments, rf pulses are used to manipulate the spin system. The pulses are generated by the $\mathbf{B}_1$ coil, c.f. fig. 4.1 in chapter 4. It is aligned with the x-axis in the laboratory frame (LF). The effect of the rf pulses can be described analogously to the Zeeman interaction: An additional magnetic field $\mathbf{B_1} = \mathrm{B}_1\hat{\mathbf{e}}_x$ is applied. The Hamiltonian is

$$\mathscr{H}_{\mathrm{rf}} = -\gamma\hat{\boldsymbol{I}}\mathbf{B}_1 = -\gamma\hat{\mathrm{I}}_{\alpha}\mathrm{B}_1. \tag{3.17}$$

The field B_1 is irradiated with the frequency ω_{rf} in the LF:

$$\mathrm{B}_1^{\mathrm{lab}}(\mathrm{t}) = 2|\mathrm{B}_1|\cos\left(\omega_{\mathrm{rf}}\mathrm{t}\right) \tag{3.18}$$

This can be decomposed into two counter-rotating, harmonic oscillations with angular frequencies $\pm\omega_{\mathrm{rf}}$ and amplitude $|\mathrm{B}_1|$. If ω_{rf} matches the Larmor frequency $\omega_{\mathrm{rf}} = \omega_0$ the resonant $+\omega_0$ component results in a static magnetic field in the rotating frame. The $-\omega_0$ component can be neglected in most practical cases since nuclear spins are only influenced efficiently by fields with frequencies close to the Larmor frequency.
In the rotating frame, the effect of $\mathbf{B_1}$ is a precession of spins. The axis of precession is in the x-y plane and specified by the phase of the rotating frame with respect to the B_1 field. Similar to the Zeeman effect, the precession frequency in the rotating frame is given by $\boldsymbol{\omega}_1 = -\gamma\mathbf{B}_1$. The angle of rotation λ is defined by the length of the pulse Δ_{p}

$$\lambda = \omega_1\Delta_{\mathrm{p}}. \tag{3.19}$$

In this work rf pulses will be named after their effect: namely the angle of rotation and the rotation axis in the rotating frame. For example 90°_{x} will be used for a pulse which rotates the magnetization by 90° around the x axis.

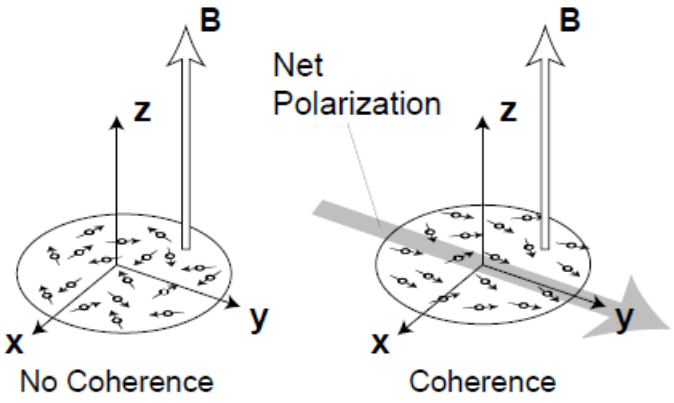

(The degree of alignment of the spins is greatly exaggerated).

Figure 3.2.: Sketch of transversal coherences between phases in a spin 1/2 systems. Taken from [154].

Besides their effect on level population, rf pulses often create so-called *coherences*, which are, mathematically spoken, the off-diagonal elements in the density matrix $\hat{\rho}$ [154]. Coherences represent the tendency of transversal spin components to exhibit the same phase and thus an aligned complex transversal magnetization, as sketched in fig. 3.2. The order of such a coherence is defined as the difference in the eigenvalues of the involved eigenstates r and s:

$$\mathrm{p_{r,s}} = m_r - m_s \tag{3.20}$$

Coherences are usually referred to as (p)-*quantum coherence* by their order p. NMR experiments are only able to detect coherences $\mathrm{p_{r,s}}$ = -1. Those represent the magnetization pointing in the same direction as the x-direction defined by the orientation of the $\mathrm{B_1}$ coil [154].

3.2.5 The quadrupolar interaction of deuterons

The main experimental method used in this work is ^{2}H NMR and the QP interaction dominates. The QP interaction originates from the interplay of the nuclear electric quadrupole moment Q with the EFG, see figure 3.1 (d). EFG tensor $\bar{\bar{V}}$ is defined using the electrical potential Φ:

$$\mathrm{V}_{\alpha,\beta} = \frac{\partial^2 \Phi}{\partial \mathrm{r}_\alpha \partial \mathrm{r}_\beta} \tag{3.21}$$

This is the matrix of second spatial derivatives of Φ at the site of the nucleus. Here, α, β = x,y,z are the axes in the LF. The EFG tensor is traceless: There is a basis in which it can be diagonalized [153, 159]:

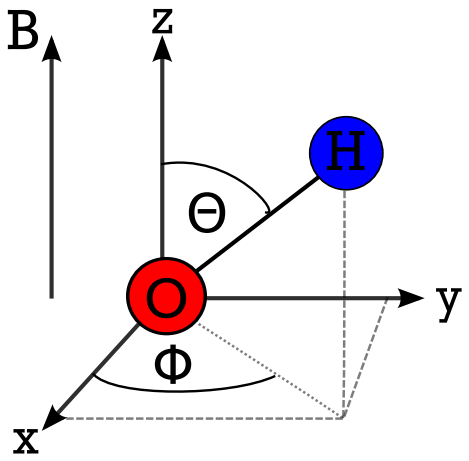

Figure 3.3.: Definition of the inclination angle Θ and the azimuth angle ϕ with respect to the external magnetic field.

$$\bar{\bar{V}} = \begin{pmatrix} V_{xx} & 0 & 0 \\ 0 & V_{yy} & 0 \\ 0 & 0 & V_{zz} \end{pmatrix} \tag{3.22}$$

The elements $V_{\alpha\alpha}$ with α = x,y,z are the principle values in the principle axis system. Conventionally, the axes are defined such that $|V_{xx}|, |V_{yy}| \leq |V_{zz}|$ holds. The elements of $\bar{\bar{V}}$ depend on the electron density around the nucleus and thus, on the bonding of the deuteron (D). In the case of a deuteron bonded to a carbon (C) or to an oxygen (O) atom the field gradient is approximately axially symmetric ($V_{xx} \approx V_{yy}$) with respect to the bond axis between the deuteron and its partner. A parameter to describe the deviation from axial symmetry is the asymmetry parameter η, defined as

$$\eta = \left| \frac{V_{xx} - V_{yy}}{V_{zz}} \right|. \tag{3.23}$$

The main component of the EFG tensor V_{zz} is orientated along the bond axis and encloses an inclination angle Θ with the external magnetic field, as is sketched in fig 3.3.
Using the definition of the EFG tensor in eq. (3.22) the Hamiltonian of the quadrupolar interaction can be written as

$$\mathscr{H}^{QP} = \frac{eQ}{2I(2I-1)} \hat{\mathbf{I}} \bar{\bar{V}} \hat{\mathbf{I}} = \frac{e^2 Q V_{zz}}{4I(2I-1)} \left[\left(3\hat{I}^2_{z,mol} - \hat{I}^2 \right) + \frac{1}{2}\eta \left(\hat{I}^2_+ + \hat{I}^2_- \right) \right]. \tag{3.24}$$

The index mol indicates that the quantization is in the molecular frame. In case of strong external fields the quantization in the molecular and the laboratory

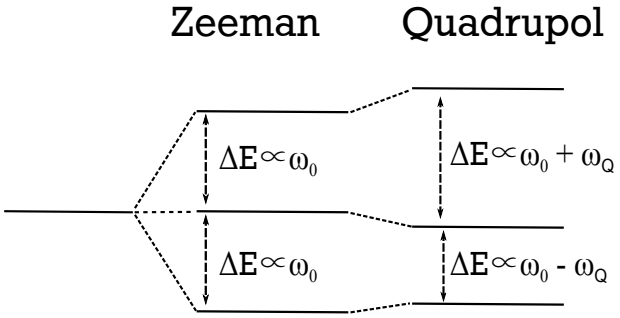

Figure 3.4.: Energy splitting under the influence of the Zeeman interaction and shift of Zeeman levels due to the quadrupolar interaction.

frames are equal [160]. The additional parameters in this equation are the electric charge e and the quadrupole moment Q. The quadrupolar frequency ω_{Q} is introduced:

$$\omega_{\mathrm{Q}} = \frac{3e^2QV_{zz}}{8}\left(3\cos^2\Theta - 1 - \eta\sin^2\Theta\cos 2\phi\right) \approx \frac{\delta}{2}\left(3\cos^2\Theta - 1\right). \quad (3.25)$$

Here, the EFG tensor is assumed to be axially symmetric ($\eta = 0$). The anisotropy parameter δ is introduced:

$$\delta = \frac{3e^2Q}{4}\mathrm{V}_{zz}. \quad (3.26)$$

Eq. 3.25 can be used to rewrite eq. (3.24) as

$$\mathscr{H}^{\mathrm{QP}} = \frac{\omega_Q}{3}\left[3\hat{I}_z\hat{I}_z - I(I+1)\right]. \quad (3.27)$$

With this result the time evolution of a spin state $\hat{\rho}(t=0)$ can be calculated using the von-Neuman formalism. After applying a 90°_{y} pulse, the initial state $\hat{\rho}(t=0^+) = \hat{I}_{\mathrm{x}}$ evolves according to

$$\hat{\rho}(t) = \hat{I}_{\mathrm{x}}\cos(\omega_{\mathrm{Q}}t) + \imath(\hat{T}_{2,1} + \hat{T}_{2,-1})\sin(\omega_{\mathrm{Q}}t). \quad (3.28)$$

The trace of the term $\mathrm{Tr}\left[\hat{I}_\alpha(\hat{T}_{2,1} + \hat{T}_{2,-1})\right]$ vanishes. Therefore, the second term in equation 3.28 is not observable [153], but it must be considered when calculating the outcome of ^{2}H NMR experiments. Using Euler's formula, the first term can be decomposed into two counter-rotating contributions with frequencies $\pm\omega_{\mathrm{Q}}$. They are usually attributed to the two possible transitions between spin states due to the quadrupolar interaction sketched in fig. 3.4.

The detectable magnetization under influence of the QP interaction can be calculated using eq. (3.28) and eq. (3.4) to be:

$$\mathbf{M}(\mathrm{t}) = |\mathbf{M}_0| \cos(\omega_\mathrm{Q}\mathrm{t}) \boldsymbol{e}_\mathrm{x}^r. \tag{3.29}$$

Here, $\boldsymbol{e}_\mathrm{x}^r$ is the unit vector in the x direction within the rotating frame. In contrast to the rotation of the magnetization under the influence of the Zeeman interaction, the magnetization is oscillating due to the QP interaction in the rotating frame.

3.3 ^{2}H NMR relaxometry and spectroscopy

In this work, several observables have been measured by a variety of pulsed ^{2}H NMR experiments. This section aims to give an overview over how the QP interaction can be utilized to measure the reorientational dynamics of molecules. Here, we will assume that the QP interaction is the only relevant interaction besides the Zeeman interaction and the rf-pulses. While a rf pulse is applied, the QP interaction is neglected. In addition, the QP interaction is assumed to be axially symmetric, i.e. $\eta = 0$, except where explicitly stated otherwise.

3.3.1 Relaxation in ^{2}H NMR

To be able to detect a NMR signal the spin system must be in a $\mathrm{p}_{\mathrm{r,s}}$ = -1 coherence state. Those states are non-equilibrium states of the magnetization. They can be generated for example by applying a $\pi/2$ pulse which flips the magnetization into the x-y plane. Fluctuations of the local fields caused by molecular motion induce relaxation effects that will bring the system back into equilibrium over the course of time.
Two relaxation mechanisms must be distinguished. The first is the longitudinal or *spin-lattice relaxation* (SLR). Here, the spin system dissipates energy into the lattice. The relaxation is usually exponential with a characteristic time constant T_1 in the laboratory frame. The second relaxation mechanism is the so called transversal or *spin-spin relaxation* (SSR). It is the dephasing of transversal spin coherences and is an energy conserving process. Therefore, SSR is also called transversal relaxation. As SLR, SSR is often exponential and exhibits a characteristic time constant T_2. In the following, both relaxation mechanisms will be discussed under the assumption of the *weak-collision limit*. In this limit fluctuations cause perturbations which are small compared to the spin Hamiltonian. The latter includes the Zeeman interaction, therefore the condition is usually satisfied in high magnetic fields. Further, the discussion is restricted to a semi-classical treatment of the lattice contributions, neglecting its quantum

mechanical properties. SLR and SSR are caused by the stochastic fluctuations which are caused by the molecular motion. To describe such a processes appropriately one often uses correlation functions (CF). In case of ^{2}H NMR molecular motion causes a variation of the angle θ between the deuterons bond axis and the external magnetic field $\mathbf{B_0}$ and thereby a variation of the QP frequency ω_0, see e.g. section 3.2.5. The normalized rotational auto-CF $F_2(t)$ correlates the initial orientation $\theta(0)$ with the orientation $\theta(t)$ at time t:

$$F_2(t) = \frac{\left\langle P_2\left[\cos\left(\theta(0)\right)\right] P_2\left[\cos\left(\theta(t)\right)\right]\right\rangle}{\left\langle \left(P_2\left[\cos\left(\theta(0)\right)\right]\right)^2\right\rangle}. \tag{3.30}$$

P_l is the l-th order Legendre polynomial. In ^{2}H NMR the rank of the observed correlation function is $l = 2$, see sect. 3.2. This is similar to e.g. *depolarized light scattering* (LS) where $l = 2$, while e.g. in *dielectric spectroscopy* (DS) the rank is $l = 1$. The most simple process that can be observed is an exponential decay of the CF

$$F_2 \propto \exp(-t/\tau), \tag{3.31}$$

where τ is the time constant that characterizes the timescale of the motion within the sample. By Fourier transformation the spectral density $J_2^D(\omega)$ in the Debye case can be obtained:

$$J_2(\omega,\tau) = \frac{\tau}{1+(\omega\tau)^2}. \tag{3.32}$$

Both quantities $F_2(t)$ and $J_2(\omega)$ contain information about the molecular dynamics in the sample. The theory of Bloembergen, Purcell and Pound (BPP) [153, 154, 161] connects the SLR time T_1 with the spectral density J_2 given by eq. (3.32), and thus, with correlation time τ. In case of a macroscopic sample, a powder averaged SLR rate can be expressed as:

$$\left\langle \frac{1}{T_1} \right\rangle = \frac{2}{15}\delta^2 \cdot \left[J_2(\omega_0,\tau) + 4J_2(2\omega_0,\tau)\right] \tag{3.33}$$

In eq. (3.33), it becomes obvious that SLR is mainly determined by fast fluctuations at the Larmor frequency and twice the Larmor frequency. Note that in the above equation the spin-lattice relaxation rate T_1^{-1} is used rather than the relaxation time T_1 itself. Both can be measured directly.
Inserting the Debye relaxation process described by eq. (3.32) into eq. (3.33) results in

$$\left\langle \frac{1}{T_1} \right\rangle = \frac{2\delta^2}{15} \cdot \left[\frac{\tau}{1+(\omega_0\tau)^2} + \frac{4\tau}{1+(2\omega_0\tau)^2} \right]. \tag{3.34}$$

By taking the derivatives of this equation, it can be easily seen that T_1 exhibits a minimum at a correlation time τ where $\omega_0\tau \approx 0.616$ holds.

The SSR originates from more slowly varying spin interactions, which do not induce spin transitions associated with an energy transfer. The coherence between the spins is lost in the SSR. When the magnetization is tilted into the x-y plane by a 90° pulse it precesses around the z-axis. The locally different fields cause different precession frequencies. The total detected signal, the FID, decays due to the SSR. In appropriate NMR experiments, so called echoes, c.f. section 3.4, parts of the SSR are reversible. Irreversibility of the SSR disturbs the use of echoes in NMR. It can arise from three factors. First, in interconnected spin networks, the evolution of the spin coherences can become chaotic and thereby irreversible over time. This is the case e.g. in solids where lots of spins are connected by dipolar coupling. In systems where QP is the only additional interaction, all spins are isolated from each other. The second reason of irreversibiliy is molecular motion. When an echo is used to reverse the SSR, this requires the spin interaction to be static on the time scale of the experiment. Molecular motion on that timescale therefore contributes to the irreversibility of SSR. Third, the translational diffusion in the presence of field gradients causes irreversible SSR. This may also happen when a field gradient is created by local difference in the magnetic susceptibility [162].
Similar to the SLR the time constant T_2, corresponding to the irreversible part of SSR, can be written in terms of the spectral density:

$$\left\langle \frac{1}{T_2} \right\rangle = \frac{\delta^2}{10} \cdot \left[3J_2(\omega = 0, \tau) + 5J_2(\omega_0, \tau) + 2J_2(2\omega_0, \tau) \right] \tag{3.35}$$

This equation is valid in this form only in the completely motionally averaged limit, where the dynamical fluctuations are fast compared to the static line width characterized by the coupling strength δ, i.e. $\delta\tau \ll 1$.

3.4 Pulsed ^{2}H NMR experiments

In this work several different ^{2}H NMR methods are used to obtain information about the dynamical behavior of supercooled liquids. For this purpose, the line-shape of one dimensional ^{2}H NMR spectra is investigated and the SLR is determined. At low temperatures two dimensional stimulated echoes are used to measure the correlation function F_2. Here, the theoretical foundations of the conducted experiments will be discussed.

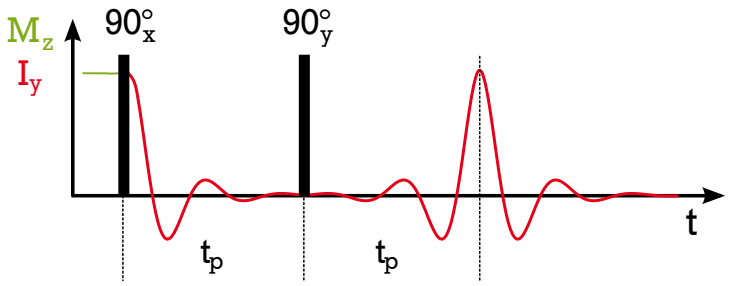

Figure 3.5.: Pulse sequence of a solid echo experiment.

3.4.1 One dimensional spectroscopy

The free induction decay is the simplest and one of the most widely used NMR experiments. It utilizes one single rf pulse to tilt the magnetization from its equilibrium direction into the x-y plane. Thus, the pulse sequence reads

$$90^\circ_x - \text{detection}.$$

In the x-y plane the magnetization precesses and thereby induces a measurable signal in the B_1-coil.
In amorphous solids, the individual spins precess with different frequencies, what results in broader spectra. This causes a loss of coherence and therefore a decay of the signal. In case of broad spectra, e.g. at low temperatures, the signal decays quickly and cannot be detected completely due to the dead time of the electronics after applying a pulse. The *solid echo* (SE) provides a simple method to refocus short time signals. As in a FID experiment, the magnetization is first transferred to the x-y plane by applying a 90° pulse. After the interpulse delay t_p a second 90° pulse is applied. It is phase shifted by 90° with respect to the first pulse:

$$90^\circ_x - t_p - 90^\circ_y - t_p - \text{detection}$$

This is sketched in figure 3.5. The effect of the sequence can be seen when calculating the density matrix $\hat{\rho}(t')$ at the time t' after the second pulse for a spin ensemble under influence of the QP interaction:

$$\hat{\rho}(t') = \left\langle \hat{I}_y \cos\left(\omega_Q(t' - t_p)\right) + \iota(\hat{T}_{2,1} - \hat{T}_{2,-1}) \sin\left(\omega_Q(t' - t_p)\right) \right\rangle \qquad (3.36)$$

The second term vanishes at $t' = t_p$ and only the initial $\hat{I}_y$ magnetization is refocused. This is called an echo, see figure 3.5. For times $t' > t_p$, the system evolves as in the FID experiment. The SE is used to measure spectra and to

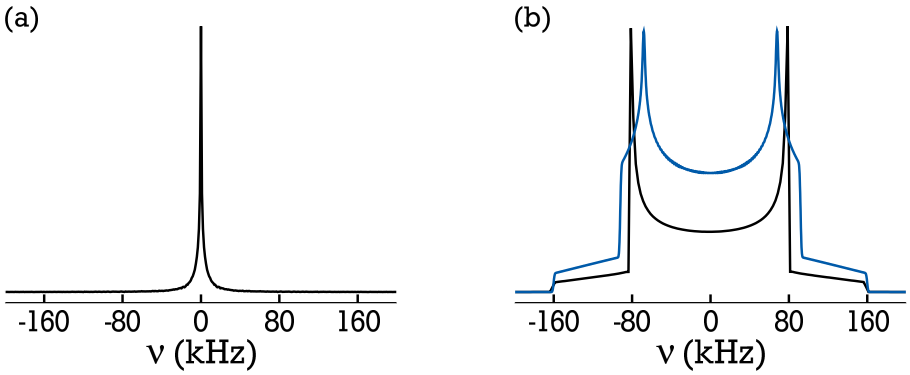

Figure 3.6.: (a) Lorentzian spectrum and (b) Pake spectra as expected in the fast motion and static limit, respectively. Black spectra have been calculated using $\delta = 160\,\text{kHz}$, $\eta = 0$ and an additional Gaussian broadening of 3 kHz. For the blue spectrum $\eta = 0.15$ was assumed.

determine the magnitude of the z-magnetization in several experiments, e.g. in saturation recovery experiments. The SE pulse sequence refocuses the signal in the limit of fast motion, where the QP interaction is motionally averaged and in the static limit where the motion is slow on the timescale of the SE experiment. In the intermediate motion range, where only few reorientation steps occur during the interpulse delay, the signal is not refocused due to irreversible SSR.

Line shape and motional narrowing

In this work, the focus is set on supercooled liquids. Therefore, spectra are measured using the above SE pulse sequence. By Fourier transformation of the time signal, starting at the echo at time t_p after the second pulse, the spectrum can be obtained. The shape of the resulting spectrum depends the time scale of the molecular dynamics in comparison to the experimental time scale. The latter is given by the inverse coupling constant δ^{-1}. Here, we discuss the spectra as measured by the SE experiment. Two limiting cases must be considered:

1. Fast motion limit: $\tau \ll \delta^{-1}$

   In this case, the molecular motion is on a timescale that is fast compared to the SE experiment time. A molecule assumes over many different orientations during the evolution period t_p. Therefore, the molecules exhibit the same averaged Larmor frequency ω_0. This results in a narrow spectrum, which is of Lorentzian shape in an isotropic liquid, as sketched in figure 3.6. The line-width at half maximum of this Lorentzian is given by the value of the SSR relaxation time:

$$\mathrm{FWHM} = \frac{1}{\pi \mathrm{T}_2}. \tag{3.37}$$

Since the relaxation time T_2 is connected to the correlation time, see eq. (3.35), this can be used to gain information about the molecular dynamics. In the limit of very fast motion, the spectrometer resolution limits the values of the observed FWHM. In the case of a non-isotropic motion QP can not be averaged completely. Then the line shape may be different from a Lorentzian and e.g. a Pake spectrum can be observed. In a situation where the rotation exhibits a C_n symmetry resulting in an equivalence of jump sites, the averaged anisotropy parameter

$$\overline{\delta} = \frac{\delta}{2}(3\cos^2\beta_\mathrm{C} - 1) \tag{3.38}$$

is observed. Here, β_C is the angle between the axis of rotation and the principle axis of the QP tensor.

2. Slow motion limit: $\tau \gg \delta^{-1}$

   In this case, all molecules are static on the experimental time scale, and thus, exhibit a quadrupolar frequency ω_Q. It us determined by the molecule's orientation which does not change during the SE experiment. In a disordered material, the molecular orientations are randomly distributed. Integration over the spatial distribution yields the well known Pake form of the spectrum [163] depicted in figure 3.6 (b). This is the so called powder average.

   Assuming vanishing asymmetry $\eta = 0$, the Pake spectrum can be described by

$$P(\omega) = \begin{cases} \frac{1}{\sqrt{6\delta}} \frac{1}{\frac{1}{2}\delta - \omega} & -\delta \leq \omega \leq -\delta/2 \\ \frac{1}{\sqrt{6\delta}} \left(\frac{1}{\frac{1}{2}\delta + \omega} + \frac{1}{\frac{1}{2}\delta - \omega} \right) & -\delta/2 < \omega < \delta/2 \\ \frac{1}{\sqrt{6\delta}} \frac{1}{\frac{1}{2}\delta + \omega} & \delta/2 \leq \omega \leq \delta \\ 0 & \text{else} \end{cases} \tag{3.39}$$

   The doublet form of the Pake spectrum is obtained in ^{2}H NMR due to the fact that there is always a doublet of lines $\pm\omega_\mathrm{Q}$. In eq. (3.39) singularities appear at $\omega_\mathrm{Q} = \pm\delta/2$. In the measurements, residual dipolar coupling is present which broadens the line and cause the singularities to be finite

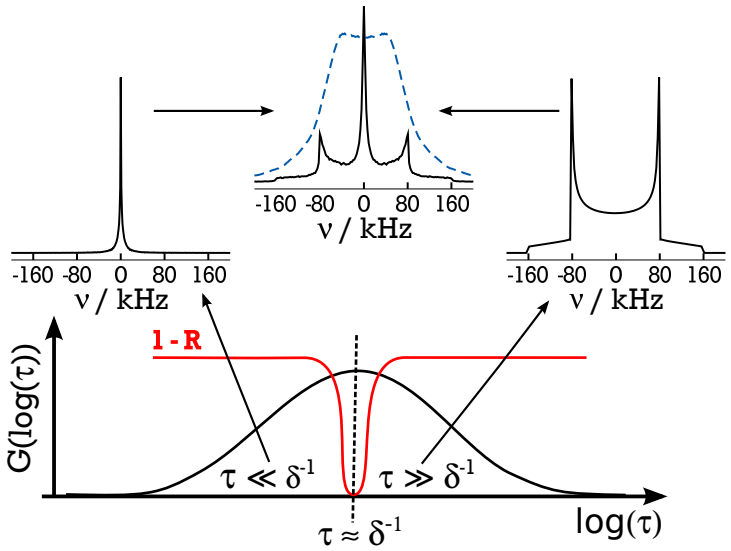

Figure 3.7.: Schematic origin of two phase spectra in SE experiments: Fast molecules from the distribution $G\left[\log(\tau)\right]$ give rise to a Lorentzian line (left hand side), while slow molecules result in a Pake pattern (right hand side). The sum of all molecules yields a two-phase spectrum (center). The reduction factor (1-R) is shown in red. Dashed blue: simulated FID spectrum with the same parameters.

peaks. The peaks move towards the center of the spectrum for a non-vanishing asymmetry $\eta > 0$, as sketched in the blue spectrum in panel (b).

Between these two limiting cases, there is the intermediate range of dynamics $\tau \approx \delta^{-1}$. There, the shape of the spectra strongly depends on the geometry and the rate of the motional process and their distribution. If a broad distribution of correlation times $G\left[\log(\tau)\right]$ exists, the spectrum consists of the contribution of both fast and of slow molecules. This is sketched in figure 3.7. The fast molecules yield a Lorentzian shape, while the slow molecules result in a Pake shape.
Molecules that reorient with $\tau \approx \delta^{-1}$ are not refocused in the SE experiment and do not contribute to the signal. This causes the detectable signal to decrease by a reduction factor R. The residual signal (1-R) is sketched in the figure. Superposition of the visible spectral contributions results in a so-called *two-phase spectrum* shown in black in the center of the figure. The shape depends not only on the distribution $G\left[\log(\tau)\right]$, but also on the geometry of the motion. Additionally to the SE spectrum figure 3.7 also shows a FID spectrum (dashed blue line), to demonstrate the influence of the non-reversible parts onto the shape of spectrum.

Evaluating two-phase spectra

In the presence of broad distributions of correlation times $G\left[\log(\tau)\right]$ two-phase spectra can be observed in an intermediate temperature range. The contributions of Lorentzian- and Pake-like spectral components can be evaluated to learn about the timescale of the motion. To determine the different contributions the Pake spectrum obtained at very low temperatures was fixed as $P(\omega)$. Additionally a temperature dependent Lorentzian line $L(\omega)$ was added to fit the temperature dependent spectra $S(\omega)$:

$$S(\omega) = W(T)L(\omega) + (1 - W(T))P(\omega) \tag{3.40}$$

When both components $L(\omega)$ and $P(\omega)$ are normalized, W(T) gives the percentage of fast molecules in the distribution $G\left[\log(\tau)\right]$. The fraction W(T) can be interpolated by

$$W(T) = \frac{1}{2} + \mathrm{erf}\left(\frac{T - T_{1/2}}{\sqrt{2}\sigma}\right). \tag{3.41}$$

Here, erf(...) is the error function. At the temperature $T_{1/2}$ the percentage of fast molecules is $W(T_{1/2}) = 0.5$ and $\tau(T_{1/2}) = (2\pi\delta)^{-}0.5 \approx 1\,\mu s$ is a good approximation for the position of the signal minimum observed in SE experiments.

The fraction W(T) can also be calculated from literature data if the temperature dependent distribution of correlation times $G\left[\log(\tau)\right]$ is known, as for example in comparison with dielectric spectroscopy. The theoretical weight factor W(T) is given by [122]:

$$W(T) = \int_{-\infty}^{a'} G(\log\tau)[1 - R(\log\tau)]\mathrm{d}(\log\tau) \tag{3.42}$$

Here, the signal reduction in the SE is taken into account by the reduction factor (1-R). The upper integration limit is given by the inverse anisotropy parameter $a' = \log(\delta^{-1}) \approx -6$.

3.4.2 Spin-lattice relaxation

The SLR is often measured using the *saturation recovery* (SR) pulse sequence. A series of n subsequent 90° pulses is used to destroy the initial magnetization. The pulses are separated by a time $T_2 \ll t_{sat} \ll T_1$. The magnetization is tilted back and forth in the x-y plane where SSR causes the magnetization to decay. In all SR experiments in this work, the number of pulses was set to $n = 9$.

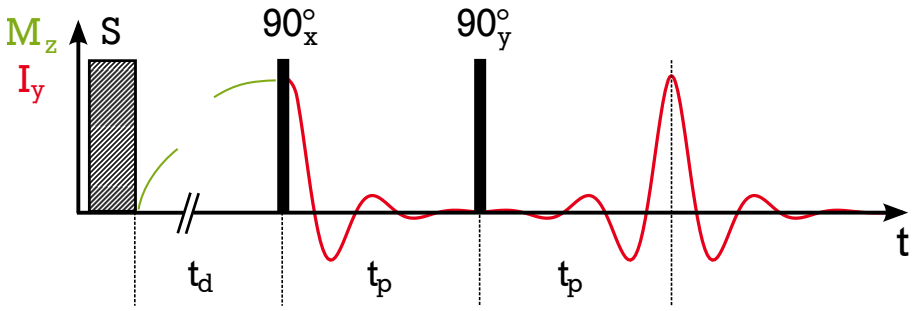

Figure 3.8.: Pulse sequence of a saturation recovery experiment. Note, that the delay time t_d can vary over several orders of magnitude.

The saturation sequence is followed by a variable delay time t_d in which the magnetization is allowed to rebuild in z-direction due to SLR. After this time a SE experiment is conducted to read out the magnetization. The experiment is sketched in figure 3.8. The magnetization build-up with increasing delay time can be described by

$$\frac{M(t_d)}{M_\infty} = \exp\left[-\left(\frac{t}{T_1}\right)\right] \tag{3.43}$$

for a monoexponential relaxation. Here, $M_\infty = M(t_d \to \infty)$ is the magnetization in thermal equilibrium and T_1 the SLR time constant. An alternative to the SR is the *inversion recovery* experiment. Instead of saturating the magnetization, a 180° pulse is used to invert the magnetization in the -z direction. This experiment requires longer waiting times, since the magnetization has to reach thermal equilibrium before the experiment, therefore mainly the SR experiment was conducted in this work.

3.4.3 SLR and distributions of correlation times

Usually a distribution of correlation times $G[\log(\tau)]$ is present in supercooled liquids. Under the assumption, that the molecules to not change their correlation time, every τ results in a relaxation time T_1 via the BPP model, see eq. (3.34). Therefore, a distribution of SLR times $V[T_1]$ exists. The observed magnetization build-up $M(t_d)$, e.g. in an SR experiment, is the average over the ensemble of all spins. A distribution $V[T_1]$ results in a non-exponential build-up which is often well described by a stretched exponential function:

$$\frac{M(t_d)}{M_\infty} = \exp\left[-\left(\frac{t}{T_1}\right)^\beta\right] \tag{3.44}$$

The arithmetic mean relaxation time $\langle T_1 \rangle$ is defined by

$$\langle T_1 \rangle = \int_0^\infty V(T_1) T_1 dT_1 = \frac{T_1}{\beta} \Gamma\left(\beta^{-1}\right) \tag{3.45}$$

where the second equality is derived by integrating eq. (3.44). The harmonic mean relaxation rate $\left\langle T_1^{-1} \right\rangle$ is given by

$$\langle T_1^{-1} \rangle = \int_0^\infty V(T_1) T_1^{-1} dT_1. \tag{3.46}$$

By fitting eq. (3.44) to experimental data the mean relaxation time is determined, while the relaxation rate can be determined by evaluating the initial slope of the magnetization recovery. In this work, the SLR times are obtained by fitting eq. (3.44) to the data.
In supercooled liquids there might be an exchange of correlation times when the molecules move and thus, change their dynamical environment. Such an exchange mechanism is for example provided by the structural relaxation process[3]. When the exchange of correlation times is faster than the SLR time T_1, then the molecules average over many positions and correlation times. This effectively averages the distribution $V\left[T_1\right]$ such that only a single relaxation time is observed. Only when the exchange becomes similar or slower than the time scale of T_1, the averaging breaks down and $V\left[T_1\right]$ becomes observable in SLR experiments, indicated by a stretching parameter $\beta < 1$.
It is possible to calculate correlation times using equation eq. (3.33) using $\langle T_1 \rangle$ rather than $\left\langle T_1^{-1} \right\rangle$, as long as the exchange averages $V\left[T_1\right]$. In this case, the relaxation time and the inverse relaxation rate are equal and the stretching parameter is $\beta = 1$. When the exchange process becomes too slow $\langle T_1 \rangle$ and $\left\langle T_1^{-1} \right\rangle$ are no longer equal. If structural relaxation is the exchange mechanism this means that the systems becomes non-ergodic. The temperature where this happens will be called T_{ne}.

3.4.4 Two-time correlation function: stimulated echoes

The *stimulated echo* (STE) experiment is designed to measure slow dynamics that are not accessible in relaxation experiments [164, 165]. For deuterons the STE can be conducted in two ways which measure the so called *Zeeman* (ze) order or *spin alignment* (sa) order. In both experiments two frequencies that are separated by a mixing time t_m are correlated with each other and correlation

[3] Another possible process is spin diffusion. There, magnetization is transported by a spin flip-flop processes not involving particle motion. Usually, in ^{2}H NMR spin diffusion slow is only effective at low temperatures.

times $\tau \sim t_m$ can be determined in the range from 10^{-5} s to 1 s. The upper limit is given by the SLR, i.e. $\tau \lesssim T_1$. The experiment consists of at least three pulses, often an additional fourth pulse is added. Here, we will focus on the three-pulse experiment. The pulse sequence is given by

$$90^\circ_x - t_1 - \psi_1 - t_m - \psi_2 - t_2 - \text{detection}. \tag{3.47}$$

ψ_1 and ψ_2 depend on whether a ze ($\psi_1 = \psi_2 = 90^\circ_x$) or sa ($\psi_1 = \psi_2 = 45^\circ_y$) experiment is performed. The sequence is sketched for the ze order in the upper part of figure 3.9 and for the sa order in the lower part. There, the possible fourth pulse is added, which is discussed below. The inter pulse distances are given by $t_m \approx \tau \gg t_1, t_2 \equiv t_p$.
At first a saturation sequence followed by a delay time t_d prepares the system in a common initial state. The first $\pi/2$ pulse tilts the magnetization into the x-y plane where it starts to precess under influence of the QP interaction with an initial frequency ω_i. At the time t_i after the first pulse the system is in the state

$$\hat{\rho}(t_i) = \left\langle -\hat{I}_y \cos(\omega_i t_i) - (\hat{T}_{2,1} - \hat{T}_{2,-1}) \sin(\omega_i t_i) \right\rangle . \tag{3.48}$$

Here and in the following calculations, the rf pulses are assumed to be infinitely short. The ψ_1 pulse applied after the time t_p transfers the spins in a storage state that is invariant in the subsequent mixing time t_m. In ze order this results in the density matrix at time t_i^+ after the second pulse this results

$$\hat{\rho}_{ze}(t_i^+) = \left\langle -\hat{I}_z \cos(\omega_i t_i) + \iota(\hat{T}_{2,2} - \hat{T}_{2,-2}) \sin(\omega_i t_i) \right\rangle . \tag{3.49}$$

By proper phase cycling [166–168] the double quantum coherence state ($\hat{T}_{2,2} - \hat{T}_{2,-2}$) can be eliminated such that only the term proportional to $\hat{I}_z$ remains. The third pulse transfers the magnetization back into a detectable state that evolves with time t_f after the third pulse as:

$$\begin{aligned} \hat{\rho}_{ze}(t_f, t_i) &= \left\langle \hat{I}_y \cos(\omega_i t_i) \cos(\omega_f t_f) + (\hat{T}_{2,1} - \hat{T}_{2,-1}) \cos(\omega_i t_i) \sin(\omega_f t_f) \right\rangle \\ &= \left\langle \hat{I}_y \cos(\omega_i t_i) \cos(\omega_f t_f) \right\rangle \end{aligned} \tag{3.50}$$

In the second step, it was exploited that the second term gives no detectable signal since its ensemble average vanishes. Analogously, the time evolution for the sa order can be calculated [164]:

$$\hat{\rho}_{sa}(t_f, t_i) = \left\langle \frac{3}{4} \hat{I}_x \sin(\omega_i t_i) \sin(\omega_f t_f) \right\rangle \tag{3.51}$$

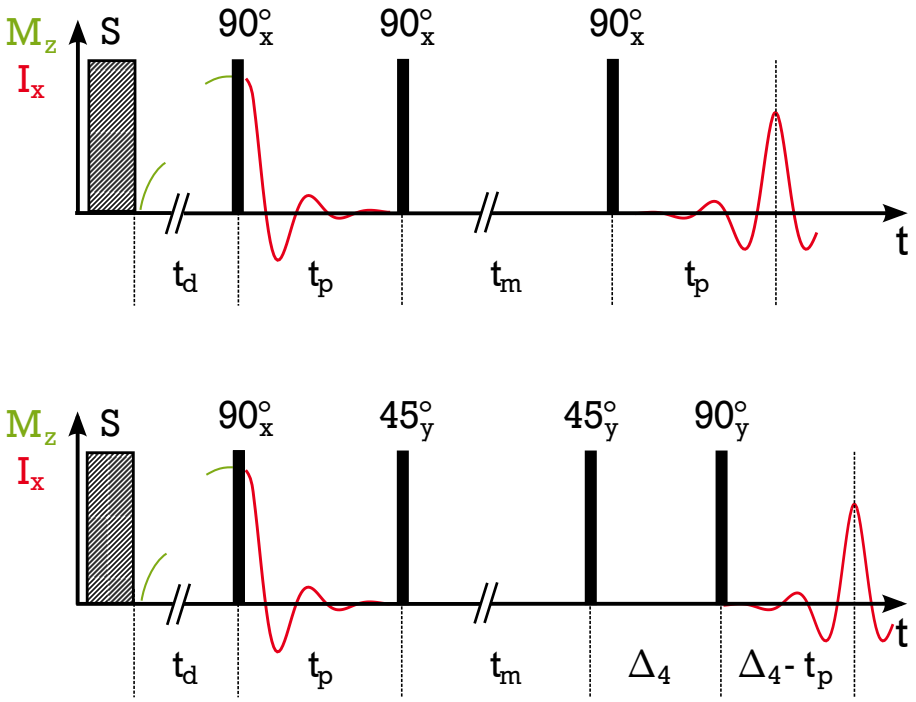

Figure 3.9.: Pulse sequence used to measure stimulated echoes: (top) three pulse Zeeman order experiment (bottom) four pulse spin alignment order experiment. Note that the delay time t_d and the mixing time t_m may vary over several orders of magnitude.

The expectation value for the measurements can be calculated using 3.4. Assuming the times $t_i = t_f = t_p$ and identifying the frequencies $\omega_i = \omega_Q(t = 0)$ and $\omega_f = \omega_Q(t = t_m)$ this gives the ze order or the sa order CFs:

$$F_2^{ze}(t_m, t_p) = \left\langle \cos\left(\omega_Q(0)t_p\right) \cdot \cos\left(\omega_Q(t_m)t_p\right) \right\rangle \tag{3.52}$$

$$F_2^{sa}(t_m, t_p) = \left\langle \sin\left(\omega_Q(0)t_p\right) \cdot \sin\left(\omega_Q(t_m)t_p\right) \right\rangle \tag{3.53}$$

The ensemble average is at maximum when both phases are equal. The echo is formed at the time t_p when the spin has not moved and the QP frequencies are equal $\omega_i = \omega_f$. Spins that have moved and thus $\omega_i \neq \omega_f$ do not contribute to the echo, they do not *refocus*. Thus, molecular motion within t_m leads to a decay of the measured signal.
Note that the storage state in the ze case is $\hat{I}_z$, which relaxes with the SLR relaxation time T_1. In sa order the storage state is $(\hat{T}_{2,1} \pm \hat{T}_{2,-1})$, which relaxes with the quadrupolar order relaxation time T_1^Q, see ref. [155] for details. It was shown that in case of rotational diffusion the two time constants are similar and obey $2/3 \cdot T_1 \leq T_1^Q \leq 5/3 \cdot T_1$ [164].

The STE experiments have several interesting properties that can be utilized to gain information on the samples. First, the sa order experiment can be used to directly measure the rotational auto-CF F_2 of a single particle. In the limit of short evolution times $t_p \to 0$ a Taylor expansion results in:

$$F_2^{sa}(t_m, t_p \to 0) \approx \left\langle \omega_i \omega_f \right\rangle \cdot {t_p}^2 \propto \left\langle P_2(\cos\Theta(0)) P_2(\cos\Theta(t_m)) \right\rangle \propto F_2. \quad (3.54)$$

It was used in this equation that the frequency ω is given by the second Legendre polynomial P_2 of the orientation Θ, see eq. (3.25), when the QP is axially symmetric, i.e. $\eta = 0$.
Secondly, STE echo experiments can be utilized to obtain information about the geometry in the samples. The phases that are correlated in the experiments depend on the QP frequency of the spin and thereby on the molecular orientation. The correlation functions F_2^{ze} and F_2^{sa} can be rewritten using trigonometric relations, here exemplary for eq. (3.52):

$$F_2^{ze}(t_m, t_p) \propto \left\langle \cos\left(\left[(\omega(0) - \omega(t_m) \right] t_p \right) + \cos\left(\left[(\omega(0) + \omega(t_m) \right] t_p \right) \right\rangle . \quad (3.55)$$

The two terms on the right hand side behave differently in the ensemble average. The first term is at maximum when both frequencies are equal and forms the STE. The second term results in a finite residual value $F_\infty^{ze}(t_p) = F_2^{ze}(t_m \to \infty, t_p)$ that oscillates with the evolution time t_p. Similar relations hold for the sa correlation function [157].
The existence of a finite plateau requires a modified description of the measured STE CF. In this work, a stretched exponential decay to the plateau $F_\infty^{ze}(t_p)$ is used:

$$F_2^{xx}(t_m, t_p) = \Psi(t_m) \left[\left(1 - F_\infty^{xx}(t_p) \right) \cdot \exp\left[- \left(\frac{t_m}{\tau^{xx}(t_p)} \right)^{\beta^{xx}(t_p)} \right] + F_\infty^{xx}(t_p) \right] \quad (3.56)$$

SLR relaxation is taken into account by a modified amplitude Ψ:

$$\Psi(t_m) = S_0 \exp\left[- \left(\frac{t_m}{T_1^*} \right)^{\beta^*} \right] . \quad (3.57)$$

Here, S_0 is the signal amplitude at $t_m = 0$. In eq. (3.56) the index xx = ze,sa indicates the correlation pathway. In Zeeman order experiments the SLR can be determined individually and thus eq. (3.57) can be fixed. In the sa order this is not the case and two more fit parameters T_1^Q and β^Q must be used.

The values obtained for $F_\infty^{xx}(t_p)$ are characteristic for the underlying motional process [169, 170]. It is very similar to the elastic incoherent structure factor (EISF) known from neutron scattering experiments [169], see section 3.9. The most prominent feature of the plateau is its value for long evolution times. It levels to a value of

$$F_\infty^{xx}(t_p \to \infty) = \frac{1}{n}, \tag{3.58}$$

where n is the number of orientational non-equivalent jump sites [169]. The residual correlation $F_\infty^{xx}(t_p$ shows an oscillatory evolution time dependence which is characteristic for the geometry of the motion.
The behavior of the observed correlation time constant $\tau(t_p)$ depends on the evolution time as well. The time t_p works as a geometric filter: When it is small, a detectable phase difference requires a larger change in the correlated frequencies ω_i and ω_f. A small angle reorientation needs a certain number of elementary jumps to be detected. Thus, at short evolution times the STE experiments are sensitive only for large angle reorientations. In contrast, at long evolution times small reorientation steps become accessible as well. By monitoring the behavior of both parameters, the correlation time $\tau(t_p)$ and the residual correlation $F_\infty^{xx}(t_p)$, it is possible to determine the geometry of the motion. Both can be modeled using random walk simulations, see section 3.8.

The determination of the auto-correlation function F_2 requires very short evolution times. Due to the dead time t_{dead} of the electronics, it is not possible to measure evolution times $t_p \lesssim 10\,\mu s$ using the three pulse sequence. The problem can be overcome by applying a fourth pulse in the STE experiment as was sketched in the lower part of figure 3.9. This pulse works as a SE sequence on the STE arising at t_p after the third pulse. It must be phase shifted to the third pulse by 90° and is separated by an interpulse delay of Δ_4. To work properly Δ_4 must be longer than the desired t_p and $\Delta_4 - t_p > t_{dead}$. Under these conditions an echo is formed at the time $\Delta_4 - t_p$ after the fourth pulse.

3.5 ^{2}H NMR experiments on supercooled liquids

The results of ^{2}H NMR experiments on supercooled liquids show some distinctive features that will shortly be discussed here. In a supercooled liquid the correlation time describing the α-process grows by many orders of magnitude, as sketched in figure 3.10. There, the correlation time follows a VFT temperature dependence, depicted as black solid line. This is often found in glass forming liquids, as for example in glycerol. When the α-process reaches a correlation time of 100 s, the liquid undergoes the dynamical glass transition at the

temperature T_g, compare e.g. section 2.1. T_g is marked as vertical blue dotted line.
Via the BPP theory, see eq. (3.33), the SLR time $T_{1,\alpha}$ can be calculated from the correlation times of the α-process, sketched as blue solid line. From the BPP theory one expects the relaxation time T_1 to increases further with decreasing temperature, approximately parallel to τ_α. In experiments this is not the case: Secondary processes as e.g. the excess wing in glycerol or the a Johari-Goldstein β-process in other glass formers dominate the relaxation. Therefore, the measured T_1 times deviate from those expected for a diverging α-process [87]. This is indicated by the dash-dotted lines in figure 3.10.
When the correlation time τ_α becomes of the order of the SLR time, the system becomes non-ergodic on the experimental timescale [12]. When this is the case, a molecule does not sample different spatial regions anymore. In the presence of dynamic heterogeneities, as usually found in glass formers [12], the SLR is not averaged anymore and the exponential relaxation becomes stretched, i.e. $\beta < 1$ [171].
In a good approximation, the deviation from unity of β happens when $\tau_\alpha \approx T_1$, as was shown e.g. in glycerol [172]. Therefore, we can approximate

$$\langle \tau_\alpha(T_{ne}) \rangle \approx T_1, \tag{3.59}$$

where T_{ne} is the temperature at which the system becomes non-ergodic. In this work, the temperature T_{ne} is defined by the point were β is significantly below unity, i.e.

$$\beta(T_{ne}) = 0.9. \tag{3.60}$$

At very low temperatures the parameter β is expected to increase again and level off at a value of $\beta = 1$. The reason is spin diffusion [38]. By energy conserving flip-flop processes the magnetization is transported without actual particle motion, what averages the distribution $V[T_1]$. In ^{2}H NMR spin diffusion is only effective at very low temperatures [173].

3.5.1 Field dependence of non-ergodicity

The characteristic behavior of the observables described above clearly depends on the timescale of the SLR time constant. Thus, the temperature T_{ne} is not a property of the material itself, but depends on the value of T_1.
Those time constants are calculated by the BPP theory from the correlation times and thereby depend on the externally applied magnetic field B_0. Hence, the temperature T_{ne} is a function of the magnetic field $T_{ne} \equiv T_{ne}(B_0)$. This can be seen when in fig 3.11. There, besides the curve sketched in fig. 3.10, a

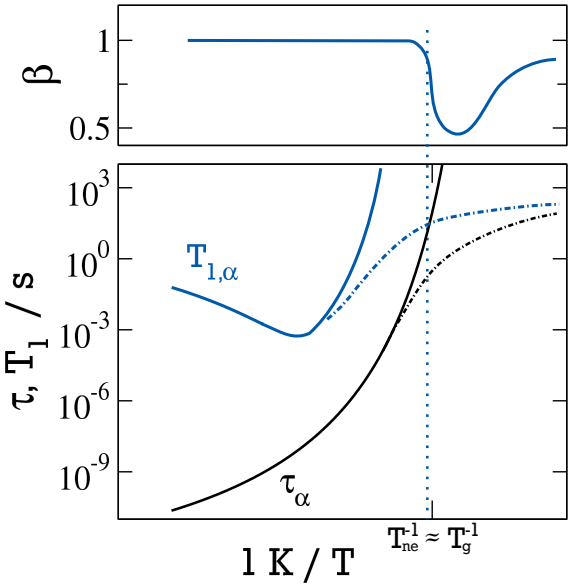

Figure 3.10.: Sketch of the behavior of correlation time τ_α and SLR relaxation time T_1 often found in supercooled liquids. Solid lines: the real behavior of τ_α (black) and the expected behavior of T_1 (blue). Dash-dotted: real behavior due to secondary processes. T_g is the glass transition temperature. The dotted line marks the point where $\tau_\alpha \approx T_1$. Upper panel: corresponding SLR stretching parameter β.

second T_1 curve is shown which would originate from a lower magnetic field. The T_1 time is inversely proportional to the spectral density at the Larmor frequency, c.f. eq. (3.33). Therefore, lower fields result in lower values of T_1 at temperatures below the T_1 minimum

The two SLR curves intercept the time scale of the α-process at different temperatures and at different correlation time values. The ergodicity breaking occurs at lower temperatures in lower magnetic fields. Correspondingly, the temperature T_{ne} monotonically increases with increasing fields. Thus, it may be possible, to map the correlation time τ_α using eq. (3.59) by measuring the field dependence of the SLR stretching parameter $\beta = \beta(T, B_0)$.

In the case of confined water, it was postulated that the α-process may not be observable or is even absent below ca. 225 K [11, 123]. By the method proposed here, it should be possible to track the α-process, if it still exists at lower temperatures. This relies on the fact that the α-process is the structural relaxation which restores ergodicity. Other relaxations may still be present in the system but cannot restore ergodicity [12]. The mapping uses the coarse approximation defined in eq. (3.59). Due to the fact that this is not a sharp transition, especially when a distribution $G\big[\log(\tau)\big]$ is present, the obtained

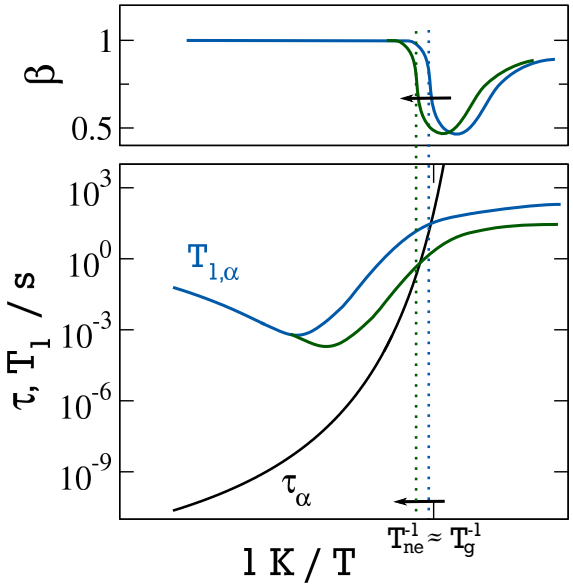

Figure 3.11.: Sketch of the breaking of ergodicity in NMR measurements, when different magnetic fields are applied. Upper panel: stretching β, lower panel: correlation time τ_α and SLR relaxation time T_1 for a higher magnetic field (blue) and a lower magnetic field (green).

correlation times have to be interpreted carefully. Instead of absolute times, mainly the temperature dependence is of interest.

3.6 Fast field cycling relaxometry

In standard NMR experiments, a static magnetic field is applied to create a Zeeman splitting of energy levels with a nuclei specific Larmor frequency ω_0. As it was shown in the previous sections, this can be used to get insights into dynamical properties. In this section the basics of *field cycling* (FC) NMR experiments will be discussed. In these experiments, the field is not generated by a superconducting magnet, but by a resistive magnet allowing to rapidly alter the external field.
By changing the magnetic field information about molecular dynamics can be obtained, which is not available in static field NMR. The SLR time T_1 depends on the spectral density at the Larmor frequency. Therefore, it is useful to measure the relaxation time T_1 at various fields with FC NMR. In this way the full dispersion $J(\omega)$, or more recently used the susceptibility $\chi(\omega) = \omega J(\omega)$ is available. A NMR susceptibility can be defined by

$$\chi_{\mathrm{NMR}}(\omega) = \frac{\omega}{T_1(\omega)}. \tag{3.61}$$

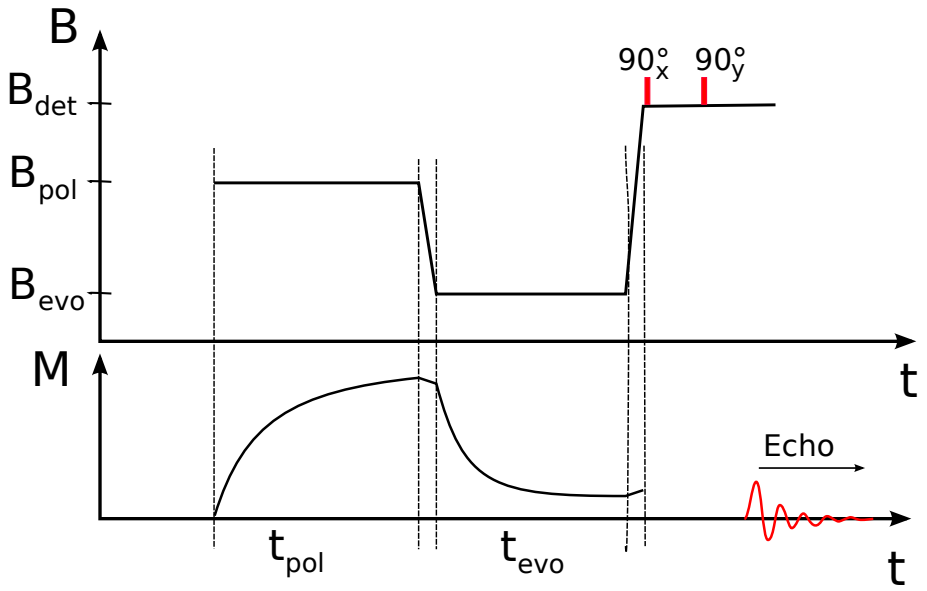

Figure 3.12.: Upper part: Sketch of the field cycle in FC NMR experiments. B_{pol} is the polarization field, B_{evo} the evolution field, and B_{det} the detection field. The applied pulses of a SE sequence are shown in red. Dashed lines separate the periods for which the fields are applied. The different fields are separated by short switching periods ($t_{switch} \backsim 1$ ms). Lower part: evolution of the magnetization in the different fields. In red: signal as measured in a SE experiment.

It has for example been utilized to determine the properties of polymer systems over a large time scale [174].

3.6.1 Principles of field cycling experiments

A scheme of a field cycling experiment is shown in figure 3.12. The experiment comprises of three time periods. They are separated by short time intervals necessary for switching and stabilizing the applied magnetic fields. In the first period t_{pol} the nuclei are polarized in a high polarization field B_{pol}. This is necessary when low evolution fields B_{evo} are applied in the evolution period t_{evo}. During the latter time the nuclear spins relax due to spin lattice relaxation towards their new equilibrium magnetization. After t_{evo}, the magnetic field is switched into the detection field B_{det}, in which the signal is measured. Switching into a high detection field has two advantages. First, the signal induced in the coil is enhanced and second the dead time of the spectrometer electronics usually decreases with higher frequencies. The detection field always has the same strength, so that the probe has to be tuned only once at the same temperature.
Usually a single pulse is applied to measure the FID of the magnetization. Figure 3.12 shows that in this work not one pulse is used, but a SE is performed in

order to overcome the dead time of the receiver for a solid sample, see section 3.4. To determine the SLR, the time t_{evo} is varied, and the magnitude of the SE signal is recorded, in analogy with saturation recovery experiments. The measured signal is proportional to the contrast $S \propto |B_{pol} - B_{evo}|$. Depending on the sign of the contrast it can be a magnetization decay or increase. To maximizes the signal the polarization is set to the highest field that can be applied when B_{evo} is small. When B_{evo} is large the pre-polarization is set to zero.[4] The feasibility of ^{2}H FC NMR for solid-state samples will be demonstrated in section. 7.1. There, it will become clear, that applications require a very good field stability.

3.7 Pulse induced sample heating

In the performed ^{2}H NMR experiments an effect was noticed that was by now only observed in studies using multi-pulse sequences [175, 176]. The rf-pulses used to manipulated the magnetization also deposit energy in the investigated sample. Usually this energy is assumed to be insignificant. For some of the samples investigated in this work this has shown to be not the case. The samples were heated in the course of the experiments. The heating has two effects: First, if the temperature dependence of e.g. the SLR is measured, the data are shifted on the temperature axis. The second effect is more subtle: Depending on the equilibrium of pulse induced heating and cooling it can create bimodalities in the measured SLR curves.
The explanation of this latter effect is sketched in fig 3.13. There the Curie corrected SE amplitude is plotted over inverse temperature. In the vicinity of the T_2-hole the pulse induced heating during the experiment can cause biomodalities. The insets in this figure show two SR experiments measured in a mixture of D_2O and glycerol confined to MCM-41 at initially $T_I = 241\,K$ and initially $T_{III} = 221\,K$. The higher temperature is above the T_2-hole. When the delay times t_d are short, the pulses heat the sample to a temperature T_{II} that is larger than T_I. The refocused signal is larger than that expected for T_I. At long delay times t_d the heat generated by the pulses can be transported away and the sample returns to T_I. The magnetization decreases to the lower value at this temperature. These effects are responsible for the maximum in signal observed at intermediate delays t_d. Below the T_2-hole the same effects creates a bimodality rather than a maximum in signal. In this case sample heating to a temperature $T_{IV} > T_{III}$ causes the magnetization to be lower for short delays t_d and to increase further when heat transport becomes effective.
Those observations allow one to determine the time that is necessary for cooling. The apparent second relaxation in both curves occurs at delay times of $t_d > 1\,s$. To test the influence on SLR relaxation times bulk glycerol-d_5 was measured

[4] Large here means $B_{evo} \leq 0.5\ B_{pol}$

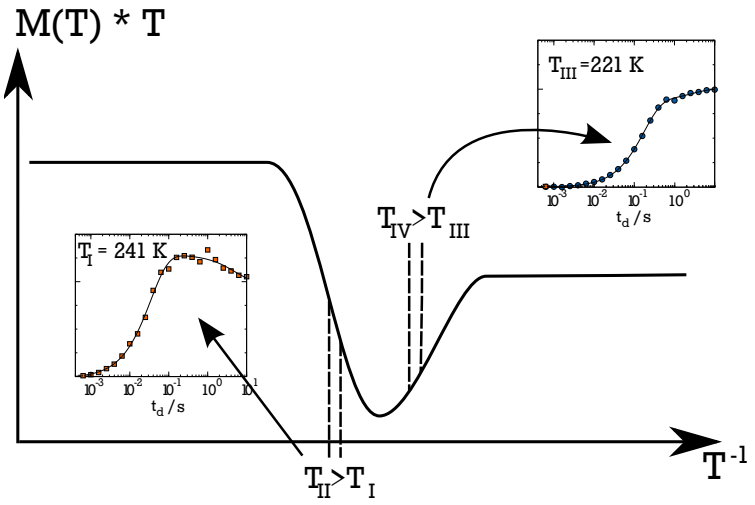

Figure 3.13.: Schematic temperature dependence of the SE reduction factor. In the temperature range, where motion is on the time scale of the inverse coupling strength the signal is not refocused, which is called the T_2-hole. Pulse heating effects may change the amplitude significantly during the experiment resulting in the behavior depicted in the insets. Depending on which side of the T_2-hole the measurement takes places, the signal decays or increases for long delay times in SR experiments.

close to its T_2-hole. Glycerol was chosen because it has a small distribution of correlation times and therefore a narrow and steep approach to the T_2-hole. The effect should be very prominent there. A SR experiment was conducted at $T = 239\,K$ using nine pulses in the saturation sequence. An additional waiting time t_x was introduced after the data acquisition.

Figure 3.14 shows the results for various times t_x. On the left hand side, the recovery curves are shown. As expected, the maximum at ca. 0.2 s increases with shorter recycle delays t_x. The effect vanishes for delays $t_x \geq 5\,s$. In panel (b) the fitted SLR times of the initial increase and of the decay are shown. To obtain those values two KWWs were fitted, the second one with negative amplitude. The short T_1-value is remarkably insensitive to the heating. The temperature dependence of the relaxation time is too small to cause an effect. The relaxation times of the slow decay are rather constant as well and vary in a range from 1 s to 3.5 s. At $t_x = 10\,s$ only a monomodal fit was performed. The magnetization is changed markedly. Panel (c) shows the ratio $M_N = M_{max} / M(t_d = 100\,s)$ of the magnetization in the maximum normalized to the final state magnetization.

The results show the necessity of using appropriate recycle delays in SR experiments. SR experiments should employ a recycle delay of at least $t_x \geq 1\,s$. To avoid sample heating less pulses in the saturation sequence should be used.

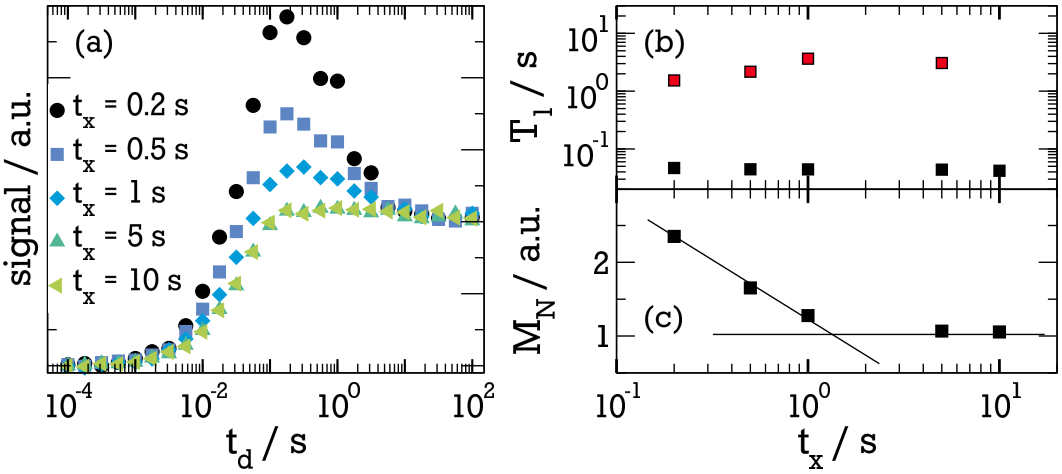

Figure 3.14.: Pulse heating for several recycle delays t_x in glycerol at 239 K. (a) SR curves. (b) Fitted T_1 relaxation times of the initial increase (black) and the decay (red). (c) Ratio $M_N = M_{max} / M(t_d = 100\,s)$ of maximum and final state of the magnetization. Black lines are guides for the eyes.

Experiments in our group have shown that n = 4 saturation pulses are sufficient in most samples. In the case of short SLR times the inversion recovery experiment can be used. In the IR no saturation sequence is applied reducing the irradiated power. As long as $5T_1 \lesssim t_x \approx 1$ applies usage of the IR does not increase measuring time compared to the SR.

3.8 Simulation of NMR observables

To enhance the power of ^{2}H NMR as a tool to investigate dynamics, *Random-Walk*(RW) simulations can be performed and compared with experiments. The simple orientation dependence of the QP interaction allows to calculate observables, as for example spectra and stimulated echo signals, by this simple method. This way qualitative information on the kind, the geometry, and the timescale of the motion can be extracted.

In this work RW simulations of different geometric models are utilized. Detailed information on the simulation programs and the utilized models can be found in ref. [177]. This section will shortly illustrate the basic foundations of the simulations. The simulations assume dynamics based on the Ivanov-model [178]. In this model the orientation of a particle is constant between two jumps and the jumps themselves happen instantaneously.

The NMR observables are calculated by averaging over multiple trajectories of molecular orientations $\vec{\Omega}(t)$. The ^{2}H NMR observables are calculated from the reorientation trajectory of the O-^{2}H-bond. The important quantity is the

orientation of the interaction tensor towards the external magnetic field $\boldsymbol{B}_0$. The orientation-dependency of the frequency must be described by eq. (3.25):

$$\omega_{\mathrm{Q}} = \frac{\delta}{2}\left[3\cos^2(\theta) - 1 - \eta\sin^2(\theta)\cos(2\phi)\right].$$

The constants δ and η are known from experiments or, in special cases, can be used as fit parameters, see below in sect. 3.8.2. With a given reorientation trajectory it is straight forward to calculate the signal for a desired pulse experiment. The calculation of NMR observables consists of two major parts: first, the generation of the trajectory $\vec{\Omega}(t)$ and second, the calculation of the signal from this trajectory. The steps are discussed in the next sections.

3.8.1 Generation of trajectories

Generating an orientation trajectory $\vec{\Omega}(t)$ consist of three steps. It utilizes a random number generator (RNG) giving equally distributed numbers $z \in [0;1[$.

1. In a first step, the geometrical model is implemented. Therefore, in models with a limited number of accessible sites, the vectors are pre-calculated. To simulate a powder the resulting set of orientation vectors is rotated by Euler rotations in a random orientation. In supercooled liquids all orientations are isotropically distributed on a unit sphere, therefore the start orientation cannot simply be chosen by chance, but must be weighted proportional to its probability. This can be established by choosing $\Theta_0 \in [0;\pi[$ in the form

$$\Theta_0 = \arccos(1 - 2z). \tag{3.62}$$

   This is equal to weight it by its solid angle element $\sin\Theta_0$. From the available orientations an initial orientation is diced, when there is no limitation of the number of accessible sites, the inital orientation is chosen by chance according to the probabilities of the angle Θ_0.

2. In the second step a waiting time t_{w} between two jumps must diced. According to a Markov process the waiting times are independent from all other waiting times. For a proper description an exponential waiting time distribution characterized by a jump correlation time τ_{j} is introduced:

$$P(t_{\mathrm{w}}) = \frac{1}{\tau_{\mathrm{j}}}\exp\left\{\frac{t_{\mathrm{w}}}{\tau_{\mathrm{j}}}\right\} \tag{3.63}$$

From the distribution a waiting time can be calculated by

$$t_w = -\tau_j \ln(1-z) \tag{3.64}$$

when using the normalization relation $P(z)\mathrm{d}z = P(t_w)\mathrm{d}t_w$ for the random numbers z [157]. When considering the timescale the geometrical filter effect discussed for STE experiments must be taken into account as well. For small angle jumps the jump correlation τ_j does not need to agree with the overall correlation time τ. This can be expressed by the relation [179]

$$\frac{\tau_j}{\tau} = \frac{3}{2}\sin^2\gamma \tag{3.65}$$

in the case of isotropic jump with an angle γ.

3. In the third step a new orientation must be chosen from all available ones when a jump happens. This step strongly depends on the implied model of motion.

The complete trajectory $\vec{\Omega}(t)$ requires repetition of step 2. and 3. until the sum of all waiting times equals the experiment length. In order to achieve good statistics many particles must be simulated. The number of virtual molecules simulated may range from 10^4 to 10^8 depending on the simulated geometry and experiment.

3.8.2 Calculation of the NMR signal

The second part in calculating NMR observables is the extraction of the time signal from $\vec{\Omega}(t)$. In this step the specific experiment plays an important role, since it is necessary to calculate the phase of the spin in every part of the experiment. For this work 1D SE and FID spectra as well as STE CF F^{xx} in ze- and sa-order were simulated.
For all simulations the initial point in time (t = 0) is set after the first pulse. This is valid due to the independence of the jump probability from the time bygone since the last reorientation [157]. In addition the time is also parted into constant, discrete increments of length Δt, which define the resolution of the experiment.

1D Spectra

The time signal of FID and SE experiments is proportional to the phase of the virtual bond. This results from the density matrix eq. (3.36) and can be expressed as [155, 157]

$$s_{\mathrm{FID}}(\mathrm{t}, \mathrm{t_p}) \propto \cos\left[\phi(0, \mathrm{t})\right] \tag{3.66}$$

in the simple case of an FID. For the SE spectrum it is:

$$s_{\mathrm{SE}}(\mathrm{t}, \mathrm{t_p}) \propto \cos\left[\phi(\mathrm{t_p}, \mathrm{t}) - \phi(0, \mathrm{t_p})\right] \tag{3.67}$$

with the phases $\phi(t_1, t_2)$ given by

$$\phi(t_1, t_2) = \int_{\mathrm{t_1}}^{\mathrm{t_2}} \omega_{\mathrm{Q}}(\mathrm{t}')\mathrm{dt}'. \tag{3.68}$$

In the simulations the phases are given by the frequency ω_0 which causes a phase shift of $\omega_0 \cdot \Delta\mathrm{t}$ in a time step $\Delta\mathrm{t}$. Hence, it is necessary to choose small time increments in order to account for all phase changes. Replacing the integrals in eq. (3.68) by discrete time steps gives

$$s_{\mathrm{SE}}(\mathrm{t}) \propto \cos\left(\sum_{\mathrm{t_i}=\mathrm{t_p}}^{\mathrm{t}-1} \omega_0(\mathrm{t_i})\Delta\mathrm{t} - \sum_{\mathrm{t_i}=0}^{\mathrm{t_p}-1} \omega_0(\mathrm{t_i})\Delta\mathrm{t}\right). \tag{3.69}$$

Note that $\Delta\mathrm{t}$ must be chosen such that $\mathrm{t_p}$ can be expressed as an integer multiple of Δt. The time signal $S_{\mathrm{t_p}}(\nu)$ is the sum over the signals $s_{\mathrm{t_p}}(\mathrm{t})$ of all trajectories. The spectrum can be obtained by Fourier transformation of the total signal. The transformation is performed starting at the time $\mathrm{t} = 2\mathrm{t_p}$ in the SE case and at $\mathrm{t} = 0$ for the FID spectra.

Fitting experimental Pake spectra

The spectra obtained from RW simulation can be fitted to experimental spectra by varying δ and η. For reasons of speed a powder average is approximated by pre-calculated sets of orientations. For each orientation the corresponding quadrupolar frequency shift is calculated and used to generate a time signal by adding up the individual signals weighted by their solid angle contribution. Additional Gaussian broadening was introduced to account for minor interactions and the spectrometer resolution. The influence of finite pulse length was attributed by convolution of a spectral resolution function $\mathrm{A}(\omega)$ [153]:

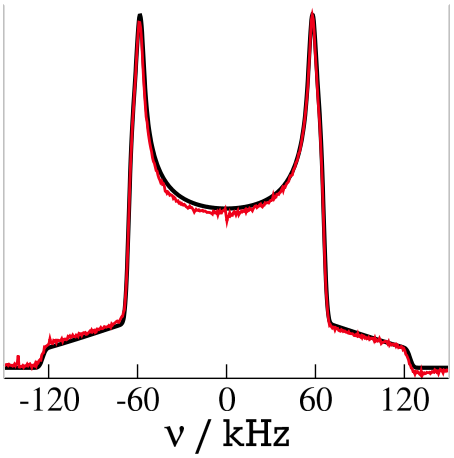

Figure 3.15.: Measured (red) and fitted (black) SE spectrum of confined glycerol (sample P49G) at T = 163 K.

$$A(\omega) = \omega_1 \Delta_{\pi/2} \left(\frac{\sin\left(\Delta_{\pi/2}\sqrt{\omega_1^2 + \frac{1}{4}\omega^2}\right)}{\left(\Delta_{\pi/2}\sqrt{\omega_1^2 + \frac{1}{4}\omega^2}\right)} \right)^3 . \tag{3.70}$$

This function approximates the shape of the Fourier transformation of a rectangle pulse. The frequency ω_1 is given as $\omega_1 = \gamma B_1$. The value of the pulse length Δ_p was fixed within experimentally set bounds, according to $\Delta_{p,fit} = \Delta_{p,exp} \pm 0.2\,\mu s$. By this procedure static spectra can be fitted using only the four free parameters δ, η, the pulse length $\Delta_{p,fit}$ and the additional Gaussian broadening. An example of such a fit is shown in figure 3.15 for glycerol confined to MCM-41 with d = 4.9 nm. Here, the assumption of static dynamics fits the spectrum very well.

Zeeman order stimulated echoes

STE signals are calculated analogous to the SE signals. The STE pulse sequence can be expressed by

$$s_{ze}(t) \propto \begin{cases} \cos\left(\phi_1(0,t_p)\right)\cos\left(\phi_2(t'_m+\Delta_4,t)-\phi_2(t'_m,t'_m+\Delta_4)\right) \\ \sin\left(\phi_1(0,t_p)\right)\sin\left(\phi_2(t'_m+\Delta_4,t)-\phi_2(t'_m,t'_m+\Delta_4)\right) \end{cases} \tag{3.71}$$

for ze and sa order, respectively. The signal depends implicitly on the evolution time t_p, the mixing time t'_m, and the time Δ_4 in case of a four pulse experiment[5]. Analogous to the 1D case the phases can be discretized. The important contributions stem from the phases in the evolution time given by

[5] In three pulse experiments Δ_4 is set $\Delta_4 = 0$.

$$\phi_1(0, t_p) = \sum_{t_i=0}^{t_p-1} \omega_Q(t_i)\Delta t \tag{3.72}$$

and the phase in the detection time given by

$$\phi_2(t'_m + \Delta_4, t) = \sum_{t_i=t'_m}^{t'_m+\Delta_4-1} \omega_Q(t_i)\Delta t \tag{3.73}$$

The abbreviation $t'_m = t_m + t_p$ is used. The calculations assume infinte short rf pulses.

3.9 Other experimental methods

In literature, the dynamical properties of confined liquids are routinely investigated using several experimental methods, for example *quasi elastic neutron scattering* (QENS) and *broadband dielectric spectroscopy* (DS). Additionally, *molecular dynamics* (MD) simulations are utilized to gain insights into structure and dynamics. Here, a short introduction into DS, MD, and QENS will be given. In addition, *differential scanning calorimetry* (DSC) will be introduced.

Broadband dielectric spectroscopy

Broadband dielectric spectroscopy allows to investigate the dynamics of supercooled liquids in a wide frequency range from 10^{-6} Hz to 10^{12} Hz. The sample is placed between the electrodes of a capacitor in a resonance circuit. The complex impedance in an alternating electric field $\vec{E}(\omega)$ is observed. The dipole relaxation and electronic charge rearrangement in the sample induces an electric displacement $\vec{D}(\omega)$ [180]:

$$\vec{D}(\omega) = \epsilon_0 \left[1 - \hat{\chi}_{DS}(\omega)\right] \vec{E}(\omega). \tag{3.74}$$

Here, $\hat{\chi}_{DS}(\omega)$ is the complex dielectric susceptibility and ϵ_0 is the vacuum dielectric constant ($\epsilon_0 = 8.85 \cdot 10^{-12} \frac{F}{m}$). On increasing the frequency, eventually the dipoles in the sample cannot relax fast enough to follow the external electrical field, causing a characteristic relaxation observable in $\hat{\chi}_{DS}(\omega)$. Usually, it is focused on the dielectric loss $\chi''_{DS}(\omega) = \mathrm{Im}\left\{\hat{\chi}_{DS}(\omega)\right\}$, where $\mathrm{Im}\{...\}$ is the imaginary part. It is related to the real part of the dielectric permittivity by the Kramer-Kronig relations [181].

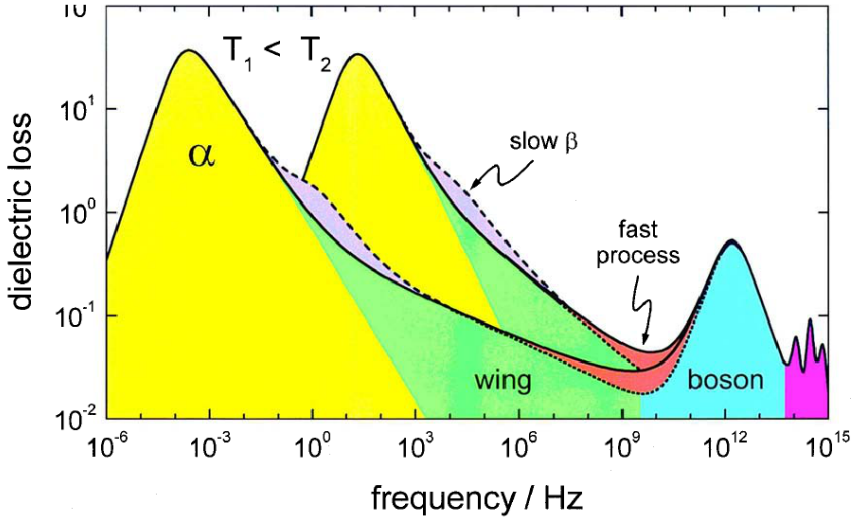

Figure 3.16.: Typical dielectric spectra at two temperatures. Figure adapted from [182].

The dielectric susceptibility $\hat{\chi}_{\mathrm{DS}}$ and equivalent the dielectric permittivity $\hat{\epsilon}_{\mathrm{DS}} = 1 - \hat{\chi}_{\mathrm{DS}}$ contain information about the reorientational correlation time of dipole moments connected to molecules in the sample. The relaxation strength of such a process is connected to the number of contributing molecules and their dipole moment. The relaxation peaks can often be described by the CC, CD, or HN functions introduced in section 2.1.3. Additionally, information about the electric conductivity and electronic mobility may be extracted.
A typical dielectric spectrum is sketched in figure 3.16, showing the peaks of the structural α relaxation, a possible β-process and the excess wing. In addition, higher frequency phenomena such as the Boson peak and electronic relaxation are indicated, but are out of scope of this work. Due to the dependence of dipole reorientation on the frequency, DS measures the rotational auto-correlation of the first Legendre polynomial $\mathrm{F}_1(\mathrm{t})$:

$$\mathrm{F}_1(\mathrm{t}_1, \mathrm{t}_2) \propto \left\langle \cos(\Theta(t_1)) \cos(\Theta(t_2)) \right\rangle \tag{3.75}$$

Here, Θ represents the orientation of the dipole and cross-correlations are neglected.

Quasi elastic neutron scattering

In QENS thermal neutrons are used to investigate dynamics and structure of systems at the (sub-)nanometer scale [183]. The De Broglie wavelength of neutrons at 300 K has a mean value of $\langle\lambda\rangle = 1.8\,\text{Å}$. The measured quantity is the double differential scattering cross section

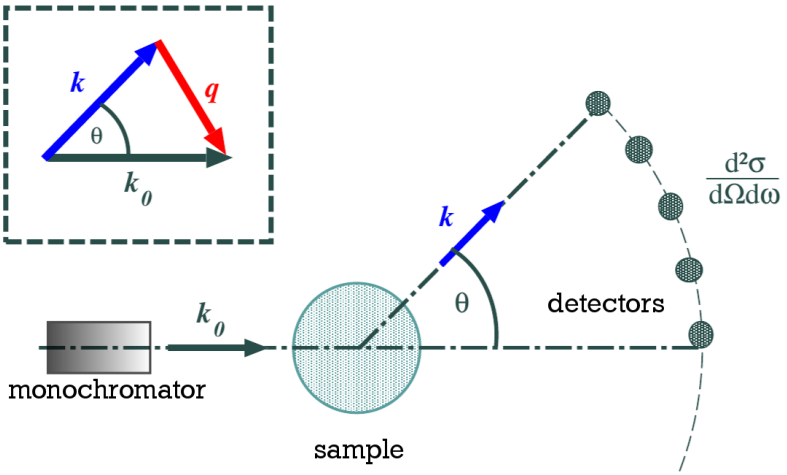

Figure 3.17.: Sketch of a neutron scattering experiment. The monochromator selects a velocity. Energy changes are detected by time of flight methods. Figure modified from [183].

$$\frac{\mathrm{d}^2\sigma}{\mathrm{d}\Omega\mathrm{d}\omega} = \frac{|\boldsymbol{k}|}{|\boldsymbol{k_0}|}\mathrm{S}(\boldsymbol{q},\omega) \tag{3.76}$$

In this equation, $\mathbf{k_0}$, $\mathbf{k}$ are the wave vectors of the incident and the scattered neutron wave, $\mathbf{q}$ is the scattering vector and ω is the energy transfer in units of $\hbar$, see figure 3.17. The information is contained in the *dynamics structure factor* $\mathrm{S}(\boldsymbol{q},\omega)$. Its information content is best seen in the Fourier transform $\mathrm{I}(\boldsymbol{q},\mathrm{t}) = \mathscr{F}\left[\mathrm{S}(\boldsymbol{q},\omega)\right]$ called the *intermediate scattering function* (ISF). It can be split into a coherent and an incoherent contribution $\mathrm{I}_{\mathrm{coh}}(\boldsymbol{q},\mathrm{t})$ and $\mathrm{I}_{\mathrm{inc}}(\boldsymbol{q},\mathrm{t})$. The coherent contribution depends on the phase relation of the waves scattered by different atoms, and thus, results in a measure of collective motion. In contrast, the incoherent part depends only on single atom contributions and results in a measure for self-correlation.

Whether coherent or incoherent scattering is measured depends on the atoms in the sample. The quantities $\mathrm{I}_{\mathrm{i}}(\boldsymbol{q},\mathrm{t}) \propto \mathrm{b}_{\mathrm{i}}^2$, $\mathrm{i} = \{\mathrm{coh}, \mathrm{inc}\}$, are proportional to the square scattering length $\mathrm{b}_{\mathrm{i}}^2$, which is an element and isotope specific constant. For example hydrogen atoms have a large incoherent scattering length and hence, the resulting ISF is dominated by their incoherent scattering. In contrast, deuterons only show a weak incoherent scattering and larger coherent scattering.

By spatial Fourier transformation the van-Hove self-correlation function can be calculated, i.e. $\mathrm{G}(\boldsymbol{r},\mathrm{t}) = \mathscr{F}_{\mathrm{r}}\left[\mathrm{I}(\boldsymbol{q},\mathrm{t})\right]$. In the case of incoherent scattering, $\mathrm{G}(\boldsymbol{r},\mathrm{t})$ can be interpreted as the probability density of a particle displacement, and thus gives a measure for single particle dynamics [183]. The long time

limit of the incoherent ISF, i.e. $I_{inc}(\boldsymbol{q}, t \to \infty)$, is of particular interest to obtain information about the type of motion. It is called the *elastic incoherent structure factor* (EISF) and gives the inverse of the average volume explored in the configuration space. The EISF is analogous to the residual correlation F_∞ measured in ^{2}H NMR STE experiments [169].
The usual time window of dynamic that can be observed is from some picoseconds to a hundred nanoseconds, by a combination of different NS techniques such as Time of flight, backscattering, and neutron spin echo. By observing the spectra at different detector positions, i.e. at different values of $\mathbf{q}$, the characteristic length scale at which dynamical processes are observed can be varied.

Molecular dynamics simulations

The dynamical and structural properties of supercooled liquids can be modeled in classical MD simulations. A detailed introduction into MD can be found in [28] and references therin. The term classical refers to the fact that the interaction of the atoms are approximated by effective potentials. Those are usually calculated using quantum chemical methods and also include effective and instantaneous electronic contributions.
In MD, the time evolution of the model system is calculated by iteratively solving Newton's equation of motion. The resulting trajectories contain all information about the system, from which all experimental observables can be calculated. MD simulations can be employed to unravel microscopic properties of a large variety of systems, that are limited only by computational costs and the availability of proper potentials. On modern computers, systems with roughly 10^5 atoms can be simulated on time scales up to the microseconds regime. In contrast to experiments, MD simulations can be used to investigate nonphysical systems were certain properties can be tuned to demonstrate the influence of certain properties, e.g. the charge distribution in a molecule. This was for example used to simulate water behavior in neutral pores [28,84]. Those possibilities render MD simulations a rather powerful tool that, in combination with experiments, can help to resolve the problems encountered in current research.
MD simulation also exhibits some drawbacks. The time scales of dynamics upon cooling towards the dynamic glass transition increases by orders of magnitude, becoming too slow for MD time scales. In addition, the system size is rather limited: Problems involving biological materials, e.g. proteins, may require too large systems or simulation times. The classical approach also neglects electronic contributions and quantum mechanical effects. Therefore, processes based on those effects, like chemical reactions and or tunneling effects, cannot be addressed with classical MD simulations. Parts of those problems can be tackled by using *ab initio* MD simulation. In this technique, the density

functional theory is applied to solve the Schrödinger equation. The problem of system size is currently addressed by coarse graining.

Comparison of QENS, DS, and MD with ^{2}H NMR

Figure 3.18 compares the accessible time and frequency ranges of the different methods. While very fast dynamics are accessible by MD and QENS, DS allows investigations in a very broad frequency range. The ^{2}H NMR time scale spans from some hundreds of picoseconds up to the seconds regime using different techniques.

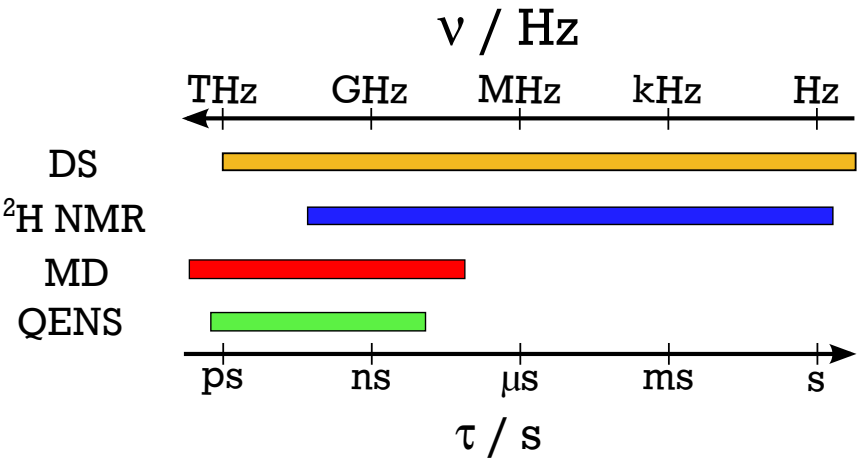

Figure 3.18.: Time scales of different methods used to characterizes the dynamics of supercooled liquids.

QENS experiments are successfully used at higher temperatures, where dynamics are still fast. There, they can provide valuable information about time and length scales of dynamical process and additionally on the mechanism of motion. Even more detailed information can be obtained by MD simulations, which rely on to the availability of appropriate potentials.
When the sample is cooled and dynamics become slow, both methods reach their limits. In this range ^{2}H NMR provides a useful tool to acquire information about the dynamics. Especially, on time scales between microseconds and seconds, this method can provide many insights into the dynamical process. The overlap of time scales with QENS and MD can be used to test the conformity of both methods.
DS can be used in an even broader frequency range. It is a very versatile method to obtain information about the time scales of the dynamical process. Nevertheless, DS usually can not provide specific information on the geometry of motion. Therefore, additional ^{2}H NMR and QENS experiments are necessary to gain a full understanding of the present dynamics.

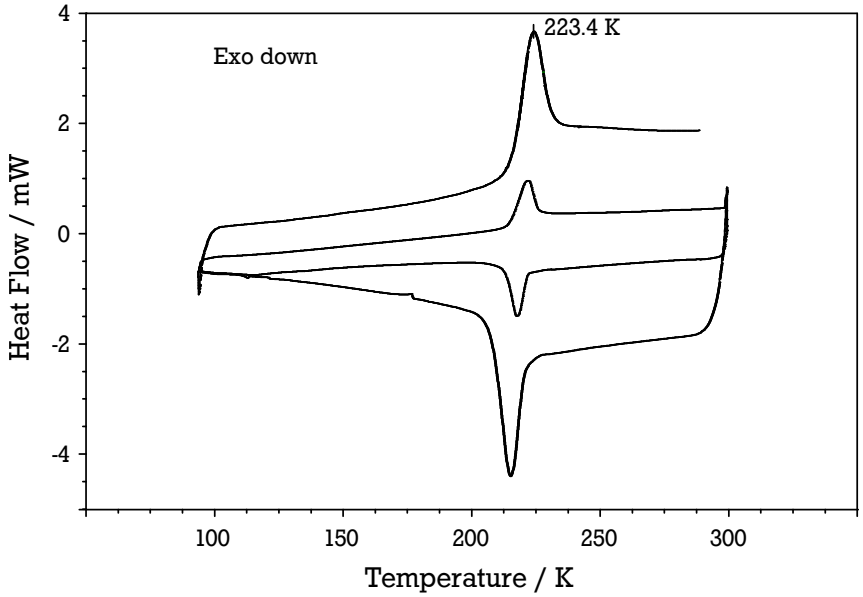

Figure 3.19.: Exemplary DSC thermogram of water confined to MCM-41 (sample P25). Cooling and heating rates were 10 $\frac{K}{min}$ (inner circle) and 40 $\frac{K}{min}$ (outer circle). Exothermic heat flow is negative. Measured by C. Lederle.

Differential scanning calorimetry

The thermal behavior of a sample upon temperature change can be quantified using DSC [180]. It is mostly used to gain information about the specific heat capacity c_p, which in turn provides insights into thermodynamic and chemical properties. When studying the behavior of supercooled liquids, c_p can be used to identify the glass transition or crystallization in the sample.
Usually, the heat flux from or to the sample is measured [180] and is compared to a reference. The desired thermodynamic quantities can be extracted from the temperature difference of the sample and the reference. In section 2.1.1, the temperature behavior of the entropy and the specific heat was introduced. A crystallization or melting event releases or requires large amounts of heat flux from or into the sample. This causes sharp peaks in a DSC thermogram. In contrast, a glass transition results in a step in the heat flow.
As an example, a thermogram obtained for water confined to MCM-41 with a pore diameter of d = 2.5 nm (P25) as obtained in this work is show in figure 3.19. The different cycles in the figure correspond to measurements upon heating and cooling with two different cooling rates. The measurement was performed by C. Lederle and shows a broad crystallization peak around 218 K and a melting peak at ca. 223 K . The DSC measurements in this work have been performed in the lab of AG Stühn, Technische Universität Darmstadt, on a *TA instruments* Q1000.

4 Setup and material

This chapter introduces the setups used in the present ^{2}H NMR experiments in section 4.1. It is focused on the three ^{2}H NMR spectrometers that have been utilized. In addition, there will be an introduction into the field cycling spectrometer which was used also used for ^{2}H measurements.
In the second part of the chapter the investigated samples are introduce. The specific properties of the confining matrix MCM-41 are discussed and the synthesis pathway that was followed in the production of the matrices is presented. Thereafter, the guest materials will shortly be presented and an overview over the different samples is given.

4.1 NMR spectrometer setups

In this thesis various NMR methods are utilized. The main method is ^{2}H NMR in static fields. Additionally ^{1}H relaxometry and field cycling measurements as well as ^{13}C relaxometry measurements are performed. The last technique is used to test whether the used MCM-41 samples have been cleaned from organic residues. They have been carried out by Msc. D. Demuth on a commercial 360 MHz TecMag spectrometer and will not be illustrated further.
The principle mode of operation of all NMR spectrometers is sketched in figure 4.1 [184]. All spectrometers run the *Darmstadt Magnetic Resonance Instrumentation Software* (*DAMARIS*) [185]. Thw software was developed at the TU Darmstadt to flexibly control home-built NMR spectrometers. For more details see the DAMARIS online documentation [186]. DAMARIS offers a *Python* based frontend with multiple pre-defined commands which allows for highly adapted pulse programs. The given scripts are translated into job-files which in turn are used by the backend to control the pulse card. All spectrometers are equipped with *SpinCore* Pulsblaster cards. They are clock-synchronized with the ADC card.
According to the programmed pulse sequence the reference frequency ω_{ref} is amplified to high power rf pulses and the pulses are passed into the probe via a directional coupler. The induced NMR signal is amplified and transmitted to the home-built receiver, where it is demodulated for quadrature detection. The signal is split into two identical signals and mixed with the reference frequency and the 90° phase shifted reference frequency. Low pass filters pass the differential component of the resulting signals.

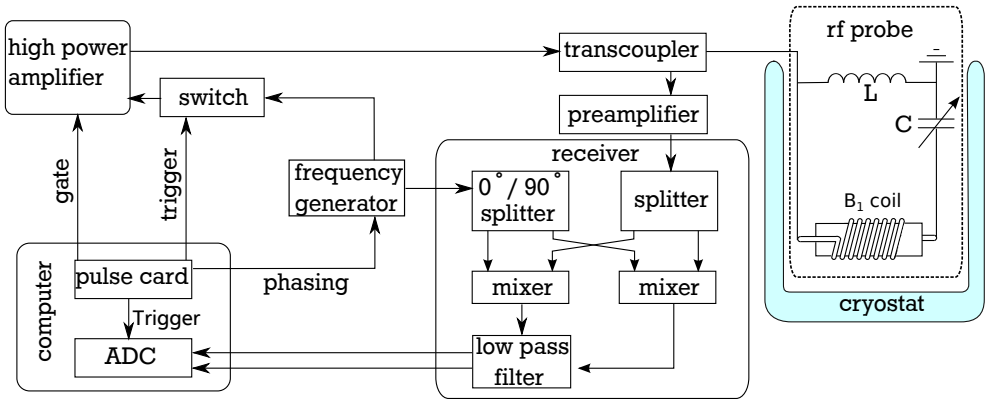

Figure 4.1.: Sketch of the general operating mode of a NMR spectrometer. Figure modified from [184].

The reference frequency in all spectrometers is generated by *Programmable Test Sources* PTS-310 or PTS-500 frequency generators (PTS). The PTS' phasing is controlled by the *DAMARIS* software. Besides those general aspects, all spectrometers posses individualized features and capabilities that will be illustrated in the subsequent sections.

4.1.1 ^{2}H NMR spectrometer

In the temperature-dependent measurements three deuteron spectrometers have been used. They are nicked 'Berta', 'Mathilda', and 'Schering'. All three feature fixed-field superconducting magnets with 4.61 T, 7.06 T and 7.15 T respectively. This corresponds to deuteron Larmor frequencies of 30.12 MHz, 46.14 MHz, and 46.71 MHz. The difference in the magnetic field of the latter two magnets is small and will be neglected in all discussions. Results from both spectrometers therefore will be referenced as measured at 46 MHz while the results of the 'Berta' spectrometer will be referenced as measured at 30 MHz. Additionally, during an re-powering of Berta measurements in a field of 1.63 T or 10.69 MHz were performed.

To conduct temperature-dependent measurements all three spectrometers are equipped with nitrogen flow cryostats. Those maintain a stable temperature by evaporating liquid N_2 and heating the gas to the desired temperature. 'Berta' is equipped with an *Oxford Instrument* cryostat and an *Oxford Instrument* ITC 502 temperature controller. The 'Mathilda' and 'Schering' spectrometers are both equipped with Konti cryostats from *CryoVac*. They are controlled by *CryoVac* TIC 304 MA control units, which allow for a temperature stability of $\Delta T \leq 0.5$ K or better. The sample temperature was measured with an additional PT-100 (or PT-1000 at 'Schering') resistance thermocouple in close vicinity to the B_1

coil. The setups enable measurements in the temperature range between 400 K and 80 K [1]. All three deuteron spectrometer are equipped with the PTS-310 frequency generator and *AMT* pulse amplifiers, delivering 1 kW (M3425) of power at 'Schering' and 2 kW at 'Berta' and 'Mathilda' (M3445 and M3435).
The setups provide the possibility to measure with a pulse length Δ_p in the range from 1.9 μs to 2.5 μs. The pulse length has adjusted to be in this range by extenuate the B_1 field strength. The pulse length has determined using a SE experiment with varying 90° pulse length. Pulse length measurements have been performed in the temperature dependent measurements at least every 10 K.
The experiments carried out in this work have been repeated with an recycle delay of at least 0.5 s in the case of water and with delays of 0.8 s to 1 s in all other samples. No sign of pulse induced sample heating was detected in confined water, c.f. section 3.7. In other samples pulse heating has been observed, see e.g. section 8.2.1. It was checked to have no influence on the measurements.

4.1.2 Fast field cycling spectrometer: FC-1

The field cycling spectrometer in the Fujara / Vogel laboratories is a state of the art home-built device called 'FC-1' [187]. It can be operated in different configurations, delivering different maximal and minimal field values, switching times, and field stability. In this thesis deuteron field cycling measurements have been performed, for which the high power current source from *Siemens* has been used in a range from 0.45 MHz to 4.5 MHz evolution field and a detection field of 12.7 MHz, compare figure 3.12. This corresponds to evolution fields of about 0.07 T to 0.7 T and a detection field of 1.95 T. In this setup switching times between the fields of 3 ms and below can be realized.
The standard setup of *FC-1* has been modified in order to measure solid state ^{2}H NMR relaxation. The samples need to be kept at low temperatures for some time. Therefore, a *CryoVac* Konti cryostat has been fitted to the setup, allowing for stable long term thermalization. The metal cryostat has been found to introduce strong eddy currents during field switching which cause temperature fluctuations. To stabilize temperature, the duty cycle of the experiments has been drastically reduced at the cost of increased measurement time.
The probe was adjusted to match the maximum detection field of B_{det} = 12.7 MHz. To reach the corresponding frequency the coil needs a high impedance. Coils with thin wire and many windings suffered from thermal problems caused by the applied high currents. To circumvent those problems, a coil with thicker wire was wound in a double layer geometry. The quality of the resonance circuit was reduced by purpose to increase the range of spectral

[1] Additionally the 'Schering' spectrometer offers the possibility to use liquid helium as cooling gas to reach temperatures down to 4 K.

excitation. The width of ^{2}H NMR spectra is usually larger than ca. 100 kHz, and thus, the full width at half maximum of the resonance was adjusted to 350 kHz in a compromise between spectral excitation and absorption of the resonance circuit. Nevertheless, the probe was not able to excite the whole spectrum equally. The utilized setup achieved a dead time of 19 μs in the detection field. An AMT M3525 power amplifier with up to 1 kW power output was utilized to irradiate the B_1 field. In this setup it is possible to measure solid echo saturation recovery in ^{2}H NMR FC. However, the usage of the SE sequence requires very stable phasing. This is discussed in the next section.

Phase stability in solid state FC

In ^{2}H NMR experiments the signal is much lower than in ^{1}H NMR experiments. Therefore, it is necessary to accumulate signal to increase the signal to noise ratio (SNR). In the performed deuteron experiments the minimum number of repetitions is eight scans to complete the SE phase cycle, see appendix C. Here, two full phase cycles have been performed in all experiments. Accumulating the signal is only possible if the phase keeps constant over the time of signal accumulation. Otherwise the signal cancels itself out rather than increasing SNR.
The field fluctuations become even more important on longer time scales: The solid echo sequence requires the second pulse to be 90° out of phase with respect to the first. If the field fluctuates, the actual Larmor frequency $\omega_0(t)$ deviates from the frequency ω_{rf} given by the frequency generator. The magnetization gathers an angle offset to the rotating frame according to:

$$\phi_M = \int_{t_p} dt(\omega_{rf} - \omega_0(t)) \approx t_p \cdot \Delta\omega. \tag{4.1}$$

Here, for the last equality it was assumed that the ω_0 fluctuates only slowly within the interpulse delay t_p. Due to the additional phase the second pulse refocuses magnetization only to a proportion of

$$S \propto |\cos(\phi_M)|. \tag{4.2}$$

This effect can be seen in figure 4.2, where the SE magnetization of dimethyl sulfone at 300 K is plotted versus $t_p \cdot \Delta\omega$. The phase was introduced by varying the field B_0 by purpose. The same effect can be observed in superconducting magnets when varying the irradiated frequency ω_{rf}, as shown in the figure for the 'Schering' spectrometer. The solid lines are fits with eq. (4.2).
The effect is a problem when measuring echoes in FC especially in the case of long SLR times $T_1 \gtrsim 1$ s. Either the polarization field or the evolution field

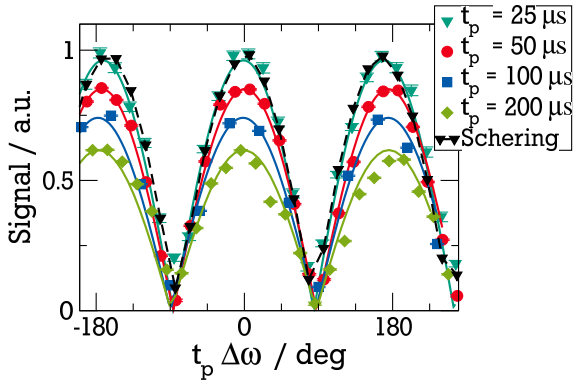

Figure 4.2.: Effect of an off-resonant field B_0 in FC NMR when using the SE experiment, compare eq. (4.1). For comparison: signal measured in 'Schering' when varying ω_{rf}. The dashed black line is a guide for the eyes, colored solid lines are fits with eq. (4.2).

must be switched on with high field strength on this time scale. This heats the main field coil, which in turn deforms slightly, causing the field B_0 to vary over experiment time and reducing the signal detected in the SE experiment.
Besides this strong side effect, the sensitivity of the SE experiment to off-resonance can be used to calibrate the field on-resonant. Similar to a pulse length measurement ω_0 must be tuned until a signal maximum is found. This is particularly useful in the solid state, where calibration using spectra is not possible due to the bad SNR.

Pulse length measurements in SE FC

As discussed in sect. 4.1, the quality factor in the resonance circuit was reduced for better spectral excitation. This does not excite the whole spectrum equally. In principle the resonance could be broadened to excite the whole spectrum, but this would require higher B_1 fields to keep the pulse length itself constant. In the present setup this was not possible due to the used coil design of the B_1 coil. Usually a certain pulse length Δ_p is required for a 90° pulse. It is dependent on the power used to irradiate B_1 and the specifics of the resonant circuit. In the SE FC experiments in glycerol pulse lengths of $\Delta_p = (4.5 \pm 1.0)\,\mu s$ where found in the liquid state. When determining the pulse length in the solid state the measured pulse length were substantially shorter. The reason for those deviations was the incomplete excitation of the spectrum. In the used setup a shorter pulse excites more spins in the solid state as a longer pulse does. The different excitation increases the signal for short pulses, even so they are actually not a 90° pulse. Thus, the pulse length were determined in the liquid, and keep constant over the whole temperature range.

In glycerol only a single narrowly distributed relaxation process is present [188], therefore effects of spectral excitation can be neglected. This is not the case in the presence of several separated processes or in case of broad distributions of correlation time. In both situations different spectral parts may represent different motions and excitation effects can severely alter the findings of NMR experiments.

4.2 Samples under investigation

This section will give an overview over the samples investigated in this thesis. To begin, the synthesis of the utilized MCM-41 confinements is discussed in section 4.2.1, followed by a section on sample preparation in section 4.2.

4.2.1 The Matrix MCM-41: Properties and synthesis

MCM-41 is utilized as a prototypical hard confinement. The abbreviation stands for *Mobils Composition of Matter No 41* and specifies a mesoporous silica sieve first synthesized by *Mobil Research and Development Corporation* in 1992 [103, 189]. MCM-41 exhibits easy to control pore properties. It shows a hexagonal ordering of the pores, which themselves are regular channels of hexagonal shape. The MCM-41 wall material consists of amorphous silica. The pore diameter shows a narrow distribution and ranges from 1.5 nm to 20 nm in a cylindrical approximation. The pore diameters can be controlled by choice of the organic template used in the synthesis (see below). The longitudinal extension is usually larger than 1 μm. The specific pore volume and surface are usually $V_p \sim 0.1$ to 1cm^3/g and $A_p \sim$1000 m^2/g, respectively.
MCM-41 is hydrophilic, thus it seems appropriate for studies on water and binary mixtures. Additionally it is possible to modify the surface of MCM-41 by linking different molecules. Thereby, the porosity and the hydrophobictiy can be controlled. This can be used to model a large number of biological and technological applications where the confinement is severe.

The MCM-41 materials used in this work were obtained from three different sources, see tab. 4.1. Most matrices were synthesized and characterized by Dr. M. Werner in the AK Buntkowsky,[2] at Technische Universität Darmstadt (TUD) within the framework of DFG project FOR1583.[3]
The synthesis has been performed following the protocol of Grün et al. [104] in the adaption of Grünberg and coworkers [190]. The organic template molecule

[2] Eduard-Zintl-Institut für Anorganische und Physikalische Chemie, Alarich-Weiss-Str. 8, 64287 Darmstadt

[3] Wasserstoffbrückenbildende Flüssigkeiten bei Anwesenheit innerer Grenzflächen unterschiedlicher Hydroaffinität

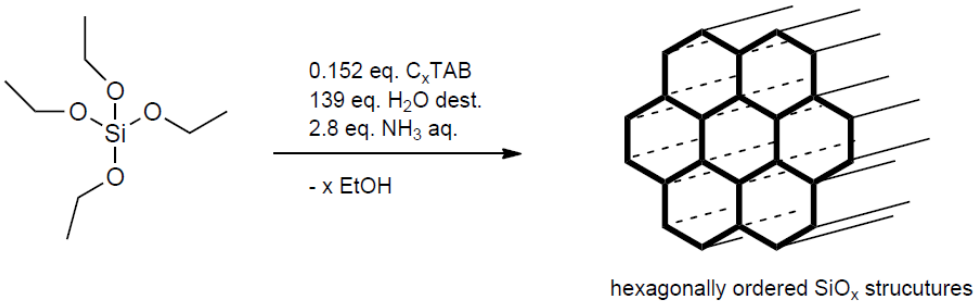

Figure 4.3.: Sketch of the pathway of MCM-41 synthesis. The figure is courtesy of Dr. M. Werner.

Tetraethoxy silane, C_nTAB (n-trimethyl-ammonium-bromide) with carbon chain length varying from n = 10 to 18, distilled water and 25 % NH_3 aq. have been mixed in the ratio of 1 : 0.1349 : 138.8 : 2.8. The as-synthesized material has been calcinated at 923 K for 16 h to remove the template. The procedure is sketched in figure 4.3. The chemicals have been obtained from Acros Organics (Tetraethoxy silane) and ABCR (C_nTABs) and have been used without further purification.
The sample were characterized employing N_2 gas adsorption. A multi-point Brunauer–Emmett–Teller (mBET) experiment [191] was used to determine the samples specific surface area S_p and the Barrett-Joyner-Halenda (BJH) analysis [192] to obtain the specific pore volume V_p as well as the diameter d_p, see also in appendix A.
In addition to the samples prepared at TU Darmstadt, a batch of MCM-41 with a pore diameter of d = 2.1 nm was used. It was synthesized and characterized by Kittaka and coworkers [102] and was used for measurements of the dynamic properties of water by means of NS, DS, and DSC experiments, see in ref. [102, 106, 120, 193–195] and chapter 5. For test and control measurements commercially available MCM-41 from Sigma Aldrich (CAS: 7631-86-9)

Table 4.1.: List of used MCM-41 samples and their physical properties as determined from standard mBET and BJH methods.

Supplier	d_p / nm	V_p / cm^3g^{-1}	S_p / m^2g^{-1}
TUD APTES	2.18	0.14	498
TUD	2.46	0.59	1002
TUD	2.76	0.82	974
TUD	2.93	0.86	1170
TUD	3.79	-	990
Sigma Aldrich	2.1 - 2.7	0.98	1000
S. Kittaka	2.14	-	1096

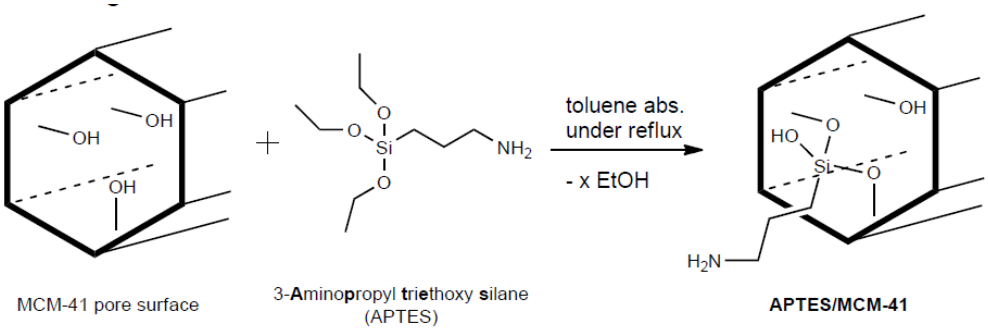

Figure 4.4.: Sketch of the pathway of the APTES modification of MCM-41. The figure is courtesy of Dr. M. Werner.

has been used. The specific properties of all MCM-41 powders are listed in table 4.1

Varying hydrophobicity: surface modification APTES

The surface of MCM-41 material is hydrophilic. To investigate the effect of a less hydrophilic environment on the water dynamics, a MCM-41 with modified surface has been investigated. In this sample, an organic linker molecule has been attached to the surface. This has achieved by adapting the grafting procedure from Adamczyk et al. [196]: Pre-activated mesoporous material MCM-41, has been prepared as described above. An amount of 3 g of powder in 50 mL of tolouene abs. has been refluxed with 3 g APTES (amino propyl triethoxy silane) for 3 h. The solid was washed with diethyl ether followed by a Soxhlett extraction with dichloromethane. Again the procedure has been performed by M. Werner in the AK Buntkowsky. It is sketched in figure 4.4.
In this procedure MCM-41 with a pore diameter of $d = 2.58\,\text{nm}$, a pore volume of $V_p = 0.18\,\frac{\text{cm}^3}{\text{g}}$ and a specific surface of $A_p = 827\,\frac{\text{m}^2}{\text{g}}$ was used. After the crafting the parameters listed in tab 4.1 were found. As can be seen in the direct comparison, all three characteristics of the MCM-41 are significantly smaller after linking the APTES to the surface. Possibly linking of APTES to the surface of MCM-41 is sketched in 4.5.

4.2.2 Sample preparation

In this thesis a variety of samples have been investigated. Here an overview over the different bulk and confined samples and their preparation is given. All samples used in this thesis were prepared either by Frank Fischer, a former now retired chemical assistant in the Vogel group, or by the author himself.

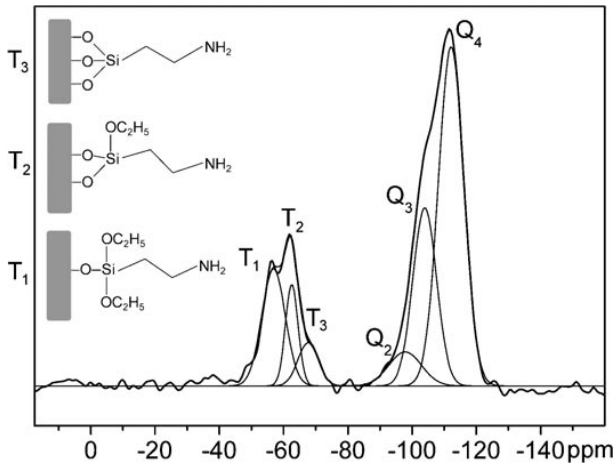

Figure 4.5.: ^{29}Si NMR spectrum of APTES modified SBA-3 T_n peaks are produced by linked carbohydrate chains, Q_n peaks stem from unmodified Si. Figure taken from Ref. [197].

Water confined to MCM-41

In chapter 5 the dynamics of water confined to MCM-41 is investigated in dependence on the pore size. The first step in preparation is the dehydration of MCM-41 powder. Most samples were dried by heating the powder to 450 K for at least 24 h. Since this doesn't remove all water from the powder a few samples were dried by evacuation to low pressures smaller than $1 \cdot 10^{-4}$ mbar for 24 h. No significant differences in water dynamics have been found comparing both methods.

To prepare the samples the dry MCM-41 was filled in the NMR tubes and the necessary amount of water was added by weighing. Table 4.2 gives a list of samples that were used in the investigations. The samples are named after the

Table 4.2.: List of samples of confined D_2O . MCM-41 is obtained from SA (Sigma Aldrich), SK (group of S. Kittaka) and TUD (Ak Buntkowsky). Additional information and references are given in the last column.

Sample	MCM-41	Size	
D_2O	-	-	Bulk D_2O
P21	SK	2.1 nm	-
P21w	SK	2.1 nm	wet preparation
P25	TUD	2.5 nm	-
P25w	TUD	2.5 nm	wet preparation
P27	SA	2.7 nm	-
P28	TUD	2.8 nm	-
P29	TUD	2.9 nm	-
P22a	TUD	2.2 nm	APTES [198]

mean pore diameter in Angström, e.g. as P21 for a pore diameter of d =2.1 nm. The table lists two samples where much more water than necessary to fill the pores was introduced into the sample. There, large amounts of excess water outside the pores are present. They will be marked with an additional suffix w. All confined water samples were sealed by two component epoxy resin separated from the powder by a teflon spacer. This method is unstable over long times when several heating and cooling cycles are performed. Therefore, all samples were measured within three months after preparation. The samples were tested for tightness by repeated weighing before and after the measurements. The used D_2O was obtain from Sigma Aldrich (CAS: 7789-20-0 and used as received.

Confined alcohols and mixtures

Besides heavy water also samples containing glycerol and mixtures of D_2O with the alcohols propylene glycol (PG), propylene glycol monomethyl ether (PGME) and the dimer DiPGME as well as bulk and confined glycerol (GLY) were investigated. The alcohols are composed of a propylene chain as basic structure unit, see also figure 2.11. In the case of glycerol, at each of the three carbons one hydroxyl (OH) group is attached. In PG only two OH groups are present at the first and the second carbon. PGME contains only a single OH group at the first carbon and a methyl ether at the third. The dynamics of the bulk liquids of all are well investigated, see e.g. in [119] and chapter 8 for details.
The glycerol samples were prepared analogous to the samples containing pure D_2O . First, the MCM-41 was dried and afterwards the glycerol was added by weighing. An overview over the studied samples is given in table 4.3. The samples were measured by different researchers: The table gives references to the original works, compare also chapter 8.
Table 4.3 also lists the other mixed systems. All mixtures are using a short notation of the guest and the water content. The water concentrations are given in terms of the mass ratio of water to guest. It is abbreviated with the prefix W, e.g. as W45 for 45 % weight of water. Additional suffixes b and c indicate bulk and confined samples. In the preparation of samples containing mixtures the liquid was not added to the MCM-41 by weighing. Here, a common procedure from literature was followed and the MCM-41 was immersed in a large amount of the mixture, see e.g. in [86, 204]. Occasional jolting prohibited segregation. After seasoning for several days the MCM-41 powder was carefully toweled with non-fuzzing lens cleaning tissue to remove external liquid. The powder was filled in NMR tubes and resin sealed thereafter.
The DiPGME samples have been prepared twice: during the second preparation the filled MCM-41 powder was wiped for several times to reduce the amount of possible pore-external liquid. The two preparations are refereed to as wet

and dry in this work. The DiPGME samples were provided by the group of Jan Swenson[4]. They were send pre-mixed and already immersed in the MCM-41 powder.
Since the different guest molecules exhibit different molecular weights the weight ratio of water is not straight forward to compare for different samples. In table 4.4 additionally to the weight ratio also the molar ratio of the mixtures is presented.
Some of the mixtures show crystallization effects upon cooling. The drop of signal in the ^{2}H NMR measurements on crystallization is given in the table as well as the approximated temperature were the phase change occurs. The drop of signal is estimated from the reduction of the signal in the fast component before and after the crystallization event. Note that this is only a coarse approximation since the amplitudes are not easy to determine precisely in ^{2}H NMR experiments, as a consequence of the signal reduction in SE experiments. Additionally the residual weight percentage of water is calculated in the table assuming that only water crystallizes.

[4] Department of Physics, Chalmers University of Technology, Gothenburg, Sweden

Table 4.3.: Investigated mixtures of alcohol and water. The water content will be given as Wxx, where xx is the mass ratio of water. MCM-41 is obtained from SA (Sigma Aldrich) and TUD (Ak Buntkowsky). Additional information and references are given in the last column.

Sample	Guest	Water	MCM-41	supplier	
gly	glycerol-d_5	-	-	-	Bulk [199]
P28G	glycerol-d_5	-	2.8 nm	TUD	-
P49G	glycerol-d_5	-	4.9 nm	TUD	[200]
PG W45	PG	45	-	-	Bulk [201]
PG W45c	PG	45	2.8 nm	TUD	[202]
PGME W40b	PG	40	-	-	Bulk
PGME W60b	PG	60	-	-	Bulk
PGME W80b	PG	80	-	-	Bulk
PGME W40c	PGME	40	2.8 nm	TUD	-
PGME W60c	PGME	60	2.8 nm	TUD	-
PGME W80c	PGME	80	2.8 nm	TUD	-
2PGME W15c	di-PGME	15	2.7 nm	SA	dry / wet [203]
2PGME W45c	di-PGME	45	2.7 nm	SA	dry / wet [203]
2PGME W75c	di-PGME	75	2.7 nm	SA	dry / wet [203]

Table 4.4.: Molar ratio and signal ratio in the mixtures given in molecules and signal of water per guest. When crystallization occurs, the approximate signal drop of the fast component, the crystallization temperature and residual water concentration is listed.

Sample	molar ratio	signal	Signal drop / %	T_f / K	residual c_w
PG W45c	3.1	3.1	60	221	W13
PGME W40b	3.0	6	-	-	-
PGME W60b	6.9	13.8	57	236	W37
PGME W80b	18.4	36.8	74	248	W50
PGME W40c	3.0	6.0	30	229	W32
PGME W60c	6.9	13.8	50	270	W43
PGME W80c	18.4	36.8	50	265	W67
2PGME W15	1.3	2.6	-	-	-
2PGME W45	6.1	12.2	51	248	W29
2PGME W75	22.3	44.6	75	261	W43

5 Dynamics of confined water

In section 2.3 the possibility of entering the *no-man's land* by confining water to narrow geometries was discussed. This approach can help to clarify the peculiarities of water dynamics in the deeply supercooled regime where a second critical point was theorized [205]. Additionally, the research on confined water in the vicinity of different types of surfaces may help to obtain information relevant to various subjects where confined water plays a crucial role, as for example in biology [2, 206] and medicine [207] or in construction and geology [208].
One of the main goals of this thesis is to contribute to the discussion whether there is a dynamical transition in confined water. At the transition temperature T_L the fragile behavior of the high temperature liquid changes to a low temperature strong behavior, as would be the consequence of the second-critical point hypothesis [209]. This hypothesis predicts the existence of a high density and a low density form of liquid water. Here, the results of the performed ^{2}H NMR experiments on heavy water confined to the amorphous matrix MCM-41 in various pore sizes are reported. ^{2}H NMR experiments are a valuable extension of the experiments that have been performed earlier in similar systems of confined water. The method covers a broad range of time scales of rotational dynamics [38, 116] in particular the scale of few nanoseconds, where the FST was postulated to take place [9].
In this chapter, the results of the investigations of D_2O confined in MCM-41 of several pore sizes will be presented. The measurements span a large range of temperatures and time scales using various ^{2}H NMR techniques. The results of the performed SLR experiments, LSA and STE will be presented and discussed together with corresponding results from literature. Combination of the three methods provides information on the characteristic time of the motion from picoseconds up to seconds. Additionally, insights into the geometry underlying the motional processes can be obtained. The discussion begins with the fast dynamics in the high temperature regime obtained from SLR measurements.

5.1 Spin-lattice relaxation of confined D_2O

In this section, the dynamics of confined water are investigating by ^{2}H NMR SLR. It yields information about the specific reorientation times in the high temperature region, where the correlation times range from picoseconds to microseconds. SLR experiments in the low temperature regime yields qualitative

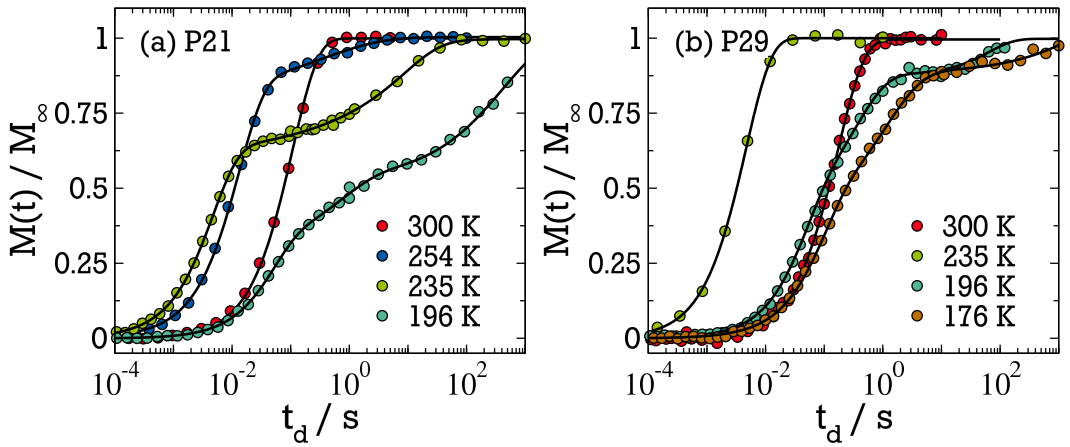

Figure 5.1.: Magnetization recovery curves of water confined in MCM-41 with pore sizes of (a) d = 2.1 nm and (b) 2.9 nm. Curves are normalized to a total magnetization $M(t_d \to \infty) = 1$. Black solid lines are fits using eq. (5.1).

information about the dynamics. They can be used in combination with other methods to gain insight into the rotational mechanism of water.

5.1.1 Saturation recovery measurements

In SR experiments the sample magnetization is destroyed and the recovery to thermal equilibrium is monitored via solid echo detection, c.f. chapter 3.4. The magnetization recovery with time is shown for some representative temperatures in figure 5.1 for the two samples P21 in panel (a) and P29 in panel (b). There, water is confined to pores of 2.1 nm and 2.9 nm respectively, being the smallest and the largest investigated pores. More details on the systems can be found in sect. 4.2. All experiments in this section have been performed at a magnetic field strength corresponding to 46 MHz Larmor frequency. At high temperatures only a single exponential relaxation is observed, which splits into three relaxations at lower temperatures. Those will be named fast relaxation (f), slow relaxation (s) and ice-like relaxation (i). Here, the last relaxation is the slowest relaxation process in the systems occurring at very long delay time t_d compared to the other two. The reasons for this nomenclature are discussed below. For all samples and temperatures an appropriate number of KWW relaxations eq. (3.43) has been used to fit the relaxation curves:

$$\frac{M(t_d)}{M_\infty} = 1 - \sum_{r=f,s,i} M_r \exp\left[-\left(\frac{t_d}{T_{1,r}}\right)^{\beta_r}\right] \tag{5.1}$$

In equation eq. (5.1) M_r represents the relative magnetization of the different components, which fulfill $\sum_{r=f,s,i} M_r = 1$. Each relaxation is characterized by

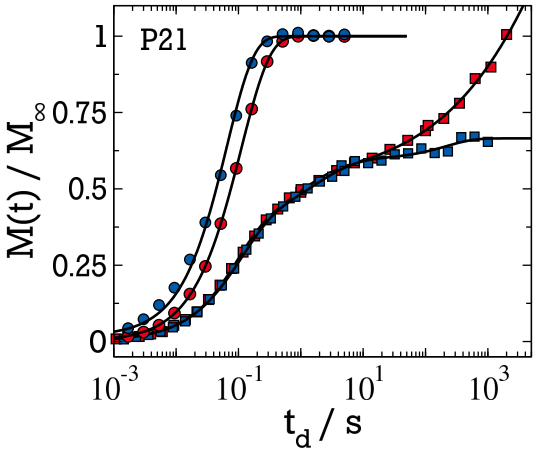

Figure 5.2.: Comparison of the magnetization recovery of sample P21 at 300 K (circles) and 167 K (squares). Blue and red dry (P21) and wet (P21w) preparation samples.

a time constant $T_{1,r}$ and a stretching parameter $0 < \beta_r \leq 1$. On decreasing temperature the recovery curves first shift to shorter delay times, as can e.g. be seen when comparing T= 300 K and 254 K in panel (a) of figure 5.1. After passing through a minimum the relaxation times increase again.

Before discussing the resulting relaxation times in the next section, the origin of the different relaxation components is clarified. Starting with the longest component (i) it can be seen from figure 5.1 that the corresponding relaxation times are long compared to the others. This suggests a crystalline component as origin [210]. Comparing the two pore sizes P21 and P29 it is clear that the relative contribution in P21 is much larger than in P29, which is counter-intuitive if this component was situated inside the pores. However, it is in agreement with the expectations if it is assumed that external water is the source of this relaxation (i). To test this idea, sample P21 was measured, with two different amounts of filling: one where there was much more water than necessary to fill the pores (denoted P21w) and one where less water was used (P21). A direct comparison of the two preparations is shown in figure 5.2 for the two temperatures 300 K and 167 K. At higher temperatures the samples differ in their T_1 times, while at the lower temperatures only the long time behavior in the relaxation curves is different. At high temperatures where both, the internal and the external components are liquid. Different averaged relaxation times are obtained in both samples, since the external water behaves bulk-like, while the pore internal water interacts with the surface. Therefore, the sample with less water P21 shows shorter T_1 times indicating slower dynamics compared to sample P21w. When the pore external water freezes, only the internal water contributes to the faster behavior, while the external ice contributes only to the (i) relaxation. The fact that the other relaxations (f) and (s) are not influenced

by the amount of water outside the pores strongly suggests that both originate from water molecules inside the pores. The freezing of external water sets in above 260 K in all samples, depending on the exact water content. Below the onset of freezing, only very minor deviations were detected, see e.g. 167 K in figure 5.2. The difference between the different preparations will therefore be neglected in the following discussion of the obtained T_1 times, when the external water is frozen.

5.1.2 Small pores: relaxation times in MCM-41 with d = 2.1 nm

To obtain an overview over the effects found in the SLR experiments, it is first focused on the smallest pores P21. In figure 5.3 (a), the measured mean relaxation times $\langle T_{1,r} \rangle$ are shown as calculated by eq. (3.45). Figure 5.3 (b) shows the fitted stretching parameters β_r.

Starting at high temperatures, several features can be noticed in the fast relaxation (f). At 300 K the already discussed difference between the two preparations P21 and P21w can be observed. It vanishes upon freezing at 268 K in a discontinuous jump in $\langle T_{1,r} \rangle$ marked by the black arrow in panel (a). At this temperature also pure D_2O crystallized in ^{2}H NMR measurements performed in the same setup.

Upon cooling, the $\langle T_{1,f} \rangle$ times pass through the expected minimum, compare table 5.2. As can be observed in the figure, the minimum does not meet the expected value of a Debye-like exponential relaxation marked by the red line. This indicates a distribution of correlation times $G\left[\log(\tau)\right]$ in the sample, which may result in a distribution of relaxation times $V\left[T_1\right]$. At temperatures above and in the vicinity of the T_1 minimum $V\left[T_1\right]$ is averaged, yielding a single exponential relaxation. This can be seen in panel (b) where the β_f parameter is plotted. It is equal to unity down to ca 180 K, showing that only one average relaxation time is detected by the experiment. Below this temperature, motional averaging becomes too slow for the SLR experiment, and the distribution $V\left[T_1\right]$ becomes observable, as indicated by $\beta_f < 1$. This is marked in the plot by a change from dark to light blue color. At the same temperature, a pronounced kink in the relaxation times $\langle T_{1,f} \rangle$ is observed. This kind of behavior has been observed in glass forming liquids at the glass transition temperature [211], c.f. section 3.5. It is due to broken ergodicity in the sample and will be discussed in detail in chapter 7.

By comparing the $\langle T_{1,f} \rangle$ of P21 to the bulk D_2O data, it can be seen that dynamics in this confinement are altered strongly. The relaxation times at 300 K are about one order of magnitude smaller in the confined sample. Due to the dependence of T_1 on the spectral density, see section 3.3, this indicates a slowed

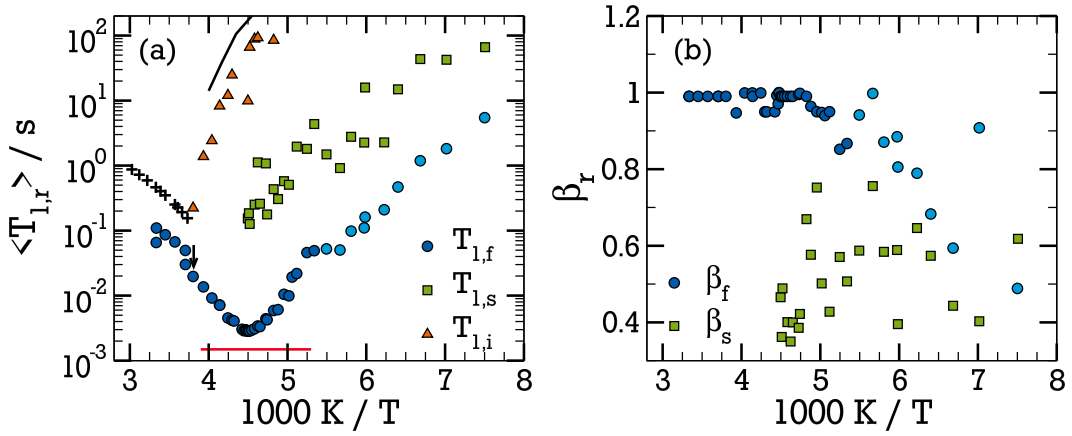

Figure 5.3.: (a) Mean SLR relaxation time of water confined in P21. The black line represents relaxation of hexagonal ice I_h by F. Löw. Black pluses (+) are bulk D_2O relaxation times measured in the same setup. The red line marks the expectation for a Debye-like relaxation. Where circles change to light blue the β parameter strongly deviates from unity. (b) KWW β parameter for fast and slow process.

down dynamics in MCM-41 at high temperatures [1]. This is a generally expected confinement effect mostly due to a slowing down of dynamics close to solid walls [83, 89, 129].

In addition to the fastest process (f), the two other observed relaxations are reported in figure 5.3 (a). The slowest relaxation (i) appears when external water freezes. The corresponding mean relaxation times are rather long and coincide well with those from hexagonal ice I_h, measured by F. Löw [210]. This supports the assignment to pore external ice. Note that even in the carefully prepared sample without substantial overhead of water, some freezing is observed. This has three possible explanations. First, there may still be a small amount of water outside the pores that crystallizes upon cooling. Second, the crystalline parts arise from larger pores where crystallization is not suppressed. The latter can be the case, since there always exists a distribution of pore radii. Third, the density of the water inside the pores is temperature dependent and decreases upon cooling [212, 213]. Since preparation was performed at room temperature, the crystalline relaxation may stem from water forced out of the pores due to density reduction in the cooling process.

The third observed process (s) exhibits relaxation times $\langle T_{1,s} \rangle$ between the fastest (f) and the ice-like (i) relaxation. The relaxation times of P21 scatter strongly, due to the low amplitude between 2 % and 20 % of the total signal,

[1] Assuming equal spectral densities, the differences between bulk and confined sample would correspond to a shift in temperature of about 40 K.

see figure 5.6 (b). In the larger samples it can be determined more reliably as will be seen below. The (s) process starts to separate from the (f) process at temperatures T ≈ 225 K. Its stretching parameter β_s is always $\beta_s \approx 0.6$, where it can be fitted reliably. This shows that the (s) component is never subject to motional averaging on the time scale of $T_{1,s}$. Absence of exchange within a species is usually only encountered in solids. Additionally, the fact that the (s) species is observable at all shows that there cannot be any exchange faster than the time $T_{1,s}$ between the molecules giving rise to the (f) and the (s) component. From the different samples P21 and P21w it is assumed that both molecular species are inside the pores, they should be in direct contact with each other. Near 225 K, the (f) component is liquid and exhibits a correlation time of about 1 ns. Thus, the slow process must stem from a solid, otherwise there would be exchange.
After having presented the general features of ^{2}H SLR for the example of P21, next the dependence on the pore size is discussed.

5.1.3 Pore size dependence of the relaxation times

SLR experiments similar to those for P21 have been performed for various pore sizes varying from the smallest pores 2.1 nm to large ones 2.9 nm. The dependence of the water dynamics on the pore size is reported in figure 5.4. Samples P28 and P29 have been prepared by using the necessary amount of water to approximately fill the pores completely. To test the influence of external pore water sample P25 has been prepared in two ways analogous to P21: A sample called P25w was filled with more water than necessary to fill the pores. A second sample P25 was filled with the amount of water necessary to fill the pores as determined by the pore characterization. Direct comparison of the samples P25 and P25w shows that the time constants $\langle T_{1,f} \rangle$ are in good agreement, below ca 260 K where the external water freezes. The same is true for the $\langle T_{1,s} \rangle$ times which are left out for clarity. Analogous to P21, this can be taken as evidence that the (f) and (s) relaxation arise from water inside the pores. Similar to the results of sample P21w, the sample P25w shows a modified high temperature relaxation above ca. 260 K, where the water outside the nanopores is liquid. The time constants $\langle T_{1,f} \rangle$ are longer indicating faster dynamics in the samples with much excess water. This affirms that the MCM-41 surface slows down water molecules in its vicinity, as is expected from other studies [11, 84, 89, 131].

Studying figure 5.4 in more detail, one observes general trends in the fast relaxation process (f) upon increasing pore size up to d ≤ 3 nm. Despite the difference of ca 0.15 nm in diameter, the relaxation times obtained from P28 und P29 are close to identical. The trends can be summarized as follows:

1. At high temperatures, the relaxation times $\langle T_1 \rangle$ increase with increasing pore size indicating faster dynamics.

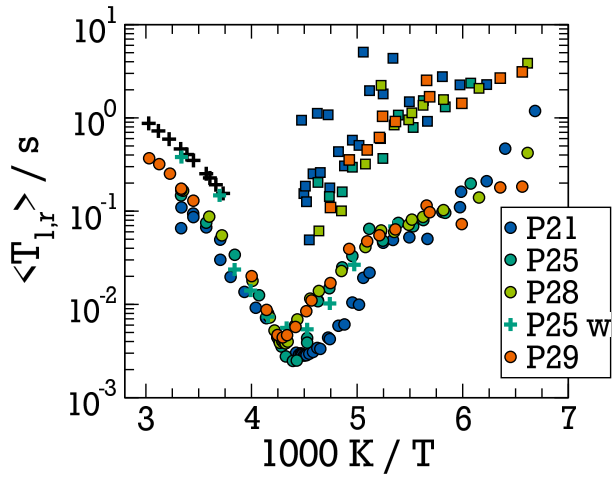

Figure 5.4.: Mean SLR relaxation time of the fastest process (f, circles) and the slower process (s, squares) in samples P21, P25, P28 and P29. Additionally bulk D_2O relaxation times (black pluses) and relaxation times from sample P25w (turquoise pluses) are shown.

2. The positions of the T_1 minima shift to higher temperatures and higher values of $\langle T_{1,f} \rangle$ in the minimum with increasing pore size. This indicates a deceleration of dynamics accompanied by a broader distribution of correlation times $G\left[\log(\tau)\right]$.

3. At temperature below the T_1 minimum the relaxation times in the larger pores are again larger and dynamics thus slower than in the smaller pores. This indicates a steeper temperature dependence of the correlation times in larger pores.

4. The change in the temperature dependence found in P21 at ca 185 K is present in all samples at roughly the same temperature. Few Kelvin below this kink, the relaxation times $T_{1,f}$ agree in all samples to a good extent.

From point 1 that the reorientational dynamics is slowest in the smallest pores. In P21 the fraction of water close to the wall is largest compared to the other

Table 5.1.: T_1 minima parameters as obtained from SLR: $\langle T_1 \rangle_{min}$ is the minimum value of the (f) process, T_{min} is the corresponding temperature, α and γ are the stretching parameters for CC and CD spectral densities.

Sample	$\langle T_1 \rangle_{min}$ / ms	T_{min} / K	α	γ
P21	2.8 ± 0.1	222.4 ± 0.4	0.66	0.30
P25	2.4 ± 0.2	227.5 ± 0.7	0.68	0.37
P28	3.8 ± 0.1	232.3 ± 0.3	0.46	0.19
P29	4.3 ± 0.1	232.9 ± 0.5	0.40	0.15

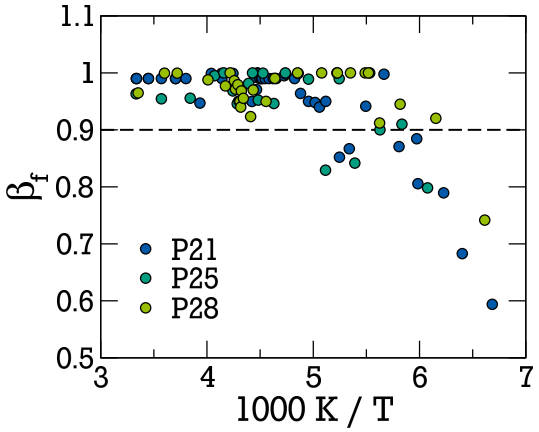

Figure 5.5.: SLR stretching parameter β_f of samples P21, P25 and P28. The horizontal line marks the threshold value β_f = 0.9.

pore sizes. The dynamics accelerate with increasing pore size and are fastest in samples P28 and P29. This behavior is reversed below the minima where, larger pores show indications for slower dynamics. This crossing behavior can be taken as evidence for a steeper temperature dependence of the correlation times, i.e. a more fragile behavior in larger confinement. All samples exhibit rising relaxation times at even lower temperatures, which kink strongly below 200 K. The temperature where the kink to a weaker temperature dependence occurs seems to be only weakly dependent on the pore size and occurs in the vicinity of 185 K. Analogous to the smallest pores, the change in temperature dependence of T_1 is accompanied by a decrease in the stretching parameter β_f of the fast process, see figure 5.5. After a second change of the temperature dependence, the relaxation times of the fast process (f) in all pores agree well below ca. 170 K.

All samples show the additional second relaxation process (s) already observed in the P21 sample. The fit quality for the time constants $T_{1,s}$ varies. It is strongly dependent on the separation of the processes (f) and (s) and also the presence of process (i) which interferes with the long time plateau of (s). Thus, the arguments concerning (s) must be taken more qualitatively rather than quantitatively. As evident in figure 5.4, the relaxation times in all samples show a similar temperature dependence and time scale. The (s) process shows the same stretching $\beta_s = 0.6 \pm 0.15$ in all pores and thus, stems from a solid component (not shown). Note that the slow process (s) in all samples exhibits a slight change in its temperature dependence at ca. 180 K.

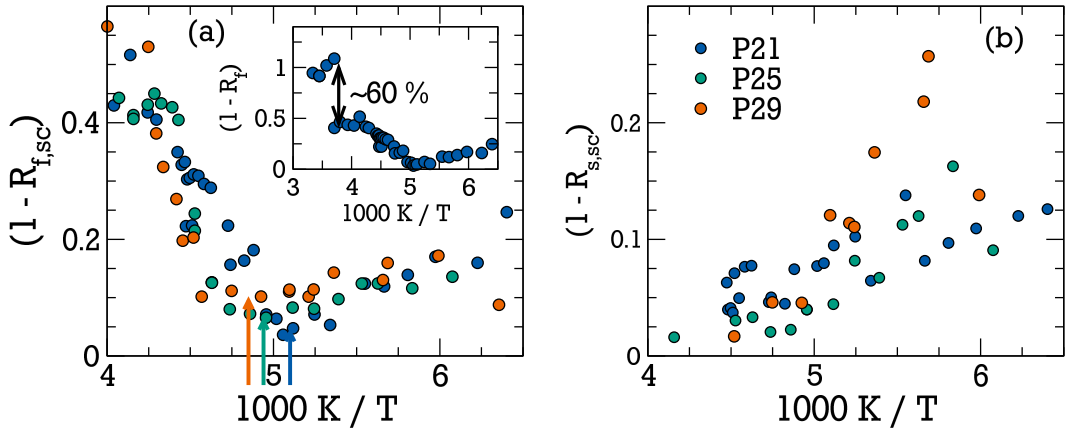

Figure 5.6.: Normalized reduction factor of samples P21, P25 and P29. In (a) for the fast relaxation component (f) and for the slow relaxation component (s) in (b). Samples P25 and P29 are scaled to match P21 in the range 250 K to 260 K. Colored arrows mark the approximate temperature T_{SE} of the signal minimum. Inset: (1-R_f) of P21 over the whole temperature range.

5.1.4 Analyzing the signal amplitudes

Another measure for the time scale of the motion is the minimum in the observed signal when applying the SE. Figure 5.6 (a) shows the behavior expected from the above SLR analysis: A few Kelvin below the T_1 minima, there is a drop of signal, where the dynamics approach the experimental time scale of $\tau \approx 1/\delta \approx 1\,\mu s$. By fitting a polynomial, the position T_{SE} of the signal minimum was approximated. The respective positions are marked by the colored arrows. The minimum shifts to higher temperatures for larger pores. Those reach the $\tau = 1\,\mu s$ limit at higher temperatures indicating slower low temperature dynamics. After the minimum the signal in the (f) relaxation recovers but does not reach its value at 250 K.

Note that for better comparison, (1 - R_r) with r = f,s is re-scaled so that it agrees in the range 250 K to 260 K for all samples, to compensate for different contributions of the freezing component (i). The data are scaled such that the factor (1 - $R_{r,sc}$) coincides with the unscaled one of P21. For clarity, P28 is excluded, since it shows similar behavior to sample P29.

It was shown in the previous section that the second relaxation can be explained best as a solid like process. In principle, one may imagine two possible origins of this relaxation: it may either be due to the reorientation of the hydroxyl groups of the pore wall or can be a solid like component that forms in the pore. Assuming a constant density of hydroxyl groups in the different MCM-41 samples, the signal of this second component should scale with the surface to volume ratio, i.e. 1/d where d is the pore diameter. The reduction factor of the (s) relaxation

($1 - R_s$) is shown in panel (b). It does not show the 1/d dependence expected from the assumption that it stems from the hydroxyl groups. Instead, it shows tendencies of increasing signal with increasing pore size. Thus, the (s) relaxation is due to a process which has increased strength on increasing pore size and is solid like ($\beta_s \approx 0.6$).

Summing the signal contributions of (f) and (s) relaxation, the low temperature values of ($1 - R_{f+s}$) agree with the values at 250 K (not shown). This indicates that the magnetization is lost from the (f) species upon cooling and transferred to the (s) species. From this observation it follows that the (s) relaxation is caused by water molecules that change their dynamical behavior on cooling. A solution that accounts for all these findings is the water dynamics of the solid core, because (a) the amount of solid water is proportional to the volume, (b) it cannot exist at high temperatures and (c) it shows $\beta \approx 0.6$.

In summary three SLR relaxation processes have been identified. The fastest one (f) exhibits a pore size dependence of the SLR time $\langle T_{1,f} \rangle$ that indicates a steeper temperature dependence in larger pores. The (f) process exhibits a non-Debye behavior, which has to be taken into account in further analysis. The slower process (s) seems to be independent of pore size. Analysis of the SLR properties hint to the origin of the two processes: the faster one seems to be due to the relaxation of water at the pore walls, while the slower one is due to molecules in the pore center. This species shows solid like features and is only observed below the T_1 minima. No minimum is observed for the (s) relaxation. To gain more information about the origin of the two relaxation processes observed, an analysis of the solid echo spectra is performed in the next section. A third process (i) was also identified. It was attributed to the relaxation of ice outside the pores by varying the amount of external water. This process will be excluded from the discussion in the rest of the chapter, since it has shown to be irrelevant for water dynamics inside the MCM-41 pores.

5.2 Spectral line-shape of confined D_2O

In the previous section the SLR analysis revealed a complex behavior of water confined in MCM-41. Here, the solid echo spectra are analyzed to gain more insight into the origin of the different processes. Since several relaxation processes are present, it is useful to compare spectra at different relaxation states. The delay time t_d within which the magnetization was allowed to recover was chosen in a way, such that from all three components (f,s,i), only the faster two (f,s) or only the fast one (f) is recovered. To do so, the time t_d must fulfill the following conditions:

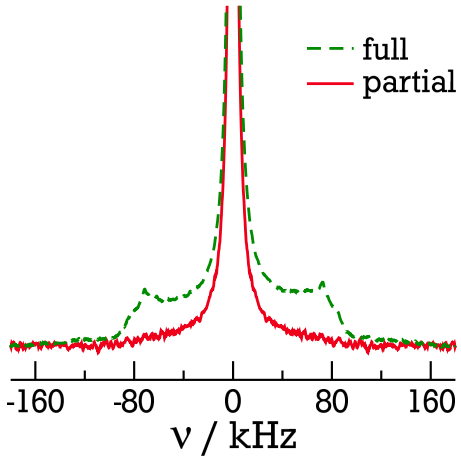

Figure 5.7.: Comparison of full and partial relaxed spectra in P21 at 205 K

$$T_{1,x} \ll t_d \ll T_{1,y}, \quad \begin{cases} x = f;\ \ y = s,i & \text{f only} \\ x = f,s;\ \ y = i & \text{without ice} \\ x = f,s,i;\ \ T_{1,y} = \infty & \text{all components} \end{cases} \tag{5.2}$$

The condition of the delay time to be much larger or smaller cannot be satisfied in all cases. This needs to be kept in mind especially when only the fast (f) component is regarded. The T_1 times of the (f) and (s) component are separated by not more than two orders of magnitude. Thus, in all cases it is necessary to choose t_d such that either parts of the fast component are not recovered or faster relaxing molecules of the slower component already contribute. The (i) relaxation is suppressed in all spectra.

5.2.1 Temperature dependence of ^{2}H NMR spectra

The spectra obtained from confined D_2O change their shape with temperature. At the highest and lowest temperatures measured, they are in the limiting cases expected for deuterons in a powder, see section 3.4. The high temperature Lorentzian shape does not contain information, except spectrometer resolution, while the low temperature Pake spectrum can be used to extract sample parameters, as for example the anisotropy δ. The temperature range between the Lorentzian and the Pake limit will be called (line-shape) transition region. It contains information on the specific type of motion and the timescale, although this range is often not easy to investigate due to the vanishing signal in SE experiments, see section 3.4. Here, two of the cases in eq. (5.2) will be discussed: the partially relaxed (PR) case which comprises only the (f) component and the fully relaxed (FR) case which incorporates also the (s) component.

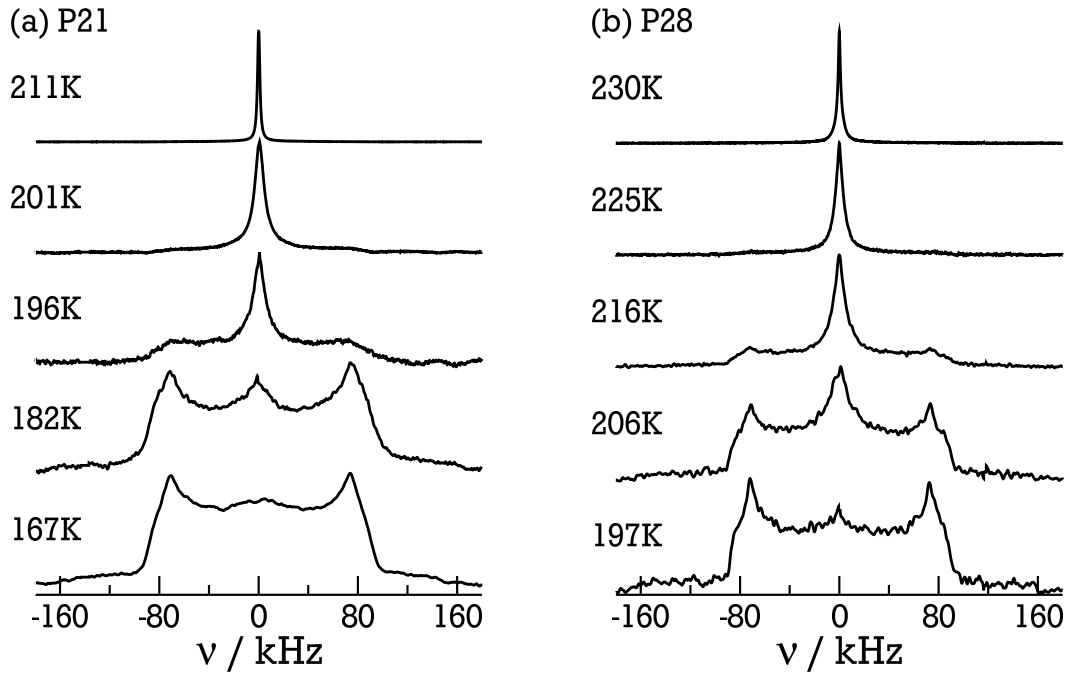

Figure 5.8.: Partially relaxed spectra of samples (a) P21 and (b) P28.

To investigate the spectral contributions arising from the (f) and the (s) relaxation, in figure 5.7 a PR and a FR spectrum obtained from P21 at 205 K are compared. The figure reveals that the contribution of the slow relaxation is an additional Pake-like component. This is true at all investigated temperatures in all samples and underlines the finding from SLR: The slow relaxing molecules are indeed solid like on the experimental time scale($\tau_s \gg 1\,\mu s$) as soon as they can be observed. From a contribution that is always Pake-like, no further information can be obtained, therefore it is focused on the PR experiments in the rest of the section.

Figure 5.8 shows exemplary PR spectra from the transition region in samples P21 and P28 in panels (a) and (b), respectively. In this temperature range they represent the samples with fastest and slowest dynamics as indicated by SLR. Between spectra of comparable shape, a temperature shift of ca. 20 K is observed. This fits well to the shift found for the minima in T_1 and and the SE signal. The spectra show a broadening of the Lorentzian component on cooling that is due to decreasing SSR time T_2. At ca 201 K in P21 and 225 K in P28, an additional Pake component starts to grow. This behavior can be explained in two ways: It could be due to the existence of two separate phases, where one phase consists of slow and the other of fast molecules. Alternatively, the spectral shape may as well be due to one single species of molecules with a distribution of correlation times $G\big[\log(\tau)\big]$. Depending on temperature, some of the molecules are fast ($\tau \ll 1\,\mu s$) and other parts are slow ($\tau \gg 1\,\mu s$) molecules. Only one SLR relaxation is observed in the partially spectra. The solid like (s)

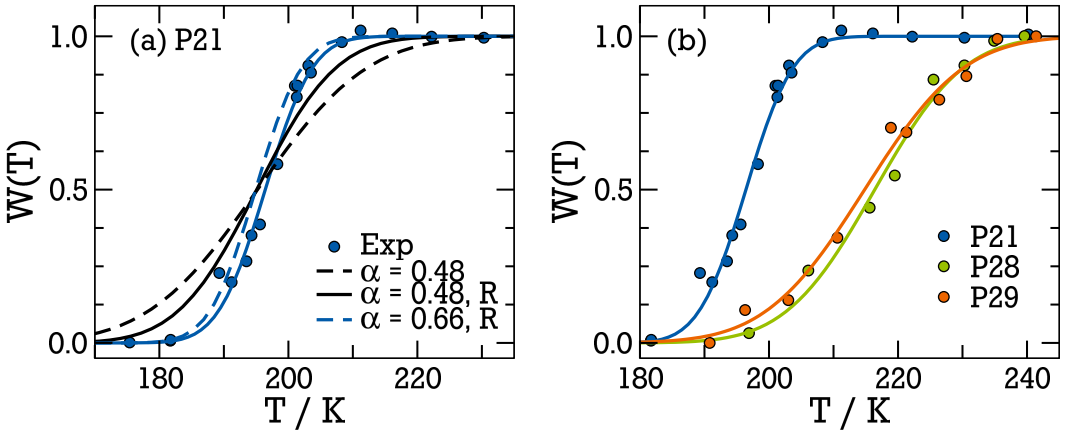

Figure 5.9.: Weight of Lorentzian line in the total spectrum W(T): In (a) sample P21. The blue solid line is a fit with eq. (3.41). Black lines are calculated from DS data [10] by neglecting (dashed) and considering (solid) dampening of signal in SE experiments, see text. The blue dashed line considers signal loss and assumes $\alpha = 0.66$ as suggested by SLR. In (b) W(T) and fits using eq. (3.41) are shown for samples P21, P28 and P29.

component is suppressed. Also, the values of $\langle T_{1,f} \rangle$ in the minima suggest a distribution of correlation times. Therefore the second possibility is very likely. The existence of such a distribution of correlation times can be shown by direct comparison with dielectric spectroscopy. From the correlation times τ_{DS} and the dielectric loss ϵ'' given in ref. [10], the weight W(T) of fast molecules can be calculated by assuming the spectra are two-phase spectra corresponding to a distribution $G\big[\log(\tau)\big]$. The fraction of fast molecules W(T) with correlation times ($\tau \ll \delta^{-1}$) can be determined using eq. (3.42). The $W_{DS}(T)$ values calculated from dielectric results [10, 120] can be compared with the experimentally determined weight $W_{exp}(T)$ defined by eq. (3.40). This is depicted in figure 5.9 (a) for sample P21. The experimental values of W(T) can be interpolated using eq. (3.41), as shown in the figure together with the $W_{DS}(T)$ values calculated from DS data [10]. In those calculations, different assumptions have been used. In a first attempt, the signal loss in the SE experiment was neglected and $\alpha = 0.48$ was used for width of the CC distribution, as measured in DS. The result reproduces the inflection point of the experimental data well, but overestimates the width of the transition region. Therefore, in a second case, the attenuation of the signal was taken into account by assuming a logarithmic Gaussian shape for $R(T)$[2], what describes the data well. The third case, interpolates the experimental values even better. Here, it was also taken into account that even so ^{2}H NMR usually finds the same spectral form as DS the width pa-

[2] A width of the logarithmic Gaussian distribution of $\sigma = 0.85$ was assumed. As estimated from RW simulations, see [122].

rameters α or γ often deviate in NMR and DS. Therefore, a value $\alpha = 0.66$ was used, as suggested by SLR. Note that here, $\alpha_{\mathrm{NMR}} > \alpha_{\mathrm{DS}}$ was found, in contrast to most studies, see e.g. [188]. The good agreement of the experimental and the calculated values W(T) justifies the assumption of two-phase spectra due to a broad distribution $G\big[\log(\tau)\big]$. Additionally, it shows that the process observed by DS is the one that gives rise to the (f) relaxation observed in SLR, but not the (s) relaxation. Such two-phase spectra were proposed for other molecules confined in mesoporous silica confinement as well, e.g. for benzene, isobutyric acid and naphthalene [214–216].

Figure 5.9 (b) shows the experimental weight factors W(T) of Samples P21, P28 and P29. In agreement to the SLR findings P28 and P29 are very similar and are exhibit a shift by about 25 K compared to P21. The transition region in the larger pore ranges over a larger temperature range is consistent with a larger distribution of correlation times as suggested by the larger $\langle T_{1,f}\rangle$ minimum values, c.f. tab. 5.1. The data can again be fitted using eq. (3.41). They provide a value for $T_{1/2}$ for which $\exp\langle\log\tau_{1/2}\rangle = \delta^{-1} \approx 10^{-6}$s holds. $T_{1/2}$ can be compared to the temperature of the signal minimum in the SLR experiments T_{SE}. In case of P21 $T_{1/2} = T_{SE} = (195 \pm 1)$ K is found, while for samples P28 and P29 one finds $T_{1/2} = 215$ K and $T_{SE} = 206$ K. This difference may have two reasons: First, depending on the exact geometry of the motion, the signal minimum is not symmetric as assumed in the determination of T_{SE} and second, the temperatures T_{SE} and $T_{1/2}$ represent different means of the distribution, i.e. the mean correlation time $\langle\tau\rangle$ and the mean logarithmic correlation time τ_{m} respectively. Both differ when the distribution of correlation times show an asymmetric broadening. Since the T_{SE} values are utilized more often in ^{2}H NMR studies, those will be used later to estimate the correlation time $\tau\left(T_{SE}\right) \approx \delta^{-1}$ in figure 5.17. The temperature T_{SE} is available for sample P25 as well, where the spectra where not measured in good enough quality to determine W(T) reliably.

Similar spectra as in the present work have been measured in an ^{2}H NMR study by Pahlke et al. [217] for D_2O in a zeolite nano-confinement. There, the spectral shape was not attributed to a broad distribution $G\big[\log(\tau)\big]$, but to a specific motional model. It was proposed that water molecules that perform a fast π-flip around the C_2 symmetry axis with an additional slow reorientation of this symmetry axis on a (distorted) tetrahedron may explain all the findings. In contrast, it was argued that a distribution of correlation times may not reproduce the findings. Three reasons were given for this argument: (a) A distribution $G\big[\log(\tau)\big]$ may not explain the broadening of the central Loretzian component. (b) By integrating different parts of the spectra, i.e. the central component and the Pake singularities, one finds equal spectrally resolved relaxation times. A distribution is supposed to result in different time constants in different parts of

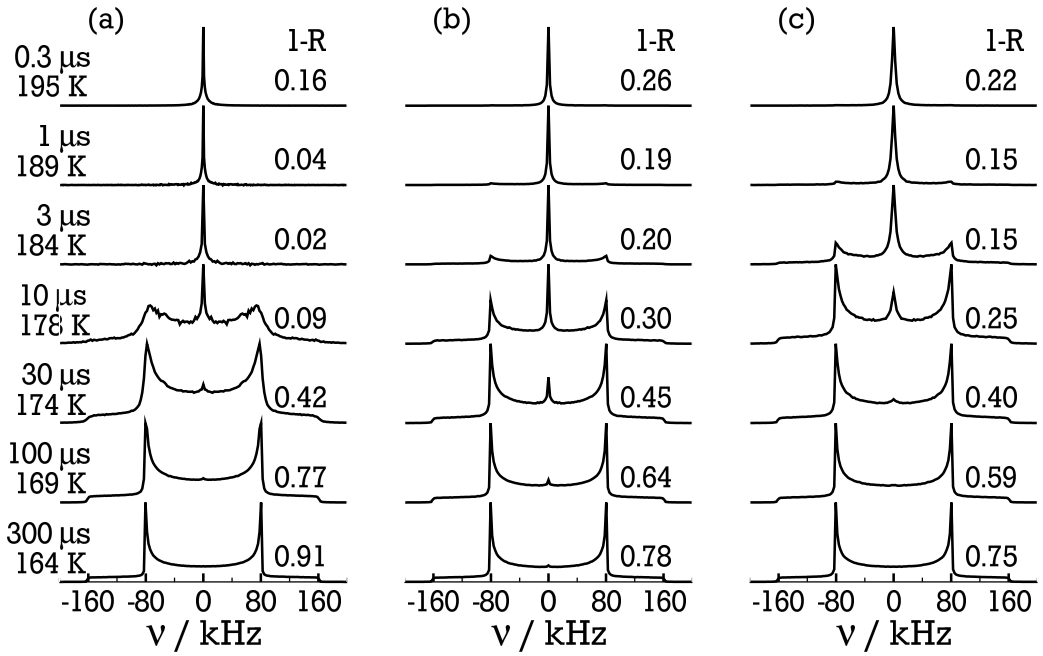

Figure 5.10.: Random Walk Simulation of SE spectra. (a) DTJ model with single correlation time (b) same model with a logarithmic Gaussian distribution of correlation times. (c) IRJ model with the same distribution of correlation times. Both distribution used a width of $\sigma = 2.1$. The times on the left indicate the mean jump time τ_j. Using DS measurements [10] the correlation times have been mapped to a temperature. The indicated values 1-R are the reduced solid-echo intensities.

the spectrum. (c) The signal reduction in the SE experiments must vanish for very broad distributions, while shallow signal minima signal small distributions. To test whether the data measured here can be explained by assuming a specific motional mechanism without a broad distribution of correlation times, RW simulations were performed. Those covered some likely model geometries of water reorientation, including the model of Pahlke, a disordered tetrahedral jump (DTJ) and large angle isotropic reorientation (IRJ). For simulation details see in [122, 177] and in section 3.8. Figure 5.10 shows the simulated spectra of a DTJ model with (a) a single correlation time and (b) a log-Gaussian distribution of jump correlation times $G\big[\log(\tau)\big]$ of width $\sigma = 2.1$. In (c) an IRJ model simulation using the same distribution as in (b) is shown. In both cases the distribution and the width were chosen to be a close approximation to the CC distribution, reported for sample P21 [10] [3]. The correlation times denoted in the figure correspond to the jump correlation time τ_j, characterizing the exponential distribution of waiting times between consecutive reorientation events.

[3] A logarithmic Gaussian distribution can approximate the CC distribution quite well. It was chosen in the simulations due to its numerical manageability.

In the IRJ model, $\tau_j = \tau$ equals the correlation time, while for an isotropic jump about a specific angle ϕ, the relation between correlation time and jump correlation time is given eq. (3.65). Exemplary, this results in $\tau = 2/3\tau_j$ for the DTJ model. The correlation times can be mapped onto the temperature by using the measured data from DS, or from SLR analysis as reported in figure 5.17. The temperatures and reduced intensities (1-R) are also indicated in figure 5.10.

From these simulation results, one can see various counterarguments to the concerns reported above: (a) While in the DTJ model, the central component is rather narrow and may not explain the findings of Pahlke et al., the second model, a large angle isotropic jump, shows considerable broadening of the Lorentzian feature, e.g. a full width half maximum of 3 kHz is found in the $\tau_j = 1\,\mu s$ spectrum. Therefore, in specific situations, a broad Lorentzian feature is not a counter argument for the existence of a distribution of correlation times. (b) The simulated distribution width $\sigma = 2.1$ is large enough to generate two-phase spectra for jump times τ_j over about 2 orders of magnitude. Nevertheless, the signal is reduced to ca. 15 % in the IRJ model and ca. 19 % in the DTJ model. Those values are compatible with those found in the SLR studies above and are not much larger than those measured by Pahlke. Therefore, a pronounced signal minimum is not at variance with a distribution $G\big[\log(\tau)\big]$, as long as it is not too shallow. Again, this is geometry dependent. Note, that this does not contradicts the Pahlke model but rather shows that the line-shape reported in this study can be explained both ways.

The DTJ model without distribution leads to a transition from Lorentzian shape to Pake shape within only 10 K. In direct comparison to the experimental spectra, see figure 5.8 this range is too narrow: In the experiment, the transition happens within ca. 25 K or more. In the cases of distributed correlation times, the simulated transition stretches over more than 20 K, which fits the experimental data much better. With a convenient choice of parameters, the spectra can as well be explained by the model of Pahlke. Nevertheless, close inspection of the simulation results shows that the model is not compatible with the data obtained in this work, e.g. the signal is close to zero in the minimum (1-R) $<$ 0.03 in all simulated parameter sets. This is not compatible with the data here, see figure 5.6. Additionally, the behavior of the simulated results of the SLR experiments contradict the present results. Therefore, the model is discarded as an explanation for the behavior of water confined to MCM-41. Likely, water molecules confined in much smaller zeolite cages (d = 0.8 nm to 1.2 nm) with additional presence of charged Na^+-ion perform a different kind of motion as water MCM-41. The results obtained for the latter can qualitatively be described by a broad distribution of correlation times $G\big[\log(\tau)\big]$.

Closer inspection reveals that the spectra at lowest temperatures, see figure 5.8, do not fully fit to the spectra calculated for a static limit and some residual motion is present on the time scale of the experiments. This signals that some

secondary process starts to dominate the behavior of the water molecules. This is the case even at the lowest temperatures, i.e. T = 105 K, that were measured in this work.

Here, the ^{2}H NMR LSA was discussed. First, it was shown that the slower SLR relaxation (s) only gives rise to a Pake feature in the spectra. This confirms this component is always solid-like. Further, the spectra of the (f) relaxation obtained from PR SE experiments were shown to be due to the process observed in DS on the similar samples [10]. It was shown that the measured weight of fast molecules W(T) can be calculated from those DS results. The LSA is qualitatively in agreement with the SLR measurements and has shown to be compatible with an explanation by a distribution of correlation times $G\big[\log(\tau)\big]$.

5.3 Stimulated echoes of confined D_2O

In the previous sections, the high temperature behavior of confined D_2O was characterized using SLR and LSA. In the regime of slow motion at low temperatures, STE experiments can measure the rotational auto-CF F_2 directly. From this, correlation times τ in the range of some microseconds and seconds can be obtained, as well as information about the geometry of the motion. Again, the difference in the SLR time constant T_1 is exploited to separate the contributions of the fastest (f) and the intermediate (s) process by PR experiments. The crystalline contribution (i) is suppressed.

5.3.1 Temperature dependent STE experiments

The temperature dependence of the measured correlation functions of D_2O in MCM-41 is presented here. The above sections have established the assumption that the fast relaxing SLR component (f) is due to the water molecules that behave liquid like. It is focused on this contribution py performing PR experiments of Zeeman (ze) order. Some representative decay curves $F_2^{ze}(t_m)$ for the samples with smallest pores P21 and larger pores P28 are shown in figure 5.11. The measured signals are stretched exponential decays. Comparing the samples in figure 5.11 (a) and (b) at similar temperatures, e.g. 172 K, the time scales are similar. This is surprising since in LSA and also in the high temperature regime of SLR, the larger pore sample P28 had shown significantly slower dynamics than the sample P21. The curves have been interpolated by a KWW decay, c.f. eq. (3.56), the fits are shown in figure 5.11. The resulting mean logarithmic correlation times τ_m are plotted in figure 5.12 for the samples P21, P25 and P28. Evolution times of $t_p = 3\,\mu s$ have been used in all cases. Note that the figure also shows data obtained from spin alignment (sa) order. Additionally, the results of the fully relaxed P29 measurements are shown. No

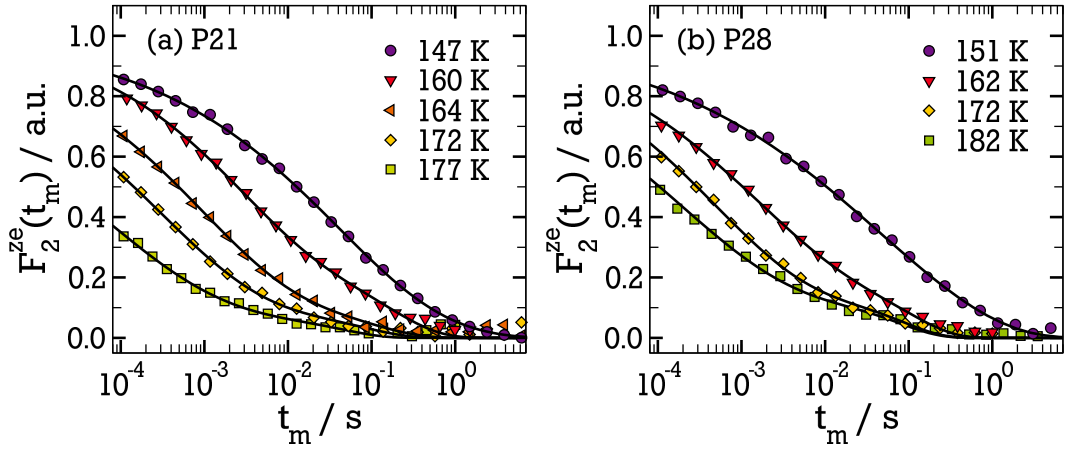

Figure 5.11.: Examples of temperature dependent STE curves of samples (a) P21 and (b) P28. The curves are obtained from Zeeman order experiments measured at evolution times of 3μs. Solid lines are fits with eq. (3.56).

partially relaxed STE have been measured in this sample. A direct comparison of PR and FR measurements using P25 revealed, the slower component only contributes to an additional constant contribution to the relaxation curves. The figure reveals that all samples show approximately the same correlation times. An Arrhenius fit to the τ_m exhibits an activation energy of $E_a = (0.50 \pm 0.05)$ eV and an attempt frequency $\tau_0 = 1.9 \cdot 10^{-19}$ s. The upper dashed line is the same Arrhenius law shifted by a factor 64 ($\tau_0^* = 1.2 \cdot 10^{-17}$ s). It nicely describes the data of the FR sample P29 up to ca. 193 K. It can be seen that all τ_m are in between those of P21 and P29. The fitted activation energy is in full agreement with the dielectric studies of water in MCM-41 [10] and lots of other systems containing water, see e.g. in [133]. Especially sample P21 fits neatly to the DS of the very same pores [120], c.f. figure 5.17 and also sample P25 is in line with DS results measured by C. Lederle, see figure 5.12. Those findings agree well with the universal features discussed in section 2.3.2. The dynamics are fastest in the P21 pores. This shows that although water dynamics at low temperatures have several universal features the time scale still depends on the properties of the system under investigation.

Besides the correlation time τ, two more parameters can be obtained from fitting the STE curves. The KWW stretching parameter $\beta = 0.30 \pm 0.06$ is similar in all measurements below 185 K. Above this temperature, the parameter increases with increasing temperature, compare e.g. [177]. A KWW function is more similar to a CD and thus its stretching parameter β can not directly by compared with the stretching α of a CC like distribution [39]. Nevertheless, the fact that β is constant in all samples is in contrast with the change in the width parameter observed in the SLR measurements, see 5.1. This again

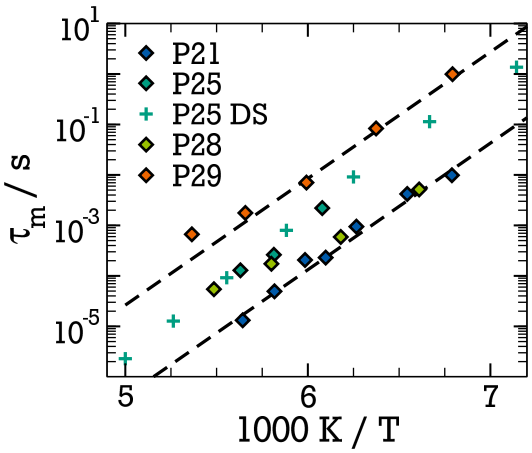

Figure 5.12.: Mean correlation times obtained from partially relaxed STE experiments at shortest evolution times of 3μs. The P29 data are fully relaxed. Pluses are DS data of P25 (by C. Lederle). The lower dashed line is an Arrhenius fit to the P21 data, the upper line shifted by a factor of 64.

indicates the universality of the low temperature relaxation, independent on the pore size. The third fit parameter in eq. (3.56) is the residual correlation $F_\infty = F_2(t_m \to \infty)$. It is manifested as a plateau for long mixing time, which is damped by the additional SLR, see e.g. T = 172 K in fig 5.11 (b). The value of the plateau reveals information on the geometry of the motion and will be presented below in the discussion of the evolution time dependence.

5.3.2 Evolution time dependence in partially relaxed STE

The dependence of the STE experiments on the evolution time t_p can be used to obtain geometrical information about the motional processes. The dependence of the correlation time on the evolution time t_p is shown in figure 5.13. There, data from sa and ze order are compiled for samples P21, P25 and P28 at temperatures of ca. 162 K [4]. The time constants are normalized to the value of $t_p = 3\,\mu s$. The different samples show a very similar dependence on the evolution time, where the values decrease by a factor of 2 (as approximated by the behavior of P21). The mean reorientation angle ψ can be approximated by using eq. (3.65) in the case of isotropic jumps. By approximating the correlation time as $\tau \approx \tau_m(t_p \to 0)$ and the jump corrlation time as $\tau_j \approx \tau_k(t_p \to \infty)$ an isotropic reorientation angle of $\psi(T = 162K) \approx 35°$ can be estimated. For comparison, the figure also includes the expectations for the correlation times, for a tetrahedral jump (solid) and an isotropic 10° reorientation. In the first case, the correlation time becomes basically independent of t_p while it decreases strongly for the small angles in the second case.

[4] The exact temperatures are 161 K for P21, 164 K for P25 and 162 K for P28.

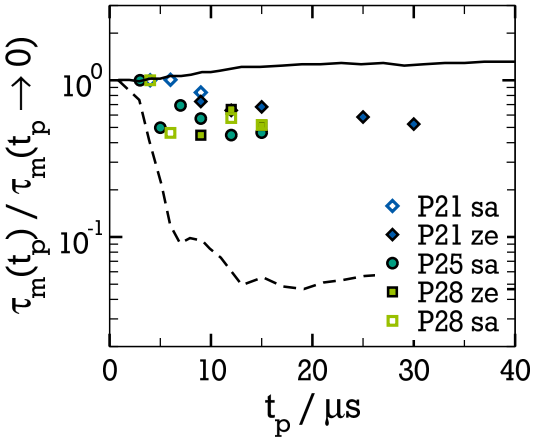

Figure 5.13.: Correlation time τ over evolution time t_p normalized to the values at shortest t_p at ca. 162 K. Lines represent the behavior for models expected from RW simulations of a tetrahedral jump (solid) and a 10°-jump (dashed).

Besides the correlation times obtained in the STE experiment, the residual correlation F_∞ is dependent on the evolution time as well. Its behavior is characteristic for the geometry of motion: The long time value $F_\infty\left(t_p \to \infty\right)$ inversely proportional to the number of non-equivalent jump sites n [169], see eq. (3.58). Some characteristic results of the different samples and at different temperatures have been plotted in figure 5.14. With decreasing temperature and decreasing pore size, the values of F_∞ become larger. For comparison, results from the RW simulations are included in the figure as well. It can be observed that below ca. 185 K the data are not compatible with an isotropic reorientation. They rather compare to the simulation of a tetrahedral jump and even better to a distorted tetrahedral jump[5]. This indicates a strong anisotropy of water reorientations at low temperatures. Several other motional models have been simulated, but none fits the measured data very well. For example, a π-flip around the symmetry axis of the a water molecule is included in figure 5.14.

In bulk water, an isotropic reorientation is expected as long as the structural α-process is measured. Thus, the process responsible for the decay in the PR STE experiments is either not the structural relaxation process or no bulk like water is measured in the confinement below 185 K. If the first point was true, the loss of correlation at low temperatures would be due to a secondary relaxation. If the second possibility applies, the observed process stems only from the subensemble of molecules. Since the STE was measured partially relaxed, only the molecules contributing to the fastest SLR process are observed. In section 5.1 it was argued that this process is very likely due to water molecules at the interface of the confinement. In that case, it can not conclusively be decided

[5] An uncertainty of 3° in the angle was simulated.

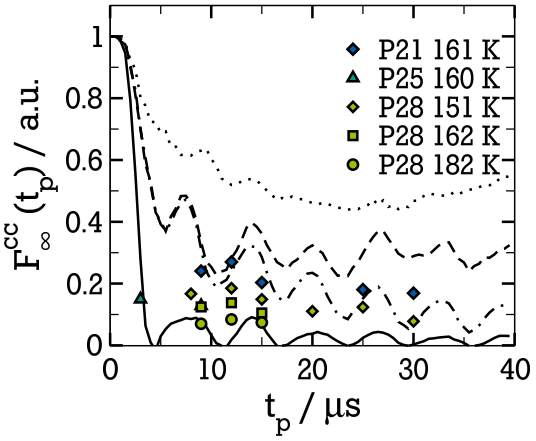

Figure 5.14.: Evolution time dependence of the residual correlation F_∞. Lines represent the expectation from RW simulations of an isotropic jump model (solid), a distorted tetrahedral jump (dash dotted), an exact tetrahedral jump (dashed) and a π-flip around the symmetry axis (dotted).

from the STE data whether the structural relaxation or a secondary relaxation is measured. Nevertheless, the results here show that this process is not the α-process of bulk water.

5.4 Discussion and Conclusion

5.4.1 Resulting rotational correlation times

Using the measured SLR relaxation times rotational, correlation times τ can be calculated with the BPP ansatz see section 3.3. For this purpose, a specific spectral density must be assumed. In DS of water confined to MCM-41 in the supercooled region below 250 K the spectra are described using the symmetrically broadened CC spectral density [10, 120]. This has been confirmed by DS measurements of sample P25 in our lab, which were performed by C. Lederle, see figure 5.15 for an exemplary spectrum. This is a considerable difference to the Debye like relaxation in bulk water. In other supercooled liquids, the structural relaxation is often found to be better approximated by the asymmetric Cole-Davidson (CD) spectral density [38] or the more general Havriliak-Negami (HN) form. Those spectral densities exhibit a broadening as defined in equations (2.12), (2.13), and (2.14). As suggested by DS, the analysis in the rest of this chapter is mainly performed using to the CC form. Nevertheless, in the next section the differences between CC and CD spectral densities are briefly discussed.

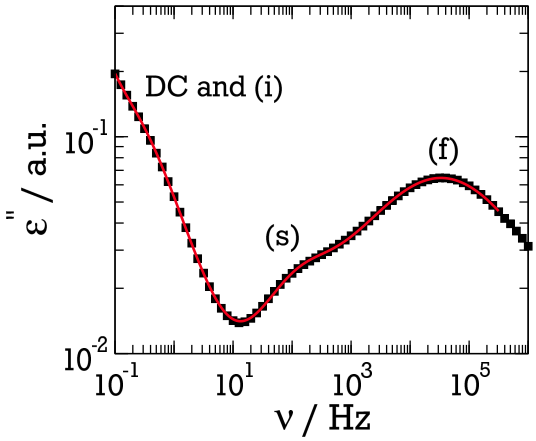

Figure 5.15.: DS spectrum of water confined to MCM-41 P25 at T = 190 K. Note, that the MCM-41 was filled with H_2O rather than D_2O , since the second relaxation process is even more pronounced. Measured by C. Lederle. Red line is a fit with three CC functions. The markings give a likely assignment to the SLR relaxation processes, where DC may be the dc conductivity.

Comparison of CC and CD spectral densities

We begin by comparing the results of two common forms of SD, the CC and the CD form. The characteristic stretching parameters α and γ can be determined from the minimum value $T_{1,\min}$ obtained from SLR measurements.[6] The comparison between the correlation times calculated using those SD is shown in figure 5.16. The mean logarithmic correlation times τ_m are plotted in panel (a) for temperatures where the SLR stretching parameter is unity $\beta \approx 1$. They allow for a better comparison between time constants obtained from STE and SLR, as well as from other methods, see sect. 2.1.3. The different averaging of different broadened SD causes a shift of the correlation times that depends on the value of the width parameters. For small values of γ the time constants τ_m obtained from CC and CD evaluation differ strongly from each other, in contrast to the mean correlation times $\langle\tau\rangle$. This is shown in figure 5.16 (b) for sample P21 exemplary.
In panel (a) of the figure, the data calculated from SLR by using the different SD are compared. There, one can observe the good agreement of the τ_m from the CC and the $\langle\tau\rangle$ of the CD calculations in the vicinity of the T_1 minimum. In contrast, the CD τ_m are shifted by a constant factor to faster time constants. For comparison, data obtained from QENS experiments [9] are plotted. Since in [9] the mean correlations times $\langle\tau\rangle$ are given, it is obvious that the QENS measurements can not be brought into good agreement with the CD data but

[6] α is determined by assuming $\tau\omega_0 = 0.616$ in the T_1 minimum. To determine γ, the curves $T_1(\gamma,\tau)$ have been calculated and compared to the experimental values.

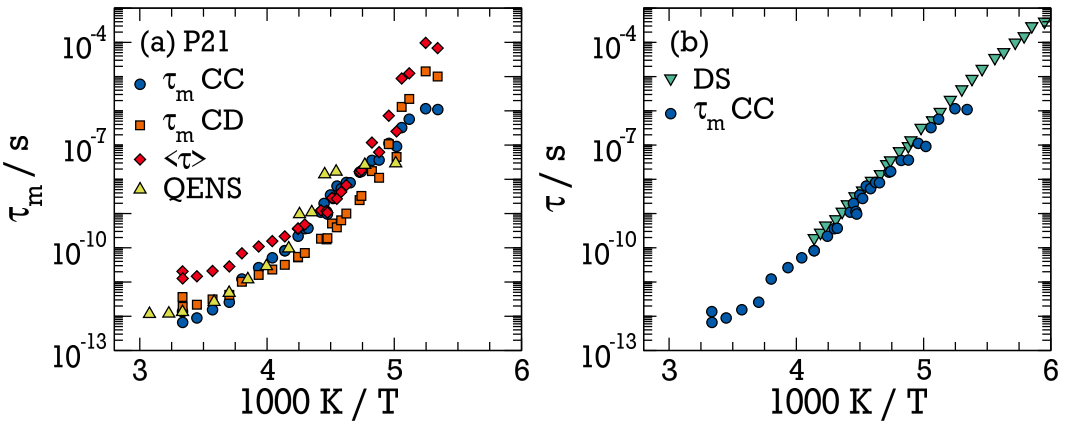

Figure 5.16.: Correlation times of sample P21 obtained using the CC and the CD spectral densities. (a) mean logarithmic correlation time τ_m and mean correlation time $\langle\tau\rangle$. QENS data are from refs. [9, 218]. (b) τ_m obtained using the CC SD in comparison with DS [10].

fit the CC data rather well above ca. 235 K. Note that in the QENS study the MCM-41 pores had a smaller mean diameter (d = 1.8 nm) than the P21 sample. In panel (b), the CC time constants are plotted together with the measured time constants from DS [10]. In both studies, the same batch of MCM-41 was used. In addition, the dielectric relaxation peak in ϵ'' was described by a CC shape. This allows for a direct comparison to the τ_m obtained in the present work. The data show a nice agreement in the temperature range where both methods overlap. Therefore, it is assumed that it is the CC SD describes the dynamics of water in MCM-41 properly. A CC spectral shape was also found in dielectric measurements performed by C. Lederle in our labs on sample P25, see figure 5.15. The time constants are presented in figure 5.17.

Pore-size dependence of correlation times

After the CC SD was established as a good description of the dynamical process, the pore size dependence of the correlation times can be determined. Figure 5.17 shows the results from SLR experiments, that have been obtained using the Cole-Cole spectral density in the BPP formalism. Additionally, the correlation times deduced from the SE analysis and the STE correlation times for short evolution times t_p are included in the figure. Sample P29 has been omitted due to the close resemblance to sample P28.
In figure 5.17 it is evident that the different samples show a different fragility at high temperatures. The system becomes more fragile the larger the pores. The correlation times are similar at ca. 235 K in all samples with a value of $\tau(235\,\mathrm{K}) \approx 50\,\mathrm{ps}$. The VFT equation eq. (2.4) can be used to describe the high temperature data, the corresponding fit values are listed in table 5.2. Note

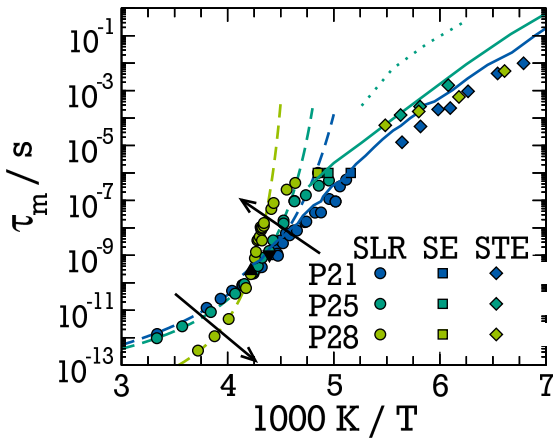

Figure 5.17.: Correlation times for the different pore sizes P21, P25 and P28. Shown are results from SLR (circles), echo intensity analysis (squares) and STE (diamonds). The arrows indicate increasing fragility on increasing pore size. Solid lines are DS results of P25 (turquoise) and P21 (blue), dotted line (turquoise) is the second process observed by DS. Black triangles are obtained from ^{1}H NMR (up: P28 at 360 MHz, down: P25 at 92 MHz, see text). Dashed colored lines represent VFT fits to high temperatures.

that the values of the resulting high temperature limit $\tau_0 = \tau(T = \infty)$ seem nonphysically low for P28 and P29, leading to very high values for the fragility m. The reason for this is the description by the CC function. This form is very sensitive to small errors, e.g. in the stretching α for high temperatures. As seen above, in the vicinity of the T_1 minimum, the calculated correlation times are rather insensitive to the form of the spectral density. Therefore, it can unambiguously be concluded that the fragility increases with increasing pore diameter. The time scale of the ^{2}H NMR measurements have been confirmed

Table 5.2.: VFT fit parameter and fragility for the different samples. m is the fragility calculated by eq. (2.5), T^* the approximate temperature where the data can not be described by the VFT anymore. The table includes the APTES modified P22a, c.f. section 5.5.

Sample	τ_0 / ps	B / (k_BK)	T_{VFT} / K	m	T^* / K
P21	$1.2 \cdot 10^{-2}$	617	173.4	87	217.1
P25	$1.9 \cdot 10^{-2}$	427	189.9	125	216.5
P28	$8.7 \cdot 10^{-4}$	349	209.2	192	227.8
P29	$2.0 \cdot 10^{-5}$	556	202.7	146	228.3
P22a	$7.6 \cdot 10^{-2}$	406	184.5	119	219.3

by ^{1}H NMR: correlation times have been obtained from the T_1 minima of SLR measurements from sample P25 and P28. The data of P25 were measured by E.

Klotz [219] at a Larmor frequency of 92 MHz, the data of P28 were measured by S. Reutter at 360 MHz Larmor frequency [122]. Both sets are shown in figure 5.17. They fit well to the ^{2}H NMR data.

At the temperature T^*, the measured data start to deviate from the fitted VFT behavior. T^* is given in tab. 5.2. It can be seen that it increases by ca. 10 K with increasing pore size. The correlation time where the deviations sets in increases by about one order of magnitude, as well. This behavior is not compatible with the proposed FST in bulk water since it should be observed at equal temperatures.

At temperatures below 185 K, the STE data are shown. Additionally, the results from DS of P21 [10] and P25 are included. The time constants of the two methods agree for both samples. It is evident in the figure that the low temperature process is weakly dependent on the MCM-41 samples used. The absolute time scale varies by about one order of magnitude at maximum. All samples exhibit the same universal activation energy $E_a = 0.5$ eV at temperatures below ca. 185 K. This results in apparent glass transitions of this process in the range from $T_g = 120$ K to 132 K.

The DS experiments measured on P25 in our labs found a second process close to the main relaxation, depicted as dotted line in figure 5.17. It is rather weak and exhibits a CC form, see in figure 5.15. Whether it is connected to the second SLR relaxation (s) cannot be answered satisfactorily in this work, but the assignment seems likely. It rises the question why this relaxation process is not found in the literature, since it is clearly observable in sample P25. Especially the observation of a second SLR relaxation process is hard to understand in terms of the two models presented in section 2.3.2. Therefore, we will propose a new model to understand the ^{2}H NMR results in the next section.

5.4.2 An interpretation: step wise solidification

The results obtained in this thesis cannot be brought into agreement with the postulated FST. The correlation times obtained from SLR and STE experiments suggest a much weaker change in the temperature dependence of the dynamics at 225 K as was measured in any NS study. The observed kink in the correlation times shifts in temperature and in the value of the correlation times in different pore sizes. Both is not to be expected if it was due to a FST. The correlation times at temperatures below 225 K measured in NS cannot be reproduced. The interpretation of our data and those reported in literature in terms of the FST of bulk water is implausible. The results are much more in favor of the model proposed by Swenson and coworkers [123]. There, it is assumed that the α-process is not observable, c.f. section 5.4.3, either because it is not detectable in DS or more to the favor of the authors because it is completely suppressed

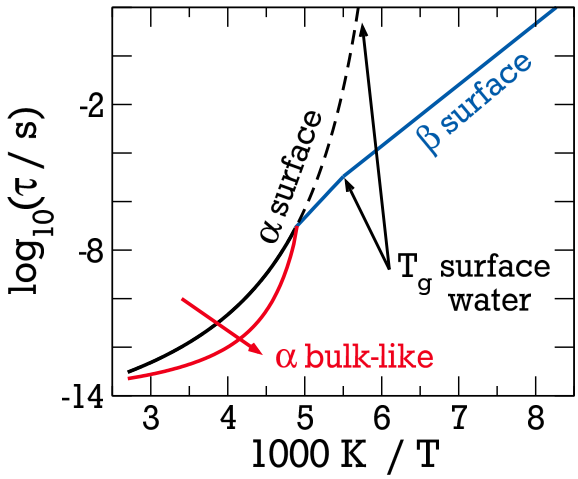

Figure 5.18.: Model to interpret the data: in small pores the high temperature dynamics are surface dominated and become more bulk like on increasing the pore size (red arrow). The low temperature dynamics are dominated by secondary relaxation of the surface water. At ca 225 K all bulk like dynamics stop due to solidification of inner water.

by finite size effects. The process observed at low temperatures thus is only a secondary process [123] or the α-process of the confined system [123].
The data obtained in this work seem compatible with this interpretation at first sight. However, the observed second relaxation process (s) lacks explanation in this model. Since it is solid like and most likely stems from molecules in the pore center, the model is extended as follows:
The relaxation of all water molecules in MCM-41 is measured at high temperatures. In pores as small as 2.1 nm, this is not bulk water but mostly water strongly influenced by the surface and some few more bulk like molecules. This shows in the increasing fragility on increasing pore size: the larger pores show a more bulk-like fragile behavior, while the smaller ones are less fragile. This explains why the QENS data in 1.8 nm pores agree well with the data in the larger 2.1 nm pores in this work, see fig. 5.16. In both cases most water molecules are strongly influenced by the MCM-41 interface. A transition occurs in the vicinity of 225 K. This is not the proposed FST but the water in the pore center solidifies. The structure of the solid material is not crystalline and depends on the pore size. In smaller pores, nucleation sets in but cannot be completed. Oguni et al. [220] found specific heat signals using adiabtic calorimetry methods in small pores below 2 nm diameter supporting this idea. Further evidence was found in DSC studies for larger pores [74, 194, 221] and are assisted by theoretical considerations of a dynamic crossover in small pores due to a freezing transition [58,222,223]. Based on the idea of a solid-like water core in the pore center, it seems plausible to attribute the second, slow relaxation component in SLR to this central component. It was argued that in this regime no or only

very weak specific heat signals should be observed [57] as was experimentally found by Oguni [220].

The properties of the solid-like water are not resolved yet. It was claimed by Johari [224] that dynamics and structure of those solidified parts should differ from that of bulk water and rather resemble that of highly distorted ice. Other authors [195] argue that no ice is formed at all, but only small nuclei form, which are unstable and dissolve for long times. The present work shows that if those nuclei form they are stable for at least the time scale of the slow SLR relaxation (s). The corresponding time constants are in the order of $T_{1,s} \sim 0.1$ s to 10 s. In this scenario, $T_{1,s}$ is a measure for the life time of those nuclei. It is interesting to note that this relaxation time is independent of the pore size of the system, and as will be seen later, also independent on the external magnetic field used in the NMR experiments.

At lower temperatures, the solidified water does not contribute to the fast (f) relaxation anymore. Only the dynamics of surface water is observed which exhibits a strong behavior below 225 K. The behavior in the performed STE echo experiments shows the features of a secondary relaxation. The same is true for DS, where the low temperature spectra exhibit all properties of a Johari-Goldstein β-process, see [10, 121, 123] for details. Thus, rather than observing the structural relaxation of this water species, NMR as DS observe the β-relaxation at least below temperatures of ca. 185 K. In the intermediate regime from 225 K to 185 K, the measured correlation times depended on the pore size. In this range, the α-process and transition from α- to β-relaxation in the water close to the surface are observed. The behavior of this transition region is influenced by the specific system and thus seem to depend on the pore topology, i.e. the curvature of the pores and possibly on the rigidity of the solidified species in the center.

The strong kink of the SLR time constants, and even more characteristic in the stretching parameter β, in the vicinity of 185 K is evidence for a glass transition in the system [38, 87, 225], as was discussed in section 3.5. During the glass transition, the correlation times of the α-process become slow, the structural relaxation can not restore the ergodicity in the system. Then, the SLR behavior is dominated by secondary relaxation processes. The temperature independence of this kink shows that it is a general feature of the liquid surface water. It marks the glass transition of surface water. The relaxation times $T_{1,f}$ at which the kink is observed are on the order of some hundred milliseconds. In type A glass formers without (observable) secondary relaxation as for example glycerol and o-terphenyl, this kink occurs on the order of tens of seconds [87, 172]. This again indicates that the (f) relaxation is caused by a secondary process. The finding of anisotropic behavior in the STE experiments supports this interpretation.

The observed kink in the SLR times is due to incomplete averaging over all possible configurations. As a consequence of the incomplete sampling of configuration space, the SLR becomes non-exponential. From this, an interesting opportunity to observe the α-correlation times of the surface dominated water arises which is discussed in chapter 7.

5.4.3 The α_{con} interpretation

In section 2.3.2, a model of interpreting the water behavior in MCM-41 was introduced which is the basis of our new interpretation. It predicts that one observes the α-process at high temperatures. At ca. 225 K, a transition to a low temperature process occurs which is likely a Johari-Goldstein β-process [11, 123]. The crossover was explained by the geometrically limited correlation length which cannot grow further. This also suppresses the α-process such that it is not observable or even completely absent [11]. The present results cannot be explained by this interpretation. There are two main aspects why this interpretation does not agree with our data. First, if the transition is due to finite-size effects, it occurs when the correlation length is on the order of the pore size. This length grows with decreasing temperature and thus reaches the limits set by the pores at a lower temperature the larger the pore is. This is not the case in the measurements presented here, but rather the opposite happens: in table 5.2, a rough estimate for the temperature of the first deviations from the high temperature behavior T^* is listed. It increases with growing pore size, at variance with a growing length scale that is limited by the pores. Second, the present measurements show an additional relaxation process, which is due to the rotation of a substantial amount of molecules, most likely in the pore center. Such a process can not be explained by the other interpretation. In fact, it is interesting that it is not even observed in DS experiments on sample P21 [10], since it was observed in sample P25.

One may argue that this second process stems from the motion of the hydroxyl groups attached to the walls, which has been observed in DS [10]. To test this idea, the DS correlation times and the shape of ϵ'' reported in [120] were used to calculate the expected relaxation times $T_{1,f}^{DS}$ using the BPP model eq. (3.33). The calculation was performed for different weights of hydroxyl molecules and water molecules. In figure 5.19, the results of the calculations are reported for weighted superpositions in steps of 10 % of both relaxations. It was assumed that both species cause only one single SLR relaxation. The inset of the figure shows the best fitting set, corresponding to 40 % OH groups. It is evident in the inset, that the measured data fit nicely to the calculated ones
A rough approximation can be used to test if this is a realistic figure: the area of a long cylindrical pore is $A \approx 2\pi r^2$. The volume is $V = hA$, where h is the

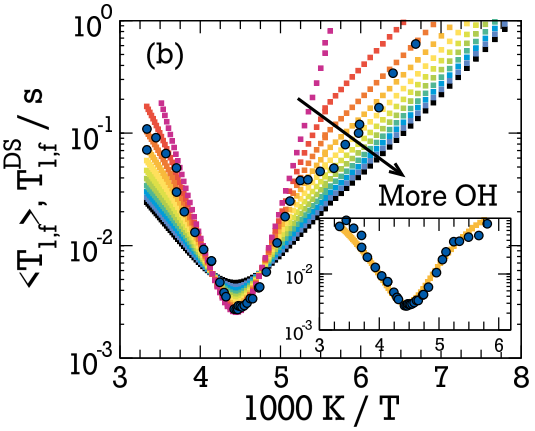

Figure 5.19.: Measured SLR times of P21 (f) (blue circles) and theoretically calculated $\langle T_1 \rangle$ from DS by assuming a weighted rate average of signal from hydroxyl groups and water molecules (squares). The contribution from the wall was assumed to range from 0 % to 100 % (pink to black) indicated by the arrow. Inset: Average $\langle T_1 \rangle$ at 40 %.

length of the pore. The volume of a water molecule can be estimated using the average density of $\rho = 1\text{cm}^3/\text{g}$ to be $V_{H20} = 0.03\text{nm}^3$. The number n of molecule in the pore is $n = V/V_{H2O}$. The average area density g of OH groups necessary to amount for a signal of 40 % can be calculated using the surface of the pore $A_O = 2\pi h$:

$$g = 0.6\frac{2n}{A_O} = \frac{3}{5}\frac{4\pi hr^2}{V_{H2O}2\pi h} = 42.8\text{nm}^{-2}. \tag{5.3}$$

Here, the additional factor 2 is due to the two deuterons carried by one water molecule. The resulting value is unrealistic for MCM-41 samples. Usual values of the OH density range from 2 nm^{-2} to 6 nm^{-2} [103]. Thus, the OH groups at the walls cannot explain the behavior of the (f) relaxation component. By a similar calculation, it can be excluded that the wall contribution is responsible for the slow (s) relaxation, since it exhibits up to 20 % of the total signal. Therefore, it can be concluded that the interpretation given by Swenson can not explain our results, even if the OH groups at the MCM-41 surface are taken into account.

5.5 Influence of surface modification with APTES

In this work, mainly the dynamics of water and water mixtures in MCM-41 confinement is studied. In many situations, e.g. in biological systems, the confinement is less defined and different interactions between guest molecules and host material are of interest. Therefore, it is important to study in how far the

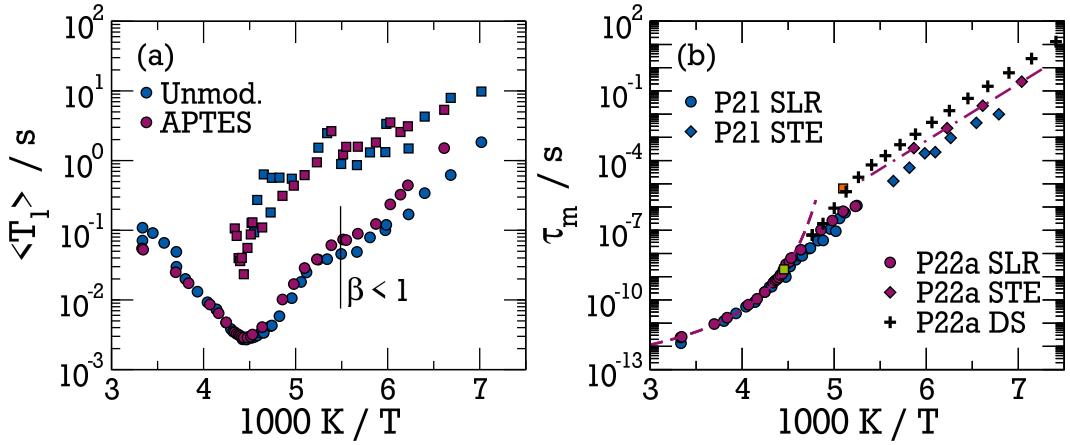

Figure 5.20.: (a) Mean relaxation times $\langle T_1 \rangle$and (b) correlation times τ obtained from P21 and P22a. The line in (a) marks the temperature where the stretching β becomes smaller than unity in P22a. the dashed line in (b) is a VFT-fit using the high temperature data only, the dash-dotted line is an Arrhenius-fit to the STE data. Squares in (b) mark the position of the minima in T_1 (green) and T_2 (orange). The empty diamond is a partially relaxed STE experiment, pluses are DS measurements performed by M. Rosenstihl.

results found in MCM-41 are valid in diverse environments. In section 2.3.2, the investigation of water dynamics in different kinds of confinements were discussed briefly. Here, the influence of surface modification of MCM-41 is tested rather than using a different confinement material, see section 4.2. This approach combines the well defined pores found MCM-41 with the possibility of changing the specific guest-host interactions. The used MCM-41 was synthesized in the AK Buntkowsky and modified by the procedure explained in section 4.2. The APTES modified silica sample was filled with D_2O and measured by F. Dietrich [198] in his Bachelor's thesis.

Figure 5.20 (a) reports the mean relaxation time $\langle T_1 \rangle$ of the modified sample P22a. Additionally, the results obtained from the unmodified sample P21 are shown. Both samples exhibit roughly the same pore diameter. The figure shows that at high temperatures above the T_1 minimum the SLR times in both samples agree well. Below the minimum, the fast process (f) shows some deviations that indicate a minor slow down of dynamics in the P22a sample. This is in accordance to the slowing down on increasing the pores that was observed above. As in all water samples confined to MCM-41 samples a second relaxation process (s) is present. Within the uncertainties, it agrees well with the same process in the unmodified sample.

The correlation times τ_m are calculated by the BPP model using the CC SD. Again, this is motivated by the findings of DS measured on the same sample (not shown). The results are reported in fig. 5.20 (b). The correlation times

coincide with the unmodified samples for temperatures above ca. 225 K. In this temperature range, they follow a VFT behavior. The corresponding fitting parameters are listed in table 5.2. As in the unmodified sample, a change in the temperature dependence is observed at $T^* \approx 219$ K. Both samples, P21 and P22a, show a similar temperature dependence, but the modified sample shows slightly slowed down dynamics compared to the unmodified one. The STE experiments show a more pronounced difference between the samples at low temperatures. They result in correlation times that follow an Arrhenius behavior with an activation energy of $E_a = 0.49$ eV. The time constants are shifted by a factor of 3, thus the APTES modification seems to slow down dynamics in this temperature range. This slowdown is situated well within the differences observed for different pore sizes, see sec. 5.3.

Additionally to the STE data, the figure shows DS data measured by M. Rosenstihl on water in the same APTES modified MCM-41. The data nicely connect to the high temperature data, but are slowed down by an additional factor of ca. 3 to 4 in comparison to the STE experiments at low temperatures. Similar deviations were found in the unmodified P21 sample, where the DS data [120] are shifted slightly with respect to the STE data. Interestingly, the DS experiments on the small samples P21 [120] and P22a do not show the slower process that was observed before in sample P25. The second process thus seems only to be observable in larger pores in DS. Possibly, this explains the shift of DS data compared to NMR STE data. In large pores, DS can resolve the two processes and therefore the shift is smaller, as e.g. evident in fig. 5.17 for sample P25. In the small pores, the slow process may be indistinguishable in DS and absorbed in the fit of the main process. Therefore, the DS time constants are shifted to larger values. Additionally this may explain the broader distribution observed in DS compared to NMR. Whether this is true should be investigated in more detail. In favor of this idea is the analysis of the SE signal minimum. It is obtained from the total signal and thus also takes the (s) process into account. The correlation time obtained from the minimum (orange square) agrees well with the data from DS.

A closer look on the spectra obtained from P22a reveals that larger differences compared to P21 exist. The line shape transition region between ca. 220 K and 180 K shows unexpected features. This is shown in figure 5.21 where fully and partially relaxed spectra are shown for selected temperatures. The following discussion focuses on the PR spectra. The FR spectra again show only an additional Pake-like contribution that, analogous to the discussion of P21, is attributed to the slow relaxation component (s). Upon cooling from high temperatures first a broadening of the Lorentzian line is observed. In the transition, region the line shape shows a non-Lorentzian feature in the center, c.f. the spectrum at 203 K. This additional spectral feature can first be observed at 211 K (not shown). At the same time as the non-Lorentzian feature, a third Pake-like

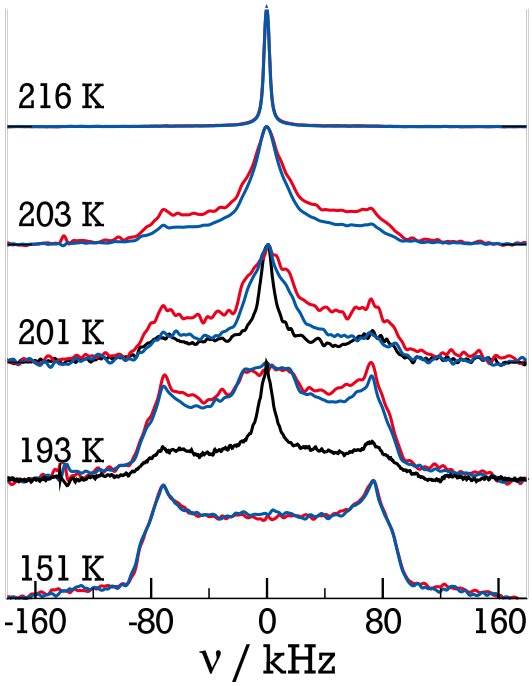

Figure 5.21.: Solid echo spectra obtained from partially (blue) and fully (red) relaxed measurements in sample P22a. In black partially relaxed spectra of sample P21.

spectral contribution starts to arise. On further cooling, the Lorentzian line vanishes, see e.g. at 193 K. At this temperature, the non-Lorentzian center component exhibits a FWHM of about 40 kHz. At very low temperatures, the central component decreases, e.g. at 151 K, only a Pake spectrum is left over. Note that this Pake spectrum is not in static, but as in the unmodified samples same residual intensity is left over in the center.

A similar spectral shape was observed before by Lusceac et al. [88, 226] in ^{2}H NMR measurements on myglobin hydration water. The authors found that the hydration water in this case performs a large angular motion with angle amplitudes of $\psi = 85°$ to 130°. A fast rotation about a symmetry axis by those angles causes an effective averaging of the anisotropy δ according to eq. (3.38). This results in an effective coupling constant of $\bar{\delta} \approx 40$ kHz which is in good agreement to the width of the central features observed in the present work. Geometries that can feature those jump amplitudes are for example strongly distorted π-flips and tetrahedral jumps. Lusceac et al. also found a possible agreement with three site jumps on a cone similar to methyl group rotation. They stressed that none of those geometries was able to explain all the features found in hydration water of myoglobin alone. Distributions of geometries could resolve the issue, but are hard to be determined unambiguously [226]. It was argued that in myoglobin a crossover from an isotropic reorientation to

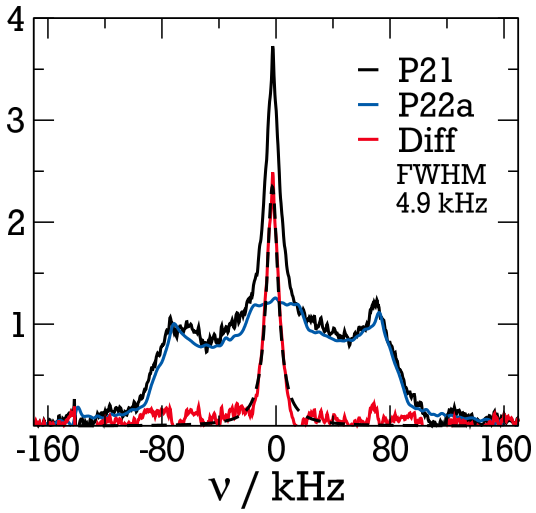

Figure 5.22.: PR spectra at T =193 K of samples P22a and P21 normalized to the height of the Pake contribution at ±71 kHz. Red is the difference between of spectra. In dashed black: Lorentzian fit to the difference spectrum.

the anisotropic reorientation occurs in the vicinity of ca. 220 K, explaining the crossover from the isotropic Lorentzian to a narrowed Pake-like spectral shape. At this temperatures, the motion of hydration water is still fast, but slows down upon further cooling. This causes the transition to a solid Pake spectrum. The line-shape transition extends to temperatures as low as 150 K in myoglobin. The crossover from isotropic to anisotropic motion is not observed in the line shape of other proteins, e.g. elastin and collagen [88]. Thus, either in myoglobin the crossover happens at higher temperatures than in other proteins or it is due to specific motional features of myoglobin.

Following this argumentation, in the case of D_2O confined to APTES modified MCM-41 at temperatures above ca. 211 K, the spectra are isotropically averaged and exhibit a Lorentzian shape. Due to the decreasing T_2, the Lorentzian broadens and exhibits a FWHM of 5 kHz at 211 K.[7] Below these temperatures, the spectra deviate from the Lorentzian form and the isotropic averaged motion becomes anisotropic. In the same temperature range, an additional broad Pake component starts to grow in the PR spectra, indicating the presence of slow molecules with ($\tau > \delta^{-1}$) due to a distribution $G\left[\log(\tau)\right]$.

Direct comparison of the PR spectra of P22a and P21 shown in fig. 5.21, shows an interesting difference between the two samples. At 201 K, both show approximately equal contributions of the Pake like spectra, while the central component is anisotopically broadened in the modified MCM-41. The situation changes on cooling: the relative contribution of the Pake component is much larger at 193 K in the modified MCM-41 compared to the unmodified

[7] This corresponds to a $T_2 \approx 64\,\mu s$

sample. This can be seen in fig. 5.22, where the spectra were normalized to their height at ±71 kHz. A much larger Lorentzian line is visible for P21, indicating that a significantly larger fraction of molecules in this sample is still fast. Subtraction of the two spectra results in the difference spectrum shown in figure 5.22. It can be described with a Lorentzian shape resulting in a FWHM of 4.9 kHz. The purely Lorentzian shape of the difference spectrum suggests that the same anisotropic line shape observed in P22a is also be present in P21. There, it is mostly concealed by the still isotropic parts. If this was the case, this would mean that the anisotropic reorientation clearly observable in P22a is not a feature of the APTES modification, but rather of the water close to (MCM-41-) surfaces.
A possible scenario is the following: the elementary water reorientation close to surfaces in general or at least close to MCM-41 surfaces is anisotropic. If the molecules are fast enough to average over many of those positions or can interchange to layers that are further away from the surfaces, this averages out most of the anisotropy. Only if the molecules become too slow, the anisotropy is detected in the experiment as for example in the STE experiments shown in section 5.3. In this scenario, the main effect of the APTES modification is to prevent the water molecules from effective averaging, e.g. by spatial constriction. The anisotropic nature of the reorientation becomes dominant at higher temperatures, while fast, isotropic motion is hindered. Whether this idea is true can not be answered conclusively in this work. Additional experiments utilizing different surfaces may help to clarify this questions.

In this short section, we have found that the water dynamics in small pores of ca. d = 2.2 nm are not influenced by the APTES modification of the confinement at high temperatures. In the surface modified sample dynamics, show a more anisotropic behavior in the line shape transition region around 200 K. Comparison to the unmodified samples suggests that this is a general feature of water that is better observable in these samples, since the APTES modification suppresses efficient averaging in this temperature region.

5.6 Summary

In this chapter, the dynamics of water confined to MCM-41 was investigated. To begin, the principle behavior of the SLR was discussed in small pores of 2.1 nm diameter. Thereafter, it was shown to be similar in larger pores. The investigation found a pore size dependent dynamics in the high temperature regime. There, relaxation was more bulk-like the larger the pores are. At ca. 225 K, a second relaxation process is found in all samples. Analyzing the SLR stretching parameter β, the signal amplitude and the line shape of this component shows that it originates from a solid-like water species. The appearance of this

component agrees with the theorized FST. The FST was claimed to be observed before, e.g. in [9]. Those studies neglect the possibility of a solid-like component, which would have consequences for the system's dynamics. Thus, it was concluded here, that the change in the temperature dependence of the dynamics is due to a change in the observed subensemble of molecules. At higher temperatures above 225 K, all water molecules are liquid and contribute to the observed process, while below this temperature, only the non-solidified water at the pore walls is observed. This is in agreement with adiabatic calorimetry [220] and other experimental studies [195, 224] as well as with theoretical arguments [57, 58, 222]. They all hint towards a freezing transition rather than a dynamical effect. The low temperature process was further analyzed. Its lineshape shows that it is in very good agreement with the process observed in DS measurements in the same pores [120]. Stimulated echo experiments showed very good agreement with DS and indicated that this process is rather a secondary process than the α-process. All those results were used to propose an alternative model to understand the data.
In the final section of this chapter, the influence of a modified MCM-41 surface was investigated. The influence of the APTES modification was found to be small. The main effect seems to be the suppression of motional averaging. Therefore, the dynamics seem to be more anisotropic. The results are similar to those encountered in myoglobin.

6 Dynamics of glycerol

In the last chapter, the dynamics of water confined to MCM-41 was investigated. Confined water has shown some unexpected properties, e.g. the formation of a second, solid like species at low temperatures. In this chapter, the well characterized model glass former glycerol is confined to MCM-41 matrices. This is done to obtain information on the influence of the confinement on material which usually does not crystallize. A comparison to water may help to identify the effects caused by the confinement itself and those that are properties of water.

6.1 Glycerol as a model system

It is an ambiguous task to learn about the properties of water from investigating the dynamics of water confined to narrow geometries. In those situations, it is, for example, not clear which effects are exclusively caused by the confinement. To gain a comparative view on dynamics of supercooled liquids in confinement the dynamics of glycerol are investigated in this chapter. It is a well known and characterized glass former, see e.g. refs. [87, 172, 188, 227, 228]. The method of choice is ^{2}H NMR to allow for direct comparison with rotational dynamics measured in confined water.

A characterization of glycerol's dynamical properties as probed by dielectric spectroscopy can for example be found in references [182] and [188]. Glycerol is usually classified as a type A glass former [87]. It exhibits an α-process of asymmetric shape that is continued to higher frequencies by the *excess wing*, a power law like frequency dependence, see section 2.3 for details. No separate peak of a β-process is found. Due the apparent absence of a β-process and the good knowledge of the bulk dynamics, glycerol is a model system for testing the influence of confinement on a glass former.

We use ^{2}H NMR to analyze the behavior of glycerol in bulk [199] and confined in MCM-41 of d = 4.9 nm [200] and d = 2.8 nm. As will be shown, glycerol is much less influenced by the confinement than water indicating that the interaction with the MCM-41 is much weaker. This is in agreement with most experimental [142, 229] and simulation [230] studies. In literature in some cases an acceleration of dynamics due to spatial restrictions is found, e.g. in free standing polymer films [231], while surface interactions decelerate the motion of guest molecules in other cases. However, noticeable finite-size effects in glycerol have been observed only in much smaller confinement, as for exam-

ple in metal organic frameworks of less than 1.8 nm size [232]. There, at a size dependent temperature T_k, a kink from the high temperature VFT behavior was found which was replaced by an ARR behavior at lower temperatures.
Glycerol has been confined to MCM-41 with pores of diameter d = 4.9 nm (P49G) and d = 2.8 nm (P28G). Additionally, bulk glycerol has been measured for comparison. The results presented in this chapter have been obtained in the Bachelor thesis of M. Schwenk [200] (P49G). Bulk glycerol was measured by M. Beykirch and Msc. D. Demuth, see in [199] for details.

6.2 Relaxation behavior of glycerol in MCM-41

The dynamics of glycerol in MCM-41 have been measured by SLR, LSA, and, STE techniques are combined to cover a large range of correlation times. The influence of the confinement is tested in MCM-41 of two different pore sizes of d = 2.8 nm (P28G) and d = 4.9 nm (P49G). Those are compared with bulk glycerol data. In alle samples glycerol-d_5 was used. There, all protons attached to a carbon atom are exchanged with deuterons, c.f. fig. 2.11. No chemical exchange with other protons, e.g. present in hydroxyl groups attached to the MCM-41 walls, is possible.

6.2.1 Results of spin-lattice relaxation

The SLR times T_1 are measured using the SR experiment, c.f. section 3.4. The measured recovery curves are monomodal in most cases. Typical curves are shown in figure 6.1 (a). They were fitted using a single exponential recovery.At some temperatures a more interesting behavior was found. Two examples are depicted in 6.1 (b):

- In all samples the heating effect discussed in section 3.7 was observed. Due to the pulse train used to saturate the magnetization the sample is heated. At temperatures above the T_2-hole this causes the magnetization to decrease for long waiting times, as can be seen in panel (b) for bulk glycerol. Below the T_2-hole, the recovery curves become bi-modal because of this effect. It does not affect the relaxation time (c.f. section 3.7) except for an offset in temperature. We will see later that this temperature shift is negligible.
- In the largest pores, sample P49G, glycerol crystallized after it was kept at intermediate temperatures of ca. 215 K for several days. This can be seen in the two measurements at T = 221 K. Comparison shows an increase in the relaxation time T_1 of at least a factor 1000. This finding is rather unexpected since glycerol in bulk hardly crystallizes at all.

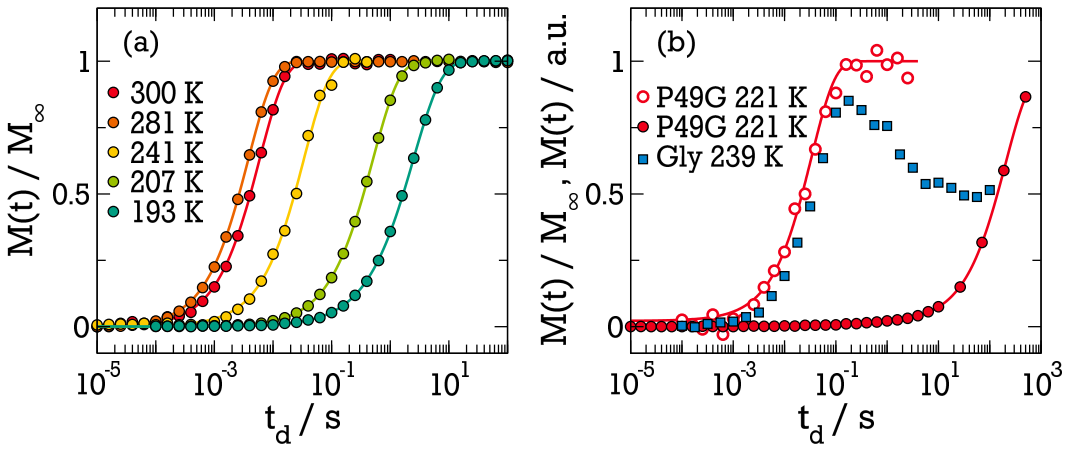

Figure 6.1.: Examples for performed saturation recovery experiments: (a) monomodal recovery in P49G and (b) examples for the found pulse heating effect and crystalline glycerol, see text.

Both effects, crystallization and heating of the sample will not be discussed further. The results of fitting the recovery curves are reported in figure 6.2. In panel (a) the mean relaxation times $\langle T_1 \rangle$ are plotted versus the inverse temperature. All three samples exhibit a very similar temperature dependence. At 280 K to 290 K the relaxation times are a minimum. As listed in table 6.1 the position of the minimum shifts to larger values and lower temperatures for decreasing pore size. This temperature shift indicates slightly accelerated dynamics in the MCM-41 confinement. The increase in $\langle T_{1,min} \rangle$ indicates a larger broadening of the distribution $G\left[\log(\tau)\right]$ of correlation times and therefore signifies larger heterogeneity in the samples. Similar results have been found in ME samples [229].

Panel (b) of figure 6.2 shows the stretching parameter β obtained from the SLR experiments. It decreases below ca. 200 K and is a minimum at ca 180 K in all samples. This behavior was observed in glass formers before and signals that the structural α-process becomes too slow to restore ergodicity on the experimental time scale, see sect. 3.5. The kinking in β happens at similar temperatures in all three samples indicating that all samples undergo the glass

Table 6.1.: Parameters obtained from bulk and confined glycerol. γ is the CD stretching parameter. T_{ne} is the approx temperature where the system becomes non-ergodic and thus $\beta < 1$.

s Sample	$T_{1,min}$ / ms	$T(T_{1,min})$ / K	γ	T_{ne} / K	T_{SE} / K
Bulk	3.65	288.2	0.52	202	232
P49G	3.75	284.1	0.49	202	233
P28G	4.2	278.8	0.4	208	236

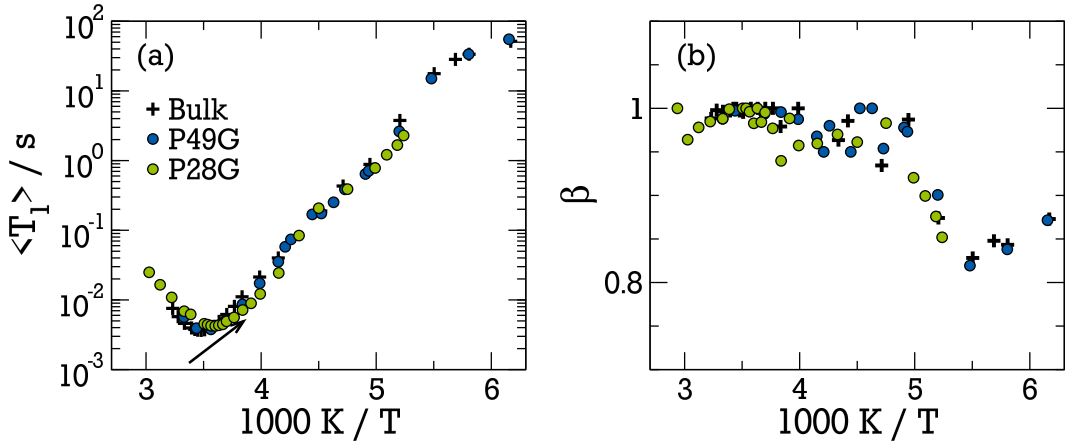

Figure 6.2.: (a) Mean spin-lattice relaxation times $\langle T_1 \rangle$ of the measured samples. The arrow marks the direction of the minimum shift on decreasing pore size. (b) corresponding stretching parameters β.

transition at similar temperatures, in agreement with the very similar T_1 times. The bulk glass transition takes place at $T_{g,bulk} = 189\,K$ [233].
The stretching parameter scatters somewhat for temperatures above 200 K. This is due to the weak signal in the SE echo signal minimum shown in figure 6.3, where the Curie-corrected signal is plotted over inverse temperature. All three samples exhibit a similar signal loss. A polynomial fit to the minima results in temperatures T_{SE} from 232 K to 236 K. The temperature T_{SE} is a good approximate for the correlation time of the motion to be $\tau = \delta^{-1} \approx 1\,\mu s$. The depth of the minimum depends on the fraction of spins that exhibit dynamics on that time scale. Very deep minima are observed in all three samples. This indicate narrow distributions of correlation times $G\big[\log(\tau)\big]$. On close inspection of the figure, sample P28G exhibits a larger signal in the minimum $R(T = 231\,K) \approx 94\,\%$ compared to bulk glycerol and sample P49G where $R(T = 231\,K) \geq 98\,\%$. This is in agreement with the higher values of T_1 in the respective T_1 minimum. This sample is more heterogeneous compared to the other.
It is interesting to note that in the low temperature limit the Curie-corrected signal becomes larger than unity, i.e. $R < 0$. A similar behavior was observed in a water-glycerol mixture confined to MCM-41 [1]. Usually effects like this are attributed to experimental artifacts, e.g. temperature dependent tuning and matching. All three samples presented here have been measured in the same setup, therefore it is unclear why the bulk system behaves differently from the confined ones which are very similar.
In summary, SLR reveals very similar temperature dependence of the dynamics in all three investigated samples. The T_1 time constants indicate a minor slow down of dynamics on decreasing confinement size, while the heterogene-

[1] Unpublished data, water-glycerol were mixed 50:50 in weight. Measured by Max Schäfer.

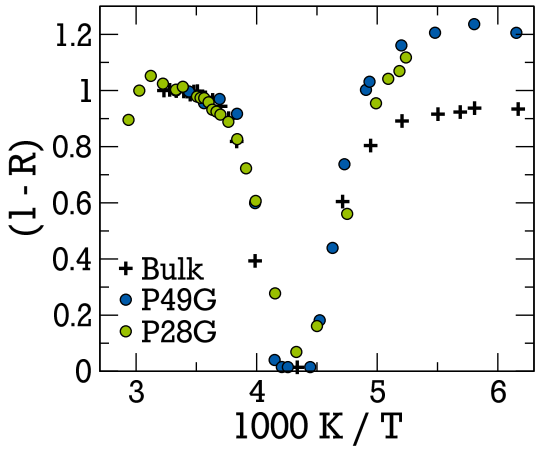

Figure 6.3.: Reduction factor (1 - R) for bulk and confined glycerol.

ity increases as the pore sizes is reduced. Consistently the confinement has no significant effect on the system's glass transition, at least as indicated by the stretching parameter β.

6.2.2 Stimulated echo experiments

In this section the low-temperature dynamics of bulk and confined glycerol are investigated by means of the STE experiments. In the above SLR experiments no significant confinement effect was observed. The temperature dependence is investigated to characterize the time scale of dynamics. In addition, evolution time t_p dependent experiments are conducted to obtain information on the mechanism of motion.

In figure 6.4 spin alignment order decay curves measured in sample P49G are shown for different temperatures and evolution times. Each panel shows the temperature dependence to a fixed value of t_p ((a) 5μs, (b) 10μs,(c) 30μs). The lowest temperature 182 K (turquoise) is already dominated by the influence of SLR. The solid lines represent fits by eq. (3.56). In figure 6.6 the temperature dependent correlation times obtained from the STE experiments of all three samples will be shown.
Besides the obvious temperature dependence, figure 6.4 illustrates that the correlation decays also vary with the evolution time. The characteristic time τ and the residual correlation plateau F_∞ are functions of the evolution time t_p. To illustrate the influence of t_p, figure 6.5 shows a comparison of all three samples at T = 203.5 K. In panel (a) the correlation curves are plotted for t_p = 5 μs. There, it can be observed that the curves slightly shift to shorter times for smaller confinement size. Dynamics are accelerated in correspondence to the findings in SLR, see figure 6.6 for an overview. Nevertheless, the normal-

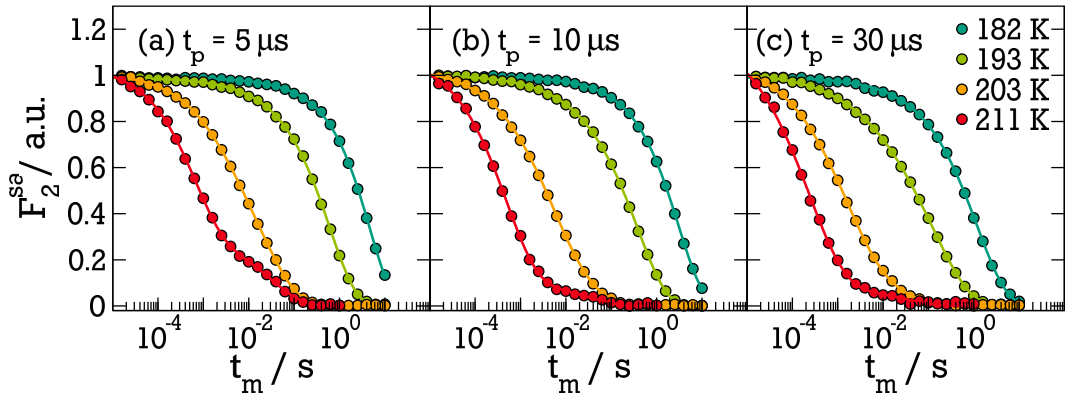

Figure 6.4.: Temperature and evolution time dependence of the spin alignment STE experiments in sample P49G. Evolution times t_p of (a) 5μs, (b) 10μs,(a) 30μs are plotted. The temperatures are given in panel (c).

ized correlation times $\tau_N^{sa} = \tau^{sa}(t_p)/\tau^{sa}(t_p \to 0)$ shown in panel (b) show very similar evolution time dependence. For better comparison to bulk, panel (b) includes bulk glycerol data measured by Böhmer et al. [234] (black solid line).

The data of P28G in panel (a) show a residual plateau F_∞^{sa} that is absent in P49G and in bulk. The plateau can be determined more reliably in ze order experiments, since there the influence of SLR can be measured individually. The plateau values F_∞^{ze} obtained from ze order are shown in panel (c). Since bulk F_∞^{ze} data have not been measured in our lab, the literature data [234] are included as well. Even so the dependence on t_p is again similar, a more pronounced difference can be observed for the confined samples: the values of $F_\infty^{ze}(t_p)$ slightly increase with decreasing pore size, as also seen in the decay curves in (a). $F_\infty^{ze}(t_p)$ is characteristic for the geometry of reorientation. In case of bulk glycerol it corresponds to an isotropic reorientation. An increase in the value of $F_\infty^{ze}(t_p)$ corresponds to some anisotropy of the reorientation. Thus, confining glycerol to very narrow pores introduces anisotropy in the reorientation. Possible reasons for this are a change in the motion itself, e.g. due to disturbance of the OH network or preferred orientations of the glycerol molecules close to the pore walls which do not allow for isotropic reorientation in their vicinity [84].

A last observation from the STE experiments can be made by comparing the values of the fitted stretching parameter β (not shown). It becomes the smaller the smaller the confinement and exhibits mean values of $\langle\beta_{Bulk}\rangle = 0.57$, $\langle\beta_{P49G}\rangle = 0.37$, and $\langle\beta_{P28G}\rangle = 0.31$ at T = 203.5 K.[2] This signals increased heterogeneity in the small MCM-41 samples, again in agreement to the findings of SLR. It is interesting to note that using the approximation given by Zorn [39]

[2] Here, the mean is taken over all evolution times t_p.

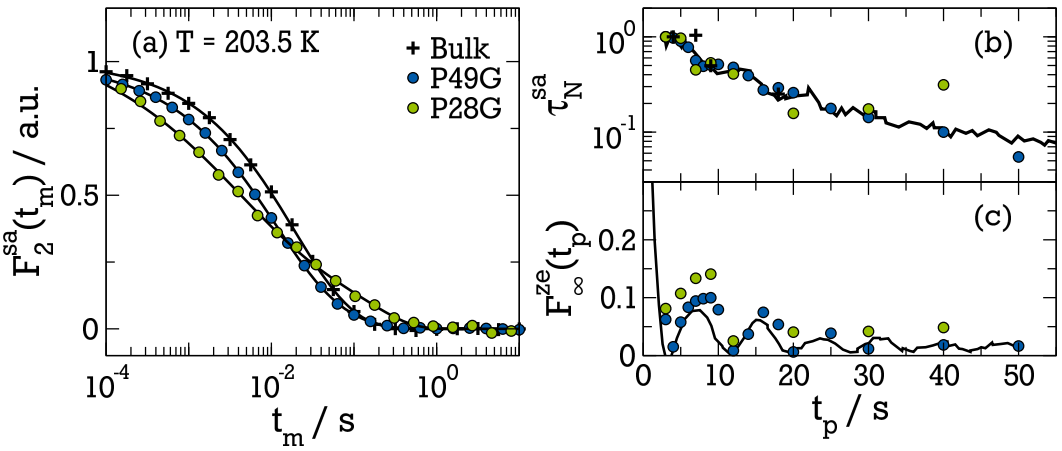

Figure 6.5.: (a) correlation decay of sa order STE T = 203.5 K for t_p = 5μs, (b) reduced correlation time $\tau_N^{sa} = \tau^{sa}(t_p)/\tau^{sa}(t_p \to 0)$ and (c) residual correlation F_∞^{ze} of bulk glycerol, P49G and P28G. Black lines in (b) and (c) are bulk data of Böhmer et al. [234].

$$\beta_{KWW} \approx \frac{\pi}{\sqrt{(6\psi'(\gamma))}} \tag{6.1}$$

where, ψ' is the derivative of the digamma function, it is found that the KWW stretching β_{KWW} and agrees with the CD stretching parameter γ in the case of the bulk liquid. However, in case of the confined liquid, the measured $\beta_{P28G} = 0.31$ is significantly smaller than expected $\beta_{KWW}(\gamma = 0.4) \approx 0.47$. This may indicate that the spectral density is temperature dependent, or that it is not purely CD like.
A change of the SD was found in MD simulations of confined water [83, 84] when approaching the pore walls: The SD in those simulations was found to be CD like in the center of the pores, while close to the walls it was more CC like. This was accompanied with a slowdown of dynamics near the wall. The dynamics observed in the present experiments, thus are a superpostion of different dynamics. Given the assumption that the asymmetry is given by the bulk value, i.e. $\gamma = 0.52$, the HN spectral density can be used. Than the SLR minimum value of P28G is met using $\alpha_{HN} = 0.83$. Calculations of the correlation times using this set of parameters does not significantly deviate from a CD form and is therefore disregarded.

The presented STE experiments have shown that confining glycerol to narrow pores leads to weak deviations from bulk behavior. In smaller confinements the dynamics are accelerated slightly, which will be discussed in more detail in the next section. Additionally, the stretching of the correlation decays indicate an increase of heterogeneity upon decreasing pore size, while at the same time

the residual correlation hints towards a slightly more anisotropic motion. The latter is likely due to a preferential orientation with respect to the wall rather than a finite-size effect.

6.2.3 Discussion of glycerol dynamics in MCM-41

The correlation times τ_m have been calculated for the different samples using the BPP ansatz, see eq. (3.33) and eq. (2.16). In those calculations $\delta = 124\,\mathrm{kHz}$ was used as obtained from fitting the spectra, c.f. sect. 3.8. The results are depicted in figure 6.6. The figure includes SLR, LSA and STE correlation times obtained from the bulk sample as well as sample P49G and P28G. Additionally literature results obtained by DS in MCM-41 of $d = 2.1\,\mathrm{nm}$ [142] are included. As discussed above, the main effect of the MCM-41 confinement is an acceleration of dynamics. The obtained correlation times τ_m are fitted using a VFT law, see eq. (2.4). The results are listed in table 6.2. From the fits the fragility m and the theoretical glass transition temperature T_g have been calculated using eq. (2.5). The acceleration of dynamics can best be seen in the glass transition temperature. It reduces by ca. 8 K in the P28G sample compared to the bulk. In the smallest MCM-41 pores taken from literature, T_g is reduced by 14 K compared to bulk. The fitted glass transition temperature of $T_{g,bulk} = 188\,\mathrm{K}$ agrees well with values reported in literature [235]. Shifts of T_g of similar order of magnitude have been observed in porous silica glasses using DSC methods [70]. There and in other studies, a linear scaling of T_g with the inverse pore diameter was found [66], in accordance to the present findings, see the inset of figure 6.6. Note, that in very recent experiments on the amount of residual water in MCM-41, it was found that the here used method of drying does not remove all water from the MCM-41. Thus, the observed acceleration of dynamics is not necessarily a confinement effect, but may be connected to residual water. In this case, the residual water to glycerol ratio should increase the larger the inner surface is compared to the inner volume, and thus, more residual water is expected in the smaller MCM-41 samples. This may explain the observed effects.

The stimulated echoes in section 6.2.2 revealed that the anisotropy of the dynamic process increases slightly when decreasing the pore size. In table 6.2 it can be observed that at the same time the fragility slightly decreases in the smaller MCM-41 confinements.

The present and previous results imply that distribution of $G\big[\log(\tau)\big]$ are a general property of confined liquids [87]. In confined glycerol, this seems to be due to a similar mechanism as found for confined water [84]. There, different SD were found in the pore centers and close to the walls. The superposition of different dynamics leads to a broadening of the observed total distributions. In contrast, the acceleration of rotational dynamics on decreasing confinement

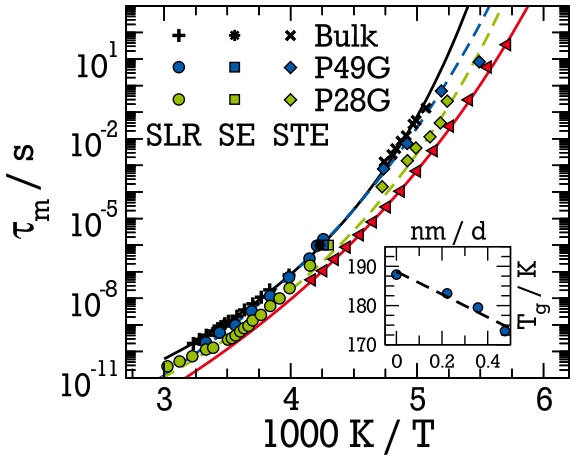

Figure 6.6.: Mean logarithmic correlation times τ_m obtained from the different samples. The lines represent VFT fits to bulk data (black solid) and to data from P49G (dashed blue) and P28G (dashed green). In red: MCM-41 d = 2.1 nm taken from ref [142]. Orange triangles have been estimated from field cycling, see section 7.1.1. Inset: estimate T_g over inverse pore diameter.

size is not a general property but only observable for some guest-host pairs. Possibly,density reduction plays a role here, since a decrease in density has shown to accelerate dynamics [204, 213].
In supercooled liquids, a growing length scale of cooperativity ξ is expected upon cooling [12]. Deviations from the bulk behavior should occur when ξ reaches the smallest length of the confinement $\xi(T_c) = d$. Then a cross-over from a VFT behavior to an Arrhenius behavior is expected at the temperature T_c [236]. The present results are not able to detect any crossover of this type in MCM-41 confinements down to 2.8 nm. Taking the data from Elamin [142] into account no transition is found down to 2.1 nm. In situ BDS studies [237] using nano-structured probes found geometrical confinement effects on glycerol only for structure sizes below 1.6 nm. In a MD simulation study [230] of glycerol in MCM-41 like channels of 2.4 nm no such effect was found either. The simulations showed only very minor deviations from the bulk behavior. The most pronounced effect was found in the number of H-bonds. The number of bonds

Table 6.2.: VFT fit parameter and fragility for the different samples. m is the fragility calculated by eq. (2.5). Sample P21G was taken from [142].

Sample	τ_0 / ps	B / (k_BK)	T_{VFT} / K	m	T_g / K
Bulk	$2.6 \cdot 10^{-3}$	1950	136.9	36	187.9
P49G	$5.7 \cdot 10^{-6}$	3282	109.0	32	183.1
P28G	$7.6 \cdot 10^{-5}$	2556	118.2	33	179.5
P21G	$1.8 \cdot 10^{-6}$	3359	99.8	31	173.7

per OH group between different glycerol molecules approximately 1.4 to 1.6 in the investigated temperature range. In contrast, this number is found to be about 1 per OH bonding towards the walls. The lifetime of both bond species between two glycerol molecules and between a glycerol and a hydroxyl group of the wall, is slightly larger than in the bulk. The H-bond properties may be an explanation for the acceleration of dynamics measured in this work.

In contrast to the above findings, Levchenko et al. [238] found a completely different behavior of glycerol in MCM-41 pores of d = 2.2 nm using ^{13}C NMR experiments. They reported an Arrhenius behavior of the confined molecules which was found to be slower than the bulk liquid at most temperatures. The findings were attributed to the strong influence of the walls. It was argued that in this confinement glycerol behaves mostly like molecules close to a surface [89]. Changes in finite-size geometries were found in only few other studies. One of them used *metal organic frameworks* (MOF) with pore sizes smaller than 2 nm as confinement material [232]. There, the glycerol dynamics are shifted with respect to the bulk behavior. Whether they are accelerated or decelerated strongly depends on the MOF itself. In a MFU-1 type MOF exhibiting pore diameters of 1.8 nm a cross-over temperature of $T_c = 225$ K was identified and attributed to the limited correlation length and $\xi(225\,\mathrm{K}) \approx 1.8$ nm was approximated. Qualitatively similar results have been obtained for salol confined to porous glass systems [80]. In smaller MOF pores (MFU-4) of size 1.2 nm no bulk like dynamics were observed at all [232], but an Arrhenius behavior was found as expected for molecules interacting with the wall only [11, 66, 89].

Summarizing the present findings, no finite-size effects can be identified investigating glycerol in MCM-41. This seems unreasonable compared to the results of Fischer et al. [232] who proposed a correlation length of $\xi(225\,\mathrm{K}) \approx 1.8$ nm. If the latter finding was true, the correlation length would grow by no more than 0.2 nm while the correlation times increase by over seven orders of magnitude. Still the results at hand leave the question unanswered whether ξ ranges only between 1.8 nm to 2.0 nm in the vicinity of the glass transition. Alternatively, the fragile-to-strong like transition attributed to the limited length scale [232] may rather a specific property of the investigated confinement. This may be because only a very limited amount of confinements leave the bulk properties unaltered such that the corresponding bulk dynamics can be observed. With regard to the very limited dynamical changes observed in the MCM-41 confinement it is unsatisfactory to assume that the influence of MCM-41 on glycerol is much more severe than the influences of a MOF. The latter exhibits charged ions which interact with the guest molecules. In addition strong structural changes with filling and with temperature have been observed in most MOFs [239]. Both effects may affect glycerol rather strongly.

Examples where glycerol is strongly affected by the presence of essentially rigid confinements are investigations of dynamics in protein matrices [240]: There, dynamics were strongly different from the bulk behavior. Possible explanations are the interaction of the molecules and the wall [66] or geometrical reasons as e.g. steric hindrance of the motions [241].
In comparison to water confined to MCM-41 glycerol in the same confinement exhibits only very minor modifications due to the geometrical restriction. Most prominent are the additional second process observed in the SLR of water, c.f. section 5.1 and the fact that the rotational correlation times of water are strongly altered by the confinement, while glycerol is only weakly influenced. Obviously, MCM-41 affects different supercooled liquids in a rather different way.

7 Spin-lattice relaxation at different magnetic fields

In chapter 3.5, it was introduced that the SLR stretching parameter β deviates from unity when the system undergoes a glass transition due to incomplete sampling of the configuration space. At the same time the T_1 times show a distinctive kink caused by secondary processes that start dominating the relaxation behavior. This was observed in the SLR experiments reported in sec. 5.1. Here, the dependence of SLR on the external magnetic field is investigated, to determine the onset of non-ergodicity at the temperature T_{ne} as a function of the magnetic field strength. This temperature can be used as a measure for the time scale of the structural relaxation, see sect. 3.5.
In the first part, glycerol-d_5 is investigate for two reason: First, the idea sketched above is tested for validity in a simple glass former. Glycerol is an appropriate system for this investigation, since it is well characterized, see chapter 6. Secondly, the method of FC NMR is a suitable tool for investigating the field dependence of SLR. The AG Vogel / Fujara possesses a state of the art fast field cycling spectrometer, which is routinely used to gain insight into dynamics of complex systems, e.g. polymers or lithium ion conductors. With glycerol the feasibility of ^{2}H FC NMR in the solid state is tested to extend the range of usability of this spectrometer. If possible, this method can be used to study the field dependence of the onset of non-ergodicity close to the glass transition in a much larger field range.
In the second part the SLR behavior of D_2O in MCM-41 is measured at different fields. It is not possible to measure the D_2O confined to MCM-41 in the FC NMR in the solid state, due to phase instability and the weak signal. Therefore, in this investigations the superconducting magnets Schering (46.7 MHz) and Berta (30.1 MHz and 10.7 MHz) are utilized, c.f. section 4.1. Note, that the Larmor frequencies are referenced in units the frequency $\nu = \omega/(2\pi)$ in the text.

7.1 Field cycling on supercooled glycerol

7.1.1 Temperature dependence of the SLR

The SLR of glycerol has been measured in the 'FC-1' field cycling spectrometer using the SE sequence. Due to phase instability only eight accumulations have

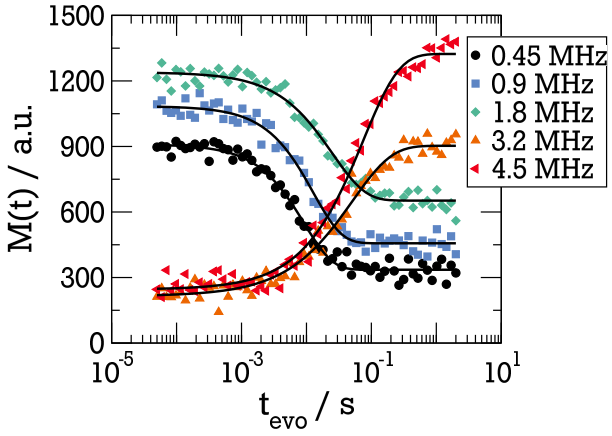

Figure 7.1.: Saturation recovery curves measured on glycerol in FC-1 at 205 K. Solid lines are best fits using a single KWW.

been performed per time step t_{evo}, while the number of steps has been increased for better statistics. Figure 7.1 shows some exemplary SLR curves at T = 205 K for different fields. Note the switching between not polarized and pre-polarized measurements at a field strength of 3.2 MHz, which causes the change from an exponential growth to an exponential decay.
The results from fitting a KWW function to the data are plotted in figure 7.2. In panel (a) the temperature dependent SLR times T_1 are reported for various Larmor frequencies, in (b) the corresponding stretching parameter β is shown for selected fields. The figure includes data measured in the superconducting setups at 46.1 MHz, 30.1 MHz and 10.7 MHz. It is evident from panel (a), that the relaxation times decrease for decreasing field strength B_0 and thus ω_0. Blochowicz et al. [188] showed that SLR data at 55 MHz can well be reproduced using the imaginary part of the dielectric susceptibility. In terms of the normalized dielectric susceptibility the DS spectra can be written as

$$\chi''(\omega) = \frac{\left(1 + \iota \frac{\omega\tau}{c_0}\right)^{\gamma-\epsilon}}{(1+\iota\omega\tau)^{\gamma}}. \tag{7.1}$$

This form comprises of an CD peak with stretching parameter γ and a power-law with exponent ϵ which dominates at frequencies higher than the CD peak frequency. Using eq. (7.1) and the fit parameters reported in [188] the temperature dependence of T_1 was calculated. In the calculation correlation times reported in [182] were used and additionally, it was assumed that $\gamma_{NMR} = 0.85\gamma_{DS}$ to account for the fact that NMR usually finds smaller stretching parameters describing the spectral density [188]. The results of the calculation are reported in the figure.
At high fields the calculated curves well agree with the measured data down to temperatures below T = 200 K. The good agreement is somewhat surprising,

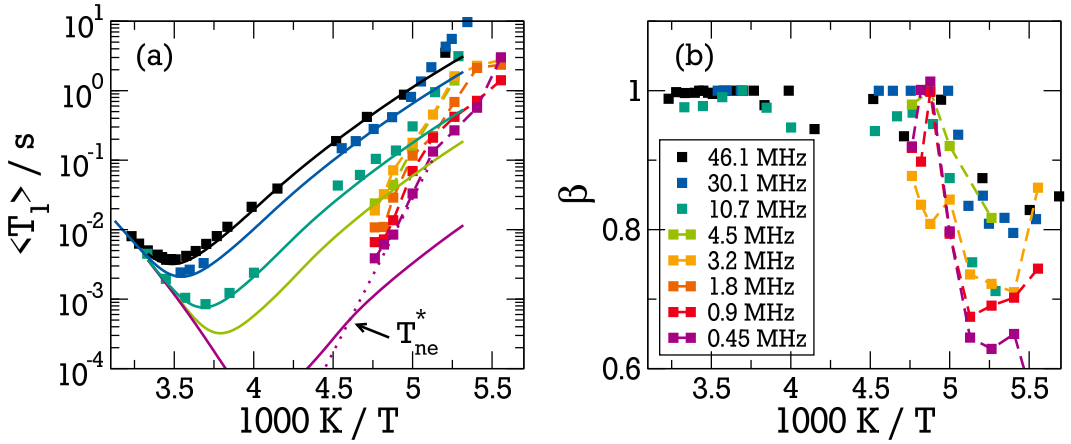

Figure 7.2.: Dependence of the SLR parameters on temperature. In (a) the fitted SLR time constant T_1. Solid lines are calculated T_1 for 46.1 MHz (black), 10.7 MHz (turquoise), 4.5 MHz (green) and 0.45 MHz (purple), see text. The dotted purple line is an interpolation to the data to estimate the interception with calculations. In (b) the corresponding stretching parameter β for selected fields. Fields are indicated by the legend in (b). Dashed lines are guides for the eye.

since Gainaru et al. found a deviation of the power-law behavior in NMR and DS using ^{1}H FC NMR [242]. For frequencies $\omega\tau \gg 1$, i.e. in the excess-wing regime the intensity of the NMR susceptibility is a factor three larger than the dielectric counterpart [242, 243]

$$\chi''_{\mathrm{NMR}}(\omega) = 3\chi''_{\mathrm{DS}}(\omega) \qquad \text{if} \quad \omega\tau \gg 1 \tag{7.2}$$

The expected higher intensity in $\chi''_{\mathrm{NMR}}(\omega)$ would cause shorter T_1 times at low temperatures. This is not observed and therefore this factor 3 is omitted. At low field strength the calculated temperature behavior deviates strongly from the measured one. This behavior cannot be explained by the anticipated difference in the susceptibilities.

The SLR stretching parameter deviates from unity $\beta < 1$ for most of the measured temperatures and frequencies, seen panel (b). This decrease of β signals the onset of non-ergodictiy, which is supposed to be determined in this section. The data show lower values of β for lower magnetic fields. Additionally, the decrease of β seems to shift slightly to higher temperatures as the external field is reduced. It may be possible to determine the onset of the deviations in β from the measurements at high fields, the data quality from *FC-1* is not good enough to determine the parameter β precisely enough to estimated T_{ne}. The main reasons for this are of technical nature: first, due to the phase fluctuations sufficient accumulation of signal was not possible, which leads to large errors

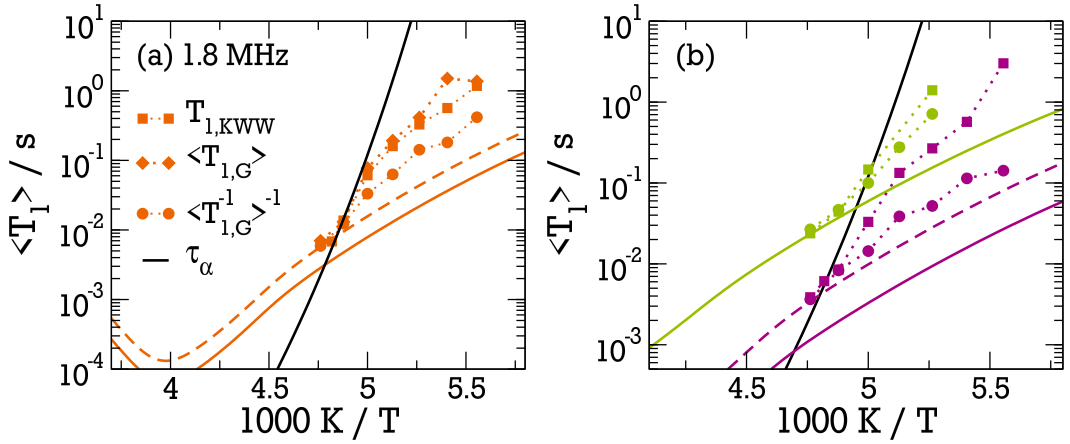

Figure 7.3.: (a) SLR time constants at 1.8 MHz: $\langle T_1 \rangle$ from fitting with eq. (5.1) (squares); $\langle T_1 \rangle$ (diamonds) and $\langle R \rangle^{-1}$ (circles) determined from fitting a logarithmic Gaussian distribution, see text. Expectation from the SD in [188] (solid orange) the dashed line is shifted by a factor of two. Black: τ_α correlation times from [182]. (b) Similar plot to (a) for 4.5 MHz (green) and 0.45 MHz (purple). The dashed purple line is the solid purple line shifted by a factor of three.

in the determination of β. Second, the main coil in the system is prone to thermal expansion that slightly alters the field. In section 4.1 this was shown to influence the detected signal in SE experiments significantly. Especially when T_1 is long, this adds artificial stretching to the measured data due to the applied evolution field B_{evo}. The effect also plays a role when polarizing the sample: for longer T_1 times, the current necessary to create B_{pol} also heats the coil and alters the signal. The polarization time can be reduced to prevent heating of the coil. However, in case of $\beta < 1$, a non-averaged distribution of relaxation times $V[T_1]$ exists and is cut for too short t_{pol}. This again decreases β artificially. Thus, without an active field stabilization the parameter β cannot be determined reliably in ^{2}H solid state FC NMR.

In a further attempt to determine T_{ne} we can return to the $\langle T_1 \rangle$ time constants. In figure 7.3 (a) the SLR data for 1.8 MHz are shown together with the calculated T_1 and the correlation times of the α-process of glycerol. The latter are determined by DS [182]. To explain the strong and unexpected increase in the relaxation times it has to be taken into account that fitting a KWW function to the magnetization decay, determines the $\langle T_1 \rangle$ rather than the mean rate $\langle R \rangle^{-1} = \langle T_1^{-1} \rangle^{-1}$. When a distribution of relaxation times $V[T_1]$ exists both mean values start to deviate from each other [244]. This results in an increase of $\langle T_1 \rangle$ compared to $\langle R \rangle^{-1}$. Usually the mean rate is determined by fitting the initial slope of the relaxation curves. In the present case of ^{2}H FC NMR, this is not feasible due to the data quality. Therefore, another approach is used

to approximate $\langle R\rangle^{-1}$. The magnetization data are fitted using a logarithmic Gaussian distribution:

$$\phi(t_{evo}) = \int_0^\infty V(T_1) \exp\left(-\frac{t_{evo}}{T_1}\right) dT_1 \tag{7.3}$$

where ϕ is the magnetization decay $\phi(t_{evo}) = M(t_{evo})/M_\infty$ in case of pre-polarized measurements and $\phi(t_{evo}) = 1 - M(t_{evo})/M_\infty$ otherwise. The distribution $V(T_1)$ is

$$V(T_1) = \frac{1}{\sqrt{2\pi}\ln(10)T_1\sigma} \exp\left(-\frac{\left[\log(T_1) - \log(t_0)\right]^2}{2\sigma^2}\right) \tag{7.4}$$

Here, the additional factors $\left[T_1 \ln(10)\right]^{-1}$ normalize eq. (7.3). Using the resulting width σ and the center of distribution t_0, values of $\langle T_1\rangle$ and $\langle R\rangle^{-1}$ can be calculated. Both are shown in figure 7.3 (a). The calculated mean relaxation times agree with those obtained from a KWW fit, while the $\langle R\rangle^{-1}$ deviate for low temperatures. Panel (b) shows similar plots for the external fields corresponding to 4.5 MHz and 0.45 MHz Larmor frequency. The figure reveals that the deviation of $\langle T_1\rangle$ and $\langle R\rangle^{-1}$ in all fields sets in when the structural relaxation time τ_α come close to the expected SLR times. The temperature where this happens will be called T^*_{ne}.
In addition, it becomes evident from the figure that the interception of the correlation times τ_α with the measured SLR times agrees with the calculated ones for 4.5 MHz, but not for 1.8 MHz and 0.45 MHz. In the latter two cases, the expected SLR times have been shifted by a factor of 2 and 3, respectively. This shift can be rationalized by the expected difference in the susceptibilities, see eq. (7.2). Since the crossing $\langle T_1\rangle = \langle R\rangle^{-1}$ to $\langle T_1\rangle > \langle R\rangle^{-1}$ happens as soon the distribution $V\left[T_1\right]$ becomes observable. The values of $T_1(T^*_{ne})$ can be used to approximate the structural correlation time τ_α as

$$\tau_\alpha \approx T_1(T^*_{ne}),$$

as can be seen from figure 7.3. This enables to observe the temperature dependence of the α-process. The method should be applicable to other systems, even though it would be more reliable to determine the deviation of β. This is, because the latter way does not relay on the knowledge of the spectral density. Both methods require careful measurements of the SLR times in different magnetic fields. This is up to now not possible with the available FC spectrometer for ^{2}H NMR in the solid state. Further technical development is necessary.

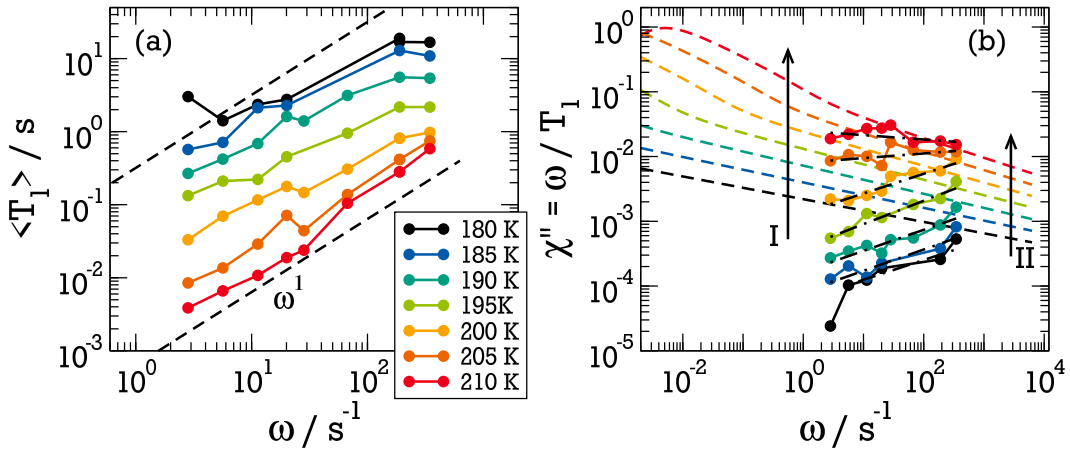

Figure 7.4.: Dependence on the external magnetic field: (a) the spin-lattice relaxation time T_1. Data at 55 MHz have been taken from [211]. Black dashed lines indicate ω^1. (b) Susceptibilities $\chi \propto \omega\langle T_1\rangle^{-1}$ calculated using the arithmetic mean $\langle T_1\rangle$, shifted vertically by a constant factor for all temperatures, see text. Dashed lines are the susceptibilities calculated after Blochwicz et al. [188]. The dash-dotted lines are fits using eq. (7.5). The arrows I and II mark cuts at equal frequency, see text.

7.1.2 Frequency dependence of glycerol SLR

The determination of $T_1(T^*_{ne})$ from the field cycling data above assumes, that the deviations from the calculated $\langle T_1\rangle$ is due to broken ergodicity in the system. Here, the data are analyzed in more detail to test the validity of this assumption. In figure 7.4 (a) the arithmetic mean $\langle T_1\rangle$ is presented as a function of the Larmor frequency ω. The dashed black lines indicate a frequency dependence of ω^κ, where $\kappa = 1$. Note that high field data from superconducting magnets have been included. Data at 55 MHz are taken from ref. [172]. The figure already indicates a power-law like behavior at all temperatures.

Panel (b) depicts the same data in the susceptibility representation $\chi = \omega/T_1$. They are shifted by a constant factor for all temperatures, such that the data at 210 K roughly agree with the susceptibilities expected from the dielectric measurements in reference [188]. It is evident from the figure that all data have been measured in a range of temperature and frequency where the excess wing rather than the α-process dominates the relaxation behavior. The data show a power-law behavior, that do not match the dielectric susceptibilities. This mismatch cannot be explained with the difference of DS and NMR, since it is expected to be the other way round, compare with eq. (7.2). In addition, The different slope of the data cannot be explained by the difference in measurement methods. To describe the data, a power-law of the from

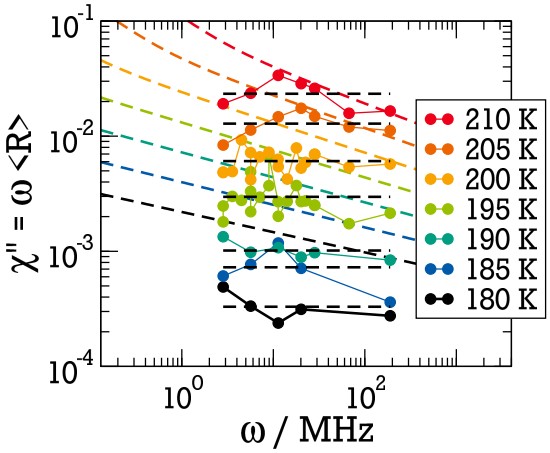

Figure 7.5.: Susceptibilities $\chi \propto \omega\langle R\rangle$ calculated using the harmonic mean time $\langle R\rangle^{-1}$, shifted vertically by a constant factor for all temperatures. Dashed colored lines are the susceptibilities calculated after Blochwicz et al. [188]. The dashed black lines are fits using eq. (7.5) with $\kappa \equiv 0$.

$$\chi''(\omega, T) = C_\chi(T)\omega^{-\kappa} \tag{7.5}$$

can be used. The data interpolations are depicted in figure 7.4 (b). A similar analysis carried out for the harmonic mean values $\langle R\rangle^{-1}$ as well, shown in figure 7.5. Again the data are interpolated using eq. (7.5). In addition, a second fit using a constant height was performed, i.e. by setting $\kappa \equiv 0$ in eq. (7.5). Only the latter interpolation is depicted in figure 7.5.
Comparing the $\langle T_1\rangle$ and $\langle R\rangle^{-1}$ data it is obvious that the harmonic mean fits the dielectric susceptibilities better than the arithmetic mean SLR times. However, there is still a height mismatch for the lower temperatures. The mismatch possibly is an artifact due to the technical problems encountered in the measurements, as described in the previous section.
The resulting fit parameters of all fits using eq. (7.5) are displayed in figure 7.6. The temperature normalized proportionality factor C_χ/T is shown in panel (a) the exponent κ in panel (b). The Curie corrected proportionality constant $C_\chi(T)/T$ increases exponential with temperature, but exhibits qualitatively different behavior for the arithmetic and compared to the harmonic SLR times. In the first case, a transition in the temperature behavior can be observed close to the glass transition temperature $T_g = 188\,K$. There, the temperature dependence decreases upon cooling. Exponential fits proportional to $\exp(T/T_C)$ resulted in temperature coefficients T_c of $T_C(T > T_g) = 4.6\,K$ and $T_C(T < T_g) = 10.3\,K$ below and above the bulk glass transition. In contrast, the data obtained fitting the frequency dependence of the harmonic mean SLR times results in a constant slope of the $C_\chi(T)/T$. The values for the two fits κ free and $\kappa = 0$ agree

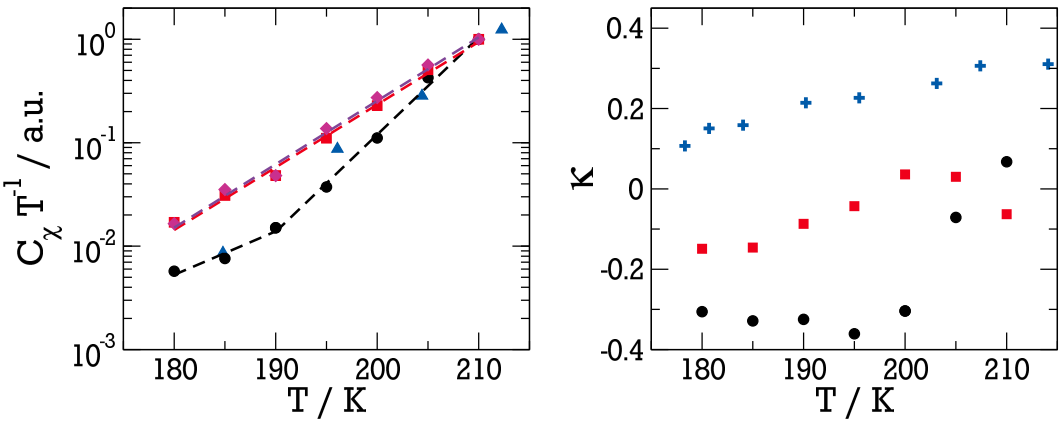

Figure 7.6.: Fit parameters obtained fitting eq. 7.5: (a) Normalized proportionality factor $C_\chi(T)$ fitted to the arithmetic mean SLR values (black circles) and to the harmonic mean (red squares (κ free) and pink diamonds ($\kappa = 0$)). Literature data from ref. [182] in blue. All data are shifted to agree at 210 K. (b) The exponent κ, symbols as in (a). Pluses are data taken from [188].

very well. Both data sets exhibit $T_C = 7.1$ K. The figure also shows values of the renormalization constant C_{DS} (blue triangles) obtained by fitting a power-law to dielectric relaxation data [182]. All data are normalized to 210 K. Gainaru et al. investigated glycerol by ^{1}H FC NMR and DS [242]. They observed a transition in the height of χ'' at a fixed frequency similar to the one observed in the analysis of the $\langle T_1 \rangle$ data. The temperature at which the kink occurs shifted with frequency and was observed at lower temperature the lower the investigated frequency. This feature can be understood revisiting figure 7.4 (b). There, the two arrows I and II mark equal frequencies. At the frequency I the susceptibilities at 180 K and 185 K are parallel to each other, while the other temperatures are already affected by the high frequency flank of the CD peak. Here, a distinct kink in $C_{\chi,\omega_I}(T)$ is expected in the temperature range from 180 K to 210 K. At frequency II all depicted susceptibilities are still parallel and thus, a transition in $C_{\chi,\omega_{II}}(T)$ is expected only at higher temperatures. Thus, by observing χ'' at different frequencies it is possible do determine the temperature where the excess-wing dominates the SLR. In the present ^{2}H NMR investigation $C_\chi(T)$ is determined frequency averaged, thus no distinctive crossing is expected to show up. The observed transition in the arithmetic data thus, seems to be an artifact of data evaluation. In [242] a value of $T_C = 33$ K was found below the glass transition, corresponding to much smaller slopes of $C_\chi(T)$ in figure 7.6 (a). In contrast, the data taken from [182] rather well agree with the present data. It is an open question why this discrepancy arises. An answer may be found by more precise measurements of the harmonic SLR times $\langle R \rangle^{-1}$.

The behavior of the exponent κ does not agree with literature, as can be seen in figure 7.6 (b). There, exponents taken from [188] are compared with the

fit results of the present data. The here measured exponent shows a negative sign at most temperatures, in correspondence to the slopes observed in figures 7.4 and 7.5. The DS data [188] in contrast show a positive sign. In the shown temperature range κ decreases from $\gamma \approx 0.3$ at 210 K linearly to $\gamma = 0.07$ at lower temperatures. The figure reveals that using the harmonic mean SLR $\langle R \rangle^{-1}$ the found exponents are close to $\kappa \approx 0$.

A similar behavior with constant susceptibility $\chi(\omega) \approx$ const. was observed in DS and FC NMR experiments on other glass formers, e.g. in ^{7}Li experiments on a solid state electrolyte, see in [245]. This behavior is called *nearly constant loss* (NCL) [246]. Even though the effect is quite common in glass forming systems, it is not yet understood. In [245] the ^{7}Li FC NMR measurements were governed by the NCL phenomenon, while in contrast the STE NMR method measured the ionic motion. Therefore, it seems possible that the unexpected behavior found in the present ^{2}H FC investigation is also governed by the NCL.

Other possible explanations involve the validity of the relaxation theory used in the data analysis. For example it is unclear whether the high-field assumption holds in the field cycling experiments, where the Larmor frequency ω_0 is at maximum one order of magnitude larger than the coupling constant $\delta = 124$ kHz. A possible explanation of the findings may be the break-down of assumed weak-collision limit, see in [155] for a detailed discussion. A hint in this direction may be given in figure 7.4 (b), where it becomes clear that the best correspondence between NMR and DS is achieved at highest field, i.e. 55 MHz.

In summary it can be concluded that the ^{2}H solid state FC measurements performed at the *FC-1* spectrometer do not fit the expectations from DS [188]. While the amplitude of the susceptibilities seem to fit DS experiments, the frequency dependence does not met the expectations. Nevertheless, it is very interesting to note that the interpolated temperatures T_{ne}^* where the SLR deviates from the literature data and the corresponding $\langle T_1 \rangle$ values approximate the structural relaxation rather well, i.e. $\langle T_1(T_{ne}^*) \rangle \approx \tau_\alpha$, see in figure 7.3. This suggest that the breakdown of ergodicity is not only connected to a decrease in the SLR β parameter but also to the onset of deviation of arithmetic and harmonic mean. Further technical developments are necessary to enable more precise measurements. Additional investigations of this topic can help to determine which quantities, β or $\langle T_1 \rangle$ and $\langle R \rangle^{-1}$, are a more reliable measure of the onset of ergodicity. Even though the measurements performed in this work can not conclusively decide whether it is possible to determine the correlation time of the α-process by measuring the field dependence of the non-ergodicity, the idea seems very promising. Additional theoretical consideration are required to exclude the possibility of other reasons for the observed effects.

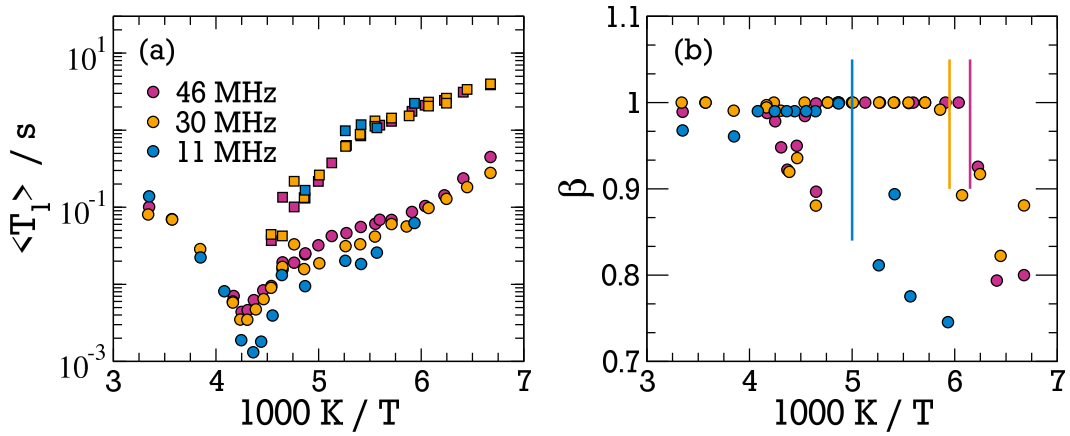

Figure 7.7.: (a) Spin-lattice relaxation time T_1 at different magnetic fields for samples P27 (Sigma). (b) Corresponding stretching parameter β. Vertical lines mark rough estimates of T_{ne}.

7.2 Field dependence of confined D_2O

In the previous section, the behavior of SLR in the neat glass former glycerol has been discussed. Here, the behavior of SLR of D_2O confined to MCM-41 is investigated depending on the external magnetic field. Due to the technical peculiarities encountered in ^2H FC NMR in the solid state of glycerol, this technique is not applied in this part of the study. Here, a MCM-41 sample obtained from Sigma-Aldrich with pore diameter d = 2.7 nm is used. As in chapter 5 the SLR is measured using the SE sequence. The resulting time constants $\langle T_1 \rangle$ and stretching parameters β are shown in figure 7.7 (a) and (b). At 46.7 MHz measured in 'Schering' the relaxation times are very similar to those found in P28, see section 5.1. Additionally, the sample was measured in the 'Berta' spectrometer at 30.1 MHz and 10.7 MHz. On decreasing the external field the high temperature flank of the $\langle T_1 \rangle$ data exhibits the same slope and therefore all, three measurements agree. As expected, the minima in relaxation times shift to lower values and lower temperatures with lower magnetic fields, c.f. table 7.1.

At temperatures below ca. 220 K, the two relaxations (f) and (s) are observable. As expected, the $T_{1,f}$ time decreases with decreasing field strength. Below ca. 165 K all (f) relaxations again exhibit a very similar behavior. The weak field dependence of $\langle T_{1,f} \rangle$ in this low temperature region possibly is due to a very weak power-law dependence of the spectral density below the glass transition [188]. This indicates that the glass transition temperature is above ca. 165 K.

Surprisingly, the (s) relaxation component is independent from the field strength B_0. This is an unexpected feature for a slow motional process. It suggest that the (s) relaxation is not due to rotational dynamics but to sec-

ondary effects. First, this may be paramagnetic relaxation, even so no obvious source of paramagnetic centers is present in the synthesis of MCM-41. A second explanation is the influence of spin diffusion caused by dipolar coupling. In this case magnetization would be transferred from the faster relaxing species (f) to the solid like species (s). Usually, it is argued that spin diffusion can be neglected in ^{2}H NMR of amorphous systems [173]. A possible third explanation was introduced in section 5.4: if the (s) relaxation is a measure for the live time of the crystallization nuclei forming in the pore centers, it may be independent of the magnetic field as well. A deeper investigation of the absent field dependence of the (s) component is out of scope of this work. Nevertheless, it deserves more attention in subsequent work on water in MCM-41 confinement.
Panel (b) of figure 7.7 shows the stretching parameter β obtained from fitting the magnetization curves. Due to the weak signal, the values of β at the 11 MHz exhibit a large error. The approximated values for the temperature where $\beta < 1$, i.e. the temperature T_{ne}, have been determined and listed in table 7.1. T_{ne} decreases with lower field strength. The approximated correlation times $\tau_\alpha \approx T_1(T_{ne})$ are only weakly dependent on the external field. It is interesting to note, that in contrast to the samples discussed in sec. 5.1 the P27 sample exhibits $T_{ne} \approx 165\,K$ rather than 185 K at 46 MHz. ^{1}H SLR measurements with MCM-41 from the same batch showed some unexplained signal contributions [219]. Possibly, this sample is contaminated with residues from the synthesis.
In figure 7.8, the field dependent correlation times τ_m are shown. The approximated τ_α times are included in figure as well. The correlation times determined by the CC SD below ca. 230 K show a strong behavior that can be extrapolated by the dashed lines. With respect to the large errors, the τ_α times roughly agree with these extrapolated trends. The temperature dependence of the obtained times $T_1(T_{ne})$ is weak and does not extrapolate to the correlation times obtained at high temperatures by SLR experiments. An Arrhenius law with $E_a = 0.19\,eV$ can be used describe the data. If this was the α-process, the glass transition were at $T_g = 110\,K$. The data obtained this way cannot be interpreted in terms of our proposed model, see figure 5.18.
Several reasons may prevent from determining the α-process: First, the determination of a reliable stretching parameter β requires great care. The data quality is not good enough to detect the desired effect in a reliable manner.

Table 7.1.: Parameters obtained from the field dependence of SLR in sample P27. α is the CC stretching parameter.

ω_0 / MHz	$T(T_{1,min})$ / K	$T_{1,min}$ / ms	α	T_{ne} / K	$T_1(T_{ne})$ / ms
46.14	233.8 ± 0.3	4.3 ± 0.1	0.41	163 ± 3	130 ± 20
30.12	233.1 ± 0.2	3.3 ± 0.1	0.35	168 ± 3	75 ± 18
10.69	230.3 ± 0.6	1.3 ± 0.2	0.32	196 ± 8	14 ± 5

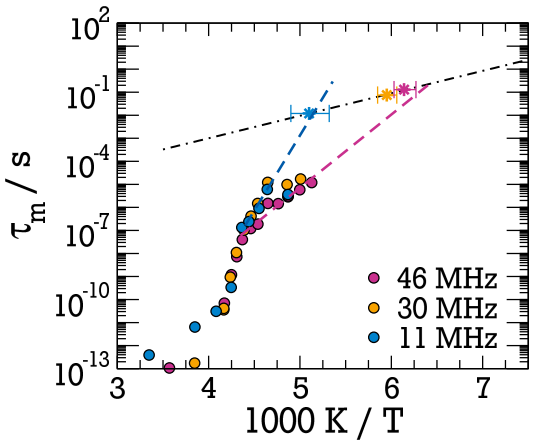

Figure 7.8.: Correlation times obtained from SLR in P27 at different external fields. Stars give the position of T_{ne} and the corresponding $T_1(T_{ne})$. The CC spectral density was used in the calculations. The dashed black line is an Arrhenius fit to stars, dashed colored lines are guide for the eyes.

Second, it may be possible that the kinking in β is influenced or completely dominated by secondary relaxation or e.g. the presence of a solid like core in the pore center. In this case, T_{ne} may not be a good approximation for τ_α. Third, side effects as e.g. paramagentic relaxations or contamination of unwanted molecules may interfere and render the determination of τ_α via T_{ne} not feasible. Especially, the last explanation is very likely, since the performed ^{1}H measurements have revealed unexplained signal contributions in this batch of MCM-41. This makes it necessary to repeat the present results with a different MCM-41 sample.

Additionally, the FC studies on glycerol have shown the possibility to obtain the time scale of the α-process by measuring the onset of deviations between the arithmetic and the harmonic mean. In fixed field magnets it is possible to obtain relaxation data in a quality enabling to determine the relaxation rate $\langle R\rangle^{-1}$ directly. This was not possible with the data measured here and therefore, should be tested in further investigations.

7.3 Summary

In this chapter the behavior of ^{2}H NMR SLR was investigated in several magnetic fields. The feasibility of FC measurements in the solid state has been shown. These measurements using neat glycerol have also shown that several quantities that are detectable in ^{2}H NMR, can be used to detect the onset of non-ergodicity in glass forming systems. This enables a new method to measure the temperature dependence of the structural relaxation. The method re-

quires great experimental care and therefore is only useful in systems where the α-process is not accessible by standard NMR or DS methods.
The discussion in literature [123] shows that one of those systems where the structural α-process may be very weak or inaccessible to usual methods is water in severe geometrical confinement. Therefore, a MCM-41 one sample was measured in three different fields. The results have shown a temperature dependence that seems nonphysical in every proposed model of confined water. Reasons for this may be the large errors and likely impurities of the used sample. Nevertheless, the measurements are promising. Further methodical development seems advisable.

8 Dynamics of aqueous mixtures

A common approach to study the dynamics of water in the supercooled range is to mix it with different guest molecules. Varying the amount of the additional solute and extrapolating the concentration dependence, can give insight into the dynamics of bulk water. The properties of water, as well as of water mixtures, are strongly affected by the network of H-bonds. To study the influence of the H-bonding, a series of studies were performed in which various alcohols were mixed with water. Some alcohols have been regularly used in those studies, since their structure is very similar. Nevertheless, they show a rather different H-bonding behavior. By variation of the water concentration in the mixture, diverse effects have been observed, see sections 8.1 and 8.2 for more detailed discussions. These alcohols are propylene glycol (PG), propylene glycol monomethly ether (PGME), and glycerol (GLY). All three have been well characterized in bulk mixtures with water [11, 119, 124, 130, 134, 144–152]. In order to learn about the effects of confinement on H-bonded liquids, aqueous mixtures of these alcohols have been investigated in different confinements [86, 101, 129, 142, 143, 204, 247–253]. Those studies were performed to understand the complex balance of the different effects of confinement on the enclosed liquid, see also section 2.3.1. Many of the investigations focused on two slow processes which were found in confining geometries and attributed to a liquid surface-layer and polarization effects [80, 254].

In this chapter, mixtures of water with PG, PGME and its dimer (DiPGME) are confined to MCM-41 of d = 2.8 nm diameter. They are investigated in a large temperature range by means of ^{2}H NMR. Here, it is focused on the dynamics of the structural relaxation and the faster w-relaxation of water and their behavior in confined geometries. MCM-41 is used as confinement due to its rather smooth and defined surface. It provides narrow confinement sizes which allow for a study of the geometrical confinement effects. The results of the confined mixtures are compared to those of the bulk liquids in order to extract information about the influence of the confinement on those two types of binary mixtures. Section 8.1 starts by discussing the effects on the PG-water mixture, thereafter, the results obtained from PGME and DiPGME mixtures are presented in section 8.2.

8.1 Dynamics of confined PG-water mixtures

In the bulk state, PG can form H-bonded chains of molecules which, due to their large size, exhibit a rather slow relaxation. Upon adding water, the chains are broken into smaller units which relax faster [130]. This results in a constantly decreasing glass transition temperature with increasing water content. In addition, a secondary process is found, the w-process, which is to a large extent dominated by the local water relaxation [11, 130]. Like the structural relaxation, the w-relaxation is accelerated with increasing amount of unfrozen water. At a concentration slightly above a mass ratio of water $c_w = 60\,\%$ (W60) the water in the mixture crystallizes [130]. A very similar behavior was found in a study of the same mixtures below the freezing concentration W60 confined to Na-vermiculite clay exhibiting an interlayer spacing smaller than 0.65 nm [86]. The confinement has shown to have basically no effects on the structural relaxation of the mixtures. Only the w-relaxation was found to be somewhat decelerated, due to the interactions with the sodium ions incorporated in the material. The small overall influence of the confinement was explained by the nearly two-dimensional character of the material. The latter was proposed to leave enough room for the H-bond network to form properly and adapt to the topology [86].

In the one-dimensional confinement provided by MCM-41, much more severe effects were observed for a pore size of $d = 2.1$ nm [143]. Rather than an acceleration of the α-process with increasing water content, the structural relaxation was found to be equal to that of pure PG for all concentrations of water c_w. The w-process in those systems was determined to be very close to that of pure water in the same MCM-41 pores. The findings imply a strong distortion of the H-bond network leading to demixing of the two liquids at all concentrations. Elamin et al. [143] proposed that the water preferentially coordinates to the surface of the confinement, while the alcohol clusters in the pore center. Interestingly, the w-relaxation was detected also in nominally pure PG (W0) samples. This was attributed to the secondary β process of PG. Demixing in confinement was predicted from MD studies of similar binary mixtures of ethanol and water [255]. In contrast to the interpretation of the experiments on PG-water mixtures, the simulations predict an increased alcohol density at the confinement wall.

In this work, the experimental results of PG-water mixtures confined to MCM-41 of larger size $d = 2.8$ nm are presented. In the larger pores investigated here, the ratio of surface to liquid volume is reduced to help to determine the effect of guest-host interaction on the enclosed liquid. Especially, the proposed demixing behavior can be investigated. The results will be discussed in context with results of the bulk liquid obtained in a recent study of Sauer et al. [124] and a dielectric study of PG mixtures in MCM-41 confinement of $d = 2.1$ nm [143].

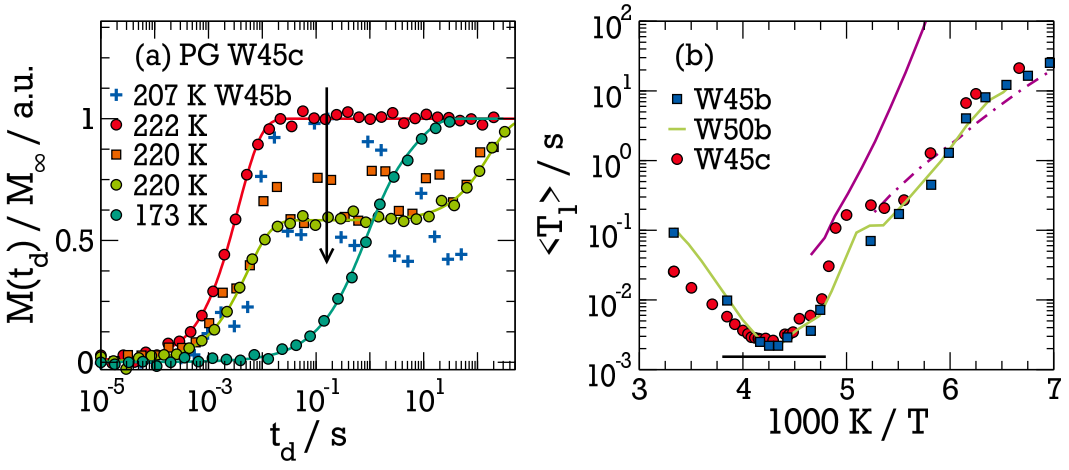

Figure 8.1.: (a) Magnetization recovery of PG W45c. The arrow indicates the crystallization process. Blue pluses are from PG W45b at 207 K [201]. (b) SLR relaxation times $\langle T_1 \rangle$ of samples W45b and W45c. The horizontal black line is the $\langle T_1 \rangle$ minimum of a Debye process. Pink lines are calculated T_1 values from the DS data [143]: solid and dash-dotted lines result from α- and w-relaxation, respectively, see text.

The presented experiments were carried out by P. Wendel in his bachelor's thesis [202].

8.1.1 Spin-lattice relaxation of PG mixtures

The SLR measurements on the mixture of deuterated water and PG have been performed using the SR experiment, see section 3.4. The bulk and confined sample will be abbreviated by their water mass ratio and an appended b or c as W45b and W45c, respectively. Some resulting magnetization recovery curves of the confined PG sample are shown in figure 8.1 (a). An interesting behavior is observed: above $T = 222\,K$ the relaxation is exponential and monomodal. Below this temperature, the recovery curve at $T = 220\,K$ shows a different behavior: It is measured in the staggered range mode where two out of four delays are skipped in a first run and measured in a second run. The figure reveals that in the first run, the signal saturates at some plateau at intermediate delays $t_d \approx 1\,s$ followed by a weak second step at long delays t_d. The absolute signal in the plateau is weaker than at $T = 222\,K$. In the second run the plateau is even lower while the second relaxation has grown larger in amplitude. During the measurement, magnetization is lost from the fast relaxing species (f) and transferred to a slowly relaxing species (i). This is evidence for a very slow

Table 8.1.: SLR parameters obtained from the fits: the minimal value of $\langle T_1 \rangle$ ($\langle T_1 \rangle_{min}$), the corresponding temperature (T_{min}), the stretching parameters for CC and CD SD (α; γ), the approximated temperature T_{ne}, and the SE signal minimum temperature (T_{SE}).

Sample	$\langle T_1 \rangle_{min}$ / ms	T_{min} / K	α	γ	T_{ne} / K	T_{SE} / K
PG W45b	2.14	234.0	0.76	0.48	182	200
PG W45c	2.48	234.5	0.68	0.37	210	207

crystallization. In the final state ca. 60 % of the signal is contributed by the crystalline component[1].

A similar phase transitions has been observed in the bulk liquid, as can be seen for example in the relaxation curve at T =207 K, which is also shown in figure 8.1 (a) [201]. A DSC measurement showing this effect is depicted in appendix B. The crystallization in the bulk is similar to that of the confined sample at 220 K. In both the bulk and the confined mixture, the transition takes place in a time span of several hours. This is rather slow compared to freezing processes observed in other mixtures. An example are the confined PGME-mixtures shown in section 8.2.1. There, crystallization happens fast so that it is not observable in any SLR measurement.

When it is assumed that only water freezes during the transient state and the alcohol itself does not crystallize [101], the residual mixture would consist of ca. c_w = 13 % (weight, W13) of water. This can be estimated from the signal drop at the crystallization temperature, see section 4.2.2. The concentration W13 corresponds to a molar ratio of 0.6 water to one PG molecule, c.f. table 4.4 for details. The idea of only water crystallizing is supported by an observations of Wendel [202]. Comparing the different isothermal relaxation curves during the slow crystallization, he observed a continuous increase of the relaxation time $\langle T_{1,f} \rangle$. This indicates a slow decrease of water concentration, since higher PG concentrations were found to exhibit slower dynamics [130]. The slow phase transition may explain why the effect was not observed in measurements utilizing DS [86, 124, 143]. There, cooling rates are usually fast and likely the demixing is quenched.

In the following the results of fitting the SR curves are shown. For simplicity only temperatures where no crystallization effect was observed during the measurement are regarded. Excluding the crystalline component, only one single relaxation is observed at all temperatures, even though in the mixture a signal ratio of 3:1 water to alcohol is expected due to deuteron exchange[2]. This indi-

[1] The amplitude at 0.6 s drops from ca 786 to 310 absolute units leaving over ca. 39 % signal.

[2] After the crystallization process is completed at 220 K a ratio of 1.2:1 is expected, when only water has crystallized.

cates that either an averaging process between the different molecules exists or a combined relaxation of both species, as was observed in the bulk [124].

The mean SLR times $\langle T_1 \rangle$ shown in figure 8.1 (b) over inverse temperature for samples W45b and W45c and additionally for a second bulk sample with slightly higher water content W50b [201]. First, it is concentrated on temperatures above 220 K. At those high temperatures, the two bulk samples exhibit identical dynamics and the confined sample shows somewhat shorter relaxation times. The values of T_1 in the minima of the bulk mixture are smaller compared to the confined liquid, indicating a broader distribution of correlation times $G\big[\log(\tau)\big]$ in the confinement. The obtained SLR parameters are listed in table 8.1. Similar broadening is found in other supercooled liquids in confinement, e.g. in confined glycerol, see chapter 6. The minimum temperatures T_{min} are similar in both samples, indicating that the absolute time scale of the dynamics hardly changes. This will also be shown in section 8.1.3.

The temperature dependence below 220 K exhibits more interesting features. The confined W45c sample shows a steep increase of the relaxation times from 210 K to 200 K followed by constant values of T_1 down to 185 K. A similar but slightly shifted behavior is found in the bulk W50b sample, while the W45b sample shows no such steep increase. The different temperature dependencies of W45b and W45c can be explained by the phase transition. Sample W45c as well as W50b were measured upon cooling, thus parts of the liquid have crystallized below 220 K. In contrast, sample W45b was quenched to lowest studied temperatures and measured upon heating and a different temperature behavior is observed, in the intermediate range from 185 K to 207 K. At the latter temperature, the slow phase transition is observed in W45b as well, but in the range where W45b and W45c differ strongly, the conducted ^{2}H NMR experiment measure samples, where alul molecules are in a liquid state or parts of water have crystallized.

The NMR relaxation times can be compared with the DS measurements in the smaller confinement d = 2.1 nm [143]. Using the correlation times reported in that publication and a CD spectral density with the stretching obtained from the T_1 minimum, see table 8.1, SLR time constants have been calculated, as shown in figure 8.1 (b). In the vicinity of 200 K the DS α-process agrees rather well with the ^{2}H NMR relaxation times of the confined system W45c in the partly frozen state. This comes as surprise since DS does not observe crystallization. At temperatures below 185 K, the ^{2}H NMR time constants $\langle T_1 \rangle$ of both samples, W45b and W45c, agree well with each other. Additionally, they are in good agreement with the DS results for the T_1 values calculated for the secondary process. In this range all methods, observe the w-relaxation which is similar in confinement and in bulk [86, 143].

The stretching parameter β obtained from the magnetization buildup of sample W45c shows a sharp decrease from unity to $\beta = 0.7 \pm 0.1$ at 210 K, caused by the presence of crystalline patches in the liquid. Thus, correlation times calculated from the SLR, see section 8.1.3, can be interpreted straightforward only down to 210 K. The deviation of β coincides with the steep increase of T_1 in W45c supporting that this is a feature of the partially crystalline system. A possible interpretation will be discussed in section 8.1.3.

The results presented in this section show a phase transition in PG W45 samples. The transition is observable in the bulk mixture and in the confined mixture. The confinement influences the SLR of the W45c sample only weakly. The only observable effect is a broadening of the distribution of correlation times $G\big[\log(\tau)\big]$ which is often found in confined liquids. In both cases, bulk and confined, the phase transition takes place on the time scale of hours. A similar transition process was also observed in a PPG-water W45 mixture measured by M. Schmitt in his bachelor's thesis [256]. There, it was shown that it can be circumvented by applying a temperature protocol where the sample is heated to room temperature and then quenched quickly to the desired temperature. Using this method a temperature dependence close to the bulk PG W45b sample was found[3] [256]. Further investigations of the slow crystallization are interesting and may involve quenching of the W45c sample, to measure upon heating. Note, that the DSC measurement in figure B shows melting of the cold crystallized W45b sample at $T_m = 240$ K. It is unclear whether this hysteresis occurs also in the confined sample.

8.1.2 Stimulated echoes of confined PG

The high temperature dynamics of the confined PG-water mixture W45c have been analyzed in the previous section by means of ^{2}H NMR SLR. Here, the low temperature dynamics are investigated using the STE method. As in the case of water confined to MCM-41, the experiments are carried out partially relaxed, to suppress the contributions of the crystalline species. The results will be compared with that for the bulk mixture, which was discussed in [124, 201]. There, it was found that the motion of PG molecules and water molecules are strongly coupled below the glass transition of the liquid. Since there is no sign of a bimodality in the STE decays, it was concluded that both molecular species contribute to the observed β-process.
The STE experiments have been carried out in the temperature range from 182 K to 163 K using the Zeeman experiment. In this temperature range, SLR detected very similar relaxation in bulk and confinement. The correla-

[3] The temperature dependence showed similar curvature, but was shifted by 13 K due to the less mobile PPG molecule.

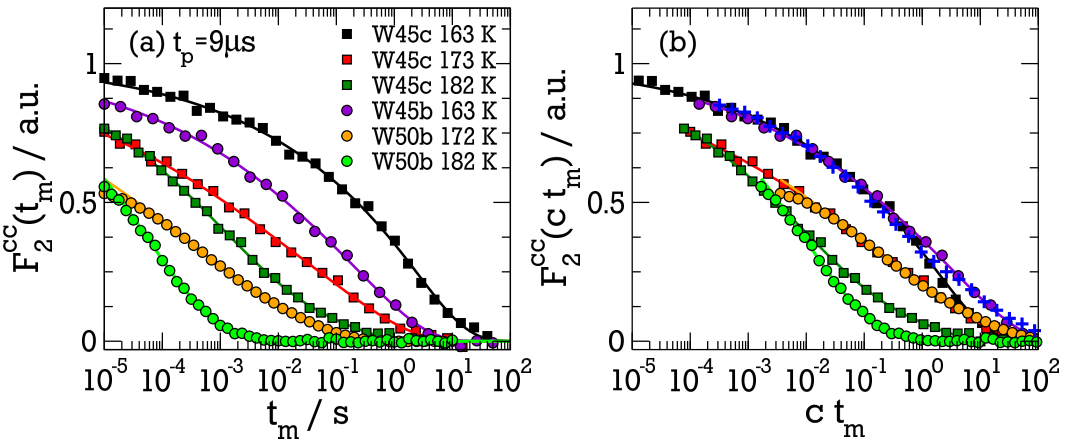

Figure 8.2.: (a) STE decays measured in sample W45c (squares) at different temperatures at evolution time t_p = 9μs. For comparison: correlation decays measured in bulk W45b and W50b (circles) samples taken from [201] (b) The same correlation decays as in (a). The bulk data have been shifted on the time axis by a temperature dependent factor c(T). Additionally, shifted STE decay of bulk water in MCM-41 P21 at 161 K (blue pluses).

tion curves $F_2^{cc}(t_m)$ measured by STE in sample PG W45c are shown in figure 8.2 (a). The figure additionally shows the corresponding measurements in the bulk liquid [124, 201]. Note, that in the bulk no difference between a W50b and a W45b mixture was observed. Therefore, data of W45b and W50b are shown in the figure for better temperature agreement. The figure reveals that the correlation decays slower in the confined liquid than the bulk at all temperatures. To compare the bulk and the confined samples, figure 8.2 (b) shows the bulk data shifted by a factor c(T) on the time axis such that they agree with the curves for W45c at the value $F_2^{cc}(t_m) = 1/e$. Values of the shift factor of c = 18.5, 32, 12 have been used at 182 K, 172 K, and 163 K, respectively. The STE decays at different temperatures are discussed individually in the following.

At the highest temperature 182 K, the STE decays in bulk and confinement differ somewhat in their long time behavior. The SLR times $\langle T_1 \rangle$ are equal in both samples, see in section 8.1.1. Nevertheless, the F_2^{cc} curve of the confined sample is considerably more stretched and shows a long time tail. Such a behavior is often connected to a symmetrically broadened distribution of correlation times [89]. MD simulation studies [83, 84] found a similar type of broadening in the vicinity of solid interfaces. Thus, this stretching is most likely due to the interface in the W45c sample. It is provided by the MCM-41 confinement on the one hand and by the formed ice crystals on the other hand.

To learn about the characteristics of the reorientational process, the evolution time dependence of the STE parameters can be taken into account. The fitted correlation times $\tau(t_p)$ are shown in figure 8.3 (a). There, it can be observed

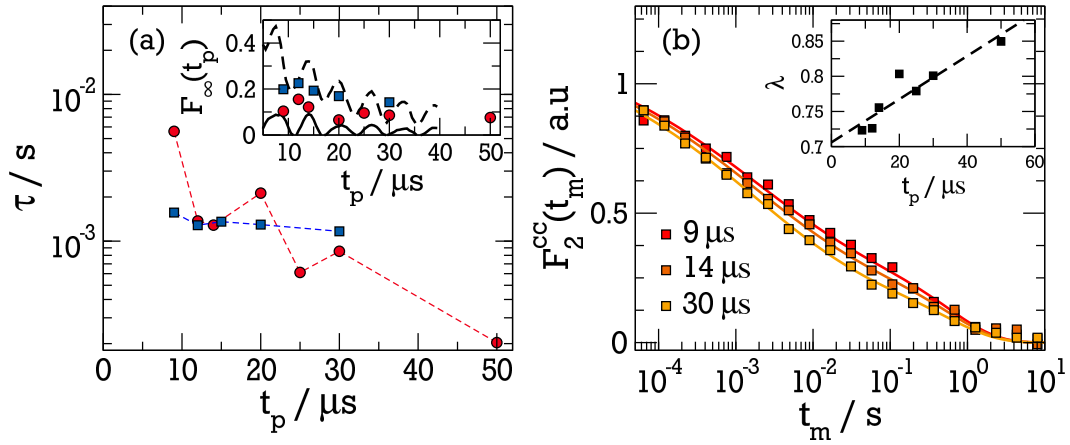

Figure 8.3.: (a) Fitted correlation time τ over evolution time t_p for 182 K (blue) and 173 K (red) in sample W45c. Inset: corresponding plateau value $F_\infty^{cc}(t_p)$. Lines represent RW simulation of a isotropic jump (solid) and of a distorted tetrahedral jump (dashed). (b) Fitted STE decays at 173 K fitted by using the WWA eq. (8.1). Inset: WWA coupling parameter λ over evolution time t_p.

that there is no strong dependence on t_p at 182 K. Thus, the molecules perform large angular reorientation as was found for pure water in confinement as well, see chapter 5. The figure also shows the residual correlation $F_\infty^{cc}(t_p)$ in the inset. It's evolution time dependence does not fit to an isotropic reorientation, but rather to some spatially restricted large angle jump, as can be observed by the comparison with a disordered tetrahedral jump. Note, that at this temperatures in STEs on pure water in alike MCM-41 a secondary relaxation process was observed, see section 5.3.

At intermediate temperature 173 K, the STE decay in the confined sample well agrees with the shifted bulk measurement. This data set was measured after the confined sample was stored at room temperature for several days and then quenched to 173 K. The data can be fitted using eq. (3.56), the corresponding results are shown in 8.3 (a). Here, a much stronger dependence of the correlation times on the evolution time t_p is observed. Using eq. (3.65) the decay in the correlation time is compatible with a reorientation by an angle of $\phi = 9°$ or less. The residual correlation $F_\infty^{cc}(t_p)$ shows a reduced anisotopy compared to the measurement at 182 K. Nevertheless, $F_\infty^{cc}(t_p \to \infty)$ levels at a finite plateau of about 8 % of the initial magnetization. This indicates that not all correlation is decayed due to this process. Assuming the leftover correlation decays by the α-process, the Williams-Watts ansatz (WWA) can be utilized to describe the data [30]. This approach assumes a combined relaxation of α-process F_α and secondary process F_w according to:

$$F_2(t_m) = F_\alpha(t_m)[(1-\lambda) + \lambda F_w(t_m)]\Psi(t_m) \tag{8.1}$$

Here, λ is the relative contribution of the secondary process and $\Psi(t_m)$ is the SLR relaxation as defined in eq. (3.57). The WWA has been utilized in [124] to describe the shape of the measured dielectric spectra of the bulk liquid. All measured evolution times t_p have been globally fitted with two stretched exponential relaxations. Figure 8.3 (b) shows the fitting results for three evolution times. It is obvious that the fit reproduces the data well resulting in mean logarithmic correlation times $\tau_{m,w} = 0.36\,\text{ms}$ and $\tau_{m,\alpha} = 1.6\,\text{s}$. The corresponding stretching parameters are $\beta_\alpha = 0.78$ and $\beta_w = 0.29$. The inset of figure 8.3 (b) shows the weighting parameter λ which increases with increasing evolution time. It ranges between 0.7 and 0.85, thus if the WWA is a valid description, the main part of the relaxation is due to the secondary process. In the bulk liquid $\lambda_{W45b}(173\,\text{K}) \approx 0.8$ was found in good agreement with the present results. The correlation times using the two approaches will be discussed in section 8.1.3.

At the lowest temperature 163 K, the shifted STE decays in bulk match those in the confinement. Only at very long t_m times deviations caused by the SLR are observable. In this temperature regime, the dynamics in W45c are slowed down by about one order of magnitude compared to those in the bulk, while the shape of the STE decay indicates similar motional mechanisms. This is consistent with the good agreement of the low temperature SLR times, c.f. section 8.1.1 and also with the DS experiments on PG mixtures in MCM-41 of 2.1 nm diameter [143]. Panel (b) of figure 8.2 also includes a STE curve measured in the pure D_2O sample P21 at T = 161 K scaled to the STE curves of PG W45. The STE decay of confined water agrees well with those measured in the mixtures. This observation suggests that the correlation functions in the low temperature region is dominated by the water motion in all samples, but the absolute timescale is dependent on the water content, see also [11]. The scaling factor used for the STE decay of the P21 sample is $c_{P21}(161\,\text{K}) = 32$. Compared to $c_{W45b}(163\,\text{K}) = 12$, this means that water w-relaxation at low temperatures is fastest in pure water confined to hard MCM-41, probably due to the larger amount of unfrozen water compared to the mixtures.

In this section the slower relaxation was called the α-process. Due to the unknown degree of crystallization it is not straightforward to interpret the process as the structural relaxation of the W45c mixture. The freezing depletes the water concentration in the mixture, thus the slow process is the structural relaxation of some mixture with unknown concentration in the confinement. It results from an anisotropic reorientation of large angular amplitude. The anisotropy is likely introduced by the inner surfaces. At lower temperatures besides the α-process the secondary w-relaxation can be observed which dominates the STE experiments at lowest temperatures. The w-process is slowed down compared to the bulk liquid as well. In the present study, it was not pos-

sible to obtain information about the mechanism of the α-process of the liquid without partial crystallization.

8.1.3 Discussion of the results

Using the BPP model eq. (3.33), the SLR times obtained in section 8.1.1 can be used to calculate rotational correlation times τ_m. In DS on a similar system of d = 2.1 nm pore size, the spectral density describing the α-process was found to be of the asymmetric HN shape [143], see eq. (2.14). Using the shape parameters reported there, it is not possible to reproduce the $\langle T_1 \rangle$ minimum found in the SLR. Since the stretching parameters in DS vary from those in NMR, it is not straightforward to use the HN SD as reported in DS. It was shown for pure liquids, that in the vicinity of the confinement the susceptibility $\chi(\omega) = \omega J(\omega)$ broadens symmetrically [84, 89]. Here, this fact is used to assume the value of γ to be constant and equal to the bulk value, i.e. $\gamma' = 0.48$. Variation of the parameter α results in a value of $\alpha' = 0.88$ in order to fit the SLR $\langle T_1 \rangle$ minimum. A second approach to estimate the HN SD is to use the dielectric stretching parameter γ_{DS}. Usually the NMR parameter is somewhat smaller, therefore according to [188] $\gamma'' = 0.85\gamma_{DS} = 0.74$ is used and by varying α to fit the SLR a value $\alpha'' = 0.75$ is found. The two parameter sets $J' = J_{HN}(\alpha', \gamma')$ and $J'' = J_{HN}(\alpha'', \gamma'')$ can be compared with the respective time constants obtained from the CD SD. The time constant in all three cases varies by less than a factor of two, even though the curvature is slightly altered. The errors introduced by using the CD spectral density are small. Therefore, the CD is used for simplicity, allowing for better comparison with the bulk ^{2}H NMR results. There the CD SD was used for data evaluation as well.

Figure 8.4 shows the correlation times τ_m obtained by the different ^{2}H NMR methods from the confined PG-water mixture W45c. Additionally, data for the bulk PG sample W45b are reproduced [124]. The bulk and the confined sample exhibit equal temperature dependence in the high temperature regime. Thus, the small differences in $\langle T_1 \rangle$ can be attributed to the altered distribution $G\big[\log(\tau)\big]$. The correlation times in the low temperature range, obtained by STE experiments, show a slowdown of the w-process in confinement, when the results of the single KWW evaluation are considered, see in figure 8.4. In contrast, the WWA at 173 K indicates a different behavior. If this evaluation is true, the w-process is not slowed down, but an additional contribution of the α-process is observed.

In direct comparison to the data obtained by DS in the d = 2.1 nm MCM-41 [143], the high temperature data in the present confinement are nearly two orders of magnitude faster. This indicates that a demixing as used to explain the observed relaxation in the smaller confinement does not occur in the larger pores used in the present study. Rather than this, a temperature dependent

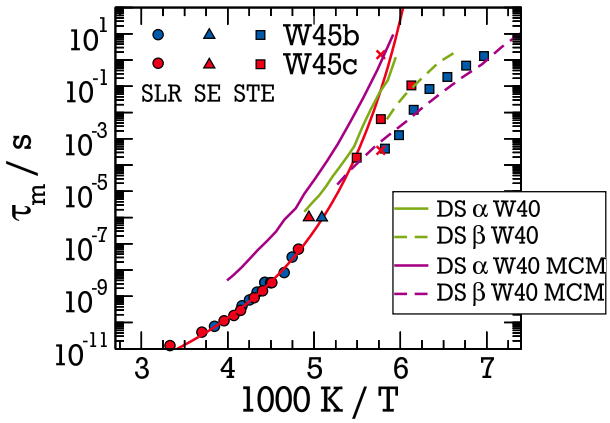

Figure 8.4.: Mean logarithmic correlation times τ_m of the PG-D_2O mixtures in W45b and W45c obtained from the different ^{2}H NMR methods. Red pluses are obtained by the WWA. Dielectric data (DS) are take from references [130, 143]. Red solid line is a VFT fit.

demixing is observed, setting in at a critical temperature of ca. 220 K. This phase separation was also observed in the bulk mixture, but at 207 K. Whether this difference is due to the applied temperature protocol or it is introduced by the confinement cannot be clarified here and should be subject to further investigations.
All ^{2}H NMR data can be approximated by a VFT fit, resulting in a glass transition temperature of $T_g = 163.9$ K and a fragility of $m = 44.9$. This value for T_g is lower than expected for the confined W45c mixture [143], but agrees well with the value expected in the bulk liquid at W45 [130]. The fragility is larger than in the DS measurements and is further increased if the STE experiments are neglected in this fit. This may suggest a further reduction of the water content in the sample upon cooling to lower temperatures.

The literature data correspond to two limiting cases, i.e. the ^{2}H NMR data of W45b represent the dynamics of the bulk mixture. In contrast, the results obtained in the 2.1 nm MCM-41 are those of the completely phase separated liquid. This rises the question of how the liquids order themselves in the confinement. Figure 8.5 shows two possible scenarios for the phase separation. Crystalline water ice will likely form as far away from the confinement walls as possible and the ice nuclei are centered in the MCM-41 pore. The PG molecules can be in direct neighborhood to the MCM-41, as sketched in panel (a). Then the water-like w-process stems from molecules at the edge of the ice crystal. A second possibility is shown in panel (b). There, the PG molecules are connected to the surface of the nuclei, and the w-process stems from water molecules in between the PG molecules and the MCM-41 wall. A third possibility is not sketched: There the PG is separated by a liquid water layer to each side in be-

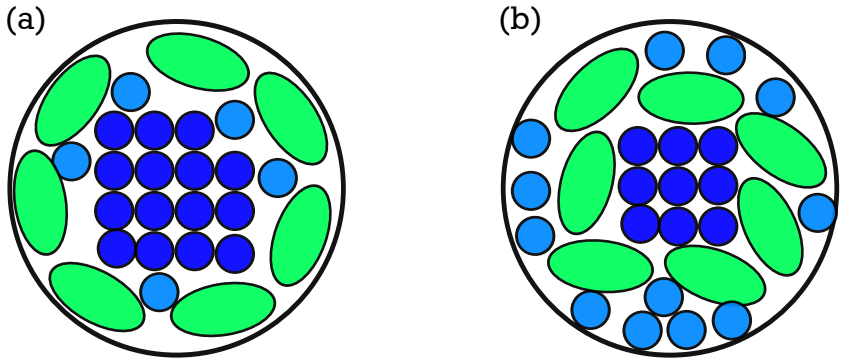

Figure 8.5.: Possible scenarios of the phase separation in PG-water mixtures in MCM-41. colors indicate the PG molecules (green), liquid-like water molecules (light blue), and solid-like water molecules (dark blue).

tween the nucleus and the MCM-41. Due to the limited size in the confinement, this seems unlikely.

In section 8.1.2 the WWA was utilized to describe the correlation function F_2^{cc} under the assumption that both, the w-process and the α-process contribute to the loss of correlation. The resulting correlation times are depicted in figure 8.4 as well. Rather than a slowdown of the w-process, they show agreement with the data obtained by Elamin et al. in the small MCM-41 pores with d = 2.1 nm [143]. A possible scenario thus may also be, that in the present MCM-41 confinement the liquids are completely phase separated and the same dynamics as in DS are measured at least at this low temperatures. Fitting a single KWW function does not capture the dynamics, since both $\alpha-$ and w-process are present and overlap each other. The measurement at T = 173 K was performed by quenching the sample after storing it at room temperature for several days. Therefore, the very slow phase transition process had only little time to take place.

In this investigation of PG-water mixtures confined to MCM-41 of 2.8 nm diameter no strong confinement effects have been found. At higher temperatures, the motion exhibits a broader distribution of correlation time $G\left[\log(\tau)\right]$. Below 220 K a long term crystallization process is observed which takes place in the course of several hours, even below the reported limiting concentration W60, where the mixture is stable. This process is also present in the bulk liquid, but to the best of the authors knowledge, was not reported for this particular system so far. The influence of this process on data presented in literature studies is not clear and should be further investigated. Phase separation was also reported in smaller confinements of MCM-41, where it seems to be present also at high temperatures. Therefore, systematic studies on the concentration and the size dependence of this process are interesting to further understand the

interactions of binary aqueous mixtures in severe geometrical confinement. It must be clarified in how far the dynamical processes observed in confinement are influenced by the phase transition. The present study suggests, that the main effect is a reduction of the water concentration in the residual liquid, and thereby, a slowdown of dynamics. This is accompanied by an increase of inner surfaces provided by the crystals, what increases the heterogeneity.

8.2 Dynamics of PGME-water mixtures

PGME-water mixtures were found to feature different properties than PG-water mixtures. One of the hydroxyl groups is replaced by a methyl group, reducing the number of available H-bonding sites. Therefore, a PGME molecule can only form one H-bond to one other PGME molecule. In the pure bulk liquid, the relaxing unit is a pair of molecules [69, 130]. These pairs show faster dynamics than a chain of PG molecules does, resulting in a glass transition temperature for pure PGME that is ca. 26 K lower than bulk PG. When water is added, the water molecules increase the overall number of possible H-bond connections, thereby bridging several PGME molecules and larger PGME-water clusters can be formed. The increased size and mass of those *entities* [149] causes a deceleration of their dynamics and an increase of the glass transition temperature. At a water concentration of ca. $c_w = 55\,\%$ the glass transition temperature T_g is a maximum. At higher water concentrations, the dynamics are accelerated again up to $c_w \approx 65\,\%$, where the bulk mixture crystallizes [149]. The acceleration is caused by the plasticization effect of water.
For PGME-mixture in 2D confinement of Na-vermiculite clay with interlayer distance of ca. 0.65 nm the dynamics were unaltered compared to the bulk [86], similar to the findings for PG. Again, this was explained by the idea that the H-bonding network can adapt to the 2D structure of the confinement. In contrast, the formation of the larger PGME-water entities is suppressed in MCM-41 confinement of 2.1 nm pore diameter [143], where the confinement is effectively one dimensional. It was suggested that the mixtures demix and the water coordinates to the MCM-41 surface, while the alcohol molecules cluster in the center [143,204]. The w-relaxation was found to be compatible with that found in pure water in the same confinement. The confined α-process was independent of the water concentrations and substantially slowed down compared to the bulk.
In this work, PGME- and DiPGME-water mixtures are investigated in somewhat larger MCM-41 confinements with diameters of ca. 2.7 nm to 2.8 nm diameter, see section 4.2. In the larger confinements, the geometrical restrictions are less severe and the dynamics are expected to be more bulk-like. To study the effects of confinement, bulk PGME mixtures are investigated as well. Additionally, the larger dimer of PGME is investigated in confinement to reveal the size depen-

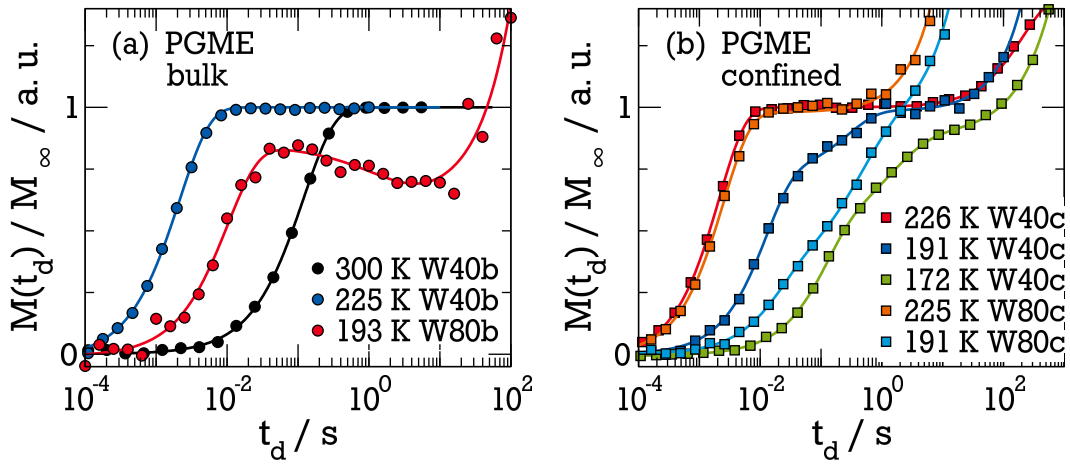

Figure 8.6.: Magnetization recovery of bulk (a) and confined (b) PGME-water mixtures. Lines are best fits to eq. (5.1).

dence of the confinement effects. DiPGME was already investigated at high temperatures in a larger d = 2.7 nm confinement by QENS [204]. There, a shift in the concentration dependence compared to bulk was observed. In cooperation with the Swenson group, the dynamics in similar samples are investigated. The SLR measurements on the confined DiPGME samples were performed by M. Reuhl in her bachelor's thesis [203].

8.2.1 Spin-lattice relaxation of PGME mixtures

The SLR of bulk and confined PGME- and DiPGME-water mixtures has been measured using the SR sequence, see section 3.4. PGME-water mixtures with water mass ratios of c_w = 40 % (W40), 60 % (W60) and, 80 % (W80) have been investigated, see section 4.2 for details.
Some selected SLR magnetization recovery curves are shown in figure 8.6: the bulk PGME samples in panel (a), the confined PGME samples in panel (b). The bulk samples exhibit one single exponential relaxation for the lowest water concentration W40b at all temperatures. The higher concentrations W60b and W80b show an additional relaxation at very long delay times t_d. This component appears first at 250 K in both samples. Similar to pure water in MCM-41, see chapter 5, the relaxation steps will be named (f) for the fastest relaxation and (i) for the slowest. The figure also reveals indications for a pulse induced heating as seen at 193 K in W80b. The effect is weak and was tested to have no significant influence on the relaxation times of the (f) relaxation. Even though there should be chemical exchange of deuterons between D_2O and the OH group of the PGME molecules, no second relaxation component is found in the bulk liquids. In W40b, the alcohol-connected deuterons should contribute about 16 % to the total signal when assuming stochastic distribution. The ab-

sence of a second component can be explained by a fast chemical exchange, or alternatively by coupled dynamics of both molecular species. Similar findings were reported for the PG-water mixtures [124]. Both possibilities require the two different molecules to be in close proximity. Thus, there is no observable demixing besides the freezing of water at 250 K. The time constants of all (i) relaxation are rather long. DSC measurements support that at 250 K parts of the liquid crystallize and therefore, the relaxation step (i) is attributed to ice, see appendix B.

The relaxation curves have been fitted using eq. (5.1) with an appropriate number of KWW functions, resulting in the arithmetic mean relaxation times $\langle T_1 \rangle$ shown in figure 8.7 (a) and (b). All bulk PGME samples show a very similar temperature dependence. At high temperatures above 250 K the relaxation times are concentration dependent and exhibit higher values of $\langle T_1 \rangle$ the higher the water concentration. Longer relaxation times signal faster dynamics on this side of the minimum, under the assumption that the distribution of correlation time $G\big[\log(\tau)\big]$ is equal below and above crystallization. This is in accordance with the findings in [130]. At 250 K the (i) relaxation stakes in samples W60b and W80b. It is accompanied by a noncontinuous jump in the relaxation times of the (f) component. The decrease in the $\langle T_1 \rangle$ times above the minimum indicates a deceleration of the residual liquid, agin when $G\big[\log(\tau)\big]$ is influenced only weakly. Since pure PGME does not crystallize it is again reasonable to assume that only water freezes. From the drop of signal, the residual water concentration can be estimated, see table 4.4. This results in water mass ratios of $c_w = 43\,\%$ and 67 % for the W60b and W80b samples respectively. Thus, it seems intuitive that W60b exhibits a similar dynamics to W40b when the influence of ice crystals is neglected. By extrapolating the data of the T_g shift [130] it also seems reasonable that the crystallized W80b mixture exhibits similar dynamics to the W40b sample.

Below the crystallization temperature the (f) relaxations of all sample are alike and the $\langle T_1 \rangle$ minima are only weakly dependent on the sample, see also table 8.2. The values in the minima are close to the expectation for a Debye relaxation and hence, the corresponding distributions of correlation times $G\big[\log(\tau)\big]$ are narrow in the bulk samples. The fact that the T_1 minima of all samples are very similar, and that from the above estimation of the residual water content all three samples are expected to have similar dynamics assists the idea that the ice nuclei have only weak influence on dynamics and heterogeneity. This can be understood by the idea that water crystallizes in few large crystals rather than in many small nuclei. Following this idea, the deviations of the relaxation times of samples W60b and W80b compared to the unfrozen W40b below the T_1 minimum can be interpreted as acceleration caused by the difference in water content. If, for example, the water content reduces on cooling, e.g. by further growth of the nuclei, the dynamics are accelerated. This is a straightforward

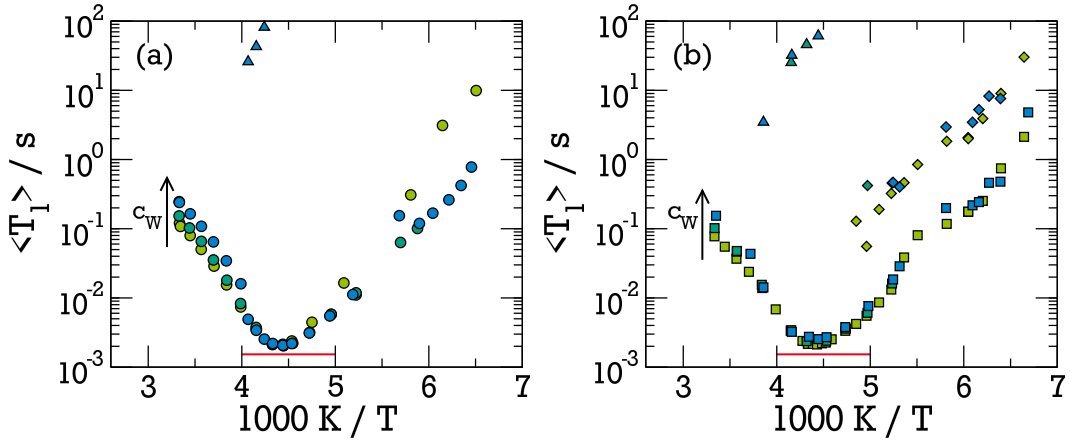

Figure 8.7.: SLR relaxation times for bulk (a) and confined (b) PGME water mixtures. Shown are water concentrations of W40 (green), W60 (turquoise) and, W80 (blue). Triangles are the (i) components, diamonds the (s) component. The (f) component are circles (bulk) and squares (confined). Red lines are the T_1 minimum in case of a Debye relaxation.

interpretation for the W60b sample, which according to [130] would accelerate upon further reduction of water content. In contrast, if $c_w = 67\,\%$ for sample W80b, the dynamics of this sample need to first decelerate when passing to the concentration of maximal T_g at $c_w = 55\,\%$. Alternatively, the differences may be due to the influence of the ice crystals.

The confined PGME-water mixtures exhibit a more complex behavior. There, three relaxations are found, see figure 8.6 (b). In addition, to the fastest (f) and the crystalline component (i) a third relaxation is observable at intermediate temperatures, which will be referred to as (s) relaxation. Fitting the recovery curves results in a quite different temperature behavior compared to the bulk liquids, see figure 8.7. At highest temperatures a concentration dependent

Table 8.2.: SLR parameters obtained from the fits: The minimal value of $\langle T_1 \rangle$ ($\langle T_1 \rangle_{min}$), the corresponding temperature (T_{min}), the stretching parameters for CC and CD SD (α; γ), the approximated temperature T_{ne}, and the SE signal minimum temperature (T_{SE}).

Sample	$\langle T_1 \rangle_{min}$ / ms	T_{min} / K	α	γ	T_{ne} / K	T_{SE} / K
PGME W40b	2.12	226.7	0.76	0.47	176	192
PGME W60b	1.95	225.6	0.81	0.45	< 170	181
PGME W80b	2.05	225.7	0.78	0.50	161	182
PGME W40c	2.11	226.8	0.76	0.47	164	186
PGME W60c	2.35	225.7	0.69	0.39	< 190	< 190
PGME W80c	2.50	224.9	0.66	0.35	162	188

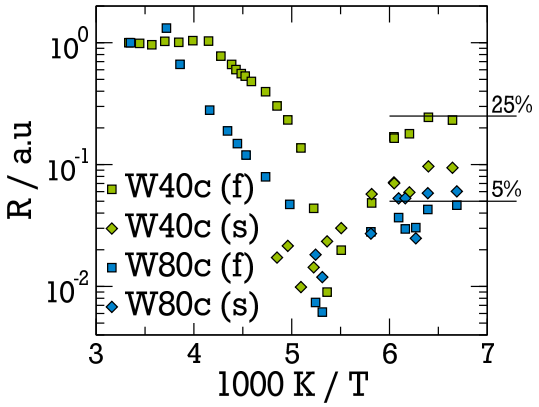

Figure 8.8.: Reduction factor of PGME W40c and W80c over temperature. Lines indicate the low temperature level of the (f) relaxations

single exponential behavior is found, similar to the bulk liquid. Freezing of water is observed in all confined samples upon cooling in the temperature range from 270 K to 260 K, including the lowest concentration W40c. Besides affecting all concentrations, the crystallization event occurs at temperatures higher than in the bulk samples. Both observations show that the crystallization tendency of water is increased in MCM-41 rather than suppressed. Like in the bulk samples, the $\langle T_{1,f} \rangle$ minima are found at similar temperatures for all studied concentrations, see table 8.2. For the confined samples the minimum values of $\langle T_{1,f} \rangle$ slightly increase with increasing water concentration. Hence, the heterogeneity is more pronounced when more water is present, suggesting that the crystal nuclei have more contact to the residual liquid. Alternatively, the increase of the SLR minima might be caused by possible concentration differences.

In addition, to the (f) relaxation, an intermediate (s) relaxation is found in the confined samples. Both processes show a temperature dependence, which is similar to that found in the pure confined water sample P21, see section 5.1. The (s) relaxation shows a KWW stretching of $\beta \approx 0.6$ at all temperatures. The fact that the species is observed at all, demonstrates that the molecules giving rise to the (f) and the (s) relaxation do not exchange so that they are either spatially separated, or if they are in contact, one of the two species is solid. The low β parameter suggests that the (s) relaxation is a solid like component.

Finally, the amplitudes of the (f) and (s) relaxations are briefly discussed. Figure 8.8 shows the normalized reduction factor R of the two samples W40c and W80c. In both samples, the magnetization starts to decrease below the crystallization temperature. The (f) components pass through deep minima and recover towards lower temperatures. At lowest temperatures $T \approx 150$ K final levels of the amplitude of ca. 25 % and 5 % are found for W40c and W80c, respectively. Assuming statistical distribution of the deuterons to all OH-sites,

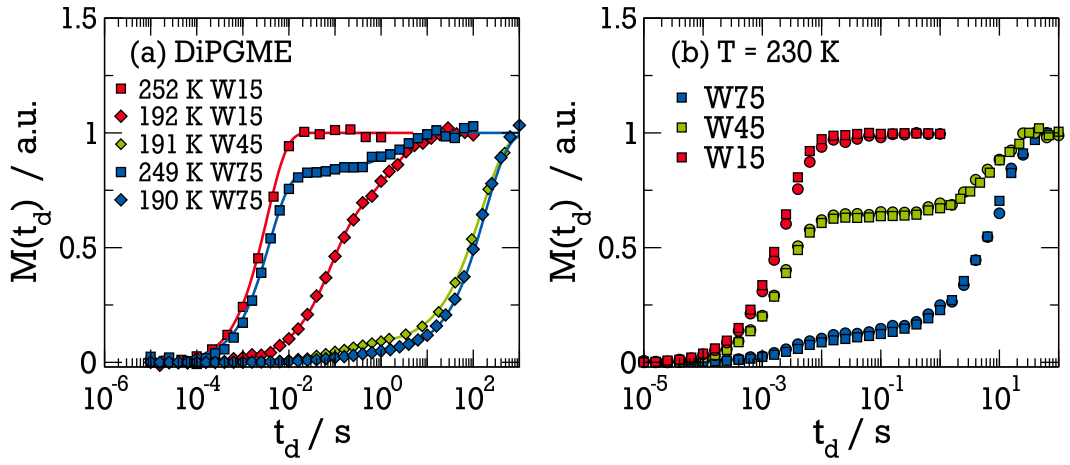

Figure 8.9.: Magnetization recovery in confined DiPGME (a) at several temperatures and concentrations. Lines are best fits using eq. (5.1). (b) recovery curves at 230 K for the all concentrations in dry (squares) and wet (circles) preparation.

those percentages coincide with the deuterons expected to bind to the PGME molecules, c.f. table 4.4. A second interesting feature related to the (f) component is the decrease of magnetization below the freezing point, in the vicinity of the $\langle T_1 \rangle$ minima. In this temperature region, dynamics are usually far from the SE signal minimum, see e.g. figure 6.3 for confined glycerol. Thus, the strong decay of (1-R) in this region, indicates a decreasing number of molecules contributing to the (f) species. A possible process may be dynamical clustering of water to existent nuclei. The slower (s) relaxation does not show a minimum in (1-R). As soon as it can be distinguished it starts with small amplitudes which increase to a level of approximately 8 % of the overall signal in both samples, independent on water concentration.

Confined DiPGME-water mixtures

The magnetization recovery curves of DiPGME-water mixtures with mass ratios of W15, W45 and, W75 are shown in figure 8.9. The behavior in these samples is similar to the one in confined PGME-water mixtures. Again, a total of three relaxations can be observed, but not all of them in all samples. In the W15c sample, the two relaxation processes (f) and (s) are observable, but no crystallization occurs. In contrast, samples W45c and W75c exhibit strong crystallization features (i). The phase transition occurs at 241 K and 261 K, respectively.

To test whether the observed dynamics are dependent on the amount of excess liquid outside the MCM-41 pores, two sets of samples were prepared, see section 4.2.2. The first set of samples is dried thoroughly to minimize the amount of external liquid, while the second set is left with a larger amount of excess

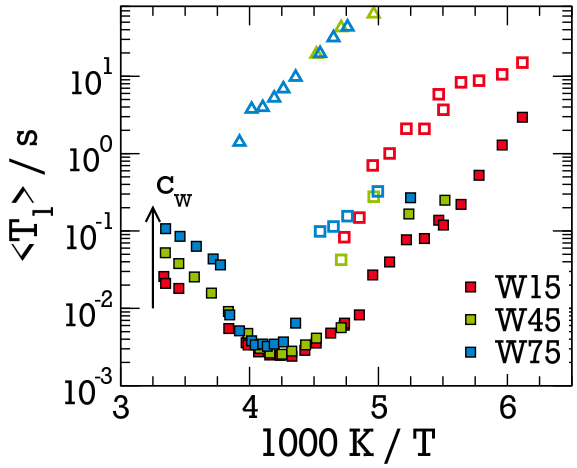

Figure 8.10.: Magnetization recovery in confined DiPGME (a) at several temperatures and concentrations. Lines are best fits using eq. (5.1). (b) recovery curves at 230 K for the all concentrations in dry (squares) and wet (circles) preparation.

liquid. A comparison of both samples at 230 K is shown in figure 8.9 (b). There, it becomes clear that both sets of samples exhibit a very similar SLR behavior. Therefore, the rest of the discussion focuses on the dry samples. The resulting mean relaxation times $\langle T_{1,f} \rangle$ from fitting the recovery curves of the dry samples are shown in figure 8.10. As before, a strong concentration dependence is found for the relaxation times at highest temperatures, where the sample with highest water content shows the fastest dynamics when $G\left[\log(\tau)\right]$ is assumed to be similar for all concentrations. Upon cooling, the samples crystallize causing a jump in the time constants $\langle T_{1,f} \rangle$. In analogy to the monomer discussed above, this suggests a reduction of the water concentration in the residual liquid, c.f. table 4.4.

At temperatures below the crystallization events, the minima in $\langle T_{1,f} \rangle$ are found, see table 8.3. The samples W15c and W45c exhibit approximately equal minima positions, while the W75c sample is shifted to higher temperatures and values of $\langle T_{1,f} \rangle$. In sample W15c, the two processes (f) and (s) can be well distinguished at all temperatures below 210 K, see e.g. figure 8.9. Due to the

Table 8.3.: SLR parameters: $\langle T_1 \rangle_{min}$ is the $\langle T_1 \rangle$ value in the minimum, T_{min} is the corresponding temperature, α and γ are the stretching parameters for CC and CD spectral densities, T_{ne} is the approximated temperature where $\beta < 1$.

Sample	$\langle T_1 \rangle_{min}$ / ms	T_{min} / K	α	γ	T_{ne} / K	T_{SE} / K
PGME W15c	2.4	236.0	0.70	0.40	191	199
PGME W45c	2.5	236.6	0.67	0.36	212	199
PGME W75c	3.2	241.0	0.54	0.25	212	212

strong contribution of the crystalline component, the evaluation of the magnetization recovery curves of samples W45c and W75c becomes ambiguous in the vicinity of the T_2-hole, since the two anticipated processes (f) and (s) cannot be distinguished reliably. Fitting only one KWW function for both components causes a steep increase of $\langle T_{1,f} \rangle$, since the (s) relaxation is absorbed in the fit of the faster component. Below the T_2-hole, the combined fit of the relaxations (f) and (s) causes an apparent decrease of the relaxation times observed in W45c and W75c. Therefore, in the vicinity T_2-hole the fitted time constants represent two relaxations rather than one and are disregarded in the following. Due to this effect, it is not straightforward to interpret the shift of the $\langle T_{1,f} \rangle$ minimum in sample W75c as a slowdown of dynamics. The position of the minimum can also be influenced by this crossover in the observable processes. Nevertheless, the large shift in the signal minimum of the SE, given in table 8.3, indicates some deceleration of the fastest dynamical process. This is likely due to the presence of large amounts of crystalline water.

8.2.2 Stimulated echoes of PGME mixtures

After having established the dynamical behavior at high temperatures, the low temperature dynamics are investigated using the STE experiment. To begin with the behavior of PGME-water mixtures in the bulk is investigated. Thereafter, it is turned to the confined PGME- and DiPGME-water solutions. All experiments are carried out with delay times t_d after saturation chosen such that the crystalline components are suppressed. In the confined samples where two relaxation processes are present, it is additionally discriminated between fully and partially relaxed (FR and PR) measurement such that the SLR relaxations (f) and (s) or mainly the (f) relaxation are observed, see also the definition eq. (5.2).

STE of bulk PGME mixtures

Temperature-dependent STE measurements of spin alignment (sa) order for sample W40b are shown in figure 8.11 (a) for an evolution time of $t_p = 3\,\mu s$. At 186 K the dynamics enter the time window of the method. A fit at this temperature is rather ambiguous: to do so the stretching parameter β was fixed to a value between 0.3 and 0.4. Those limits are determined by the double logarithmic representation show in panel (b). There, the data are given in the form

$$y = -\ln\left(1 - F_2^{sa}(t_m)\right). \tag{8.2}$$

In this representation, the parameter β is given by the slope of the curves. Deviations from a straight line are caused by the influence of a finite plateau

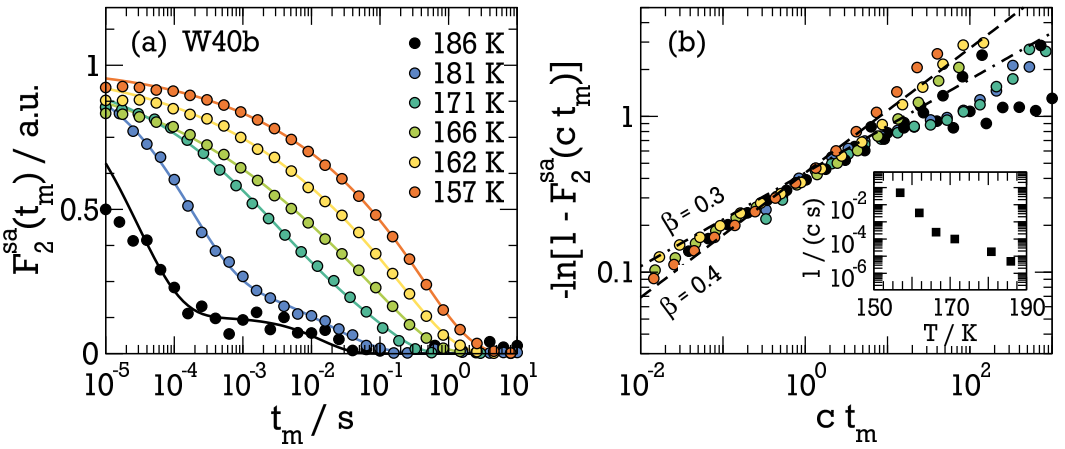

Figure 8.11.: (a) STE correlation function (spin alignment) in W40b at several temperatures for evolution times t_p = 3μs. (b) Same data as in (a) rescaled on the x-axis by a factor c(T) to agree at 1 s in the linearized representation, see eq. (8.2). Inset: inverse scaling parameter 1/c over temperature.

and SLR. As can be seen by the calculated model cases $\beta = 0.3$ and $\beta = 0.4$, the stretching parameter is within those limits for all measurements. Note that in (b), all curves have been rescaled on the time axis by a factor c given in the inset. Similar procedures have been used in the case of the confined PGME to determine limits for the stretching parameter.

Panel (a) of figure 8.11 shows some qualitatively different features of the correlation decays F_2^{sa} at high and low temperatures. Above ca. 171 K the curves shift fast with decreasing temperature and show some pronounced residual plateau. Below this temperature, the shift with temperature variation slows down and the plateau is absent. A behavior similar to that for W40b is observed for sample W80b. All measured data sets are fitted using eq. (3.56). The temperature dependence of the correlation times will be discussed in section 8.2.3. Here, it is focused on the information about the motional process obtained from the evolution time dependence. In figure 8.12 (a) and (b) exemplary evolution-time dependent measurements are shown. In the figure the influence of SLR has been eliminated by dividing by SLR relaxation T_1^Q . The latter was determined by fixing T_1^Q in the limits $2/3T_1 \leq T_1^Q \leq 5/3T_1$ given in [164] and simultaneously fitting of the decays curves for all t_p times at a given temperature. The fitted correlation times $\tau(t_p)$ are shown in panel (c). For better comparison, the correlation times are normalized to the value at 3μs. At highest temperatures, the values $\tau(t_p)$ exhibit only a weak dependence on the evolution time t_p. When temperature is decreased, a decay of τ with evolution time can be observed. A constant behavior of $\tau(t_p)$ is expected in the case of a motional process with large angular amplitude [38]. In contrast, a decay of $\tau(t_p)$ is expected when the mean rotation angle becomes small, see eq. (3.65). For comparison the ex-

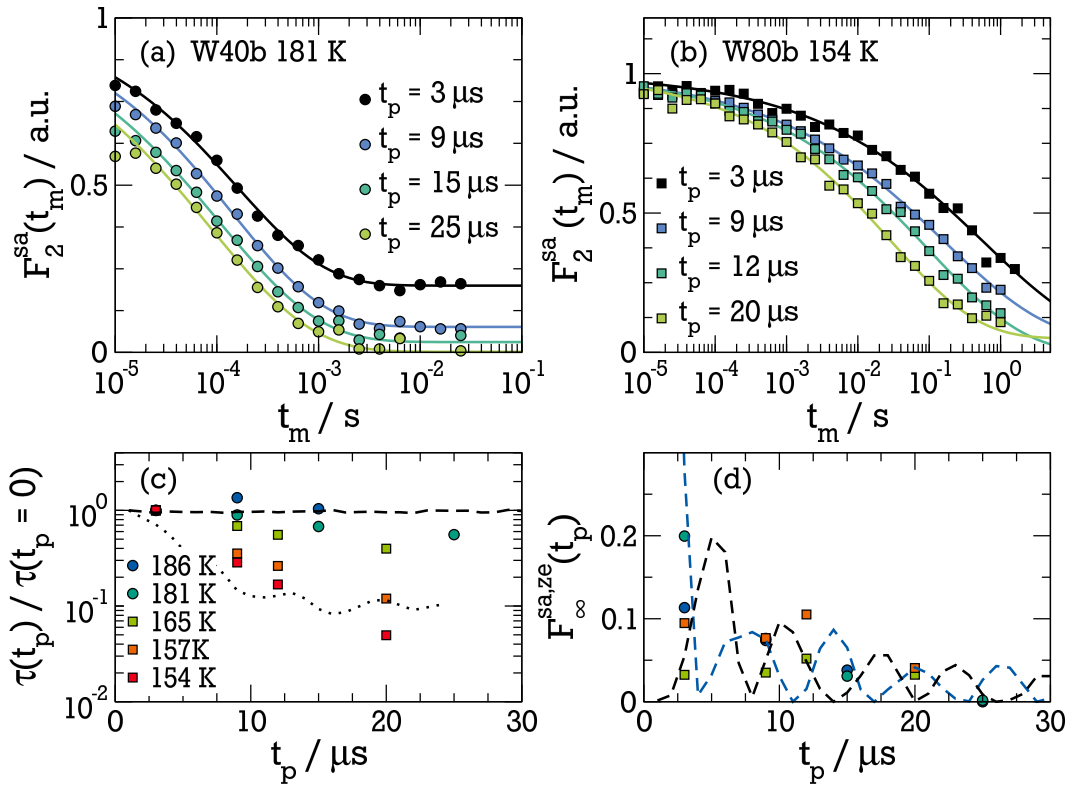

Figure 8.12.: STE decay curves from (a) W40b at T = 181 K and (b) W80b at 154 K, for several evolution times t_p. Solid lines are fits with eq. (3.56). (c) Correlation time $\tau(t_p)$ normalized to t_p = 3μs. (d) Residual correlation F_∞ and RJ simulation. Symbols in (c) and (d) are equal, circles correspond to W40b and squares to W80b. Lines are expectation from RW simulations, dashed for the IRJ model, dotted for an isotropic 10° jump motion. In (d) expectations of a IRJ are shown for sa (black) and ze (blue) experiments.

pectations for an isotropic random jump and a 10° jump motion are included in the figure, as calculated from RW simulations.

Using the sa STE experiment, the residual plateau $F_\infty(t_p)$ can be determined reliably only at temperatures T $\geq$ 180 K. Below, the Zeeman (ze) STE experiment was utilized to obtain the $F_\infty(t_p)$ values, since the SLR time constants can be measured individually in this case. The results are shown in panel (d). The determined values $F_\infty(t_p)$ conform to the expectation of an isotropic jump at all temperatures. Note that the t_p values given here are set values, the real values can be up to 2μs longer due to a finite pulse length, see [257] for details.

The change in the evolution time dependence of the correlation times $\tau(t_p)$ towards lower temperatures indicates a change in the observed motional process. If the structural relaxation is observed at higher temperatures and a secondary relaxation starts to dominate the dynamics at lower temperatures [38], a change of $\tau(t_p)$ is observed, where the angle amplitudes decrease upon cool-

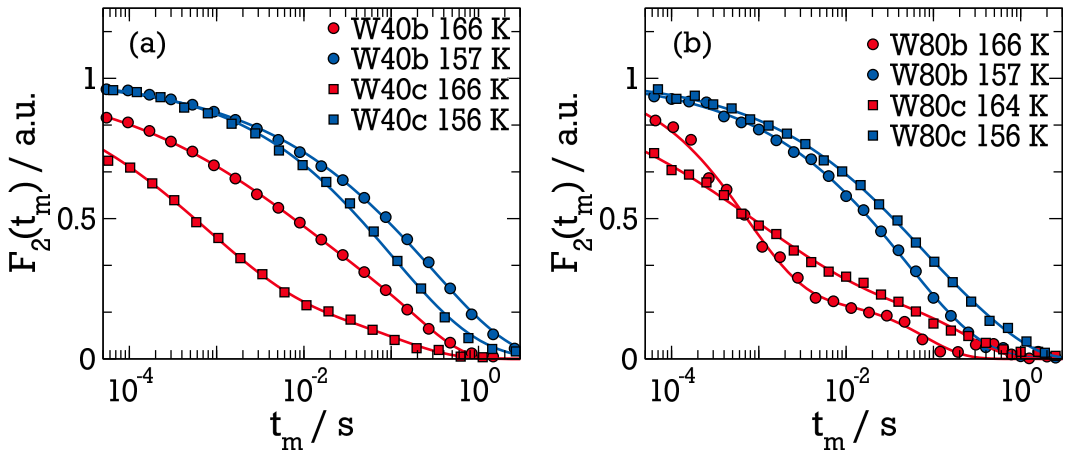

Figure 8.13.: Comparison of the STE decays of bulk (circles) and confined (squares) PGME-water mixtures (a) W40 and (b) W80. Solid lines are fits with eq. (3.56).

ing. Additionally, even at low temperatures no anisotropy in the relaxation process is observed. This is in contrast to the behavior obtained for bulk water in confinement, see section 5.3. The observations suggest that the dynamical mechanism of the water molecules is alter by the presence of the alcohol molecules and possibly by the ice nuclei. A similar small angular jump was found in the bulk PG-water mixture [124] at low temperatures, where water and alcohol were found to perform a common motion. The change of the correlation time dependence towards higher temperatures may indicate a decoupling of dynamics of both molecular species. Literature indicates that the low temperature process is the secondary w-relaxation [124, 134]. If so, it is not clear why it shows no visible anisotropy, as would be expected for a faster secondary process, especially since DS detects a slower structural relaxation [134].

STE in confined PGME mixtures

The SLR experiments have revealed altered dynamics of the PGME-water mixtures confined in MCM-41 pores of d = 2.8 nm in comparison to the bulk liquids, i.e. an additional intermediate process is found in confinement. Here, the STE experiment is employed to investigate the behavior at low temperatures. In FR STE experiments the second process (s) only contributes a static signal contribution to the STE experiments, see e.g. figure 8.14 (b). Therefore, here it is focused on the PR experiment where the (s) relaxation is not allowed to build up after saturation, compare with eq. (5.2).
Figure 8.13 shows a direct comparison of bulk and confined liquids for the lowest and highest water concentration W40c and W80c respectively. At T = 166 K, the W40c sample exhibits substantially faster dynamics than the bulk

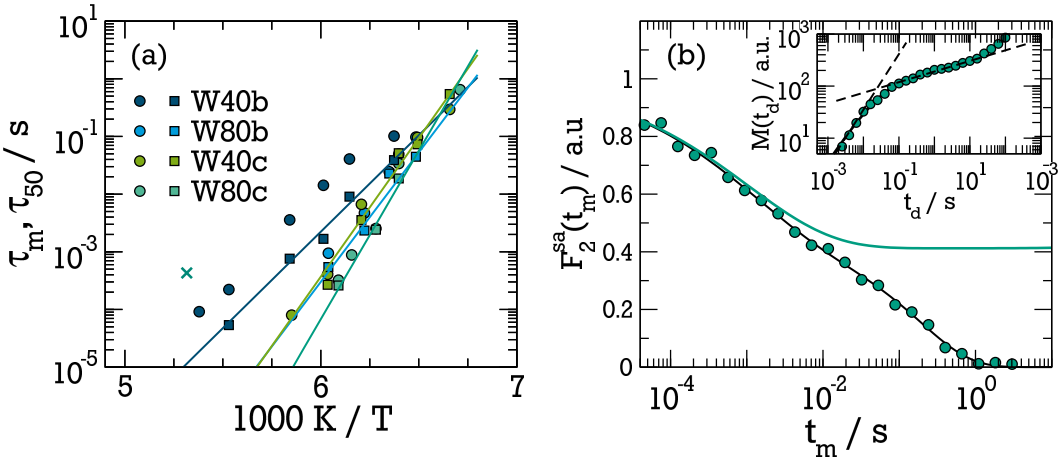

Figure 8.14.: (a) Correlation times τ_m (squares) and τ_{50} (circles) obtained from the PGME-water mixtures W40b, W80b, W40c, and W80c. Solid lines are Arrhenius fits to τ_m. The cross is obtained from W80c, see panel (b). In (b) the STE decay of W80c at 188 K is shown. Solid black line is the fit using eq. 3.56, solid turquoise line is the fit of the decay curve divided by the SLR. Inset: SLR measurement at T = 188 K, dashed lines indicate the (f) and (s) relaxation.

sample W40b, while the shape of both curves is alike. In contrast to this, the W80c sample shows a decay on the same time scale as W80b, but the decay curve of the confined sample is much more stretched than that of the bulk liquid. The W80c decay curve at 164 K is similar to the decay in W40c at T =166 K. At lower temperatures, T ≈ 156 K the results become more similar in all cases: The confined samples well agree with each other.

The varying shape of the correlation decays renders a straightforward comparison of the corresponding correlation time constants sophisticated. Two different definitions of the characteristic time τ are used to test the influence of the different shapes. In addition to the usual definition of τ_m, see eq. (2.16), figure 8.14 (a) shows the correlation times τ_{50}. The latter times are obtained from determining the time where the correlation function has decayed to $F_2^{xx}(t_m) = 0.5$. The figure reveals that both definitions result in similar correlation times. In the case of W40b the time constants differ by a factor of four. Both time constants, τ_{50} and τ_m, show a similar temperature dependence for all samples. The figure also shows that all time constants become similar at temperatures T ≈ 155 K. Whether the samples exhibit similar temperature dependence below this temperature cannot be determined due to an interference of SLR. The temperature dependence of all samples can be described using an Arrhenius law. This is shown in the figure for the τ_m values. The resulting fit values are listed in table 8.4. It can be observed that a higher water concentration in the samples leads to a higher activation energy E_a. In addition, the confined samples exhibit higher values of E_a than the corresponding bulk solutions.

Table 8.4.: Parameters obtained from fitting the STE correlation times τ_m of the PGME-water mixtures with an ARR law.

Sample	τ_0 / s	E_a / eV	T(τ_m = 100s) / K
W40b	$1.9 \cdot 10^{-23}$	0.66	135.3
W80b	$3.6 \cdot 10^{-31}$	0.89	138.3
W40c	$5.3 \cdot 10^{-33}$	0.95	140.3
W80c	$6.2 \cdot 10^{-40}$	1.16	141.7

In sample W80c the STE decay at T = 188 K exhibits a behavior deviating from all other measurements. The data of the FR measurement are shown in figure 8.14 (b). The resulting time constant is shown in panel (a). It exhibits a slower decay than the measurements at lower temperatures. To clarify the origin of this different behavior, the amplitudes in the SLR can be taken into account. The corresponding SLR measurement is shown in the inset of panel (b). Here, the (f) relaxation has a total amplitude of 79 units, the (s) component an amplitude of 120 units, corresponding to 40 % and 60 % of the total signal, respectively. In the STE experiment the (i) relaxation is suppressed and can be disregarded. When the SLR (f) relaxation is faster than the STE timescale, as suggested by SLR, see table 8.2, it is expected to result in an static background of up to 40 % in the STE experiment[4]. The observed decay shows a residual plateau of 39 %, affirming that this is the case. The observed STE decay is that of the slow (s) relaxation. It was only observed at this temperatures, while at lower temperatures, PR experiments have been carried out such that mainly the faster (f) relaxation is observed. Hence, this particular measurement gives a single time constant for the process connected to the slow SLR component.

The dynamics of the bulk PGME-water mixtures is dominated by an isotopic large angle jump at higher temperatures. With lowering the temperature, the mean jump angle was found to be reduced, while the isotropy of the motion is preserved. Since dynamics are faster in the confined samples, no reliable information on the mechanism of motion in the temperature regime T > 170 K can be obtained. The evolution time dependence at lower temperatures is depicted in figure 8.15. Panel (a) shows the dependence of the correlation times τ_m on t_p. A decay by about one order of magnitude is found when increasing the evolution time. This again indicates a small angular jump amplitude, e.g. of $\phi \leq 7°$ at T = 156 K, estimated from eq. (3.65). The correlation times are in good agreement with the bulk samples, as indicated by the measurement of W80b shown in figure 8.15. This also suggests a similar angular amplitude of the motion in all samples.

[4] The complete background is observed only in the ze order experiment, in sa order it contributes to only partly to the signal.

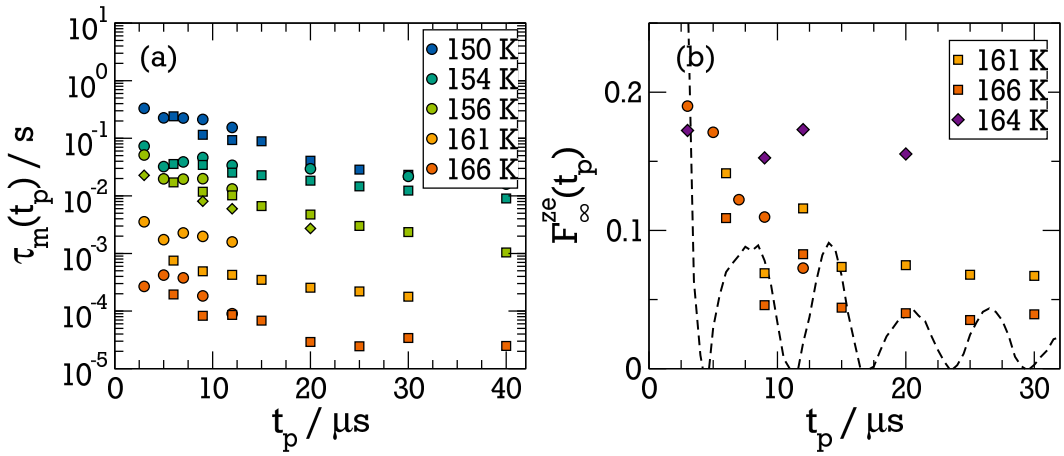

Figure 8.15.: (a) Logarithmic mean correlation times of sample W40c obtained from the STE experiments (sa: circles; ze: squares). Green diamonds are obtained from sample W80b at T = 157 K. (b) Residual plateau F_∞^{xx} of ze order (squares) and sa order (circles) STE experiments on sample W40c (diamonds: W80c). Dashed line is the expectation for an isotropic reorientation of ze order.

Panel (b) of figure 8.15 reveals some differences between bulk and confined samples. While the bulk liquids exhibit a more or less isotropic motion, the confined samples show tendencies of an anisotropic motion for the temperatures at which the plateau value $F_\infty(t_p)$ can be determined. The plateau is increased in W40c. W80c exhibits a residual correlation indicative of substantial anistropy.

Confined DiPGME-water mixtures

Turning to the dimer DiPGME samples, the behavior of the STEs becomes even more interesting. In SLR it was shown that the crystalline (i) component is rather strong and overlaps with the (s) relaxation component in W45c and W75c. Due to this interference it is focused on the lowest water concentration W15c. There, the (f) and (s) relaxation can be well distinguished.
Figure 8.16 (a) shows a FR and a PR sa order STE measurement at T = 182 K. As found in the PGME-water samples, the (s) component only contributes a static background to the overall signal in the FR measurement. From the SLR measurement shown in the inset a total STE signal of

$$F_2^{sa} = \frac{3}{8} M_\infty \approx 1700$$

is expected, c.f. eq. (3.51). The observed signal is only 70 % of this value., suggesting that a significant part of the magnetization decays in a process that is

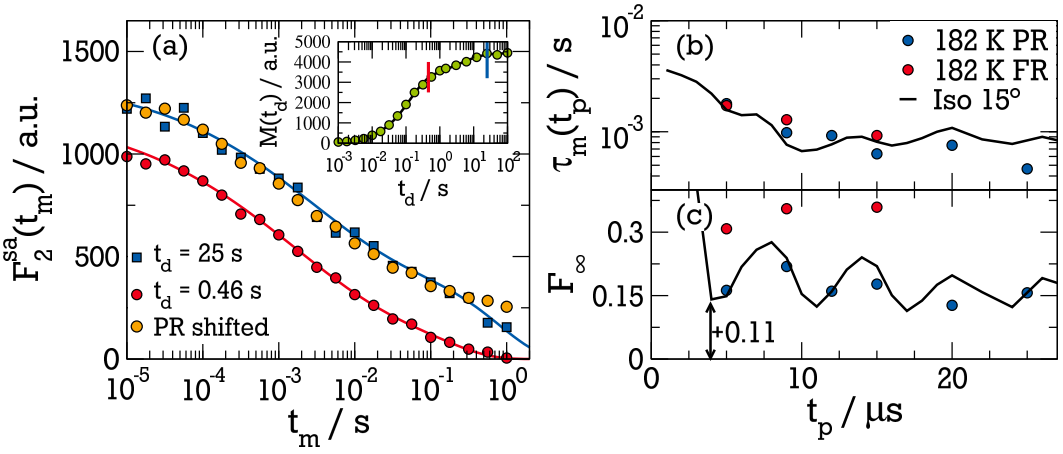

Figure 8.16.: (a) Partial (red) and fully (blue) relaxed sa STE at T = 182 K in DiPGME W15c (t_p = 3μs). Orange circles: vertically shifted PR measurement. Solid lines are fits with eq. 3.56. Inset: corresponding SLR measurement. Lines mark the t_d times at which the STE curves are measured. (b) and (c) evolution time dependence of fit parameters $\tau(t_p)$ and $F_\infty(t_p)$ at T = 182 K. Solid line: RW simulated expectation of an isotropic 15° jump.

faster than the time window of the STE experiment at this temperature. Further calculations show that at the chosen delay t_d the (s) relaxation contributes 11 % and 32 % to the total signal in PR and FR experiments, respectively.

The evolution time dependence of the correlation time and the residual correlation are shown in panels (b) and (c). The correlation times exhibit a slight decrease with t_p corresponding to an jump angle of $\phi < 32°$. An isotropic 15° jump is shown for comparison. The residual correlation $F_\infty(t_p)$ in panel (c) can be well approximated by an isotropic reorientation model that is shifted by a constant offset of 11 % in the PR experiments and 30 % in the FR case. This offset is due to the contribution of the SLR (s) relaxation. The STE decay is dominated by an isotropic relaxation process at 182 K. This is possibly the structural relaxation, which partly comprises the SLR (f) relaxation.

At lower temperatures evaluation of the STE experiments becomes more complicated, as can be seen in figure 8.17 (a). The shape of the low temperature decay curves at short mixing time t_m suggests, that an additional process is observed in the measurements. Rather than fitting two exponential decays to the data, the results obtained by our collaborators in the group of J. Swenson by DS are used to analyze the decays [258]. In DS three relaxations process P_j (j = I, II, III) were found. The fitting procedure is discussed in the following for the data set at 172 K, see figure 8.17 (b). At this temperature, a FR ze order STE was performed, as well as FR and PR sa order for several evolution times. Using a single relaxation the data sets can not be fitted satisfactory. Therefore, the data were interpolated by three exponential relaxations in the form

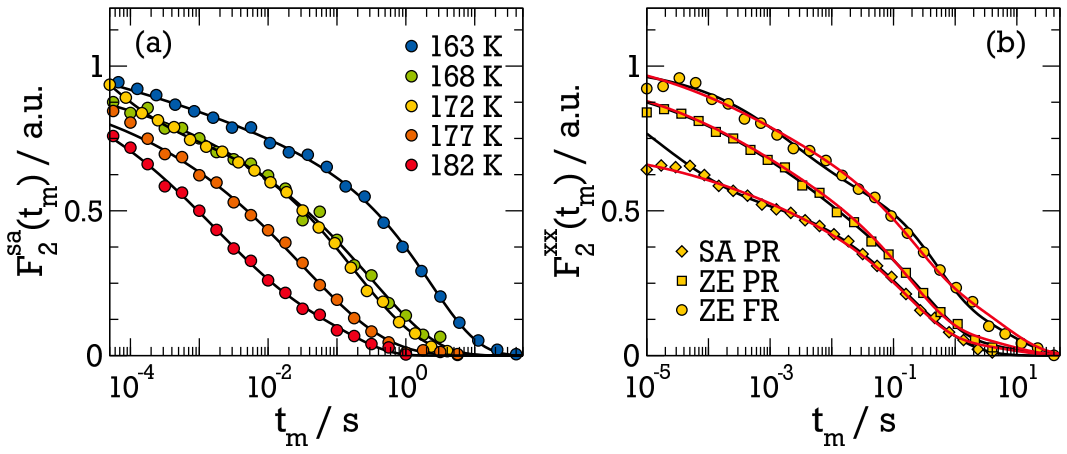

Figure 8.17.: STE decays in DiPGME W15c: (a) Temperature dependent sa order. (b) 172 K: FR ze order (circle) and PR ze (squares) and sa (diamonds) order STE at t_p = 3μs. Black lines are fits using eq. 3.56, red lines are fits using results obtained by DS, see text.

$$F_2^{xx}(t_m) = \psi_f(t_m)\left[P_I(t_m) + P_{II}(t_m)\right] + d\psi_s(t_m) \tag{8.3}$$

In the equation, the relaxations ψ_f and ψ_f are the (f) and the (s) relaxation obtained by SLR. Thus, it is assumed, that the fastest (I) and the intermediate process (II) found in DS are observable in the STE experiment and relax with the fast (f) relaxation. Even though this is unexpected, the analysis above, see figure 8.16, suggests that the (s) relaxation is only attributable to a static background. Therefore, only the slowest dielectric process (III) is assumed to be affected by the (s) relaxation. P_{III} is very slow and modeled by a static contribution d. The fitting was performed using different approaches:

1. The time constants of the processes have been fixed at the values obtained in DS. The free fit parameters are the stretching parameters β_j and the relative weights of the processes. The resulting contributions are plotted in figure 8.18 (a).

2. In the second approach the correlation times of process P_I and P_{II} are left free and fitted. The relative contribution from this ansatz are shown in 8.18 (b) the fitted correlation times in figure 8.19.

3. As for the PG sample, the Williams-Watts ansatz eq. (8.1) was tested. It proved to be numerically unstable and was disregarded.

4. The more intuitive interpolation

$$F_2^{xx}(t_m) = \psi_f(t_m)P_I(t_m) + \psi_s(t_m)\left[P_{II}(t_m) + d\right]$$

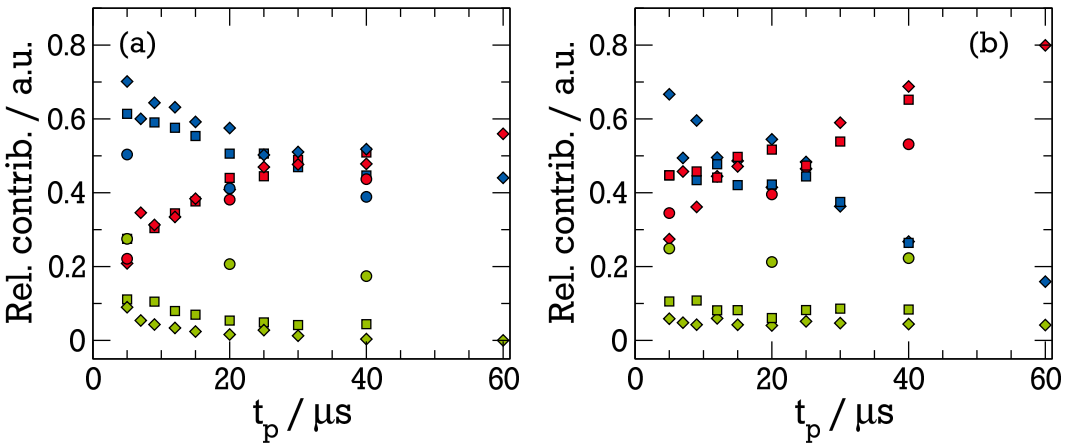

Figure 8.18.: Relative contributions of the DS processes P_I (red), P_{II} (blue) and static background (green) for FR ze order (circle) and PR ze (squares) and sa (diamonds) order STE on DiPGME W15c at 172 K. (a) Correlation times fixed at the DS values (b) correlation times free.

was used. The general features of the fit results are unchanged, but the static background is reduced , while mainly intensity of P_{II} is increased. This ansatz is not discussed further.

Even though the results vary somewhat between the two approaches 1. and 2. both share some common features. Both panels, 8.18 (a) and (b), reveal, that the static background is about 10 % in the PR and about 30 % in the FR measurement, in agreement with the discussion for T = 182 K. It is due to the molecular species that gives rise to the (s) relaxation in SLR. It is possibly connected to process P_{III} in DS. In both fitting approaches, the weight of the faster process P_I increases compared to P_{II}. The reason for this behavior is unclear. Possibly it is due to different motional mechanisms of the processes and therefore, a different evolution time dependence.
The correlation times obtained from ansatz 2 are plotted in figure 8.19. There, it becomes clear that the time constants of the faster process P_I are approximately constant and about a factor 8 slower than the ones obtained from DS. The slower process P_{II} exhibits correlation times that decrease with increased t_p by a factor of ten. At evolution times $t_p > 20\,\mu s$ it well agrees with the time constants from DS. The features of this slower process are similar to the process measured at 182 K.

In summary the findings for DiPGME agree well with the data obtained from DS [258]. The measured STE can be described by two dynamical processes, likely the α-process and the secondary w-relaxation as found in DS. Both relaxations stem from molecules giving rise to the faster SLR (f) relaxation, while the slower component (s) is static in all STE measurements. The latter finding affirms

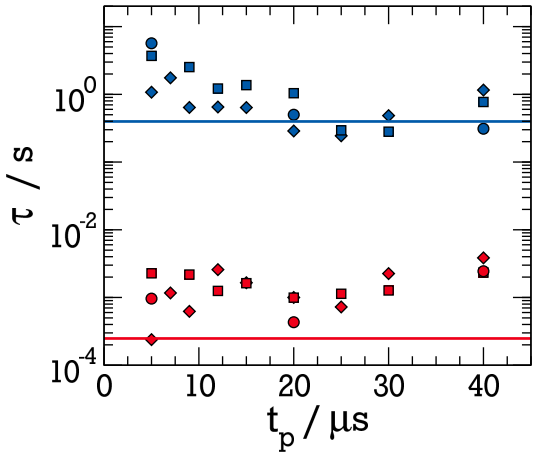

Figure 8.19.: Correlation times obtained from DiPGME-water W15c at T = 172 K for the process P_f (red) and P_s (blue). Colored lines indicate the time constants obtained from DS.

that the (s) component stems from a solid like species. The process called P_{II} exhibits a small angular amplitude and is isotropic at 182 K. It is compatible to an isotropic reorientation with an average jump angle of 15°. The faster process P_I shows indications of large angular amplitude. The isotropy of this process can not be determined in the present study. The third DS process, P_{III}, is static in all experiments and is possibly connected to the motional process responsible for the SLR (s) relaxation.

8.2.3 Discussion of the results

The discussion starts with the mean logarithmic correlation times τ_m. They have been calculated from SLR using the CD spectral density in the BPP ansatz, as motivated by the findings of DS [258]. Additionally, the correlation time from the LSA has been included together with those obtained from STE experiment in the last section.
In the case of the bulk PGME mixtures the interpretation of the correlation times shown in figure 8.20 (a) is straightforward. Starting at high temperatures the data follow a fragile temperature dependence that can be described by the VFT equation eq. (2.4). The resulting fit parameters are listed in table 8.5. The fit implies a glass transition temperature of $T_g \approx 162$ K for the W40b sample, which agrees well with that found in DSC measurements on the same mixture [130]. At ca. 180 K the time constants obtained from the STE experiment deviate from the VFT behavior. Here, the observed dynamics are dominated by the secondary w-relaxation.
The figure also shows the results obtained from DS on the same bulk mixture [130]. The paper only gives the peak correlation times, which in case of the w-

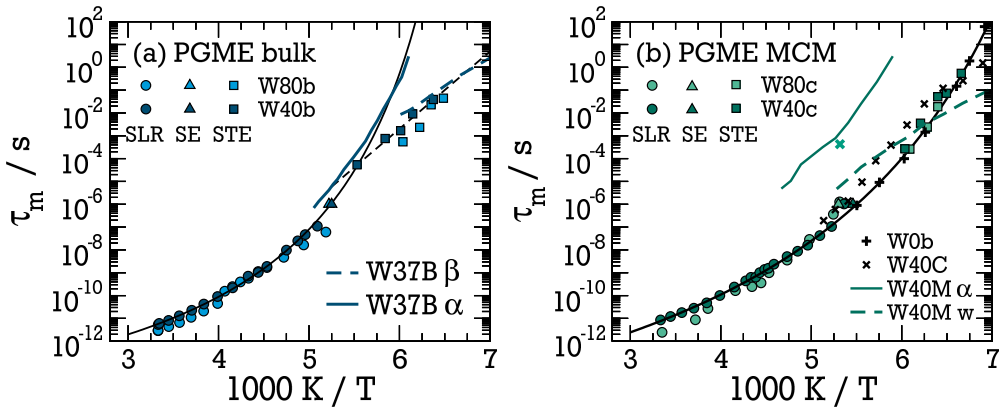

Figure 8.20.: Correlation times τ_m of PGME-water mixtures obtained by ^{2}H NMR methods: (a) bulk mixtures W40b and W80b. Black solid line is a VFT fit to the ^{2}H NMR data above 180 K, see eq. (2.4). Black dashed line is an ARR fit to the STE data of W40b, see table 8.4. Dark blue lines are DS data [130] of the α-process (solid) and the w-process (dashed). (b) confined mixtures W40c and W80c. The turquoise cross is the correlation time obtained from the FR STE at 188 K. Black line is a VFT fit, to the ^{2}H NMR data, turquoise lines are α-process (solid) and w-process (dashed) in d = 2.1 nm confinement [143]. Black pluses are bulk PGME behavior and black crosses are a PGME W40 mixture confined to Clay [86].

process are compatible with the τ_m reported here, since a CC function was used in DS. Larger deviations are expected for the α-process, since it is of a HN-like shape. At lower temperatures the correlation times of the STE well agree with those measured for the secondary process in DS. Presumably, the NMR data would follow the temperature dependence of the w-process on lowering temperature, if SLR would not prevent measurements below 154 K. Basically no anisotropy was measured at any temperature in the STE experiments. This indicates that the correlation is mostly lost on the STE time scale and thus, nearly all molecules take part in the motional process down to the lowest measured temperatures. Some residual correlation must be left over by the w-process, since the DS experiments detect the α-process at temperatures where the w-process is present. Even though the STE experiments do not detect the residual correlation it can be more pronounced in DS experiments due to the difference in the measured correlation functions in both methods. Similar results were found for bulk PG-water mixtures of alike water concentrations [124].

Sample W80b shows a behavior very similar to that of W40b, see in the figure 8.20 (a). Under the assumption that the shape of the distribution of correlation times $G\big[\log(\tau)\big]$ is similar in both samples, it is found that the SLR time constants around the $\langle T_{1,f}\rangle$ minimum are identical at all concentrations. At higher temperatures, the dynamics in W80b are faster due to the larger amount of

Table 8.5.: Parameters obtained from fitting the PGME-water mixtures W40b and W40c using a VFT law eq. (2.4).

Sample	τ_0 /s	B	T_{VFT} / K	m	T_g / K
W40b	$9.5 \cdot 10^{-15}$	1070.6	132.8	47.9	161.9
W40c	$2.9 \cdot 10^{-15}$	1554.2	102.6	34.6	143.4

water, again if $G\big[\log(\tau)\big]$ is unchanged in the unfrozen sample. At lower temperatures, the higher water concentrations seem to be slightly faster, as can e.g. be observed in the STE. This is likely due to the residual water content in the liquid, see table 4.4. The idea that the crystallization has negligible effects on $G\big[\log(\tau)\big]$ can be understood either by formation of a single large ice crystal, or several smaller nuclei which are well separated from each other.

The situation is different in the case of the confined PGME-water mixtures. The respective mean logarithmic correlation times are shown in panel (b) of figure 8.20. Focusing on the W40c first, the time constant obtained by the different ^{2}H NMR methods can be described by a single VFT law over the whole temperature range. Comparing to the results obtained in a smaller MCM-41 confinement of d = 2.1 nm [143], a clear difference can be observed [5]. The dielectric w-process shows a rather different temperature dependence than the observed NMR process. A better agreement is achieved when the ^{2}H NMR data is compared to either a W40 PGME-water mixture confined to vermiculite clay (W40C) [86] or bulk PGME (W0, without confinement) [143], both data are shown in the figure. The agreement with the bulk W0 PGME is strikingly good. The W80c mixture shows a very similar behavior as the W40c mixture, thus likely the same dynamics are observed. Taking into account the STE measurement in W80c at 188 K the following scenarios may explain the findings:
In the larger MCM-41 pores used in the present study, phase segregation occurs introduced by the confinement. Since the water is freezing, it is likely to do so in the pore center, pushing the alcohol molecules towards the surface, as was e.g. found in MD simulations of ethanol-water mixtures [255]. Thus, at lower temperatures, the alcohol molecules are sandwiched between the MCM-41 walls and the ice core of the pore, as sketched for PG in figure 8.5 (a). Then the observed dynamics corresponding to the SLR (f) relaxation below the freezing temperature is mainly due to PGME molecules. This is assisted by the temperature evolution of the SLR amplitude below the T_2-hole, compare figure 8.8. The slow SLR (s) relaxation is related to either to still liquid water molecules or to some α-process-like relaxation. A large amount of water molecules freezes in the crystallization event at high temperatures. The reduc-

[5] Note that in the case of confined PGME-water mixtures the shape parameters of the HN functions are reported and thus here the time constants τ_m have been calculated.

tion factor R (figure 8.8) suggests, that upon lowering temperature more water molecules cluster to the existing nuclei, reducing the concentration of water in the residual liquid and thereby the observable signal in the temperature range around the $\langle T_1 \rangle$ minimum. At lowest temperatures where STE experiments can be employed, the dynamics are dominated by the PGME molecules. Since a single VFT is able to describe the dynamics, this demixing must happen already at room temperature.
The situation is different in the even smaller confinement in [143]. It seems likely that a similar demixing as in the larger pores occurs in this confinement. Assuming a PGME layer with at least 0.3 nm thickness at the walls and an additional unfrozen water layer with equal thickness to be present [259], the 2.1 nm MCM-41 pores could house a crystal of three molecules of water across. Due to this limited size, it is possible that crystallization is completely suppressed here. The residual water could explain why the DS correlation times of the w-process do resemble the universal water process. The present results cannot conclusively proof this model, making further inquiries necessary. Opposing this interpretation is the question why the PGME molecules relax bulk like. If they are in close vicinity to the confinement interface, a severe deceleration of their dynamics is expected [89]. A potential resolution of this question may be the fact that ^{2}H NMR observes the dynamics of the deuterated OH groups only, which are maybe less restricted than the whole PGME molecules. Then the resemblance to bulk PGME dynamics would be a coincidence.

Dynamics of DiPGME

The data measured in the DiPGME-water mixtures are interpreted in light of the idea proposed in the previous section. They will be compared to unpublished dielectric data in identical systems, kindly provided by the group of J. Swenson, Gothenburg [258]. Three relaxation processes have been identified at all water concentrations in the DS experiments. Figure 8.21 shows the three processes exemplary for the concentration W15. They are very similar for all other concentrations, already indicating phase separation. Again, the mean logarithmic correlation times τ_m are displayed. Note that the designated w-process is basically identical to the fastest dielectric process in the confined PGME-water mixture, see figure 8.20 (b).
The figure shows the ^{2}H NMR data obtained in this work. At highest temperatures above crystallization, a strong concentration dependence can be observed in these systems, owing to the vastly different number of water molecules in the three samples. Again, if it is assumed that $G\big[\log(\tau)\big]$ does not change upon crystallization the highest water concentration W75c exhibits the fastest dynamics, comparable to those of liquid water, while the lowest concentration W15c shows correlation times that are about one order of magnitude slower.

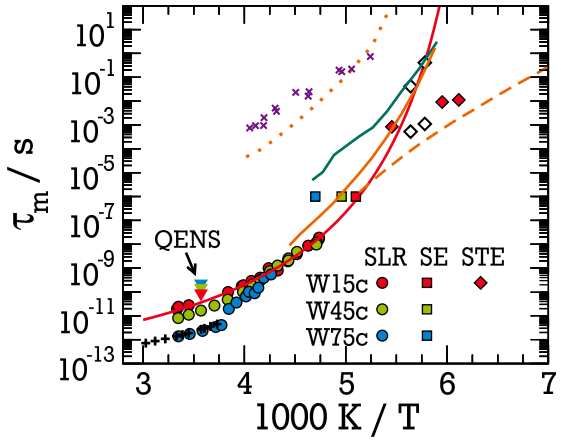

Figure 8.21.: Mean logarithmic correlation times τ_m obtained from DiPGME-water mixtures. Diamonds are values obtained by the STE experiment: filled by fitting a single exponential, empty by utilizing the WWA ansatz. Additionally shown: data from a QENS study [204] (triangles), and from DS [258] as orange lines: α-process (solid), w-process (dashed), ice process (dotted). Purple crosses are ice data from [260]. Turquoise solid line: PGME-water α-process from [143]. Black pluses: bulk D_2O .

The latter time constants are in good agreement with a QENS study at 280 K on this system [204]. At variance to the present results, that investigation found a deceleration of water dynamics upon increasing water content. This was interpreted as imperfect mixing: at low water concentrations, water and DiPGME molecules do not mix and exhibit individual dynamics. Only at higher water concentrations the liquids mix and the water bridges between several DiPGME molecules, forming larger and thereby slower molecular entities. Whether this discrepancy between QENS and ^{2}H NMR can be resolved by assuming a different distribution $G\left[\log(\tau)\right]$ above and below crystallization must be clarified.

Below the freezing temperatures, all studied samples begin to show similar dynamics. While the correlation times obtained from W15c, where crystallization does not occur, follow a continuous temperature behavior, the higher concentrations show an altered temperature dependence. The τ_m values of W45c curve onto the W15c samples, W75c exhibits a discontinuous jump and an altered slope. All three samples well agree at ca. 235 K. The LSA also well agrees in case of W45c and W15c, while in W75c the SE signal minimum occurs at higher temperatures. This is likely due to the (s) relaxation that cannot be resolved in the W75 case. Thus the signal minimum is determined from the combined (f+s) signal shifting it to higher temperatures. In addition, the position of the SLR T_1 minimum indicates a slowdown in W75c.

Compared to the dielectric α-process, the process measured in SLR is about a factor of 3 faster. Such difference is expected for isotropic rotational diffu-

sion [38], compatible with the finding of small-angle rotational jump in the STE experiments discussed in section 8.2.2, c.f. figures 8.16 and 8.19. The trend is continued by the STE time constants: at 183 K only one process is observed, resulting in a value of correlation time that well agree with DS and also the fitted value at 177 K agrees with the α-process. Additionally, it was discussed in section 8.2.2, that all STE experiments can be described using the two faster dielectric processes. At 163 K and 168 K only the fastest process was necessary to describe the STE decay, since the slower one has moved out of the STE time window, similarly at 182 K the faster process has not yet entered the time window of the STE. The time constants obtained by fitting those temperatures with eq. (3.56) are shown in the figure. They are close to the time constant measured in DS affirming, that ^{2}H NMR and DS measure both, the α-process and the w-process. In addition the STE experiments at 172 K and 177 K have been evaluated using the WWA ansatz eq. (8.1). The results are shown in figure 8.21. They well agree the other data.

The measurement at 163 K exhibited approximately constant values of $\tau_m(t_p)$ with varying evolution time (not shown), assisting the finding from section 8.2.2 that the dynamics underlying the w-process involves large angular reorientation. In addition, a residual plateau of at least 45 % is found. Since the W15c mixture comprises 28 % of deuterons bound to the DiPGME this fact shows that the low temperature process must involve the reorientation of water molecules. Comparison with ice relaxation data [260] shows that the third process in DS is due to crystalline ice. The time constants are compatible with those of the SLR (i) relaxation, when the latter is used together with the shape parameters given by DS to calculated correlation times.

It can be concluded that, the dynamics in the DiPGME mixtures are different in nature compared to the monomer mixture. In the monomer case, the findings can be explained by a full decoupling of the dynamics of water and alcohol. In case of the dimer the confined mixtures exhibit coupled dynamics: causing an acceleration of the observed α-process, and an additional w-process. In the PGME mixture the observed dielectric α-process, is likely due to few water molecules in severe confinement, while in DiPGME mixtures it is the combined relaxation of water and alcohol. The w-process is only present when water and alcohol molecules are intermixed or when unfrozen water molecules exist, as in the pure water systems. In the phase separated PGME-water mixtures no such process is observed in the present study. A possible reason for the different behavior of PGME and DiPGME mixtures is the length of the molecules and the additional oxygen in DiPGME. The latter can form hydrogen bonds with water molecules. In combination with the longer, more flexible carbon chain, this may prevent the DiPGME to cluster close to the wall. When the DiPGME molecules loom into the pore center they frustrate the formation of

stable water nuclei. It is interesting to note, that DS and ^{2}H NMR agree well in the case of DiPGME, but show rather different results in PGME mixed with water. A plausible reason for the latter case is the different confinement size that prevents the full demixing of water and alcohol in case of the PGME-water mixtures.

8.3 Summary

In this chapter the molecular dynamics of alcohol-D_2O mixtures in bulk and confined to MCM-41 have been investigated. In the first part, propylene glycol (PG) has been investigated. No considerable effects of the confinement on the dynamics of this mixture have been observed. As was found before [75, 87, 88], the dynamics in confinement exhibit a broader distribution of correlation time $G\big[\log(\tau)\big]$, but the relaxation mechanism seems to be unaltered. A very slow phase transition process was observed, that is to the best of the authors knowledge not yet reported in literature.
In the second part of this chapter, aqueous mixtures of PGME and DiPGME have been investigated. In the bulk liquids, the α-process and the w-process observed in DS have been identified. They well agree with the literature data. In the confined PGME mixtures a different behavior has been observed. A model was proposed to explain the findings by phase separation of the two liquids. In this model, the alcohol clusters at the pore walls and the water in the pore center. There, it forms a solid crystal, leaving only few liquid water molecules at its surface. The observable relaxation then is the one of the PGME molecules at the walls, which are rather uninfluenced and relax like bulk PGME. The question why PGME is not decelerated by the confinement walls remains unanswered and opposes the proposed phase separation.
In a similar MCM-41 confinement the dimer DiPGME was found to exhibit different dynamics from its monomer. As the bulk liquids, again an α-process and a w-process are identified. They well agree with the findings of DS. In all but one confined PGME samples crystallization has been observed. In the confined samples the water crystallized even at concentrations for which freezing is not observed in the bulk. This suggests that the different interactions of water and PGME with MCM-41 promote phase separation, which in all cases cause water to freeze. This shows the necessity to properly chose the confinement in order to achieve or prevent phase segregation. Studies of aqueous mixtures in functionalized confinement are necessary to establish the dependence of the segregation process on the hydroaffinity.

9 Conclusion

In this thesis, the dynamical behaviors of water and aqueous mixtures in bulk and confined in MCM-41 were characterized by several ^{2}H NMR techniques.
For confined water, the pore size dependence of the temperature behavior was determined. At higher temperatures, a single dynamical process was found. This process is slowed down when the water becomes less bulk-like, i.e. it is slowed down in smaller pores. At 225 K a dynamic crossover was observed and the temperature dependence of the correlation times was found to be altered from the high temperature behavior. In other studies, this crossover was observed much more pronounced and was interpreted as the fragile-to-strong transition of water [9, 60] predicted by the second critical point hypothesis [4]. In this work, it was shown that the transition is accompanied by the emergence of a second dynamical species of water molecules. This species was identified to be a solid-like component. It forms for all studied confinement sizes, in contrast to the general assumption that water in very small confinements d $\lesssim$ 2.1 nm is liquid at all temperatures [74]. The appearance of the second species suggests that the apparent FST observed in [9] is due to solidification of water in the center of the confinement rather than to a liquid-liquid phase transition.
Those findings inspired the proposal of a new model interpretation of water behavior in hard confinement. This model postulates the high temperature dynamics of water to be strongly dependent on the system under investigation. It shows faster and more fragile motion when more water is present, becoming more bulk-like. When the second dynamical species forms and the water in the pore center solidifies, possibly into a nano-crystalline phase [220], it gives rise to a solid-like relaxation component. The residual liquid water is sandwiched between the silica walls and the solid water species and the dynamical process of the liquid species is monitored at temperatures below ca. 225 K. The experiments at low temperatures show that the observed process exhibits all signs of a secondary β-process, which shows indications for a glass transition of the system at ca. 185 K. The corresponding structural α-process of the interface layer, if existent, is not directly but indirectly observable in the present measurements.
To characterize the influence of different surfaces on the confined water, a MCM-41 sample with functionalized surface was investigated. The modification has no effect on the overall time scale of the dynamics of the liquid water species. A spectral analysis indicates suppression of motional averaging in the surface layer, possibly due to spatial hindrance of water translation by the functionalization.

In contrast to water, the investigation of glycerol in MCM-41 confinement revealed no strong alterations of the dynamics. The main effects are a broadening of the correlation time distributions, likely due to increased heterogeneity. Additionally, the dynamics are somewhat accelerated with decreasing confinement size. It was not clarified whether this is a confinement effect or is due to residual water in the MCM-41 pores. This question should be addressed in subsequent studies. The results suggest, that the strong effects of confinement on the water behavior are a feature of water and the specific guest-host interactions with the confinement material rather than a general effect of confined supercooled liquids.

In conclusion, the results in this thesis show that it is not possible to interpret the dynamics measured in MCM-41 confinement as those of bulk water. At confinement sizes, where crystallization is suppressed, the effects of the confinement are severe and the bulk properties of water are strongly altered. The investigated systems can help to gain understanding on the properties of interfacial water, which itself is of enormous interest. The existence of a FST in bulk water cannot be clarified in this study. Therefore, no statement on the possible LLPT can be given. The results insinuate that it is not possible to observe bulk water dynamics at low temperatures, since water solidifies as soon as it becomes too bulk-like.

To further investigate the properties of interfacial water, a new method was proposed to determine whether an α-process of the interface layer of water exists and to measure its temperature dependence. The method monitors the temperature at which ergodicity is broken in dependence on the external magnetic field. First measurements have shown promising results, but are not reliable enough to verify the new method.

In addition to water in confinement, the dynamics of aqueous mixtures in bulk and confinement were investigated. The study of those mixtures aims at a better understanding of the phase behavior of such mixtures as well as the possibility of extrapolation of the findings towards the dynamics of water and biologically relevant molecules. In this thesis, first measurements were performed to characterize the concentration dependence and the effect of increasing molecular weights of the solvent in aqueous mixtures. Measurements of the bulk liquids are able to reproduce the findings of literature and thus support the interpretations given there. The present studies increase the studied temperature range significantly and give a characterization of the motional mechanisms in the low temperature domain. A very slow phase transition process in PG-water mixtures was identified, that has not been reported so far. Its effect on the studies on this mixture must be determined. The present measurements suggest that even though crystallization occurs at high water content in the bulk mixtures,

the formed ice crystals have no major effect on the dynamics besides a reduced water content. In all cases, the universal features of the low temperature water process are not affected.
In the confined aqueous mixtures, the measurements show the importance of the interaction between the liquid constituents. The structurally similar alcohols PG and PGME show very different behavior in mixture with water, due to the different H-bonding capabilities of both cosolvents. The first mixture is mostly unaffected by the confinement and the bulk behavior is preserved. In contrast, the PGME-water mixture shows phase separation at all studied concentrations. In case of the monomer, the separation seems to cause all water to crystallize in the pore center and only the alcohol motion is preserved. No crystallization occurs in mixture with the dimer DiPGME. On the one hand, those results demonstrate how important the proper choice of confinement is, when the properties of the enclosed liquid are supposed to be investigated or when controlled results are necessary, as for example in technological applications. On the other hand, the measurements show how subtle differences even in simple molecules can change the overall behavior. An extrapolation to biomolecules like proteins therefore requires great care and precise determination of the interaction. An extrapolation of the behavior of water from aqueous mixtures can only be successful when water does not become too bulk-like. This is not the case when water completely phase separates from the cosolvent.

A Characterization of MCM-41 materials

The MCM-41 samples were characterized by BET and BJH methods on commerically available gas adsorption machines. Characterization was performed by A. Grüenberg, M. Werner, and M. Brodrecht in the group of G. Buntkowsky at Technische Universität Darmstadt. The MCM-41 surface was estimated using the multi-point BET method. The pore size and specific pore volume was determined using the BHJ method of the desorption branch. The analysis gas was nitrogen and data evaluation was performed with the *Quantachrome* NovaWin and the *Surfer* Advanced Data Processing software. Detailed reports on sample characterization are available in the Buntkowsky group. Examples for the characterization of the MCM-41 used for sample P25 and P28 are shown in figures A.1 and A.2, respectively.

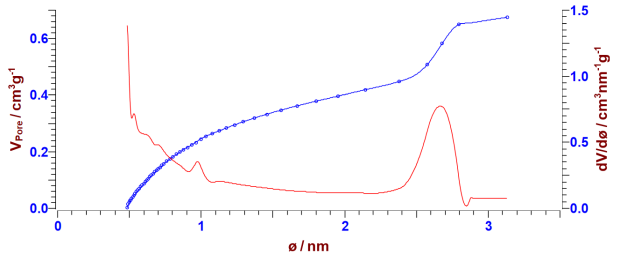

Figure A.1.: BJH pore characteriszation for sample P25 using the Horvath and Kawazoe method for micropores.

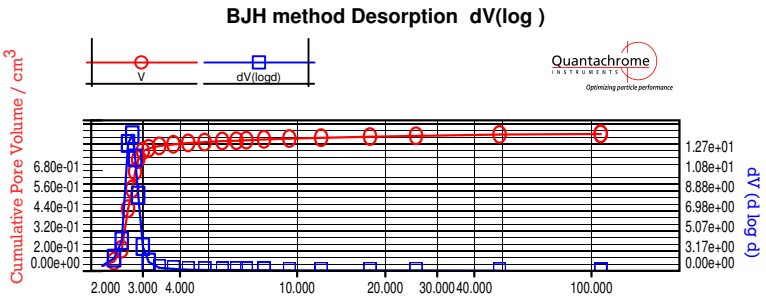

Figure A.2.: BJH pore characteriszation for sample P28 using the desorption branch.

B Supplemental DSC measurements

Slow phase transition in PG-water mixtures

To show that the long term effect observed in the PG-water mixtures is a crystallization effect, a DSC measurement was performed by T. Blochowicz. The sample was cooled to 197 K and kept at this temperature for 20 h. Thereafter a heating thermogram was measured at a heating rate of 10 $\frac{\mathrm{K}}{\mathrm{min}}$. It is depicted in figure B.1 and exhibits a pronounced melting peak at ca. 240 K.

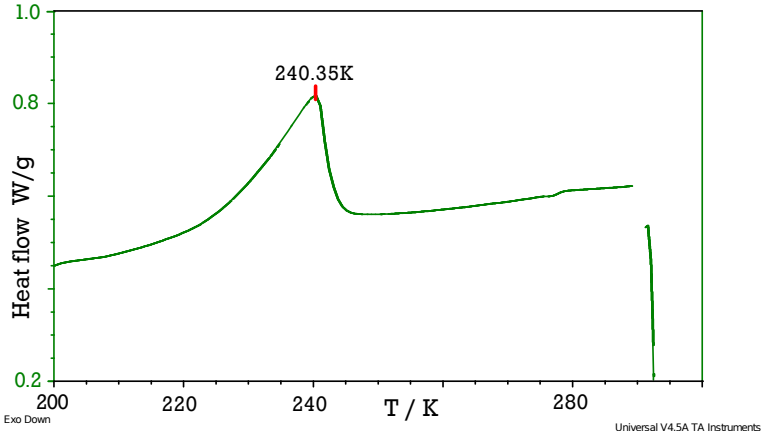

Figure B.1.: DSC heating curve after keeping sample PG W45b at 197 K for 20 h.

Bulk and confined PGME-D_2O mixtures

Here, DSC measurements of the PGME-water mixtures W80 (figure B.2) and W60 (figure B.3) are shown in bulk and in confinement. The measurements were performed in the group of Stühn at Technische Universität Darmstadt by T. Nickels. Shown are cooling and rates of 10 $\frac{\mathrm{K}}{\mathrm{min}}$. In the W80 samples only crystallization and melting of water are observed. The W60 samples show no freezing on cooling, but a cold crystallization followed by a subsequent melting.

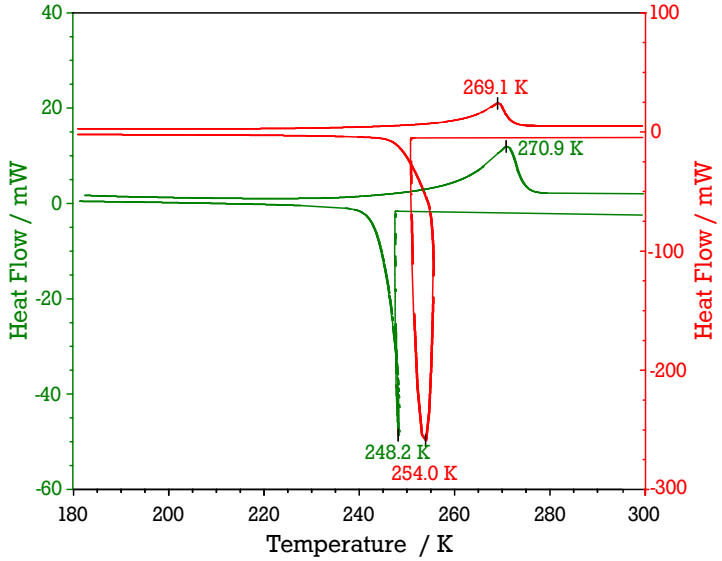

Figure B.2.: DSC curve at a hating rate of 10 $\frac{K}{min}$ of the PGME-D_2O mixtures W80b (red) and W80c (green). Note, the different scales.

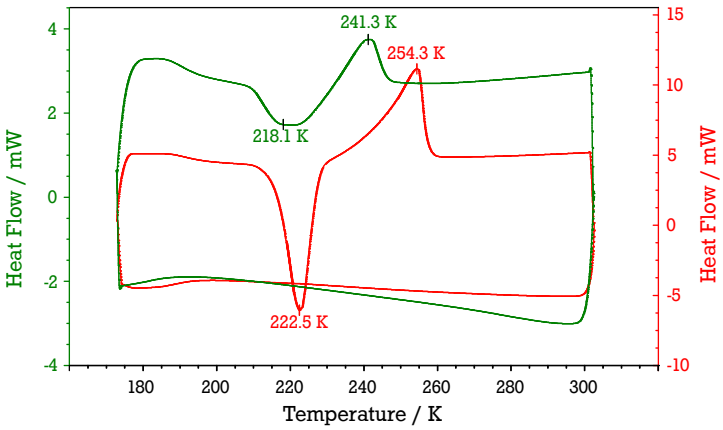

Figure B.3.: DSC curve at a hating rate of 10 $\frac{K}{min}$ of the PGME-D_2O mixtures W60b (red) and W60c (green). Note, the different scales.

C Details of NMR Experiments

This chapter briefly lists the used phase cycles in the various performed experiments. A short description about the working principles will be given as well. Note that all phase cycles make use of CYCLOPS, which is a fourfold repetition of all other steps, where every time all phases are shifted by 90°. This compensates for channel imbalance and DC offset.

Phase cycle in SE experiments

In all performed experiments using solid echo (SE) detection an eight fold phase cycle is employed. It is listed in table C.1. The first pulse α and the second pulse β are always phase shifted by 90° with respect to each other. As can be see in the table, the phase of pulse β is flipped by 180° in every other step to compensated leftover FID signal.

Table C.1.: Eight fold phase cycle used in SE experiments. Shown are the first two cycles with 180° shift in pulse β. The three dots abbreviate the additional 6 CYLCOPS cycles.

step	$\alpha = 90°$	$\beta = 90°$	Receiver
1	+x	+y	-y
2	+x	-y	-y
⋮			

Phase cycle in STE experiments

Tables C.2, C.3, and C.4 list the phase cycles used in STE experiments of ze order and sa order. The cycle in tab. C.2 was used for Zeeman experiments where only evolution times longer as the electronic dead time t_p ¿ 10μs were measured. In all other cases, the four pulse experiments have been utilized with the phase cycles in tab. C.2 and tab. C.2.

Table C.2.: Eight fold phase cycle for ze order STE experiments.

step	$\alpha = 90°$	$\beta = 90°$	$\gamma = 90°$	Receiver
1	x	x	x	-x
2	x	-x	x	x
3	y	y	x	-x
4	y	-y	x	x
5	-x	-x	x	-x
6	-x	x	x	x
7	-y	-y	x	-x
8	-y	y	x	x

Table C.3.: 16 step phase cycle in STE experiments of ze order.

step	$\alpha = 90°$	$\beta = 90°$	$\gamma = 90°$	$\delta = 90°$	Receiver
1	x	x	x	y	-x
2	x	-x	x	y	x
3	-x	-x	x	y	-x
4	-x	x	x	y	x
5	y	y	x	y	-x
6	y	-y	x	y	x
7	-y	-y	x	y	-x
8	-y	y	x	y	x
9	x	x	x	-y	-x
10	x	-x	x	-y	x
11	-x	-x	x	-y	-x
12	-x	x	x	-y	x
13	y	y	x	-y	-x
14	y	-y	x	-y	x
15	-y	-y	x	-y	-x
16	-y	y	x	-y	x

Table C.4.: 16 step phase cycle in STE experiments of sa order.

step	$\alpha = 90°$	$\beta = 90°$	$\gamma = 90°$	$\delta = 90°$	Receiver
1	x	y	y	y	-x
2	x	-y	y	y	x
3	-x	-y	y	y	-x
4	-x	y	y	y	x
5	y	-x	y	y	-x
6	y	x	y	y	x
7	-y	x	y	y	-x
8	-y	-x	y	y	x
9	x	y	y	-y	-x
10	x	-y	y	-y	x
11	-x	-y	y	-y	-x
12	-x	y	y	-y	x
13	y	-x	y	-y	-x
14	y	x	y	-y	x
15	-y	x	y	-y	-x
16	-y	-x	y	-y	x

Bibliography

[1] N. A. Campbell, J. B. Reece, Urry, Cain, Wasserman, Minorsky, and Jackson. *Biologie*. Pearson Education, 2008.

[2] M. Chaplin. Do we underestimate the importance of water in cell biology? *Nature Rev.*, 7:861–866, 2006.

[3] R. J. Speedy. Stability-limit conjecture. an interpretation of the properties of water. *J. Phys. Chem.*, 86:982 – 991, 1982.

[4] P. H. Poole. Phase behaviour of metastable water. *Nature*, 360:324–328, 1992.

[5] S. Sastry, P. G. Debenedetti, F. Sciortino, and H. E. Stanley. Singularity-free interpretation of the thermodynamics of supercooled water. *Phys. Rev. E*, 53:6144 – 6154, 1996.

[6] T. Koop. Homogeneous ice nucleation in water and aqueous solutions. *Z. Phys. Chem.*, 2004:1231–1258, 2004.

[7] C. Austen Angell. Insights into phases of liquid water from study of its unusual glass-forming properties. *Science*, 319:582 – 587, February 2008.

[8] O. Mishima and H. E. Stanley. The relationship between liquid, supercooled and glassy water. *Nature*, 396:329 – 335, 1998.

[9] L. Liu, S.-H. Chen, A. Faraone, C.-W. Yen, and C.-Y. Mou. Pressure dependence of fragile-to-strong transition and a possible second critical point in supercooled confined water. *Phys. Rev. Lett.*, 95:117802, 2005.

[10] J. Hedström, J. Swenson, R. Bergman, H. Jansson, and S. Kittaka. Does Confined Water Exhibit a Fragile-to-Strong Transition? *Eur. Phys. J. Special Topics*, 141:53–56, 2007.

[11] J. Swenson and S. Cerveny. Dynamics of Deeply Supercooled Interfacial Water. *J. Phys.: Conden. Matt.*, 27:033102, 2015.

[12] A. Cavagna. Supercooled Liqudis for Pedestrians. *Physical Reports*, 476:51 – 124, 2009.

[13] M. D. Ediger and Peter Harrowell. Perspective: Supercooled liquids and glasses. *J. Chem. Phys.*, 137:080901, 2012.

[14] Pablo G. Debenedetti and Frank H. Stillinger. Supercooled liquids and the glass transition. *Nature*, 410:259 – 267, 2001.

[15] C. A. Angell, K. L. Ngai, G. B. McKenna, P. F. McMillan, and S. W. Martin. Relaxation in glassforming liquids and amorphous solids. *J. Appl. Phys.*, 88:3113, 2000.

[16] J. A. Sellberg, C. C. Huang, T. A. McQueen, N. D. Loh, H. Laksmono, et al. Ultrafast x-ray probing of water structure below the homogeneous ice nucleation temperature. *Nature*, 510:381 – 384, 2014.

[17] M. D. Ediger. Spatially Heterogeneous Dynamics in Supercooled Liquids. *Annu. Rev. Phys. Chem.*, 51:99–128, 2000.

[18] M. D. Ediger, C. A. Angell, and Sidney R. Nagel. Supercooled liquids and glasses. *J. Phys. Chem.*, 100:13200 – 13212, 1996.

[19] W. Kob and H. C. Andersen. Scaling Behavior in the β-Relaxation Regime of a Supercooled Lennard-Jones Mixture. *Phys. Rev. Lett.*, 73:1376, 1994.

[20] W. Kob and H. C. Andersen. Testing mode-coupling theory for a supercooled binary Lennard-Jones mixture. *Phys. Rev. E*, 24:1179–1198, 1995.

[21] J. Qvist, C. Mattea, E. P. Sunde, and B. Halle. Rotational dynamics in supercooled water from nuclear spin relaxation and molecular simulations. *J. Chem. Phys.*, 136:204505, 2012.

[22] W. Kauzmann. The nature of the glassy state and the behavior of liquids at low temperatures. *Chem. Rev.*, 43:219 – 256, 1948.

[23] P. J. Flory. Phase equilibria in solutions of rod-like particles. *Proc. R. Soc. Lond. A*, 234:1196, 1956.

[24] J. H. Gibbs. Nature of the glass transition in polymers. *J. Chem. Phys.*, 25:185, 1956.

[25] J. H. Gibbs and A. DiMarzio. Nature of the glass transition and the glassy state. *J. Chem. Phys.*, 28:373, 1958.

[26] G. Adam and J. H. Gibbs. On the temperature dependence of cooperative relaxation properties in glass-forming liquids. *J. Chem. Phys.*, 43:139–146, 1965.

[27] E. Jenckel. Zur Temperaturabhängigkeit der Viskosität von Schmelzen. *Z. Physik. Chem. A*, 184:309, 1939.

[28] F. Klameth. *From Brownian motion to supercooled water in confinements - a molecular dynamics simulation study*. PhD thesis, Technische Universität Darmstadt, 2014.

[29] R. Kohlrausch. Theorie des elektrischen Rückstandes in der Leidener Flasche. *Ann. Phys. Chem.*, 91:179–214, 1874.

[30] G. Williams and D. C. Watts. Non-symmetrical dielectric relaxation behaviour arising from a simple empirical decay function. *Trans. Faraday Soc.*, 66:80–85, 1970.

[31] R. Böhmer, G. Diezemann, G. Hinze, and E. Rössler. Dynamics of supercooled liquids and glassy solids. *Prog. Nucl. Magn. Reson. Spectrosc.*, 39:191– 267, 2001.

[32] J. Gabriel, O. V. Petrov, Y. Kim, S. W. Martin, and M. Vogel. Lithium ion dynamics in $Li_2S+GeS_2+GeO_2$ glasses studied using ^{7}Li NMR field-cycling relaxometry and line-shape analysis. *Solid State NMR*, 70:53–62, 2015.

[33] R. Richert. Homogeneous dispersion of dielectric responses in a simple glass. *J. Non-Cryst. Solids*, 209:172 – 174, 1994.

[34] M. Vogel and T. Torbrügge. Nonexponential polymer segmental motion in the presence and absence of ions: ^{2}H NMR multitime correlation functions for polymer electrolytes poly(propylene glycol)-$liclo_4$. *J. Chem. Phys.*, 126:204902, 2007.

[35] P. A. Beckmann. Spectral densities and nuclear spin relaxation in solids. *Physics Reports*, 171(3):85 – 128, July 1988.

[36] R. Metzler and J. Klafter. From stretched exponential to inverse power-law: Fractional dynamics, Cole-Cole relaxation processes, and beyond. *J. Non-Cryst. Solids*, 305:81–87, 2002.

[37] C. P. Lindsey and G. D. Patterson. Detailed comparison of the Williams–Watts and Cole–Davidson functions. *J. Chem. Phys.*, 73:3348 – 3357, 1980.

[38] R. Böhmer, G. Diezemann, G .and Hinze, and E. Rössler. Dynamics of supercooled liquids and glassy solids. *Prog.Nucl. Magn. Res. Spectr.*, 39:191–267, 2001.

[39] R. Zorn. Logarithmic moments of relaxation time distributions. *J. Chem. Phys.*, 116(8):3204–3209, Februar 2002.

[40] D. Eisenberg and W. Kauzmann. *The structure and properties of water*. Oxford : Clarendon Press, 1969.

[41] P. G. Debenedetti. Supercooled and glassy water. *J. Phys.: Conden. Matt.*, 15:R1669–1726, 2003.

[42] M. Chaplin. Water structure and science, `http://www1.lsbu.ac.uk/water/water_structure_science.html`, 2015.

[43] T. Bartels-Rausch, V. Bergeron, J. H E. Cartwright, R. Escribano, J. L. Finney, et al. Ice structures, patterns, and processes: A view across the icefields. *Rev. Mod. Phys.*, 84:885–944, 2012.

[44] F. H. Stillinger. Water Revisited. *Science*, 209:451–467, 1980.

[45] L. Pauling. *General Chemestry*. Dover Publications; 3rd Revised ed. edition, 1988.

[46] R. J. Speedy and C. A. Angell. Isothermal compressibility of supercooled water and evidence for a thermodynamic singularity at −45°c. *J. Chem. Phys.*, 65:851, 1976.

[47] D. Mongk. Elctronically puplished, Montana State University, `http://serc.carleton.edu/research_education/equilibria/phaserule.html`.

[48] R. J. Speedy. Limitin Forms of the Thermodynamic Diverences at the Conjectured Stability Limits in Superheated and Supercooled Water. *J. Phys. Chem.*, 86:3002 – 3005, 1982.

[49] M.-C. Bellisent-Funel, S. H. Chen, and J.-M. Zanotti. Single-particle dynamics of water molecules in confined space. *Phys. Rev. E*, 51:4558 – 4569, 1995.

[50] C. A. Tulk, C. J. Benmore, J. Urquidi, D. D. Klug, J. Neuefeind, B. Tomberli, and P. A. Egelstaff. Structural Studies of Several Distinct Metastable Forms of Amorphous Ice. *Science*, 297:1320–1323, 2002.

[51] R. Car J. C. Palmer and P. G. Debenedetti. The liquid–liquid transition in supercooled st2 water: a comparison between umbrella sampling and well-tempered metadynamics. *Faraday Discuss.*, 167:77 – 94, 2013.

[52] J. C. Palmer, F. Martelli, Y. Liu, R. Car, A. Z. Panagiotopoulos, and P. G. Debenedetti. Metastable liquid–liquid transition in a molecular model of water. *Nature Lett.*, 510:385–388, 2014.

[53] Y. Li, J. Li, and F. Wang. Liquid-Liquid Transition in Supercooled Water Suggested by Microsecond Simulations. *PNAS*, 110:12209–12212, 2013.

[54] L. G. M. Pettersson and A. Nilsson. The structure of water; from ambient to deeply supercooled. *J. Non-Cryst. Solids*, 407:399–417, 2015.

[55] P. Demontis, J. Gulín-Gonzáles, M. Masia, M. Sant, and G. B. Suffritti. The interplay between dynamic heterogeneities and structure of bulk liquid water: A molecular dynamics simulation study. *J. Chem. Phys.*, 142:244507, 2015.

[56] V. Molinero and E. B. Moore. Water modeled as an intermediate element between carbon and silicon. *J. Phys. Chem. B*, 113:4008, 2009.

[57] D. T. Limmer and D. Chandler. Phase diagram of supercooled water confined to hydrophilic nanopores. *J. Chem. Phys.*, 137:044509, 2012.

[58] D. T. Limmer and D. Chandler. The putative liquid-liquid transition is a liquid-solid transition in atomistic models of water. ii. *J. Chem. Phys.*, 138:214504, 2013.

[59] E. B. Moore and V. Molinero. Structural transformation in supercooled water controls the crystallization rate of ice. *Nature*, 479:506 – 509, 2011.

[60] K. Ito, C. T. Moynihan, and C. A. Angell. Thermodynamic determination of fragility in liquids and a fragile-to-strong liquid transition in water. *Nature*, 398:492 – 495, 1999.

[61] O. Mishima and H. E. Stanley. The relationship between liquid, supercooled and glassy water. *Nature*, 396:329 – 335, 1998.

[62] G. P. Johari, A. Hallbrucker, and E. Mayer. The glass-liquid transition of hyperquenched glassy water. *Nature*, 330:552 – 55, 1987.

[63] A. Hallbrucker, E. Mayer, and G. P. Johari. Glass-liquid transition and the enthalpy of devitrification of annealed vapor-deposited amorphous water. *J. Phys. Chem*, 93:4986 – 4990, 1989.

[64] K. Hofer, E. Mayer, and G. P. Johari. Glass-liquid transition of water and ethylene glycol solution in poly(2-hydroxyethyl metharcrylate) hydrogel. *J. Phys. Chem.*, 94:2689 – 2696, 1990.

[65] G. B. McKenna. Size and confinement effects in glass forming liquids: Perspectives on bulk and nano-scale behaviours. *J. Phys. IV France*, 10:7 – 53, 2000.

[66] R. Richert. Dynamics of Nanoconfined Supercooled Liquids. *Annu. Rev. Phys. Chem.*, 62:65–84, 2011.

[67] T. R. Böhme and J. J. de Pablo. Evidence for size-dependent mechanical properties from simulations of nanoscopic polymer structrurs. *J. Chem. Phys.*, 116:9939–9951, 2002.

[68] M. Vallet-Regi, A. Rámila, R. P. del Real, and J. Pérez-Pariente. A New Property of MCM-41: Drug Delivery System. *Chem. Mater,*, 13:308–311, 2001.

[69] J. Swenson and J. Teixeira. The glass transition and relaxation behavior of bulk water and a possible relation to confined water. *J. Chem. Phys.*, 132:014508, 2010.

[70] J. Zhang, G. Liu, and J. Jonas. Effects of Confinement on the Glass Transition Temperature of Molecular Liquids. *J. Phys. Chem.*, 96:3478–3480, 1992.

[71] D. Morineau, Y. Xia, and C. Alba-Simionesco. Finite-size and surface effects on the glass transition of liquid toluene confined in cylindrical mesopores. *J. Chem. Phys.*, 117:8966 –8972, 2002.

[72] R. Schmidt, E. W. Hansen, M. Stoecker, D. Akporiaye, and O. H. Ellestad. Pore Size Determination of MCM-41 Mesoporous Materials by means of ^{1}H NMR Spectroscopy, N_2 adsorption, and HREM. A Preliminary Study. *J. Am. Chem. Soc.*, 117:4049–4056, 1995.

[73] E. W. Hansen, M. Stöcker, and R. Schmidt. Low-Temperature Phase Transition of Water Confined in Mesopores Proped by NMR. Influence on Pore Size Distribution. *J. Phys. Chem.*, 100:2195–2200, 1996.

[74] S. Jähnert, F. Vaca Chavez, G. E. Schaumann, A. Schreiber, M. Schonhoff, and G. H. Findenegg. Melting and freezing of water in cylindrical silica nanopores. *Phys. Chem. Chem. Phys.*, 10:6039–6051, 2008.

[75] M. Vogel. NMR studies on simple liquids in confinement. *Eur. Phys. J. Special Topics*, 189:47 – 64, 2010.

[76] C. Le Quellec, G. Dosseh, F. Audonnet, N. Brodie-Linder, and C. Alba-Simionesco. Influence of surface interactions on the dynamics of the glass-former ortho-terphenyl confined in nanoporous silica. *Eur. Phys. J. Special Topics*, 141:11–18, 2007.

[77] J. Y. Park and G. B. McKenna. Size and confinement effects on the glass transition behavior of polystyrene/o-terphenyl polymer solutions. *Phys. Rev. B*, 61:6667–6676, 2000.

[78] W. Zheng and S. L. Simon. Confinement effects on the reactivity and properties of nanoconfined bisphenol m dicyanate ester in controlled pore glass. *Macromol.*, 127:194501, 20007.

[79] Y. P. Koh and S. L. Simon. Trimerization of monocyanate ester in nanopores. *J. Phys. Chem.*, 114:7727–7734, 2010.

[80] M. Arndt, R. Stannarius, W. Gorbatschow, and F. Kremer. Dielectric investigation on the dynamic glass transition in nanopores. *Phys. Rev. E*, 54:5377–5390, 1996.

[81] R. Richert and M. Yang. Surface induced glass transition in confined molecular liquid. *J. Phys. Chem. B*, 107:895–898, 2003.

[82] R. Richert and M. Yang. Solvation dynamics of molecular glass-forming liquids in confinement. *J. Phys.: Conden. Matt.*, 15:S1041–S1050, 2003.

[83] F. Klameth, P. Henritzi, and M. Vogel. Structure and dynamics of supercooled water in neutral confinement. *J. Chem. Phys.*, 138:134503, 2013.

[84] F. Klameth and M. Vogel. Slow Water Dynamics near a Glass Transition or a Solid Interface: A Common Rationale. *J. Phys Chem. Lett.*, 6:4385–4389, 2015.

[85] R. Bergman and J. Swenson. Dynamics of supercooled water in confined geometry. *Nature*, 403:283–286, 2000.

[86] K. Elamin, J. Björklund, F. Nyhlén, M. Yttergren, L. Martensson, and J. Swenson. Glass transition and relaxation dynamics of propylene glycol-water solutions confined in clay. *J. Chem. Phys.*, 141:034505, 2014.

[87] S. A. Lusceac, C. Koplin, P. Medick, M. Vogel, N. Brodie-Linder, C. LeQuellec, C. Alba-Simionesco, and E. A. Rössler. Type A versus Type B Glass Formers: NMR Relaxation in Bulk and Confining Geometry. *J. Phys. Chem. B*, 108:16601–16605, 2004.

[88] S. A. Lusceac, M. R. Vogel, and C. R. Herbers. ^{2}H and ^{13}C NMR studies on the temperature-dependent water and protein dynamics in hydrated elastin, myoglobin and collagen. *BBA Prot.*, 1804:41–48, 2010.

[89] M. Rosenstihl, K. Kämpf, F. Klameth, M. Sattig, and M. Vogel. Dynamics of interfacial water. *J. Non-Cryst. Solids*, 407:449 – 458, 2015.

[90] R. Richert. Geometrical confinement and cooperativity in supercooled liquids studied by solvation dynamics. *Phys. rev. b*, 54:15762, 1996.

[91] F. Klameth and M. Vogel. Static and dynamic length scales in supercooled liquids: Insights from molecular dynamics simulations of water and tripropylene oxide. *J. Chem. Phys.*, 140:144501, 2014.

[92] R. Valiullin and I. Furó. Low-temperature phase separation of a binary liquid mixture in porous materials studied by cryoporometry and pulsed-field-gradient NMR. *Phys. Rev. E*, 66:031508, 2002.

[93] R. Valiullin and I. Furó. Phase separation of a binary liquid mixture in porous media studied by nuclear magnetic resonance cryoporometry. *J. Chem. Phys.*, 116:1072, 2002.

[94] S. Lacelle, L. Tremblay, Y. Bussière, F. Cau, and C. G. Fry. NMR Studies of Phase Separation of a Binary Liquid in a Porous Glass. *Phys. Rev. Lett.*, 74:5228, 1995.

[95] C. A. Angell, J. Shuppert, and J. C. Tucker. Anomalous properties of supercooled water: heat capacity, expansitivity, and PMR chemical shift from 0 to -38°C. *J. Phys. Chem.*, 77:3092 – 3099, 1973.

[96] P. Levitz, G. Ehret, S. K. Sinha, and J. M. Drake. Porous vycor glass: The microstructure as probed by electron microscopy, direct energy transfer, small-angle scattering, and molecular adsorption. *J. Chem. Phys.*, 95:6151, 1991.

[97] A. Faraone, L. Liu, C.-Y. Mou, C.-P. Shih, J. R. D. Copley, and S.-H. Chen. Translational and rotational dynamics of water in mesoporous silica materials: MCM-41-S and MCM-48-S. *J. Chem. Phys.*, 119(7):3963–3971, 2003.

[98] H. Pahlke. *Die Dynamik von Wasser in Zeolithen*. PhD thesis, Technische Universität Darmstadt, 2012.

[99] R. M. Barrer. Syntheses and reactions of mordenite. *J. Chem. Soc.*, 1:2158–2163, 1978.

[100] C.-W Hsu, Y.-W. Chen, B. S. Rana, R. Kumar, and Sinha A. K. Dynamics of Water in Hierarchical Mesoporous H-ZSM-5 by Fast Field-Cycling NMR Relaxomtery. *J. Phys Chem. C*, 118:20481–20487, 2014.

[101] S. Cerveny, J. Mattsson, J. Swenson, and R. Bergman. Relaxation of Hydrogen-Bonded Liqudis Confined in Two-Dimensional Vermiculite Clay. *J. Phys. Chem. B*, 108:11596 – 11603, 2004.

[102] S. Takahara, M. Nakano, S. Kittaka, Y. Kuroda, T. Mori, H. Hamano, and T. Yamaguchi. Neutron Scattering Study on Dynamics of Water Molecules in MCM-41. *J. Phys. Chem. B*, 103(28):5814–5819, 1999.

[103] C. T. Kresge, M. E. Leonwicz, W. J. Roth, J. C. Vartuli, and J. S. Beck. Ordered mesoporous sieves synthesized by a liquid-crystal template mechanism. *Nature*, 359:710–712, 1992.

[104] M. Grün, K. Ungera, A. Matsumotob, and K. Tsutsumib. Novel pathways for the preparation of mesoporous MCM-41 materials: control of porosity and morphology. *Micropor.and Mesopor. Mat.*, 27:207–216, 1999.

[105] Toshinori Mori, Yasushige Kuroda, Yuzo Yoshikawa, Mahiko Nagao, and Shigeharu Kittaka. Preparation of a Water-Resistant Siliceous MCM-41 Sample, through Improvement of Crystallinity, and Its Prominent Adsorption Features. *Langmuir*, 18:1595–1603, February 2002.

[106] K. Yoshida, T. Yamaguchi, S. Kittaka, M.-C. Bellissent-Funel, and P. Fouquet. Thermodynamic, structural, and dynamic properties of supercooled water confined in mesoporous MCM-41 studied with calorimetric, neutron diffraction, and neutron spin echo measurements . *J. Chem. Phys.*, 129:054702, 2008.

[107] S.-H. Chen, L. Liu, E. Fratini, P. Baglioni, A. Faraone, and E. Mamontov. Observation of fragile-to-strong dynamic crossover in protein hydration water. *Proc. Natl. Acad. Sci. U.S.A.*, 103:9012–9016, 2006.

[108] F. Mallamace, C. Corsaro, P. Baglioni, E. Fratini, and S.-H. Chen. The dynamical crossover phenomenon in bulk water, confined water and protein hydration water. *J. Phys.: Condens. Matter*, 24:064103, 2012.

[109] F. Mallamace, M. Broccio, C. Corsaro, A. Faraone, U. Wanderlingh, L. Liu, C.-Y. Mou, and S. H. Chen. The fragile-to-strong dynamic crossover transition in confined water: nuclear magnetic resonance results. *J. Chem. Phys.*, 124(16):161102, 2006.

[110] Y. Zhang, M. Lagi, L. Dazhi, F. Mallamace, P. Fratini, E. Baglioni, E. Mamontov, and S.-H. Hagen, M. Chen. Observation of high-temperature dynamic crossover in protein hydration water and its relation to reversible denaturation of lysozyme. *J. Chem. Phys.*, 130:135101, 2009.

[111] S.-H. Chen, L. Liu, Y. Chu, X. Zhang, E. Fratini, P. Baglioni, A. Faraone, and E. Mamontov. Experimental evidence of fragile-to-strong dynamic crossover in DNA hydration water. *J. Chem. Phys.*, 125:171103, 2006.

[112] Y. Zhang, M. Lagi, F. Ridi, E. Fratini, P. Baglioni, E. Mamontov, and S.-H. Chen. Observation of dynamic crossover and dynamic heterogeneity in hydration water confined in aged cement paste. *J. Phys.: Conden. Matt.*, 20:502101, 2008.

[113] A. Cupane, M. Fomina, I. Piazza, J. Peters, and G. Shirò. Experimental Evidence for a Liquid-Liquid Crossover in Deeply Cooled Confined Water. *Phys. Rev. Lett.*, 113:215701, 2014.

[114] D. Turton, C. Corsaro, D. F. Martin, F. Mallamace, and K. Wynne. The Dynamic Crossover in Water Does not Require Bulk Water. *Phys. Chem. Chem. Phys.*, 25:8067–8073, 2012.

[115] W. Doster, Busch S., A. M. Gaspar, M.-S. Appavou, J. Wuttke, and H. Scheer. Dynamical Transition of Protein-Hydration Water. *Phys. Rev. Lett.*, 104:098101, 2010.

[116] M. Vogel. Origins of the apparant fragile-to-strong transition of protein hydration waters. *Phys. Rev. Lett.*, 101:225701, 2008.

[117] M. Rosenstihl and M. Vogel. Static and pulsed field gradient nuclear magnetic resonance studies of water diffusion in protein matrices. *J. Chem. Phys.*, 135:164503, 2011.

[118] G. P. Johari. Water's character from dielectric relaxation above its T_g. *J. Chem. Phys.*, 105:7079–7082, 1996.

[119] J. Mattsson, R. Bergman, P. Jacobsson, and L Börjesson. Relaxation processes in supercooled confined water and implications for protein dynamics. *Phys. Rev. B*, 79:174205, 2009.

[120] Johan Sjöström, Jan Swenson, Rikard Bergman, and Shigeharu Kittaka. Investigating hydration dependence of dynamics of confined water: Monolayer, hydration water and Maxwell–Wagner processes. *J. Chem. Phys.*, 128(15):154503, 2008.

[121] J. Swenson, H. Jansson, and R. Bergman. Relaxation Processes in Supercooled Confined Water and Implications for Protein Dynamics. *Phys. Rev. Letters*, 96:247802, 2006.

[122] M. Sattig, S. Reutter, F. Fujara, M. Werner, G. Buntkowsky, and M. Vogel. NMR studies on the temperature-dependent dynamics of confined water. *Phys. Chem. Chem. Phys.*, 16:19229–19240, 2014.

[123] S. Cerveny, F. Mallamace, J. Swenson, M. Vogel, and L. Xu. Confined Water as Model of Supercooled Water. *Chem. Rev.*, 0:0, 2016.

[124] D. Sauer, B. Schuster, M. Rosenstihl, S. Schneider, V. Talluto, T. Walther, T. Blochowicz, B. Stühn, and M. Vogel. Dynamics of water-alcohol mixtures: Insights from nuclear magnetic resonance, broadband dielectric spectroscopy, and triplet solvation dynamics. *J. Chem. Phys.*, 140:114503, 2014.

[125] H. Jansson and J. Swenson. Dynamics of water in molecular sieves by dielectric spectroscopy. *Eur. Phys. J. E*, 12:51–54, 2003.

[126] S. Cerveny, Á. Alegría, and J. Colmenero. Universal features of water dynamics in solutions of hydrophilic polymers, biopolymers, and small glass-forming materials. *Phys. Rev. E*, 77:031803, 2008.

[127] M. Tyagy and S. S. N. Murthy. Dynamics of water in supercooled aqueous solutions of glucose and poly(ethylene glycol)s as studied by dielectric spectroscopy. *Carbohydr. Res.*, 341:650, 2006.

[128] S. Cerveny, G. A. Schwartz, J. Otegui, J. Colmenero, J. Loichen, and S. Westermann. Dielectric study of hydration water in silica nanoparticles. *J. Phys. Chem. C*, 116:24340–24349, 2012.

[129] J. Swenson, K. Elamin, H. Jansson, and S. Kittaka. Why is There no Clear Glass Transition of Confined Water? *Chem. Phys.*, 424(0):20 – 25, 2013.

[130] J. Sjöström, J. Mattsson, R. Bergman, E. Johansson, K. Josefsson, D. Svantesson, and J. Swenson. Dielectric Secondary Relaxation of Water in Aqueous Binary Glass-Formers. *Phys. Chem. Chem. Phys.*, 12:10452 – 10456, 2010.

[131] J. Swenson, H. Jansson, J. Hedström, and R. Bergman. Properties of Hydration Water and its Role in Protein Dynamicss. *J. Phys.: Conden. Matt.*, 19:205109, 2007.

[132] K. L. Ngai, S. Capaccioli, S. Ancherbak, and N. Shinashiki. Resolving the ambiguity of the dynamics of water and clarifying its role in hydrated proteins. *Phil. Mag.*, 91:1809–1835, 2011.

[133] S. Cerveny, G. A. Schwartz, A. Alegria, R. Bergman, and J. Swenson. Water dynamics in n-propylene glycol aqueous solutions. *J. Chem. Phys.*, 124(19):194501, 2006.

[134] J. Sjöström, J. Mattsson, R. Bergman, and J. Swenson. Hydrogen Bond Induced Nonmonotonic Composition Behavior of the Glass Transition in Aqueous Binary Mixtures. *J. Phys. Chem. B*, 115:10013 – 10017, 2011.

[135] I. Popov, A. Greenbaum, A. P. Sokolov, and Y. Feldman. The puzzling first-order phase transition in water-glycerol mixtures. *Phys. Chem. Chem. Phys.*, 17:18063, 2015.

[136] F. Mallamace, C. Corsaro, D. Mallamace, C. Vasi, S. Vasi, and H. E. Stanley. Dynamical properties of water-methanol solutions. *J. Chem. Phys.*, 144:064506, 2016.

[137] P. W. Fenimore, H. Frauenfelder, B. H. McMahon, and R. D. Young. Slaving: Solvent fluctuations dominate protein dynamics and functions. *Proc. Natl. Acad.*, 99:16047 – 16051, 2002.

[138] W. Doster, N. Hakagawa, and M.-S. Appavou. Scaling analysis of biomolecular dynamics derived from elastic incoherent neutron scattering experiments. *J. Chem. Phys.*, 139:045105, 2013.

[139] S. Capaccioli, K. L. Ngai, S. Ancherbak, and A. Paciaroni. [Evidence of Coexistence of Change of Caged Dynamics at T_g and the Dynamic Transition at T_d in Solvated Proteins. *J. Phys. Chem. B*, 116:1745–1757, 2012.

[140] K. Kämpf. *Untersuchung von Protein- und Hydratationswasserdynamik mit Experimenten und Simulationen*. PhD thesis, Technische Universität Darmstadt, 2014.

[141] A. L. Agapov, A. I. Kolesnikov, V. N. Novikov, R. Richert, and A. P. Sokolov. Quantum effects in the dynamics of supercooled water. *Phys. Rev. E*, 91:022312, 2015.

[142] K. Elamin, H. Jansson, S. Kittaka, and J. Swenson. Different Behavior of Water in Confined Solutions of High and Low Solute Concentrations. *Phys. Chem. Chem. Phys.*, 15:18437, 2013.

[143] K. Elamin, H. Jansson, and J. Swenson. Dynamics of aqueous binary glass-formers confined in MCM-41. *Phys. Chem. Chem. Phys.*, 17:12978, 2015.

[144] A. Puzenko, Y. Hayashi, Y. E. Ryabov, I. Balin, Y. Feldman, U. Kaatze, and R. Behrends. Relaxation dynamics in glycerol - water mixtures: I. glycerol-rich mixtures. *J. Phys. Chem. B*, 109:6031 – 6035, 2005.

[145] Y. Hayashi, A. Puzenko, I. Balin, Y. E. Ryabov, and Y. Feldman. Relaxation dynamics in glycerol - water mixtures. 2. mesoscopic featurein water rich mixtures. *J. Phys. Chem. B*, 109:9174 – 9177, 2005.

[146] K. Murata and H. Tanak. Liquid-liquid transition without macroscopic phase separation in a water-glycerol mixture. *Nature Mat.*, 11:436 – 443, 2012.

[147] Y. Feldman, Y. Hayashi, and A. Puzenko. Slow and fast dynamics in glycerol-water mixtures. *J. Non-Cryst. Solids*, 352:4696–703, 2006.

[148] R. Bergman, H. Jansson, and J. Swenson. Slow Debye-type peak observed in the dielectric response of polyalcohols. *J. Chem. Phys.*, 132:044504, 2010.

[149] J. Swenson, J. Sjöström, and F. Fernandez-Alonso. Reduced mobility of di-propylene glycol methylether in its aqueous mixtures by quasielastic neutron scattering. *J. Chem. Phys.*, 133:234506, 2010.

[150] H. Jansson, R. Bergman, and J. Swenson. Hidden Slow Dynamics in Water. *Phys. Rev. Letters*, 104:017802, 2010.

[151] H. Jansson, R. Bergman, and J. Swenson. Slow dielectric response of Debye-type in water and other hydrogen bonded liquids. *J. Mol. Struct.*, 972:92–98, 2010.

[152] J. Sjöström, R. Bergman, C. Wadell, T. Moberg, and J. Swenson. Effects of Water Contamination on the Supercooled Dynamic of a Hydrogen-Bonded Model Glass Former. *J. Phys. Chem. B*, 115:1842–1847, 2011.

[153] Klaus Schmidt-Rohr and Wolfgang Spieß. *Multidimensional Solid-State NMR and Polymers*. Academic Press Ltd., London, 1994.

[154] M. H. Levitt. *Spin Dynamics — Basics of Nuclear Magnetic Resonance*. Wiley, West Sussex, August 2000.

[155] R. Kimmich. *NMR Tomograhpy Diffusometry Relaxometry*. Springer Berlin Heidelberg, 1 edition, 1997.

[156] P. T. Callaghan. *Principles of Nuclear Magnetic Resonance Microscopy* . Clarendon Press, 1994.

[157] M. Vogel. *^{2}H-NMR-Untersuchungen der Sekundärrelaxation in organischen Glasbildern*. PhD thesis, Universität Bayreuth, 2000.

[158] S. A. Lusceac. *Study of relaxation processes in simple glass formers by means of ^{2}H NMR spectroscopy*. PhD thesis, Universität Bayreuth, Bayreuth, November 2005.

[159] Lynne S. Batchelder. *Deuterium NMR in Solids*. John Wiley & Sons, Ltd, 2007.

[160] L. G. Werbelow. *Relaxation Theory for Quadrupolar Nuclei*. John Wiley & Sons, Ltd, 2007.

[161] N. Bloembergen, E. M. Purcell, and R. V. Pound. Relaxation effects in nuclear magnetic resonance absorption. *Phys. Rev.*, 73:679–712, Apr 1948.

[162] G. C. Borgia, R. Brown, and P. Fantazzini. Scaling of spin-echo amplitudes with frequency, diffusion coefficient, pore size, and susceptibility difference for the NMR of fluids in porous media and biological tissues. *Phys. Rev. E*, 51:2104, 1995.

[163] G. E. Pake. Nuclear resonance absorption in hydrated crystals: Fine structure of the proton line. *The Journal of Chemical Physics*, 16(4):327–336, 1948.

[164] W. Spiess. Deuteron spin alignment: A probe for studying ultraslow motions in solids and solid polymers. *J. Chem. Phys.*, 72:6755, 1980.

[165] C. Schmidt, B. Blümich, and H. W. Spiess. Deuteron two-dimensional exchange NMR in solids. *J. Magn. Reson.*, 79:269–290, 1988.

[166] J. Jeener and P. Broekaert. Nuclear magnetic resonance in solids: Thermodynamic effects of a pair of rf pulses. *Phys. Rev.*, 157:232, 1967.

[167] D. Schäfer, J. Leisen, and H. W. Spiess. Experimental Aspects of Multidimensional Exchange Solid-State NMR. *J. Magn. Reson.*, 115:60–79, 1995.

[168] G. Hinze, R. Böhmer, G. Diezemann, and H. Sillescu. Experimental determination of four-time stimulated echoes in liquids, colloidal suspensions, and crystals. *J. Magn. Reson.*, 131:218–223, 1998.

[169] F. Fujara, S. Wefing, and H. W. Spiess. Dynamics of molecular reorientations: Analogies between quasielastic neutron scattering and deuteron NMR spin alignment. *J. Chem. Phys.*, 84(8):4579 – 4584, April 1986.

[170] M. Vogel and E. Rössler. Effects of Various Types of Molecular Dynamics on 1D and 2D ^{2}H NMR Studied by Random Walk Simulations. *J. Magn. Reson.*, 147:43–58, 2000.

[171] W. Schnauss, F. Fujara, K. Hartmann, and H. Sillescu. Nonexponential ^{2}H Spin-Lattice Relaxation as a Signature of the Glassy State. *Chem. Phys. Lett.*, 66:381–384, 1990.

[172] W. Schnauss, F. Fujara, and H. Sillescu. The molecular dynamics around the glass transition and in the glassy state of molecular organic systems: A ^{2}H - nuclear magnetic resonance study. *J. Chem. Phys.*, 97:1378 – 1389, 1992.

[173] G. Diezemann. Dipolar interactions in deuteron spin systems. I. Spin diffusion. *J. Chem. Phys.*, 103:6368, 1995.

[174] B. Kresse, M. Hofmann, A. F. Privalov, N. Fatkullin, F. Fujara, and E. A. Rössler. All Polymer Diffusion Regimes Covered by Combining Field-Cycling and Field-Gradient ^{1}H NMR. *Macromol.*, 48:4491–4502, 2015.

[175] A. C Wang and A. Bax. Minimizing the effects of radio-frequency heating in multidimensional NMR experiments. *J. Biomol. NMR*, 3:715–720, 1993.

[176] S. V. Dvinskikh, V. Castro, and D. Sandström. Heating caused by radiofrequency irradiation and sample rotation in 13C magic angle spinning NMR studies of lipid membranes. *Magn. Resin. Chem.*, 42:875, 2004.

[177] M. Sattig. ^{2}H NMR study on the dynamical behavior of heavy water in hard confinement. Master's thesis, TU Darmstadt, Institut für Festkörperphysik, 2012.

[178] P. C. Ivanov, L. A. Amaral, A. L. Goldberger, and H. E. Stanley. Stochastic feedback and the regulation of biological rhythms. *Europhys. Lett.*, 43:363–368, 1998.

[179] J. E. Anderson. General discussion: Environmental fluctuations and rotational processes in liquids. *Faraday . Symp. Chem. Soc*, 6:82, 1972.

[180] K. Elamin. *Relaxation dynamics of aqueous solutions*. PhD thesis, Department of Applied Physics, Chalmers University of Technology, 2014.

[181] F. Kremer and A.gu Schönhals. *Broadband Dielectric Spectroscopy*. Springer-Verlag, Berlin Heidelberg, 2003.

[182] P Lunkenheimer, U Schneider, R Brand, and A Loidl. Glassy dynamics. *Contemporary Physics*, 41:15–36, 2000.

[183] G. R. Kneller. Quasielastic neutron scattering. Lecture Notes; Centre de Biophysique Moléculaire, 2004.

[184] M. Scheuermann, A. Gädke, S. A. Lusceac, B. Geil, and F. Fujara. Magnetische Kernspinresonanz zum Studium der molekularen Dynamik. Lab course manaul, *IFP, TU Darmstadt*, 2209.

[185] A. Gädke, C. Schmitt, H. Stork, and N. Nestle. DAMARIS — a flexible and open software platform for NMR spectrometer control. *Magn. Reson. Imag.*, 25:576, 2007.

[186] *DAMARIS* online documentation, `http://element.fkp.physik.tu-darmstadt.de/damaris_cms/`, Feb 2016.

[187] F. Fujara, D. Kruk, and A. Privalov. Solid state Field-Cycling NMR relaxometry: Instrumental improvements and new applications. *Prog. Nucl. Magn. Reson. Spectrosc.*, 82:39–69, 2014.

[188] T. Blochowicz, A. Kudlik, S. Benkhof, J. Senker, E. A. Rössler, and G. Hinze. The spectral density in simple organic glass formers: Comparison of dielectric and spin-lattice relaxation. *J. Chem. Phys*, 110:12011 —12022, 1999.

[189] J. S. Beck, J. C. Vartuli, W. J. Roth, M. E. Leonowicz, C. T. Kresge, K. D. Schmitt, C. T. W. Chu, D. H. Olson, and E. W. Sheppard. A new family of mesoporous molecular sieves prepared with liquid crystal templates. *J. Am. Chem. Soc.*, 114(27):10834–10843, 1992.

[190] B. Grünberg, T. Emmler, E. Gedat, I. Shenderovich, G. H. Findenegg, H.-H. Limbach, and G. Buntkowsky. Hydrogen Bonding of Water Confined in Mesoporous Silica MCM-41 and SBA-15 Studied by ^{1}H Solid-State NMR. *Chem. Eur. J.*, 10(22):5689–5696, 2004.

[191] S. Brunauer, P. H. Emmett, and E. Teller. Adsorption of Gases in Multimolecular Layers. *J. Am. Chem. Soc.*, 60:309–319, 1938.

[192] E. P. Barrett, L. G. Joyner, and P. P. Halenda. The determination of pore volume and area distributions in porous substances. I. Computations from nitrogen isotherms. *J. Am. Chem. Soc.*, 73:373–380, 1951.

[193] S. Takahara, N. Sumiyama, and S. Kittaka. Neutron Scattering Study on Dynamics of Water Molecules in MCM-41. 2. Determination of Translational Diffusion Coefficient. *J. Phys. Chem. B*, 109:11231–11239, 2005.

[194] S. Kittaka, S. Ishimaru, M. Kuranishi, T. Matsuda, and T. Yamaguchi. Enthalpy and interfacial free energy changes of water capillary condensed in mesoporous silica, MCM-41 and SBA-15. *Phys. Chem. Chem. Phys*, 8:3223 – 3231, 2006.

[195] S. Kittaka, S. Takahara, H. Matsumoto, Y. Wada, T. J. Satoh, and T. Yamaguchi. Low temperature phase properties of water confined in mesoporous silica MCM-41: Thermodynamic and neutron scattering study. *J. Chem. Phys.*, 138:204714, 2013.

[196] A. Adamczyk, Y Xu, B. Walaszek, F. Rielofs, T. Pery, K. Pelzer, K. Philippot, B. Chaudret, H. H. Limbach, H. Breitzke, and G. Buntkowsky. Solid State and Gas Phase NMR Studies of Immobilized Catalysts and Catalytic Active Nanoparticles. *Top. Catal*, 48:75–83, 2008.

[197] A. Grünberg, X. Yeping, H. Breitzke, and G. Buntkowsky. Solid-State NMR Characterization of Wilkinson's Catalyst Immobilized in Mesoporous SBA-3 Silica. *Chem. Eur. J.*, 16:6993–6998, 2010.

[198] F. Dietrich. ^{2}H-Kernspinresonanzspektroskopie an $^{2}H_2O$ in oberflächenmodifiziertem Confinement MCM-41. Bachelor's thesis, TU Darmstadt, Institut für Festkörperphysik, 2014.

[199] M. Beykirch. ^{2}H NMR-Untersuchungen der Dynamik von Glycerin in isoviskosem Confinement. Bachelor's thesis, TU Darmstadt, Institut für Festkörperphysik, 2015.

[200] M. Schwenk. ^{2}H NMR Messungen von Wasser-Alkohol-Mischungen in hartem Confinement. Bachelor's thesis, TU Darmstadt, Institut für Festkörperphysik, 2015.

[201] D. Sauer. Deuteronen-NMR-Untersuchungen der Dynamik in Wassermischungen. Master's thesis, TU Darmstadt, Institut für Festkörperphysik, 2013.

[202] P. Wendel. ^{2}H NMRUntersuchungen der Dynamik in Wassermischungen in hartem Confinement. Bachelor's thesis, TU Darmstadt, Institut für Festkörperphysik, 2013.

[203] M. P. Reuhl. ^{2}H NMRMessungen von Wasser-Alkohol-Mischungen in hartem Confinement. Bachelor's thesis, TU Darmstadt, Institut für Festkörperphysik, 2015.

[204] J. Swenson, K. Elamin, G. Chen, W. Lohstroh, and V. G. Sakai. Anomalous Dynamics of Aqueous Solutions of di-Propylene Glycol Methylether Confined in MCM-41 by Quasielastic Neutron Scattering. *J. Chem. Phys.*, 141:214501, 2014.

[205] H. E. Stanley, C. A. Angell, U. Essmann, M. Hemmati, P. H. Poole, and F. Sciortino. Is there a second critical point in liquid water? *Physica A:*, 205:122–139, 1994.

[206] P. Ball. Water as an Active Constituent in Cell Biology. *Chem. Rev.*, 108:74–108, 2008.

[207] P. Horcajada, A. Rámila, K. Pérez-Pariente, and M. Vallet-Regí. Influence of pore size of MCM-41 matrices on drug delivery rate. *Micro. Meso. Mat.*, 68:105–109, 2004.

[208] W. M. Ye, Y. J. Cui, L. X. Qian, and B. Chen. An experimental study of the water transfer through confined compacted GMZ bentonite. *Eng. Geo.*, 108:169–176, 2009.

[209] C. A. Angell. Liquid Fragility and the Glass Transition in Water and Aqueous Solutions. *Chem. Rev.*, 102:2627 – 2650, 2002.

[210] F. Löw. *Untersuchungen zur molekularen Dynamik in amorphem Eis*. PhD thesis, TU Darmstadt, 2012.

[211] K. Hartmann W. Schnauss, F. Fujara and H. Sillescu. Nonexponential ^{2}h spin-lattice relaxation as a signature of the glassy state. *Chem. Phys. Lett.*, 166:381–384, 1990.

[212] W. A. Kamitakahara, A. Faraone, K.-H. Liu, and C.-Y. Mou. Temperature dependence of structure and density for D_2O confined in MCM-41-S. *J. Phys.: Condens. Matt.*, 24:064106, 2012.

[213] C. E. Bertrand, Y. Zhang, and S.-H. Chen. Deeply-cooled water under strong confinment: Neutron scattering investigations and the liquid-liquid critical point hypothesis. *Phys. Chem. Chem. Phys*, 15:721 – 745, 2013.

[214] E. Gedat, A. Schreiber, J. Albrecht, I. Shenderovich, G. Findenegg, H.-H. Limbach, and G. Buntkowsky. ^{2}H-Solid-State NMR Study of Benzene-d_6 Confined in Mesoporous Silica SBA-15. *J. Phys. Chem. B*, 106:1977–1984, 2002.

[215] A. Vyalikh, T. Emmler, I. Shenderovich, Y. Zeng, G. H. Findenegg, and G. Buntkowsky. ^{2}H-solid state NMR and DSC study of isobutyric acid in mesoporous silica materials. *Phys. Chem. Chem. Phys.*, 9:2249–2257, 2007.

[216] B. Grünberg, A. Grünberg, H. H. Limbach, and G. Buntkowsky. Melting of Naphthalene Confined in Mesoporous Silica MCM-41. *Appl. Magn. Reson.*, 44:189 – 201, 2013.

[217] H. Pahlke, S. A. Lusceac, B. Geil, and F. Fujara. NMR Study of Local and Long Range Dynamics of Adsorbed Water in Zeolite NaY(Br). *Z. Phys. Chem.*, 226:1093–1113, 2012.

[218] A. Faraone, L. Liu, C.-Y. Mou, C.-W. Yen, and S.-H. Chen. Fragile-to-strong liquid transition in deeply supercooled confined water. *The Journal of Chemical Physics*, 121(22):10843–10846, 2004.

[219] E. Klotz. Master proposal, TU Darmstadt, Institut für Festkörperphysik, 2016.

[220] Masaharu Oguni, Yasuhiro Kanke, Atsushi Nagoe, and Seiaro Namba. Calorimetric Study of Water's Glass Transition in Nanoscale Confinement, Suggesting a Value of 210 K for Bulk Water. *J. Phys. Chem. B*, 115:14023–14029, August 2011.

[221] J. Deschamps, F. Audonnet, N. Brodie-Linder, M. Schöffel, and C. A. Alba-Simionesco. Thermodynamic Limit of the Melting/Freezing Processes of Water under Strongly Hydrophobic Nanoscopic Confinement. *Phys. Chem. Chem. Phys*, 12:1440–1443, 2010.

[222] D. T. Limmer and D. Chandler. The putative liquid-liquid transition is a liquid-solid transition in atomistic models of water. *J. Chem. Phys.*, 135:134503, 2011.

[223] A. K. Soper. Density profile of water confined in cylindrical pores in MCM-41 silica. *J. Phys.: Condens. Matter*, 24:064107, 2012.

[224] G. P. Johari. Origin of the enthalpy features of water in 1.8 nm pores of MCM-41 and the large C_p increase at 210 K. *J. Chem. Phys.*, 130:124518, 2009.

[225] S. Capaccioli, K. L. Ngai, S. Ancherbak, P. A. Rolla, and N. Shinyashiki. The role of primitive relaxation in the dynamics of aqueous mixtures, nano-confined water and hydrated proteins. *J. Non-Cryst. Solids*, 357:641 – 654, 2011.

[226] S. A. Lusceac and M. Vogel. ^{2}H NMR Study of the Water Dynamics in Hydrated Myoglobin. *J. Phys. Chem. B*, 114:10209 – 10216, 2010.

[227] F. Fujara, W. Petry, R. M. Diehl, W. Schnauss, and H. Sillescu. Localized Motion in Supercooled Glycerol as Measured by ^{2}H-NMR Spin-Lattice Relaxation and Incoherent Neutron Scattering. *Europhys. Lett.*, 14:563–568, 1991.

[228] J. Wuttke, W. Petry, G. Coddens, and F. Fujara. Fast dynamics of glass-forming glycerol. *Phys. Rev. E*, 52:4026, 1995.

[229] M. Lannert. *To be published*. PhD thesis, TU Darmstadt.

[230] R. Busselez, R. Lefort, Q. Ji, F. Affouard, and D. Morineau. Molecular dynamics simulation of nanoconfined glycerol. *Phys. Chem. Chem. Phys.*, 11:11127–11133, 2009.

[231] S. Herminghaus, K. Jacobs, and R. Seemann. The glass transition of thin polymer films: some questions, and a possible answer. *Eur. Phys. J. E: Soft Matter Biol. Pyhs.*, 5:531–538, 2001.

[232] J. K. H. Fischer, P. Sippel, D. Denysenko, P. Lunkenheimer, D. Volkmer, and A. Loidl. Metal-organic frameworks as host materials of confined supercooled liquids. *J. Chem. Phys.*, 143:154505, 2015.

[233] M. Vogel, C. Brinkmann, H. Eckert, and A. Heuer. Origin of nonexponential relaxation in a crystalline ionic conductor: A multidimensional ^{109}Ag NMR study. *Phys. Rev. B*, 69:094302, 2004.

[234] R. Böhmer, G. Diezemann, and H. Hinze, G. amd Sillescu. A nuclear magnetic resonance study of higher-order correlation functions in supercooled ortho-terphenyl. *J. Chem. Phys.*, 103:890–899, 1998.

[235] M. Vogel and E. Rössler. On the nature of slow β-process in simple glass formers: A ^{2}H NMR study. *J. Phys. Chem. B*, 104:4285 – 4289, 2000.

[236] M. Arndt, R. Stannarius, H. Groothues, E. Hempel, and F. Kremer. Length scale of cooperativity in the dynamic glass transition. *Phys. Rev. Lett.*, 79:2077 – 2080, 1997.

[237] S. Capponi, S. Napolitano, N. R. Behrnd, G. Coduerc, J. Hulliger, and M. Wübbenhorst. Structural Relaxation in Nanometer Thin Layers of Glycerol. *J. Phys. Chem. C*, 114:16696–16699, 2010.

[238] A. A. Levchenko, P. Jain, O. Trofymluk, P. Yu, A. Navrotsky, and S. Sen. Nature of Molecular Rotation in Supercooled Glycerol under Nanoconfinement. *J. Phys Chem. B*, 114:3070–3074, 2010.

[239] G. Férey and C. Serre. Large breathing effects in three-dimensional porous hybrid matter: facts, analyses, rules and consequences. *Chem. Soc. Rev.*, 38:1380–1399, 2008.

[240] C. R. Herbers, D. Sauer, and M. Vogel. ^{2}H NMR studies of glycerol dynamics in protein matrices. *J. Chem. Phys.*, 136(12):124511, 2012.

[241] M. Alcoutlabi and G. B. McKenna. Effects of confinement on material behaviour at the nanometre size scale. *J. Phys.: Conden. Matt.*, 17:R461–R524, 2005.

[242] C. Gainaru, O. Lips, A. Troshagina, R. Kahlau, A. Brodin, F. Fujara, and E. A. Rössler. On the nature of the high-frequency relaxation in a molecular glass former: A joint study of glycerol by field cycling nmr, dielectric spectroscopy and light scattering. *J. Chem. Phys.*, 128:174505, 2008.

[243] A. Brodin, R. Bergman, J. Mattsson, and E. Rössler. Light scattering and dielectric manifestations of secondary relaxations in molecular glass-formers. *Eur. Phys. J. B*, 36:349–357, 2003.

[244] B. Geil and G. Hinze. Influence of data treatment on the shape of ^{2}H NMR T_1 curves. *Chem. Phys. Lett.*, 216(1–2):51 – 55, 1993.

[245] M. F. Graf, B. Kresse, A. Privalov, and M. Vogel. Combining ^{7}Li NMR field-cycling relaxometry and stimulated-echo experiments: A powerful approach to lithium ion dynamics in solid-state electrolytes. *Solid State Nuclear Magnetic Resonance*, 51-52:25–30, 2013.

[246] K. L. Ngai. Properties of the constant loss in ionically conducting glasses, melts, and crystals. *J. Chem. Phys.*, 110:10576, 1999.

[247] W. Gorbatschow, M. Arndt, R. Stannarius, and F. Kremer. Dynamics of h-bonded liquids confined to nanopores. *Europhys. Lett.*, 35:719–24, 1996.

[248] P. Pissis, A. Kyritsis, G. Barut, R. Pelster, and G. Nimtz. Glass transition in 2- and 3-dimensionally confined liquids. *J. Non-Cryst. Solids*, 235-237:444–449, 1998.

[249] P. Pissis, A. Kyritsis, D. Daoukaki, G. Barut, R. Pelster, and G. Nimtz. Dielectric studies of glass transition in confined propylene glycol. *J. Phys.: Conden. Matt.*, 10:6205–6227, 1998.

[250] R. Bergman, J. Mattsson, C. Svanberg, G. A. Schwartz, and J. Swenson. Confinement effects on the excess wing in the dielectric loss of glass-formers. *Europhys. Lett.*, 64:675, 2003.

[251] J. Swenson, G. A. Schwartz, R. Bergman, and W. S. Howells. Dynamics of propylene glyvol and its oligomers confined in clay. *Eur. Phys. J. E*, 12:179–183, 2003b.

[252] J. Swenson, D. Engberg, W. S. Howells, T. Seydel, and F. Juranyi. Dynamics of propylene glycol and its oligomers confined to a single molecular layer. *J. Chem. Phys.*, 122:244702, 2005.

[253] H. Jansson and J. Swenson. The slow dielectric Debye relaxation of monoalcohols in confined geometries. *J. Chem. Phys.*, 134:104504, 2010.

[254] J. Schüller, Yu. B. Melnichenko, R. Richert, and E. W. Fischer. Dielectric studies of the glass transition in porous media. *Phys. Rev. Lett.*, 73:2224–2227, Oct 1994.

[255] Xiang-Yang Guo, Tobias Watermann, and Daniel Sebastiani. Local microphase separation of a binary liquid under nanoscale confinement. *J. Phys. Chem. B*, 118:10207–10213, 2014.

[256] M. Schmitt. ^{2}H NMRUntersuchungen zu Dynamik von Wassermischungen. Bachelor's thesis, TU Darmstadt, Institut für Festkörperphysik, 2013.

[257] B. Kremmling. ^{2}H-NMR-Untersuchungen der Dynamik von C-Phycocyanin. Masterthesis, TU Darmstadt, Darmstadt, Juli 2011.

[258] K. Elamin and J. Swenson. DS measurments on DiPGME-water mixtures in MCM-41 (Sigma Aldrich). Unpublished data.

[259] M. Erko, G. H. Findenegg, N. Cade, A. G. Michette, and O. Paris. Confinement-induced structural changes of water studied by raman scattering. *Phys. Rev. B*, 84:104205, 2011.

[260] B. Geil, T. M. Kirschgen, and F. Fujara. Mechanism of proton transport in hexagonal ice. *Phys. Rev. B*, 72:014304, 2005.

List of Abbreviations

^{2}H NMR	Deuteron nuclear magnetic resonance
AG	Adam-Gibbs (theory)
ARR	Arrhenius (equation
BPP	Bloembergen Purcell Pound (theory)
BET	Braunauer-Emmett-Teller (method)
BJH	Barrett-Joyner-Halenda (method)
CRR	Cooperative rearranging regions
CS	Chemical shift
CC	Cole-Cole
CD	Cole-Davidson
DS	Dielectric spectroscopy
DSC	Differential scanning calorimetry
DTJ	Disorderd Tetrahedral Jump
EFG	Electrical field gradient
FC	Field cycling
FID	Free induction decay
FR	Fully relaxed
FST	Fragile-to-strong transition
GLY	Glycerol; 1,2,3-propanetriol
HDL	High density liquid
HN	Havriliak-Negami
IRJ	Isotropic Random Jump
ISF	Intermediate scattering function
KWW	Kohlrausch-Williams-Watt (function)
LDL	Low density liquid

LF	Laboratory frame
LLPT	Liquid-liquid phase transition
LLCP	Liquid-liquid critical point
LSA	Line-shape analysis
MCM-41	Mobils Composition of Matter No. 41
MD	Molecular dynamics
MOF	Metal-organic framework
NCL	Nearly constant loss
NMR	Nuclear magnetic resonance
NS	Neutron Scattering
PG	Propylene glycol; 1,2-propanediol
PGME	Propylene glycol monomethyl ether
PR	Partially relaxed
QENS	Quasi elastic neutron scattering
QP	Quadrupolar (interaction)
rf	Radio frequency
sa	Spin alignment
SD	Spectral density
SE	Solid Echo
SFI	Singularity free interpretation
SLC	Stability limit conjecture
SLR	Spin-lattice relaxation
SNR	Signal-to-noise ratio
SR	Saturation recovery
SSR	Spin-spin relaxation
STE	Stimulated Echo
TMD	Temperature of maximum density
VFT	Vogel-Fulcher-Tamman (equation)
ze	Zeeman

List of Figures

Publications and Contributions

[I] M. Sattig, M.Vogel Dynamic Crossovers and Stepwise Solidification of Confined Water: A ^{2}H NMR Study *J. Phys. Chem. Lett.*, 2014, 5, 174–178

[II] M. Sattig, S. Reutter, F. Fujara, M. Werner, G. Buntkowsky, M. Vogel NMR studies on the temperature-dependent dynamics of confined water *Phys. Chem. Chem. Phys*, 2014, 16, 19229–19240

[III] M. Rosenstihl, K. Kämpf, F. Klameth, M. Sattig, M. Vogel Dynamics of interfacial water *J. Non-Cryst. Solids*, 2015, 407, 449–458

[A] *Deuteron-NMR investigation of the dynamics of supercooled, confined water*, Talk, GdCH Halle (2012)

[B] *Deuteron NMR investigation on the dynamics of supercooled, confined water*, Talk, DPG Regensburg (2013)

[C] *^{2}H NMR Experiments on Water and Water-Mixtures in Confinement*, Talk, AK Meeting Paderborn (2014)

[D] *Dynamic Crossover and Stepwise Solidification of Confined Water*, Talk, DPG Dresden (2014)

[E] *Effects of Confinement on the Dynamics of Aqueous Mixtures*, Poster, GdCH Darmstadt (2015)

[F] *Influence of MCM-41 on the dynamical and phase behavior of aqueous mixtures*, Talk, DPG Regensburg (2016)

Curriculum Vitae

Name	Matthias Sattig
Date of birth	16. Juli 1986 in Dieburg, Germany

Education

May 2012 - Jul. 2016	Doctorate Physics	TU Darmstadt
Oct. 2009 - Mar. 2012	Master of Science Physics	TU Darmstadt
Oct. 2009 - Jun. 2010	Erasmus studies in Sweden	KTH Stockholm
Apr. 2007 - Sep. 2009	Bachelor of Science Physics	TU Darmstadt
Jun. 2006	Abitur	Alfred-Delp-Schule Dieburg

Danksagung

Am Ende dieser Arbeit ist es Zeit einen Dank auszusprechen an all diejenigen, die einen Anteil an der Entstehung des *monumentalen* Werkes hatten.
Der größte Dank geht an meine Familie und Freunde, die mit ihrer Unterstützung diese Arbeit erst möglich gemacht haben und mich in einigen verzweifelten Stunden wieder motiviert haben. Besonderer Dank geht dabei an meine Eltern Walter und Christine sowie meinen Bruder Thomas und an die beste Telefonistin des Landes Yvonne, der vermutlich die Ohren bluten von dem vielen Gejammer. Ihr seid die Besten.
Danken möchte ich auch Prof. Michael Vogel, unter dessen Anleitung ich die Möglichkeit hatte, diese Arbeit anzufertigen. Der stete Strom an Ideen und Bachelorstudenten hat dazu beigetragen, dass diese Arbeit seeehr gewichtig wurde. Den Studenten, die einen ansehnlichen Teil der experimentellen Arbeit erledigt haben, gebührt an dieser Stelle ebenfalls ein großer Dank. Philipp Wendel, Maximilian Schmitt, Felix Dietrich, Melanie Rheul und Markus Schwenk, ihr habt mein Genörgel gut ertragen.
Gleichfalls meinen Dank entrichten möchte ich auch allen anderen Mitglieder der AG Vogel und der AG Fujara für die jahrelange fruchtbare Zusammenarbeit auch nach Feierabend. Die Freundlichkeit und Geselligkeit in der Gruppe sucht seinesgleichen. Besonders zu erwähnen sind dabei Markus Rosenstihl, Alexei Privalov, Dominik Demuth, Benjamin Kresse und Max Schmitt für die Unterstützung in allerlei experimentellen und technischen Belangen und ertragreichen Diskussion. Für weitere nützliche Anregungen hat Prof. Franz Fujara gesorgt, wofür auch ihm Dank gebührt, genauso wie für seine Bereitschaft trotz des verdienten Ruhestands das Zweitgutachten zu erstellen. Nicht in Vergessenheit geraten sollen auch die Mitglieder des AK Buntkowsky, insbesondere Mayke Wener und Martin Brodrecht für das Panschen der Proben, sowie Khalid Elamin und Jan Swenson für die wertvolle Zusammenarbeit.
Wertvollen Input und Korrekturen kamen von Kerstin Kämpf, Rebecca Schmitz, Christoph Maurer und Jan Stockemer, denen ich hier Respekt zollen möchte dafür, dass sie sich durch Teile der Arbeit gekämpft haben, ohne sie in die Ecke zu werfen.
Zu guter Letzt bleibt nur der Dank an die Kaffeemaschine und den Kühlschrank, außerdem an Mathilda und Schering aber nicht an Berta ☺.